JOHANNES GUTENBERG
UNIVERSITÄT MAINZ

# Computer simulation of rod-coil block copolymers and tetrapod/polymer mixtures

**Dissertation**

zur Erlangung des Grades
*„Doktor der Naturwissenschaften“*
am Fachbereich Physik, Mathematik und Informatik
der Johannes Gutenberg-Universiät in Mainz

**Stefan Dolezel**

geboren in Hanau

Mainz, den 6.7.2015

Erster Berichterstatter:
Zweiter Berichterstatter:
Datum der mündlilchen Prüfung: 8.12.2015

This work has lead to the following publications:


[73] S. Dolezel, H. Behringer, and F. Schmid. A model for rod-coil block copolymers. *Polymer Science Series C*, 55(1):70–73, July 2013.

[151] J. Lim, L. zur Borg, S. Dolezel, F. Schmid, K. Char, and R. Zentel. Strategy for Good Dispersion of Well-Defined Tetrapods in Semiconducting Polymer Matrices. *Macromolecular rapid communications*, 2014.

[230] F. Schmid, S. Dolezel, O. Lenz, and S. Meinhardt. On ripples and rafts: Curvature induced nanoscale structures in lipid membranes. *Journal of Physics: Conference Series*, 487(1):012004, 2014.

[169] F. Mathias, A. Fokina, K. Landfester, W. Tremel, F. Schmid, K. Char, and R. Zentel. Morphology Control in Biphasic Hybrid Systems of Semiconducting Materials. *Macromolecular Rapid Communications*, 36(11):959–983, 2015.

## Abstract

In this thesis I present a new coarse-grained model suitable to investigate the phase behavior of rod-coil block copolymers on mesoscopic length scales. In this model the rods are represented by hard spherocylinders, whereas the coil block consists of interconnected beads. The interactions between the constituents are based on local densities. This facilitates an efficient Monte-Carlo sampling of the phase space. I verify the applicability of the model and the simulation approach by means of several examples. I treat pure rod systems and mixtures of rod and coil polymers. Then I append coils to the rods and investigate the role of the different model parameters. Furthermore, I compare different implementations of the model. I prove the capability of the rod-coil block copolymers in our model to exhibit typical micro-phase separated configurations as well as extraordinary phases, such as the wavy lamellar state, percolating structures and clusters. Additionally, I demonstrate the metastability of the observed zigzag phase in our model. A central point of this thesis is the examination of the phase behavior of the rod-coil block copolymers in dependence of different chain lengths and interaction strengths between rods and coil. The observations of these studies are summarized in a phase diagram for rod-coil block copolymers. Furthermore, I validate a stabilization of the smectic phase with increasing coil fraction.

In the second part of this work I present a side project in which I derive a model permitting the simulation of tetrapods with and without grafted semiconducting block copolymers. The effect of these polymers is added in an implicit manner by effective interactions between the tetrapods. While the depletion interaction is described in an approximate manner within the Asakura-Oosawa model, the free energy penalty for the brush compression is calculated within the Alexander-de Gennes model. Recent experiments with CdSe tetrapods show that grafted tetrapods are clearly much better dispersed in the polymer matrix than bare tetrapods. My simulations confirm that bare tetrapods tend to aggregate in the matrix of excess polymers, while clustering is significantly reduced after grafting polymer chains to the tetrapods. Finally, I propose a possible extension enabling the simulation of a system with fluctuating volume and demonstrate its basic functionality. This study is originated in a cooperation with an experimental group with the goal to analyze the morphology of these systems in order to find the ideal morphology for hybrid solar cells.

## Zusammenfassung

In dieser Arbeit präsentiere ich ein neues vergröbertes Modell, das geeignet ist das Phasenverhalten von Rod-Coil-Blockcopolymeren auf mesoskopischen Längenskalen zu untersuchen. In diesem Modell werden die Rods durch harte Spherozylinder dargestellt, während der Coilblock aus miteinander verbundenen Perlen besteht. Die Wechselwirkungen zwischen den Bestandteilen basiert auf lokalen Dichten. Dies ermöglicht ein effizientes Monte-Carlo-Sampling des Phasenraumes. Ich überprüfe die Anwendbarkeit des Modells und des Simulationsansatzes anhand mehrerer Beispiele. Ich behandle reine Rodsystemen und Mischungen von Rod und Coil Polymeren. Dann füge ich Coils an die Rods an und untersuche die Rolle der verschiedenen Modellparameter. Des Weiteren vergleiche ich verschiedene Umsetzungen des Modells. Ich belege die Fähigkeit der Rod-Coil-Blockcopolymere in unserem Modell typische mikrophasenseparierte Konfigurationen, sowie außergewöhnliche Phasen wie den wellenförmig lamellären Zustand, perkoliernde Strukturen und Cluster aufzuweisen. Darüber hinaus zeige ich die Metastabilität der beobachteten Zickzack-Phase in unserem Modell. Ein zentraler Punkt dieser Arbeit ist die Untersuchung des Phasenverhaltens der Rod-Coil-Blockcopolymere in Abhängigkeit unterschiedlicher Kettenlängen und Wechselwirkungsstärken zwischen Rods und Coils. Die Beobachtungen dieser Studien sind in einem Phasendiagramm für Rod-Coil-Blockcopolymere zusammengefasst. Darüber hinaus bestätige ich eine Stabilisierung der smektischen Phase mit zunehmendem Coil Anteil.

Im zweiten Teil dieser Arbeit präsentiere ich ein Nebenprojekt, in dem ich ein Modell herleite, das die Simulation von Tetrapoden mit und ohne aufgepfropfte halbleitende Blockcopolymere ermöglicht. Die Wirkung dieser Polymere wird auf implizite Weise durch effektive Wechselwirkungen zwischen den Tetrapoden hinzugefügt. Während die Verarmungs-Wechselwirkung näherungsweise im Asakura-Oosawa Modell beschrieben wird, errechnet sich die freie Energie Strafe für die Kompression der Bürsten innerhalb des Alexander-de Gennes Modells. Jüngste Experimente mit CdSe Tetrapoden zeigen, dass gepfropfte Tetrapoden eindeutig viel besser in der Polymermatrix dispergiert sind als blanke Tetrapoden. Meine Simulationen bestätigen, dass blanke Tetrapoden dazu neigen in der Matrix überschüssiger Polymere zu aggregieren, während die Clusterbildung deutlich reduziert wird, wenn Polymerketten auf die Tetrapoden gepfropft werden. Schließlich schlage ich eine mögliche Erweiterung vor, welche die Simulation von Systemen mit schwankendem Volumen ermöglicht und demonstriere ihre grundlegende Funktionalität. Diese Studie ist in Kooperation mit einer experimentellen Arbeitsgruppe mit dem Ziel entstanden, die Morphologie dieser Systeme zu analysieren, um die ideale Morphologie für Hybrid-Solarzellen zu finden.

# 국문 초록

본 논문에서는 로드-코일 블록 공중합체의 상거동을 연구하는데 적절한 대단위 모형을 개발한다. 이 모형에서 로드는 강체 구원기둥으로 표현하고, 코일은 서로 연결된 구들로 나타내며, 구성요소 사이의 상호작용은 국소 밀도에 의해 결정된다. 이러한 모형을 이용하면 위상 공간상의 몬테카를로 샘플링을 효율적으로 할 수 있다. 본 연구에서는 위와 같은 시뮬레이션 방법을 여러가지 계에 적용하였다. 로드로만 이루어진 계와 로드-코일의 혼합물로 이루어진 계 뿐만이 아니라, 로드에 코일을 붙여서 여러가지 모형 매개변수의 역할에 대해 연구한다. 이 모형을 구현하여 로드-코일 블록 공중합체의 전형적인 상 분리 현상 뿐 아니라 물결무늬 라멜라 상태, 퍼콜레이팅 구조와 클러스터 등의 새로운 상도 보일 수 있다. 또한 지그재그 상의 준안정성도 보일 수가 있다. 이 논문에서 가장 중점적인 내용은 사슬의 길이, 로드와 코일 사이의 상호작용 세기에 따른 로드-코일 블록 공중합체의 상분리 현상 변화를 관찰하는 것이다. 그 결과는 본문의 상평형도에 요약되어 있다. 코일의 분율이 증가함에 따라 스멕틱 상의 안정성이 높아지는 현상 역시 설명할 수 있다.

본 논문의 두번째 부분에서는 반도전성 접목 블록 공중합체의 유무에 따른 네발입자의 시뮬레이션 방법을 설명한다. 이들 고분자의 효과는 네발입자 사이의 상호작용에 의해 간접적인 방법으로 결정된다. 아사쿠라-오사와(Asakura-Oosawa) 모형에서 비움 상호작용이 근사적 방법에 의해 표현되지만, 알렉산더 드장(Alexander-de Gennes) 모형을 이용하면 브러쉬 압축에 따른 자유에너지 페널티를 계산할 수 있다. CdSe 네발입자를 사용한 최근의 실험에 따르면 고분자 기질에 접목된 네발입자의 순수한 네발입자에 비해 잘 퍼지는 것으로 나타났다. 따라서 본 연구에서는 고분자 기질 내에서 네발입자가 서로 뭉쳐 있다가 고분자에 접목되면서 뭉치는 현상이 줄어듦을 확인한다. 위와 같은 연구는 부피가 변화하는 계에 대한 시뮬레이션으로 확장할 수 있고, 또한 그 기본 기능들을 보일 수 있다. 본 연구는 복합태양전지를 위한 이상적인 구조를 갖는 물질을 찾기 위한 실험 그룹과의 협력으로 이루어졌다.

# Contents

# Part I

# Computer simulation of rod-coil block copolymers

Chapter 1

# Introduction

**Contents**



In this introductory chapter we first give the motivation for this thesis. Then we present a general introduction to polymers before we introduce basic polymer models. Afterwards, we discuss the phases different polymer systems may exhibit. Finally, we introduce basic concepts of computer simulations before we emphasize the role of rod-coil block copolymers for photovoltaic devices.

## 1.1 Motivation

In this thesis we present a model to study the self-assembly of rod-coil block copolymers using Monte-Carlo simulations. Such systems have a much higher phase diversity than conventional flexible diblock copolymers. Although, they are extensively studied they are by far less well understood [141, 191]. So far, not all of the large number of self-assembled structures produced in experiments [141, 157] are specified in theoretical studies [141, 191, 243, 280]. There are still very few computer simulations on this topic [11, 12, 42, 50, 59, 103, 110, 115, 124, 156, 208]. With our study we want to contribute to a deeper understanding of the phase behavior of rod-coil block copolymer systems.

The investigation of conjugated rod-coil block copolymers forming structures on a nanometer scale with optimized domain sizes and large interface areas is not only of academic interest, but highly relevant from a technological point of view. Former studies show that the existence of domains with a size comparable to the exciton diffusion length is highly beneficial for the efficiency of light-emitting or photovoltaic devices [98, 188, 222, 296]. Conventionally, techniques such as spin coating are used to deposit the most commonly used thin multilayer films on substrates. A major disadvantage of such deposition methods is that they are highly non-equilibrium processes. Drawbacks of these non-equilibrium states are that their structures have a limited lifetime due to interdiffusion at higher temperatures and are hard to control, since they depend critically on details of the fabrication process [108, 258]. That motivates the research on alternative systems that spontaneously form the desired nanostructures as equilibrium states.

Promising candidates are block copolymers with two covalently linked components [63, 108, 141, 157, 188, 189, 222, 231, 253, 254, 258]. These $\pi$-conjugated polymers are often rigid and can add various functionalities, like photophysical properties, to the supramolecular materials. The stiffness asymmetry between rigid rod and flexible coil blocks influences the details of molecular packing and so imparts a microphase separation into a variety of nanostructures with tunable morphologies already at relatively low molecular weight [141]. The much richer phase behavior of rod-coil block copolymers can be exploited to design functional materials with adjustable properties and, thus, to achieve low-cost, large-area electronic devices [62]. Former works demonstrate that a variation of the rod to coil volume ratio allows a precisely controllable manipulation of the supramolecular structures desired for such devices [141]. Therefore, this ratio is an important parameter for our simulations.

This thesis is structured as follows. After a short introduction to polymers, their general phase behavior and examples for their application in this chapter we give a short overview over research on polymers done so far in the next chapter. In Chapter 3 we introduce the model we use to represent the rod-coil block copolymers in our simulations. In Chapter 4 we investigate the role and interplay of the model parameters before we present the phase diagram and some further results in Chapter 5.

In the second part of this work we simulate tetrapod/polymer mixtures. After reviewing some selected work in Chapter 6 we explain the used model in Chapter 7. In Chapter 8 we present the results of our simulations. Finally, we summarize our results in Chapter 9 and give an outlook on future work.

## 1.2 Introduction to polymers

In this section we present general properties of polymers. Polymers are large molecules or macromolecules for their part consisting of multiples of repeated, simpler units called monomers. The process of monomer molecules forming polymer chains in a chemical reaction is called polymerization. The usually very long chains of polymers often mainly consist of carbon atoms. Polymers containing only one type of monomer are called homopolymers. If the chains consist of different types of monomer units they are denoted as copolymers. A series of identical monomers is called a block. Copolymers with two or three distinct blocks are denoted as diblock or triblock copolymers, respectively. If the number of blocks is unambiguous they are usually only called block copolymers. Very short polymers are referred to as oligomers. Translated literally from the ancient Greek polymer means "many parts", whereas oligomer would translate to "a few parts".

A distinction is made between natural and synthetic polymers. While natural polymers, such as nucleic acids, DNA and proteins play a crucial role in living things, synthetic polymers like plastics and rubbers are of high importance for our everyday life. Beside linear chains there are several other architectures, such as star polymers, brush polymers, cyclic polymers or other branched structures. In most syntheses a lot of effort is put into the control of branching during the polymerization, which may otherwise occur randomly. In copolymers the monomers may arrange in different structures, for example, as alternating, grafted, statistical, periodic or block copolymer. A selection of polymer architectures is displayed in Figure (1.1).

Polymers differ greatly in their properties. A main point of distinction is the stiffness of a polymer, which has a strong influence on the phase behavior of the system. The stiffness of a polymer chain is characterized by its persistence length. Flexible homopolymers commonly have a persistence length of around one nanometer, while it is about ten to hundred nanometers for rod-like polymers [45]. The combination to rod-coil block copolymers is found to be very beneficial and, thus, of great interest. Figure (1.2a) summarizes a number of exemplary structures for rigid and flexible polymers, which may be combined to conjugated rod-coil block copolymers in various combinations. The two major synthesis methods, grafting-from and grafting-onto, some possible morphologies and potential applications of rod-coil diblock copolymers are illustrated in Figure (1.2b).

There are several length scales in a polymeric system. The smallest length scale is the microscopic length scale. It reaches from the bond length between the atoms of one Angstrom to the persistence length of a single chain, which is around one nanometer. The mesoscopic length scale starts at a few nanometers and ends at several hundred nanometers. The extension of a single polymer and the average distance between polymers falls in this range. The macroscopic length scale is of the size of the sample. In most cases this are several centimeters. Macroscopic objects are visible with the naked eye.

The size of materials like biomolecules, colloids, liquid crystals and polymers approximately ranges from a few nanometers to a micron. The predominant physical behaviors occur at an energy scale comparable with room temperature thermal energy. Therefore, the macroscopic behavior of these materials may be determined by the properties and interactions of their mesoscopic structures.

**Figure 1.1** Polymer architectures. Homopolymers consist of only one monomer type A. Diblock and triblock copolymers have a second and third monomer type labeled as B and C. Here all blocks are drawn as flexible coil blocks. But either block may also be a rigid rod block. Other structures like brush, star and cyclic polymers or combined and more complex structures are possible.

Homopolymer

$A - A - A - \cdots - A - A - A$

Diblock copolymer

$A - A - A - \cdots - B - B - B$

Triblock copolymer

$A - A - A - \cdots - B - B - B - \cdots - C - C - C$

Brush polymer

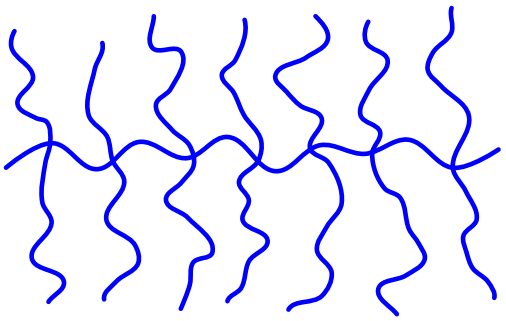

Star polymer

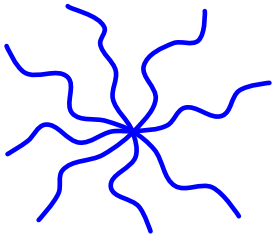

Cyclic polymer

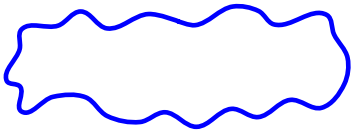

**Figure 1.2** (a) A small selection of numerous polymers used for conjugated rod-coil block copolymers. (b) Synthesis methods, morphologies and applications of conjugated rod-coil block copolymers. Both from [157].

**(a)**

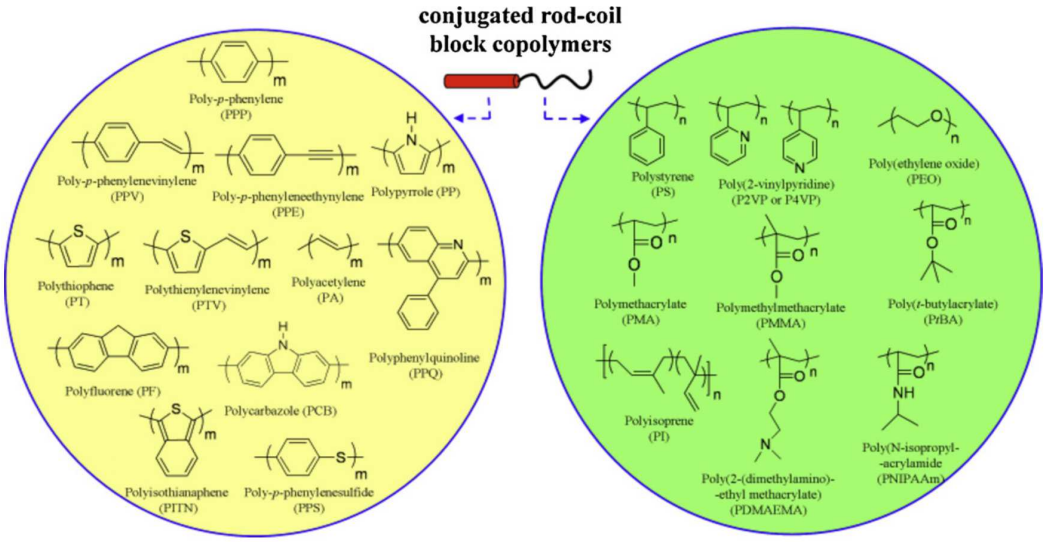


**(b)**

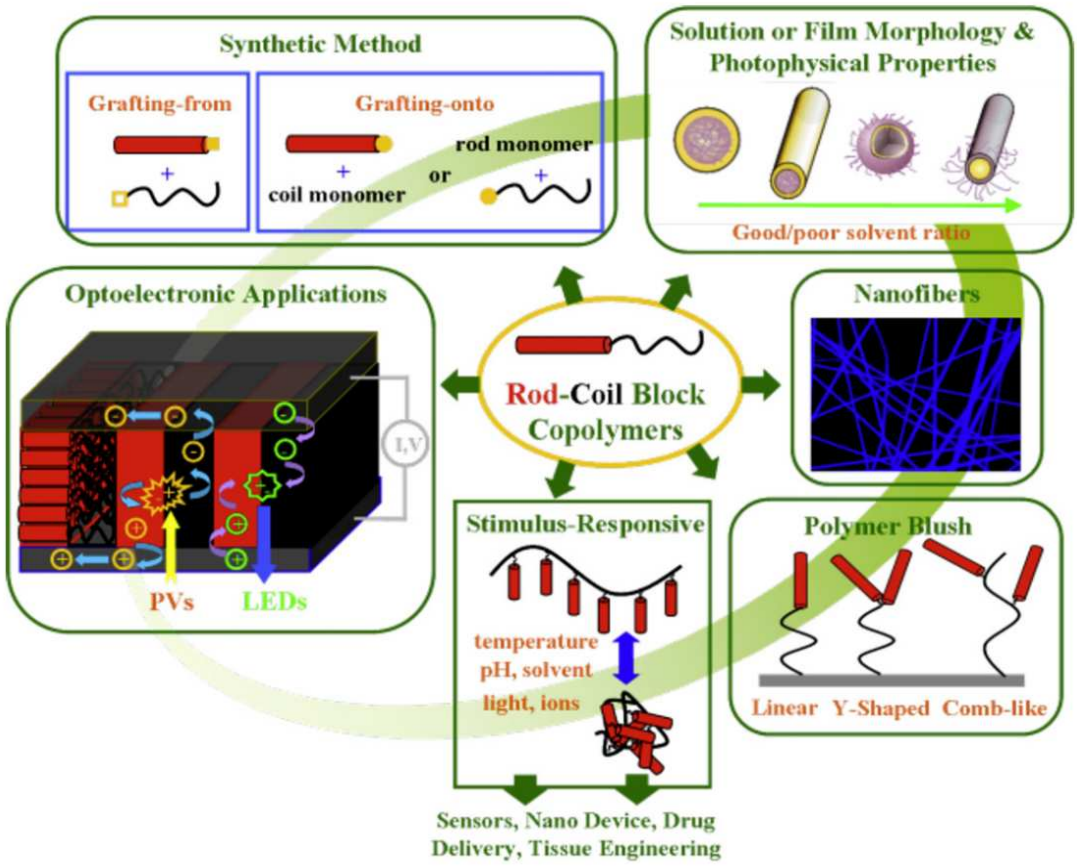

## 1.3 Polymer models

Since polymers are very large molecules and a system often contains a huge amount of polymers the properties of such systems can not be determined deterministically. Hence, a statistical approach is needed. A lot of different models have been developed to study the characteristics of polymers. In this section we introduce a few basic concepts used in these models and some theories for coil-like polymers and polymer solutions. Theories for rod-like polymers and rod-coil block copolymers are described in Chapter 2.

Coil-like polymers are usually modeled as continuous flexible chains, connected spheres or monomers with no volume. Depending on the polymer composition systems with coil-like polymers show a versatile phase behavior. It is obvious that homopolymers behave differently than complex polymer brushes or star polymers. In this work we only treat diblock copolymers with two incompatible blocks. The phases these coil-coil diblock copolymers may exhibit are described in the following section. More information can be found in the relevant literature [65, 72, 217].

A polymer chain may be modeled as ideal or real chain. In real chain models monomers avoid each other reducing the conformational possibilities of the chain. This effect is often modeled using an excluded volume interaction. Especially for lattice models this is implemented as a self-avoiding random walk.

Models using ideal chains assume that the monomers have no interaction and may, therefore, overlap. The most prominent ideal chain models are the Gaussian chain model, the freely-jointed, freely-rotating and the worm-like chain model. In the freely-jointed chain model a polymer consists of a given number of linearly connected fixed length segments. All of these segments are freely movable and the polymer can be described by a simple random walk. These ideal chains are often referred to as Gaussian chains. The freely-rotating chain model additionally takes into account that adjacent polymer segments prefer a fixed bond angle. In further improved models the angles are characterized by rotational energy potentials. The worm-like chain model is a continuous model describing the behavior of semi-flexible polymers. The model is based on the idea that bending a polymer requires energy. An important parameter for this model is the persistence length, which is a measure for the stiffness of a polymer. At a length scale below the persistence length the polymer is almost rigid.

A concentrated solution that contains no more solvent and is composed solely of polymer chains is called a polymer melt. A particular feature of such polymer chains is that their confirmation on large scales can approximately be described by an ideal Gaussian chain [65]. For other polymer solutions its behavior often strongly depends on the solvent, at which one mainly distinguishes between good, poor and $\Theta$-solvent. A coil-like polymer will contract in a poor solvent, while it will expand in a good solvent. In a $\Theta$-solvent, or more precisely at the $\Theta$-point, excluded volume interactions are neutralized and polymer coils act like ideal chains.

There are plenty of studies on coil-like copolymers [26, 33, 94, 95, 106, 146, 162, 173, 194, 223, 258]. A good review is for example given by Tseng and Darling [260]. Here, we mention some prominent theories and models for such polymers. The different approaches differ hugely in their complexity. Some models are only suitable for very coarse models, while others are very detailed and complex representations of the polymer systems.

Self-consistent field theories are closely related to the mean field approach [74, 82, 146, 170, 171, 173, 183, 227, 243, 299]. The basic idea is that the distribution of the monomers is determined by a potential which itself depends self-consistently on the positions of the particles. The equations of this theory can usually only be solved numerically and become exact in the limit $N \to \infty$ [228]. There are also lattice-based self-consistent field theories [224, 225]. But it is known that they are not well suited for the nonlamellar structures exhibited by block copolymers due to the geometric constraints associated with a lattice [173].

A prominent approach to describe polymer solutions is the Flory–Huggins theory [78, 118]. Originally it is derived for a lattice model but there are numerous improved versions for off-lattice models [77, 82, 156, 228] and extended approaches describing rod-coil block copolymers [101, 172, 184, 208].

An important formula in this model is the change of the Gibbs free energy $\Delta G$ which is of high importance for thermodynamic effects. Its final form reads

$$\Delta G = RT \left( \frac{\phi_\mathrm{A}}{N_\mathrm{A}} \ln\left(\phi_\mathrm{A}\right) + \frac{\phi_\mathrm{B}}{N_\mathrm{B}} \ln\left(\phi_\mathrm{B}\right) + \chi \phi_\mathrm{A} \phi_\mathrm{B} \right) \tag{1.1}$$

where $R$ is the gas constant, $T$ the temperature, $N_\alpha$ and $\phi_\alpha$ are the number and the volume fraction of the components $\alpha = \mathrm{A}$ or B and $\chi$ is the Flory-Huggins parameter. This parameter takes the enthalpic incompatibility of the two components into account. It is given by

$$\chi = \frac{z}{k_\mathrm{B} T} \left( \epsilon_\mathrm{AB} - \frac{1}{2} \left( \epsilon_\mathrm{AA} + \epsilon_\mathrm{BB} \right) \right) \tag{1.2}$$

with $z$ being a characteristic of the lattice, $k_\mathrm{B}$ the Boltzmann constant and the $\epsilon_{\alpha\beta}$ correspond to the interaction energies between neighboring monomers on the lattice. The Flory-Huggins $\chi$-parameter for polymer solutions is temperature dependent following the formula

$$\chi = \frac{a}{k_\mathrm{B} T} + b \tag{1.3}$$

where $a$ and $b$ are numerical values which differ for each system. The Flory-Huggins interaction can be measured from experiments, as for example done by Olsen et al. [191], for a given rod-coil block copolymer system. A positive value of $\chi$ indicates an unfavorable interaction between the different polymer segments, whereas the mixing is favorable for negative $\chi$ values [20].

The Edwards model [72] is used as basis for the interactions with coils in this thesis. We describe the model in more detail in Section 3.4.2 on page 58. Here, we just give a brief overview. In the Edwards model the polymer coil is represented as elastic string with Gaussian statistics. Especially in coarse-grained models in the majority of cases a discretized chain model is used. This way the volume interaction can be related to local number densities of the chain monomers. Thus, a fast sampling is possible while preserving the feature of the chains that they are self-repelling, but not self-avoiding. This is characteristic for ideal chains without excluded volume. The model is widely used to study block copolymers and polymer brushes [24, 25, 75, 137, 210, 238, 284].

There are a lot of different models which are capable to represent rod-like polymers in theories and simulations. Basic theories profit from the ease of a simple representation allowing an analytically closed or otherwise beneficial description of rods and their behavior. Models with a more realistic representation and behavior are often much

harder to compute. On the side of simulations computer power has always been a limiting factor, therefore, often only very simple systems can be computed. A lot of studies concentrate on small and mostly two-dimensional systems [21, 53, 101, 235] often combined with oversimplifications such as the restriction to parallel orientated rods [54, 239, 255, 271] or lattice models [1, 79, 138, 139, 233, 283]. A lot differently shaped prolate and oblate particles are used to simulate anisotropic particles. Starting with simple rods [86, 200, 207] more complex shapes like ellipsoids [6, 35, 36, 47, 89, 202, 219, 229], discs [40, 185], dumbells [219], cylinders [270] and, as in this work, spherocylinders are used to represent stiff polymers. For each of these particle shapes a variety of different interaction and simulation models can be used. Some models for rod-like polymers are mentioned in the following chapter.

## 1.4 Polymer phases

In this work we investigate the phase behavior of different polymers. Most of these polymers consist of different components with unequal properties. Isolated each of these components would show a more or less wide variety of diverse phases. If one combines these polymers single phases may be suppressed, strengthened or new phases may develop. In this section we introduce some of the most prominent polymer phases.

### 1.4.1 Coil-coil copolymer phases

At first we discuss phases of block copolymers consisting of two flexible, immiscible blocks. To characterize the copolymers we first introduce some parameters. If we assume that our diblock copolymers consists of two dissimilar blocks labeled A and B the volume fraction of polymer A is usually denoted by

$$f_{\mathrm{A}} = \phi_{\mathrm{A}} = \frac{V_{\mathrm{A}}}{V_{\mathrm{A}} - V_{\mathrm{B}}} \tag{1.4}$$

and the volume fraction of polymer B by

$$f_{\mathrm{B}} = \phi_{\mathrm{B}} = 1 - \phi_{\mathrm{A}}. \tag{1.5}$$

In most cases the incompatibility between these two blocks is characterized by the Flory-Huggins parameter $\chi$. Due to the incompatibility between the blocks these copolymers can microphase separate to form periodic structures. The morphology depends on both the volume fraction $f$ and the interaction strength. Figure (1.3) shows typical phases and a phase diagram for block copolymers. Note that the phase diagram is symmetric around a fraction $f$ of 0.5. For very low interaction strength only the disordered phase exists. For higher $\chi$ values more phases appear. An exemplary order of occupied phases is illustrated in Figure (1.3b). These phase occur in a range of around twenty to forty for $\chi N$ in the phase diagram imaged in Figure (1.3a). Starting from a spherical phase with increasing volume fraction at first a cylindrical, then a gyroid and finally a lamellar phase can be found. If the volume fraction increases further the phases recur in a symmetric manner.

**Figure 1.3** (a) Mean-field phase diagram. Here $f$ denotes the fraction of the A block and $\chi N$ is the product of the Flory-Huggins parameter $\chi$ and the number of segments $N$. The shown phases are disordered (DIS), close-packed spheres (CPS), bicontinuous Ia$\bar{3}$d cubic ($Q_{\mathrm{Ia\bar{3}d}}$), lamellar (L), hexagonal cylinders (H) and bcc spheres ($Q_{\mathrm{Im\bar{3}m}}$). From [173]. (b) Some phases of a coil-coil diblock copolymer as formed by self-assembly in the bulk with increasing volume fraction $f_{\mathrm{A}}$ of the A block. From [33].

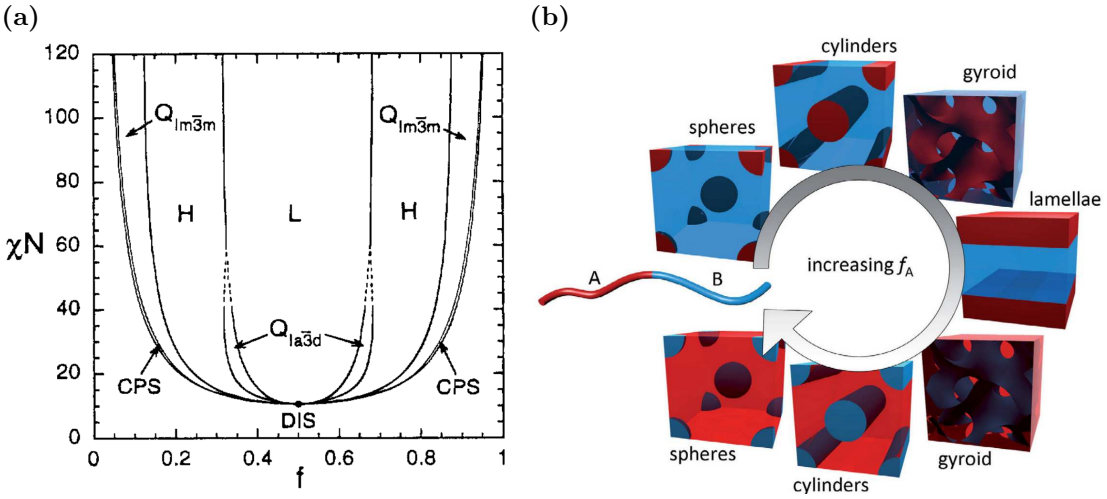


## 1.4.2 Phases of rod-like polymers

Polymers with a high inherent chain stiffness show a completely different phase behavior. Stiff polymers are most commonly represented by hard, elongated particles of different shape. Their shape anisotropy, density, interactions and other properties cause them to form liquid crystal phases in solution. These phases are located between the solid and the fluid state and are neither liquid nor crystalline. For this reason they are called liquid crystal phases or mesophases. The simplest example are hard spheres. Distributing them randomly at different densities they may end up in a fluid or a crystalline state. For anisotropic particles on the other side several additional phases may exist at intermediate densities.

Liquid crystals can be classified into two main categories: thermotropic and lyotropic liquid crystals. The phase transitions of thermotropic liquid crystals are primary induced by temperature. The molecules in lyotropic liquid crystals consist of two distinct parts, which in most cases are a nonpolar tail and a polar head group. The phase transitions depend on both temperature and solvent concentration, where the latter is the predominant parameter.

In the following, we describe some phases of thermotropic liquid crystals, which are sketched in Figure (1.4). In the liquid or isotropic phase (I) there is neither a positional nor an orientational order. Because of its lack of long-range order the isotropic phase is said to have zero-dimensional order. At lower temperatures the nematic phase (N) with one-dimensional order appears. This means that a nematic has a high long-range orientational order, but no positional order. In other words, while the long axes of the nonspherical component particles are oriented around a preferred axis the center of

mass positions are randomly distributed as in a liquid. This preferred axis is called the director and indicated by the vector **n**. The smectic phases are found at lower temperature and form well-defined layers which are characterized by the layer normal vector **k**. The molecular packing within the layers is liquid-like and has no long range positional order. Similar to the behavior of a soap the layers can slide over one another. The layered structure and the parallel orientation of the molecular axes leads to a two-dimensional order. There are different smectic phases of which we will only mention two. In the smectic A phase (SmA) the molecules are on average oriented along the layer normal **k**, while the director **n** is tilted by an angle $\theta$ relative to the layer normal **k** in the smectic C phase (SmC). The solid or crystalline phase (C) is characterized by a periodic positional and orientational long-range order of the constituents. This phase is stable for low temperatures and there are only thermal vibrations about the equilibrium positions. The solid phase has a three-dimensional order. Further phases exist, but will not be described within this work. We just note that the formation of curved interfaces is strongly hindered because of the preferred parallel arrangement of the rigid rods [141]. Studies show that the nematic, smectic A and smectic C phases do not need any attractive interactions, but can be obtained from purely packing effects [239].

**Figure 1.4** Liquid crystal phases in dependence of the temperature. At high temperatures the system is isotropic. With decreasing temperature the system first becomes nematic, then smectic and finally crystalline. The vector **n** denotes the director of the system and the layer normal is represented by the vector **k**. In the smectic C phase the director is tilted by an angle $\theta$ relative to the layer normal.

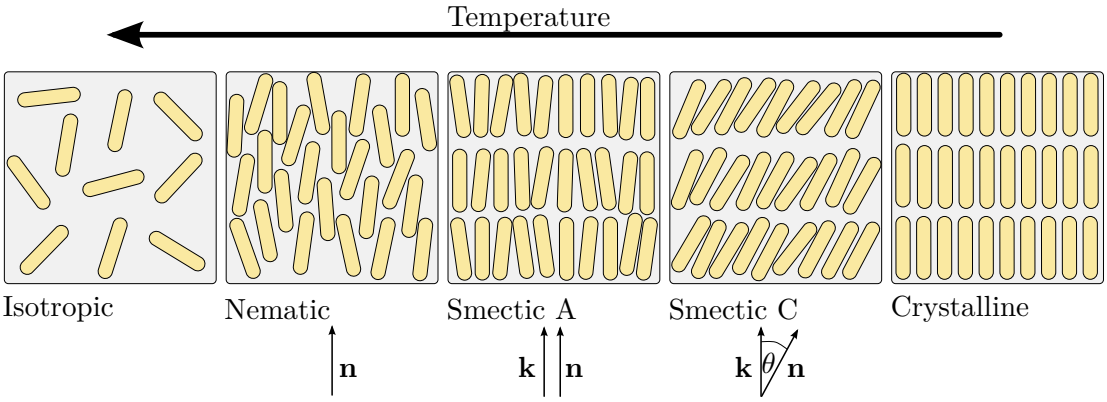


The phase behavior of lyotropic liquid crystals is more diversified, which comes not solely from the fact that the solvent concentration introduces an additional degree of freedom. Lyotropic liquid crystals are often composed of amphiphilic molecules with a hydrophilic head-group attached to a hydrophobic group. An exemplary phase diagram of an amphiphilic system imaging higher-ordered phases in dependence of the temperature and the amphiphile concentration is illustrated in Figure (1.5). The phases are similar to the phases observed for immiscible diblock copolymers displayed in Figure (1.3).

**Figure 1.5** Schematic of lyotropic phases as a function of amphiphile concentration and of temperature. Starting from micelles an increase in amphiphile concentration leads to a micellar cubic phase ($I_1$). For even higher concentrations the hexagonal phase ($H_I$), the bicontinuous cubic phase ($V_I$) and the lamellar phase ($L_\alpha$) can be found. From [285]

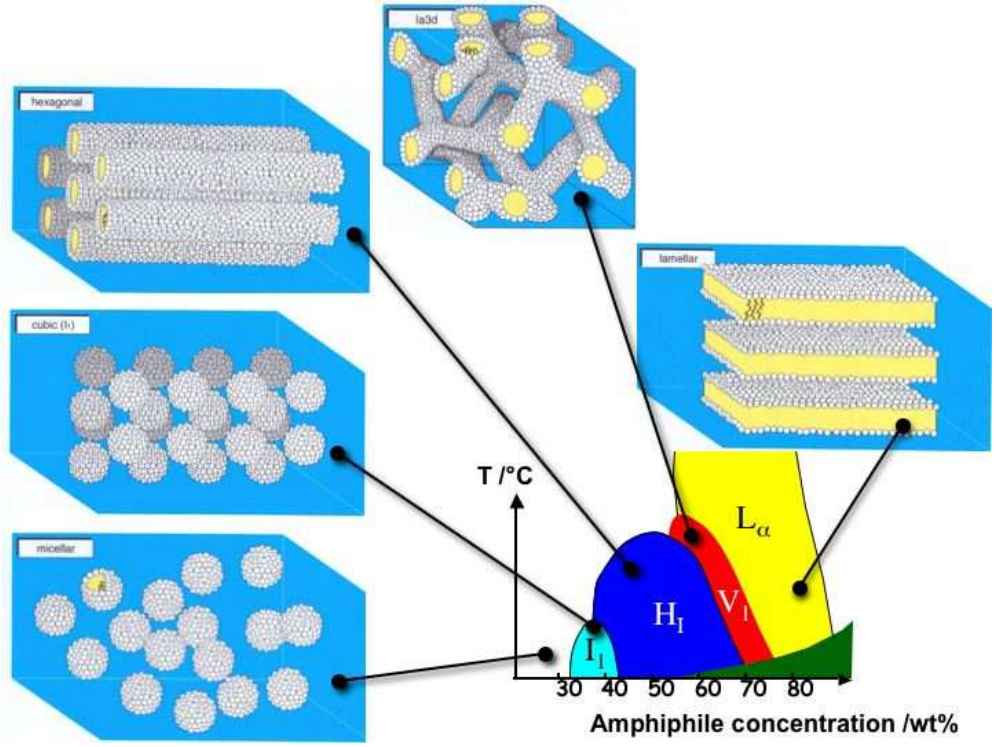


### 1.4.3 Rod-coil block copolymer phases

In contrast to flexible coil-coil block copolymers rod-coil block copolymers have substantial packing problems in the microphase-separated state [45]. As we have seen rod-like and coil-like polymers show a different phase behavior. As rod-coil block copolymers both components are chemically bound to each other and, therefore, can not segregate anymore. Hence, a macroscopic phase separation is inhibited [227]. Nevertheless, the local packing effects of the rods enforce the formation of liquid crystalline or even semi-crystalline order in the rod domains. Simultaneously, the incompatibility between the chemically different monomers results in a conformational entropy of the coils. The interplay between these two effects can lead to morphologies that are distinctly different from those exhibited by coil-coil diblock copolymers [131]. Thus, the observed phase behavior is much richer than that of pure rod polymer and coil-coil diblock copolymer systems, but it is far less understood.

Figure (1.6) shows the molecular packing of possible rod-coil block copolymer microphases. The isotropic and nematic phases do not differ much from the corresponding liquid crystal phases. For a very high coil fraction a hockey puck phase is predicted [286]. The smectic phases may occur in monolayers or bilayers. The arrowhead, zigzag and a wavy lamellar phase, which is not illustrated here, are found by several groups [44, 45, 156, 226]. The zigzag phase is also called chevron phase, whereas the arrowhead phase is sometimes referred to as smectic O phase.

**Figure 1.6** Illustration of some rod-coil block copolymer microphases. For low densities or high temperatures we have an isotropic phase. The nematic phase has a slightly higher degree of order. For very high coil fraction a hockey puck phase may be observed. In the arrowhead or smectic O phase the layers are tilted contrariwise. The smectic phases can be found in monolayer or bilayer structures. The zigzag phase is sometimes also referred to as chevron phase.

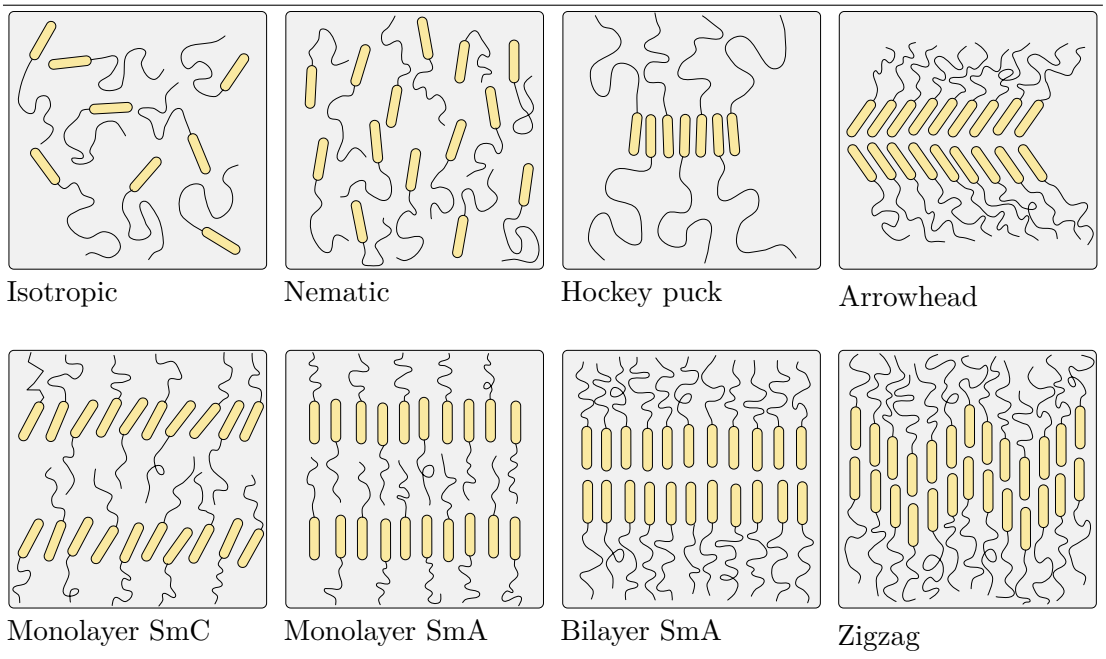


More phases, including transmission electron microscopy images, and a phase diagram for self-assembled rod-coil block copolymers are illustrated in Figure (1.7). Note that the phase diagram is not symmetric, as it is for coil-coil block copolymers (see Figure (1.3)). In addition to the already mentioned phases, we see a spherical and a hexagonal columnar phase for high coil fraction.

### 1.4.4 Measuring methods

There are plenty of techniques to characterize polymers, identify their morphology or determine other properties of interest. We only mention a couple of them here. The transmission electron microscopy (TEM) creates an image from the interaction of electrons, which are transmitted through the sample. Atomic force microscopy (AFM) images are generated by measuring the deflection of a sharp tip, which is at the end of a cantilever, with the sample surface. X-ray scattering is a non-destructive method gaining structural informations by observing the scattered intensity of a X-ray beam in dependence of, for example, the scattering angle or energy. One distinguishes between small-angle X-ray scattering (SAXS) and wide-angle X-ray scattering (WAXS). A similar technique is the neutron scattering, where neutrons are used instead of X-rays. Typically, small-angle neutron scattering (SANS) is used. In a lot of cases several methods have to be combined to gather all informations needed to fully characterize a polymer.

**Figure 1.7** Phase diagram for self-assembled rod-coil block copolymers. Each phase is displayed schematically and with a transmission electron microscopy image. The rod volume fraction is plotted against the Flory-Huggins $\chi$-parameter times the number of segments $N$. From [220].

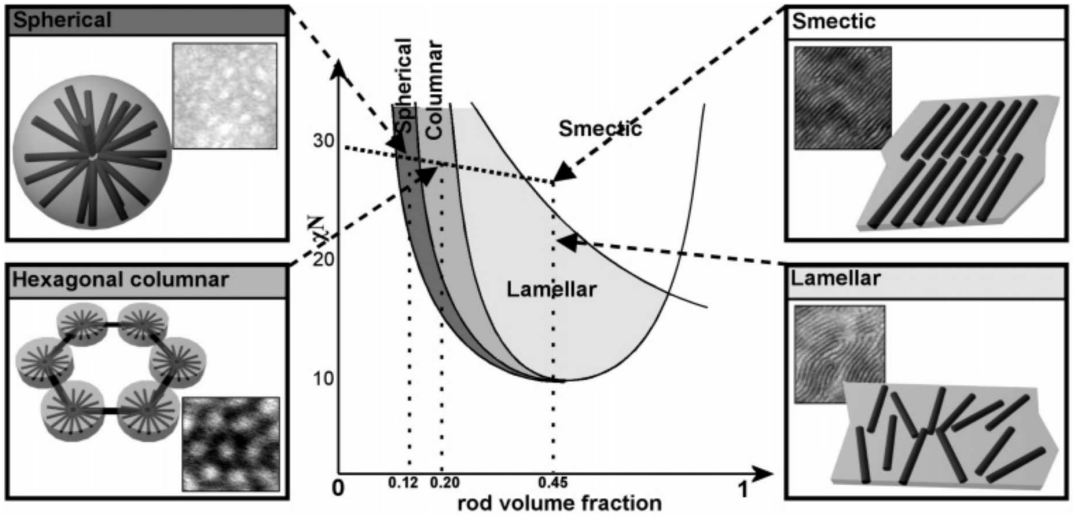


## 1.5 Computer simulations

In this section we give an overview over different computer simulation methods. The importance of computer simulations increased significantly during the last years. In the past, theories tried to describe experimental results and make predictions, which were tested by further experiments. The investigation of systems too complicated to calculate analytically, too hard to realize in experimental setups or too expensive were beyond reach. With the availability of computers and the accompanying development of new methods such systems became accessible. Due to the fast increase in computer power more complicated, detailed and bigger systems can be computed. Therefore, the implementation of such calculations rapidly gains importance in science. While comparisons with experimental results are still of paramount importance, computer simulations can help to encourage an intelligent and efficient selection of interesting systems to investigate in detail.

As computational power is still limited, it is often necessary to use advanced methods and it is not yet practicable to simulate systems efficiently on all length and time scales. Commonly methods such as Molecular Dynamics (MD), Dissipative Particle Dynamics (DPD), the Lattice-Boltzmann method and Monte-Carlo simulations (MC) are used [9, 10, 85, 135]. These methods are usually combined with highly developed algorithms [90, 273, 281] and approaches such as the so-called coarse-graining [36, 83, 130, 166, 227].

The basic idea behind coarse-graining is to concentrate on the important parameters of the system. This is done by combining different parameters to reduce the number of degrees of freedom in the system. Depending on the goal of the study this can be done on different levels. For a realistic model on the atomistic level all atoms and molecules have to be taken into account. Models on the microscopic and mesoscopic

level simplify the structure of molecules and combine several atoms to one particle. On the macroscopic scale single particles are not considered anymore, but the systems are described by continuum models. Figure (1.8) shows a schematic of a complicated polypeptide, which is replaced by a hard spherocylinder in the coarse-grained model.

**Figure 1.8** Example of a coarse-grained polymer. The relatively rigid polypeptide poly($\gamma$-benzyl-L-glutamate) is represented by a hard spherocylinder of length $L$ and diameter $D$. From [292].

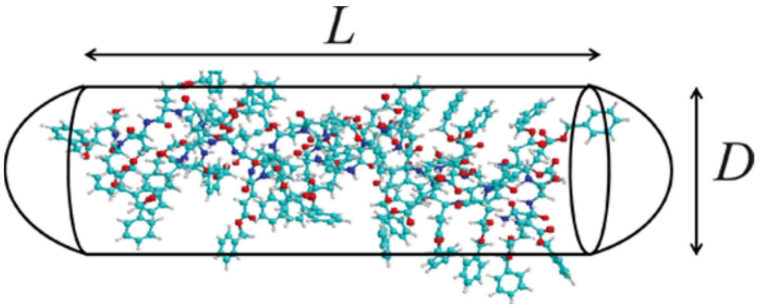


In this work we investigate the self-assembly of rod-coil block copolymers. Our model has to account for the possibility of local orientational and crystalline order of the rigid domains, as well as for the conformational degrees of freedom of the coil domains. To ensure that we capture the relevant physics we treat both domains at different coarse-graining levels. The rods are modeled as hard spherocylinders and their extended size is explicitly taken into account. The coils are represented by monomers connected via flexible chains. Their interactions are implemented via an Edwards Hamiltonian, which depends on local densities [72, 82, 228]. The interactions between rods and coils are defined in terms of a density functional. This way an efficient Monte-Carlo sampling of the configurations is feasible.

## 1.6 Photovoltaics

In this section we highlight possible applications of the systems studied in this thesis. One application for conjugated rod-coil block copolymers are optoelectronic devices. Compared to inorganic solar cells the advantages of these devices are their mechanical flexibility, the light weight, the feasibility of chemical modifications and their easy and cheap processing. Their properties are especially advantageous for the use in organic photovoltaic devices. Such devices convert light into direct current. The four steps involved in the fundamental mechanism converting photons to electrons in an organic solar cell are displayed in Figure (1.9).

The illustrated device consists of two regions. Both regions have a highest occupied molecular orbital (HOMO) and a lowest unoccupied molecular orbital (LUMO). The material with the energetically lower LUMO level is called electron acceptor, while the material with the higher LUMO level is the electron donor. Donor materials are often conjugated polymers.

**Figure 1.9** Illustration of the four steps of photon to electron conversion in an organic solar cell. (i) Photon absorption. (ii) Exciton diffusion. (iii) Charge separation. (iv) Charge collection. The single steps and meanings of the efficiencies $\eta$ are explained in detail in the text. From [247].

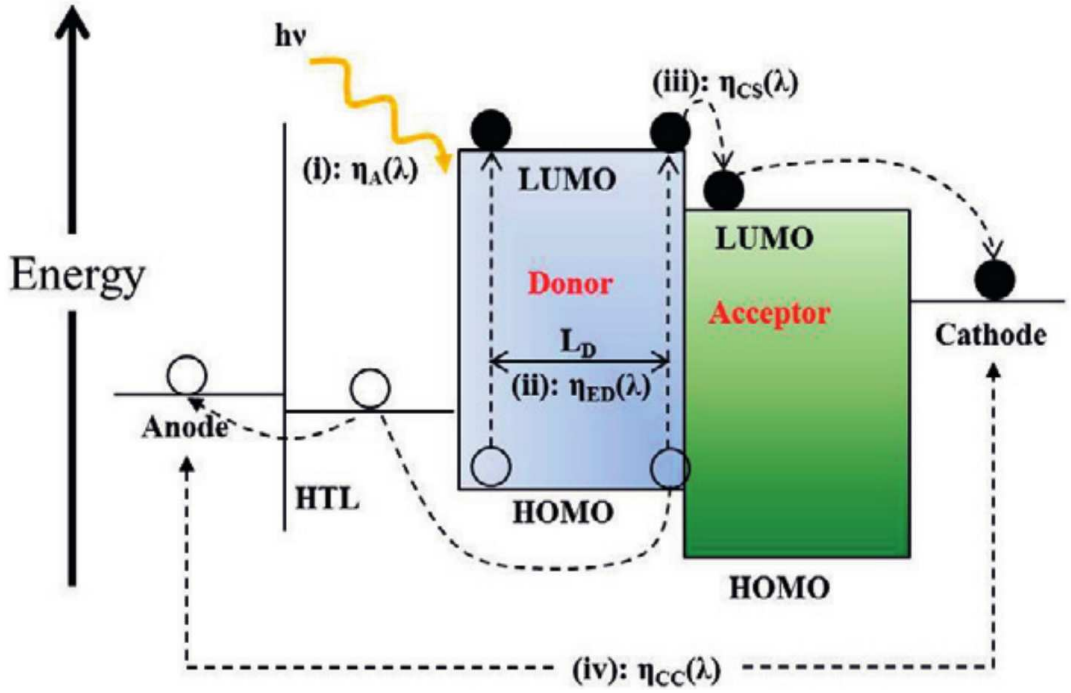


At first, the absorption of a photon creates an excited state. The photon energy $E_{\text{photon}}$ has to be high enough to excite an electron from the HOMO to the LUMO of the active layer

$$E_{\text{photon}} = \frac{ch}{\lambda_{\text{photon}}} \geq E_{\text{g}} = E_{\text{LUMO}} - E_{\text{HOMO}} \tag{1.6}$$

where $c$ is the speed of light, $h$ the Planck constant and $\lambda_{\text{photon}}$ the wavelength of the light. The band gap energy $E_{\text{g}}$ is defined as the difference between the LUMO and HOMO energies. In most organic photovoltaic devices the band gap energy is between one and four electronvolts. The resulting excited state is a coulombically bound electron-hole pair, a so-called exciton, or more precisely, a Frenkel exciton [111]. Here, we assume that the excitons are generated in the donor phase, which is usually the case.

But not all photons are absorbed in the material. In order to be absorbed photons have to traverse a certain thickness of active layer. Therefore, a thickness on the order of 100 nm and above is needed. Above the LUMO there is a continuum of states. If the energy of the photon is higher than the band gap energy $E_{\text{g}}$ the excited electron will undergo thermal relaxation until the LUMO level is reached. The energy difference is lost as heat. Choosing appropriate materials may reduce this loss. The ratio of absorbed photons to the total incident photons is characterized by the absorption efficiency $\eta_{\text{A}}$.

In the second step this exciton must diffuse to the interface between electron donor and acceptor, where a charge separation occurs. Since the exciton only has a limited lifetime this interface must be reached before the exciton can recombine to the ground

state. This happens after a diffusion length $L_D$, which usually is around 10 nm in organic materials [296]. From experience it is known that domain sizes should be slightly greater than the exciton diffusion length. Therefore, small domain sizes below 20 nm are preferable. The ratio of the excitons that reach the interface to the number of generated excitons is defined as exciton diffusion efficiency $\eta_{ED}$.

In the third step the exciton at the donor-acceptor interface gets into a charge-transfer state. In this state there is still a chance that the electron and the hole can recombine. The charge separation efficiency $\eta_{CS}$ describes the ratio of the number of excitons that have undergone the charge-transfer process to the number of excitons that have reached the donor-acceptor interface. The charge-transfer state is an intermediate state just before the electron and the hole are separated [201]. The process of charge separation is called exciton dissociation [18]. The energy difference between the LUMO levels must be greater than the exciton binding energy $E_{\text{binding}}^{\text{exciton}}$ to ensure the built-in internal field is strong enough to break up the exciton into free carriers

$$E_{\text{LUMO}}^{\text{donor}} - E_{\text{LUMO}}^{\text{acceptor}} \geq E_{\text{binding}}^{\text{exciton}}. \tag{1.7}$$

The selection of proper materials influences the binding energy of excitons. It is known that $\pi$-conjugated materials have large binding energies. In organic materials it is typically about one electronvolt [111], which is much lower than the thermal energy at room temperature being approximately 25 meV. This is a principal difference to inorganic photovoltaic devices, which have a much lower exciton binding energy so a spontaneous charge separation may already be achieved at room temperature [33].

In the last step the free electrons and holes are transported to their respective electrodes through the acceptor and donor phases, respectively. This is only possible if there is a pathway from the interface to the corresponding electrode. Therefore, the formation of continuous morphologies is inevitable. The ratio of carriers that reach the electrodes to the number of excitons that have undergone the charge-transfer process is defined as charge collection efficiency $\eta_{CC}$.

In summary, we can conclude that the choice of suitable materials is of crucial importance when engineering efficient photovoltaic devices. Not only the energy levels have to fulfill the requirements, but also the phase behavior must be readily controllable, since the most important parameter remains the size of the domains. The film must be thick enough to absorb a proper amount of photons and at the same time thin enough so the excitons can reach the interface before they recombine. For an efficient dissociation large donor-acceptor interfaces are needed. For this purpose the size of the domains has to be minimized. On the other hand percolating, ideally bicontinuous structures are required to efficiently transport holes and electrons from the interfaces to their appropriate electrodes [13]. The formation of isolated donor or acceptor domains, where charges can be trapped, should be avoided. But morphologies with all these properties are very difficult to realize.

Not only the fabrication and the processes during the synthesis [91, 117, 157, 193, 221, 279, 293, 302] have to be optimized, but also new techniques like nanopatterning [43, 215, 251], templating [32][295], ink jet printing [41, 107, 196], screen printing [198, 209] or micromoulding [99, 214] have to be developed. Several approaches to engineer better devices, such as organometallic photovoltaics [290] or nanocrystal solar cells [17, 49, 97, 98, 249] and the use of triblock copolymers [4, 59, 141, 157, 187, 246] or tetrapods [61, 81, 149, 151, 197] have been made. Among them rod-coil block copolymers are very

promising materials forming tunable morphologies with the desired characteristics. The use of backbone conjugated polymers is favorable as they have appropriate charge mobilities [254] and large exciton binding energies. Because of their delocalized electronic structures these polymers often exhibit a high stiffness. In addition, the aggregation arising from interchain $\pi$-$\pi$-orbital interactions leads to a low solubility in organic media [63] and unique morphologies on the nanometer scale. In the following, we compare different morphologies and their influence on the efficiency of photovoltaic devices.

Figure (1.10) summarizes some possible morphologies of block copolymers for photovoltaic devices. The bilayer morphology (a) comprises a very small interfacial area, but provides a direct pathway between the anode and the cathode. The disordered structure (c) has the highest interfacial area of all shown morphologies, but an uninterrupted pathway to the electrodes is very unlikely. The same drawback applies to the slightly higher ordered morphology displayed in (d), where holes or electrons are trapped in the isolated regions. A very common structure is illustrated in (b). The bulk heterojunction morphology arises from the microphase separation due to the incompatibility of the polymer blocks. It combines a big interfacial area and large structures allowing an efficient charge separation and transport. A shortcoming of this morphology is that the formation of the supramolecular structures is hard to control. Hence, rod-coil block copolymers are a promising alternative to the commonly used polymer blends. They are believed to self assemble into highly ordered structures as presented in (e) featuring the desired properties.

**Figure 1.10** Different morphologies of block copolymers. (a) The bilayer morphology has the smallest interfacial area, but the most direct pathways to the electrodes. (b) Bulk heterojunctions combine a large interfacial area and large structures, but the morphology is hard to control. (c) The disordered structure has the largest interfacial area, but it is very unlikely that there is a pathway to the electrodes for the electrons and holes. (d) This slightly higher ordered structure still has a big interfacial area, but most electrons and holes will be trapped in isolated areas. (e) Block copolymer self-assembled structures are tunable, provide a large interfacial area and continuous pathways. From [254].

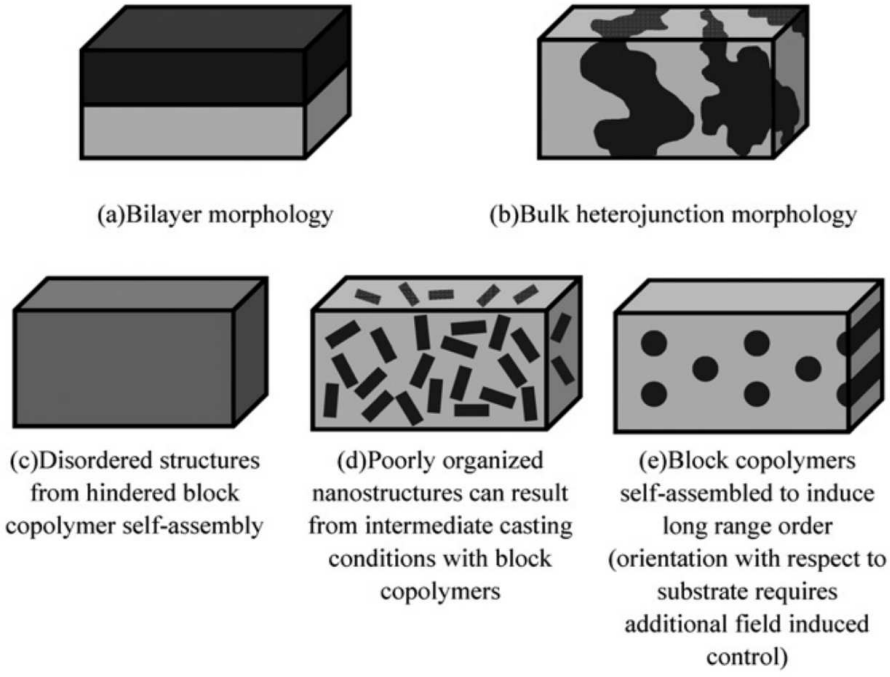


The influence of the chosen polymers on the morphology and, therefore, the efficiency of solar cells is summarized in Figure (1.11). Figure (1.11a) shows an optoelectronic device build with coil-coil block copolymers developing a bulk heterojunction morphology. The highly ordered morphology gained by using rod-coil block copolymers, displayed in Figure (1.11b), would yield a much higher photocurrent. Since the domain size of the morphology is on the nanometer scale the amount of excitons that collapse before they can reach an interface is reduced to a minimum. Additionally, the morphology guarantees an efficient charge transport to the electrodes.

The efficiency of photovoltaic devices can be determined from current versus voltage curves. A typical plot including some critical values is shown in Figure (1.12). In an ideal device the maximum power $P_{\max}$ obtainable is the product of the short-circuit photocurrent $J_{\mathrm{sc}}$ and the open-circuit voltage $V_{\mathrm{oc}}$. However, in real devices less power is generated. The power $P_{\mathrm{M_{PP}}}$ at the maximum power point $\mathrm{M_{PP}}$ is defined, where the product of the real current $J_{\mathrm{M_{PP}}}$ and voltage $V_{\mathrm{M_{PP}}}$ values reaches its maximum value. The ratio of the real maximum power $P_{\mathrm{M_{PP}}}$ to the theoretical maximum value $P_{\max}$ is denoted as fill factor FF. The product of FF and $P_{\max}$ divided by the total power of the incident light is the device efficiency $\eta_{\mathrm{eff}}$.

**Figure 1.11** Schematics of solar cells with different morphologies. (a) Bulk heterojunction morphology as typical for coil-coil block copolymers. From [63]. (b) Rod-coil block copolymers form a highly ordered morphology. From [231].

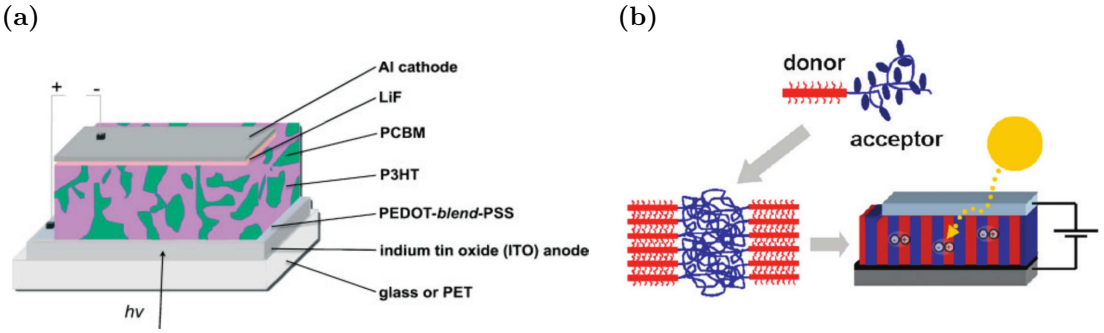


**Figure 1.12** Typical curve for the current density $J$ plotted against the voltage $V$ of an organic solar cell. Critical values determining device efficiency are marked. This includes the short-circuit current $J_{\mathrm{sc}}$, open-circuit voltage $V_{\mathrm{oc}}$ and the current $J_{\mathrm{M_{PP}}}$ and voltage $V_{\mathrm{M_{PP}}}$ for the maximum power point $\mathrm{M_{PP}}$. The ratio of the outlined area defined by the maximum power points and the product of $J_{\mathrm{sc}}$ and $V_{\mathrm{oc}}$ is the fill factor FF. The device efficiency $\eta_{\mathrm{eff}}$ is the product of $J_{\mathrm{sc}}$, $V_{\mathrm{oc}}$ and FF divided by the total power of the incident light. From [231].

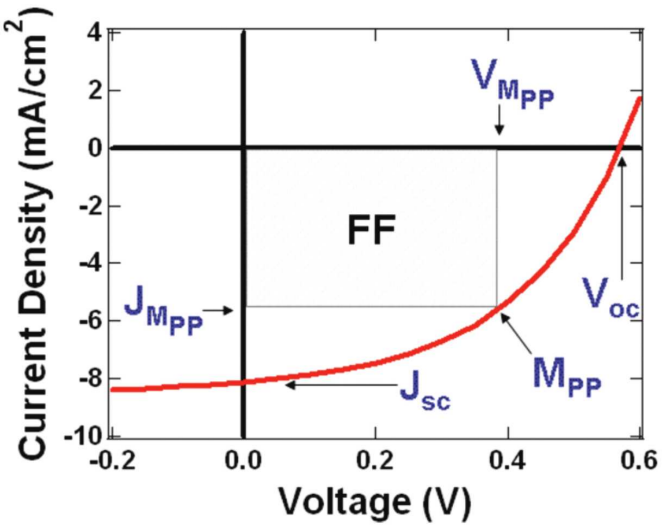


In this thesis we investigate the phase behavior of rod-coil block copolymers and tetrapod/polymer mixtures. Both are potential candidates for fine-tunable systems self-assembling into morphologies beneficial for efficient photovoltaic devices. Therefore, we hope that the results of this work are helpful to design more efficient photovoltaic devices such as solar cells.

Chapter 2

# Research Review

Contents



In this chapter we give a brief overview over the research related to our work. After a brief introduction to a few models and theories which describe rod-like polymers we concentrate on research results of pure rod systems and rod/coil polymer mixtures. Afterwards, we review results for rod-coil diblock copolymers. In the final section we show some exemplary applications.

## 2.1 Models and theories

In this section we present some models and theories for systems containing rod-like particles. The interactions between rods may be modeled with soft or hard core interactions. A prominent soft particle model is the Gay-Berne model [88]. A related model is the hard Gaussian overlap model [36, 195]. One approach to improve these models is to use Lennard-Jones sticks [275] to represent the linear molecules. But there are many more models, for example, for soft spherocylinders [7, 119, 277, 301]. Hard particle models, as used in this thesis, are also prevalent [29, 30, 147, 158, 235, 255, 266, 274, 292].

Not all studies are restricted to unary systems composed of monodisperse particles. Some studies include polydisperse particles [19, 53] or binary [2, 19, 70, 71, 270] and ternary [75, 216] mixtures. In other works the influence of external fields [92], such as magnetic fields [253], is investigated. In their Monte-Carlo study Vácha and Frenkel [265], for example, add an attractive, hydrophobic stripe at the side of their rod-like particles. De Michele et al. [68] build chains of hard quasi-cylinders with two reactive sides as model for DNA, which form a nematic phase for high densities. An overview over the phase behavior of rod-like viruses, virus-sphere mixtures, charged rods, semi-flexible rods and binary mixtures is given by Dogic and Fraden [71].

At first, we introduce some theories predicting and describing phase transitions for systems composed of rod-like particles. Based on the used model and theory phase transitions are found to be of first or second order. For some phase transitions it has been ambiguous if they are of first or second order for a long time.

In his pioneering work in 1949 Onsager [192] predicts an entropy driven isotropic-nematic phase transition for fluids of hard nonspherical particles. He introduces a now well-accepted free-energy functional for the nematic state and is the first to propose that orientational ordering in an athermal molecular fluid may be explained as an excluded volume effect. The entropy of a three-dimensional gas of hard rods has two contributions: one due to orientation $\Delta S_{\mathrm{or}}$ and one due to translation $\Delta S_{\mathrm{tr}}$. While the first has a very low entropy for a parallel orientation of the rods the latter one favors such an aligned configuration since it reduces the excluded volume $V_{\mathrm{excl}}$ to zero. The two entropy contributions are

$$\Delta S_{\mathrm{or}} = k_{\mathrm{B}} \ln\left(\frac{\Omega_N}{\Omega_I}\right) \sim k_{\mathrm{B}} \tag{2.1}$$

$$\Delta S_{\mathrm{tr}} = -k_{\mathrm{B}} \ln\left(1 - \frac{V_{\mathrm{excl}}}{V}\right) \sim k_{\mathrm{B}} \rho L^2 D \tag{2.2}$$

where $k_{\mathrm{B}}$ is the Boltzmann constant, $\Omega_I$ and $\Omega_N$ give the number of orientational states in the isotropic or nematic phase and $\rho = N/V$ is the density of the rods with length $L$ and diameter $D$. For very low densities the orientational term wins and the system is isotropic. At very high densities a nematic system with perfect alignment is most favorable. Therefore, there has to be a transition between these two phases at any point. At the isotropic-nematic transition point the two contributions of the entropy compensate each other

$$\Delta S_{\mathrm{tr}} + \Delta S_{\mathrm{or}} = 0 \tag{2.3}$$

and one obtains a critical density

$$\rho_c \sim \frac{1}{L^2 D} \tag{2.4}$$

and volume fraction

$$\Phi_c = \frac{V_{\text{rods}}}{V} \sim \frac{D}{L}. \tag{2.5}$$

Onsager thus shows that a system of infinitely long rods exhibits an isotropic to nematic transition at a vanishingly low density.

The Onsager theory is developed at the level of the second virial coefficient, which is directly related to the excluded volume [278]. Onsager demonstrates that the excess free energy can be truncated at the second virial coefficient level for a fluid of rods with large, actually infinite, length-to-width ratio. For hard spherocylinders the virial coefficients are analytically only known up to the second order [92], but are determined up to fifth order by several groups [34, 52, 182, 278].

In the Landau theory [93, 136, 244] of phase transitions the free energy $\mathcal{F}$ is expanded as a power series in an order parameter $S$. Landau suggests that the free energy should be analytic and comply to the symmetry of the Hamiltonian. For reasons of thermodynamic stability terms of odd order in the order parameter are neglected. Since the first terms dominate the power series, higher contributions can be truncated and, thus, it may be written as

$$\mathcal{F} = \mathcal{F}_i + \frac{1}{2}AS^2 + \frac{1}{4}BS^4 \tag{2.6}$$

where $\mathcal{F}_i$ is the free energy of the isotropic phase and $A$ and $B$ are coefficients which may depend on temperature and pressure. In order to find the transition points one has to minimize the derivative of this equation

$$0 = AS + BS^3 \tag{2.7}$$

and obtains the solutions

$$S = 0 \tag{2.8}$$

$$S^2 = -\frac{A}{B} \tag{2.9}$$

whereas the first solution corresponds to the isotropic phase while the others correspond to the nematic phase.

Another important theory is developed by Maier and Saupe [163, 164, 165] and widely used [36, 50, 114, 116, 160, 179, 207, 208, 213, 294]. It describes rod-like, nonpolar molecules interacting via attractive van der Waals interactions. The anisotropy stabilizes parallel alignment of neighboring rods. Using the mean field approximation and solving the theory self-consistently it predicts a first-order nematic-isotropic phase transition at a given temperature. The Maier-Saupe interaction is characterized by an interaction parameter which is most commonly labeled $\mu$ or $\omega$ and represents the steric repulsion between rods. The potential energy $U_i$ of the $i$-th molecule in dependence of the global order parameter $S$ is given by

$$U_i(\theta_i, S) = -\frac{AS}{V^2}\left(\frac{3}{2}\cos^2\theta_i - \frac{1}{2}\right) \tag{2.10}$$

where $\theta_i$ is the angle between the director and the molecular axis and $A$ is a constant. With this the Helmholtz free energy $\mathcal{F}$ for $N$ molecules can be computed as

$$\mathcal{F} = U - T\Sigma = N\langle U_i\rangle - TN\left\langle \frac{U_i}{T} + k_{\text{B}}\ln Z\right\rangle = N\left(\frac{AS^2}{2V^2} - k_{\text{B}}T\ln Z\right) \tag{2.11}$$

where $\Sigma$ is the entropy and $Z$ the partition function. In the isotropic phase $S$ is zero and $Z = 4\pi$ and hence $\mathcal{F}_{\text{iso}} = -Nk_{\text{B}}T \ln 4\pi$. It can be shown that for values of $S$ greater than 0.43 the free energy of the nematic phase is smaller than $\mathcal{F}_{\text{iso}}$ and, therefore, only stable in this regime. The predicted phase transition at $S_c = 0.43$ is of first order.

Another prominent theory is the scaled particle theory [55, 56, 71, 142, 264, 278]. The basic idea is to calculate the work required to insert an additional particle at a fixed position and so obtain the excess part of the chemical potential. This is done by expanding, or scaling, the particle from zero to its final size. In contrast to the Onsager approach this theory for hard rods takes the virial coefficients of third and higher order into account in an approximate way. The scaled particle theory may also be incorporated with other methods like Monte Carlo simulations resulting in a hybrid method [125]. The scaled particle theory predicts a first order nematic-isotropic transition for hard spherocylinders if $L/D$ is smaller than 5.44 and a continuous nematic-isotropic transition for $L/D$ greater than 5.44 [21]. Based on this theory more sophisticated theories like the extended scaled particle theory [121] and an extension to flexible, worm-like chains [127, 128, 129] are developed.

Density functional theories [76, 112, 199, 291] are another type of theories. There are several density functional theories for hard body particles [51, 92, 206, 207]. Density functional theories exploit the fact that the Helmholtz free energy of a system can be expressed as a functional of the density. Minimizing this free energy functional by a variational principle an equilibrium density profile can be derived [82]. The basis for a density field theory may for instance be a self-consistent field theory or a mean field theory.

## 2.2 Pure rod systems

In this section we summarize several studies of systems only containing rod-like particles. The group of rigid, rod-like polymers includes simple rods, cylinders, ellipsoids, spherocylinders and other elongated particles. The basic phases exhibited by such particles are introduced in Section 1.4 and summarized in Figure (1.4).

In this thesis the rods are represented by hard spherocylinders. Therefore, we put a focus on hard spherocylinder models in this review as well. The hard spherocylinder model consists of an impenetrable cylinder of length $L$, which is capped at both ends by hemispheres. Their diameters $D$ are the same as the diameter of the cylinder. Hard spherocylinders combine a simple and parameter-lean interaction and a rich phase behavior, as they are known to form nematic, smectic and crystalline phases. Another advantage of this model is that it leads to the well-known hard-sphere model for the isotropic limit $L$ to zero.

Given that hard rods have a sufficient length they show liquid crystalline phase behavior. There are several studies focusing on the nematic phase [200, 241, 282]. Using Monte-Carlo simulations Bates and Frenkel [21] demonstrate that in a two-dimensional hard rod fluid the length-to-diameter ratio $L/D$ has to be at least seven to exhibit a nematic phase. As they mention this limit is higher than in the three-dimensional case, where the nematic phase is observed for a length-to-diameter ratio around four [29]. In later works Frenkel et al. [84, 86] show that spherocylinders of finite length-to-width ratio $L/D$ may also form a smectic phase. A lot of different works demonstrate that

hard rod systems interacting through excluded volume interactions alone can exhibit a smectic phase [21, 54, 84, 86, 206]. Simulation results also demonstrate the existence of a rotator or plastic phase for short spherocylinders [29, 274]. The Monte-Carlo simulations of Casey and Harrowell [39] outline which cluster size of hard spherocylinders is sufficient to exhibit a stable nematic or smectic phase.

One of the first studies of hard spherocylinders is done by Cotter and Martire [57] using the scaled particle theory in 1970. They find a transition from a perfectly aligned to a completely isotropic system resulting from packing effects alone. This indicates that repulsive forces alone are sufficient to produce a stable aligned phase and a first-order aligned-isotropic transition at ordinary liquid densities. Figure (2.1a) shows the dependence of the transition free volume fractions $v_0$ on the length-to-width ratio $x$. One year later McMillan [179] propose a new model extending the Maier-Saupe model. Within the mean field approximation this model exhibits the isotropic, nematic and smectic A phase. The resulting phase diagram is illustrated in Figure (2.1b) where $\alpha$ is a dimensionless parameter representing the interaction strength of the smectic A phase.

**Figure 2.1** (a) Dependence of the transition free volume fractions $v_0$ on the length-to-breadth ratio $x$. From [57]. (b) Phase diagram for rods with a theoretical model parameter $\alpha$. On the left axis the transition temperature is plotted while the right axis shows the transition entropy. From [179].

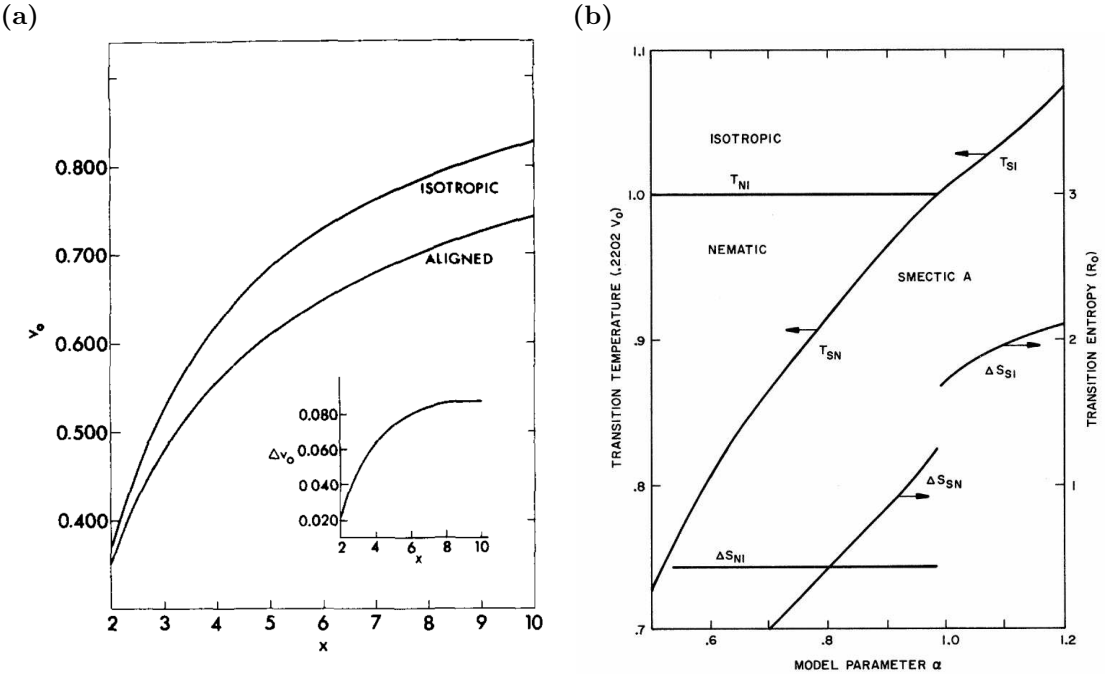


One of the first simulations performed to study the isotropic-nematic transition for hard spherocylinders by Vieillard-Baron [276] unfortunately failed due to lack of computer power at this time. In his Monte-Carlo simulations of systems containing 616 hard spherocylinders with an shape anisotropy $L/D$ equal to two and up to solid-like densities, he does not observe any ordered liquid crystalline phases. In retrospect, this is not surprising for such a short aspect ratio. As Bolhuis and Frenkel [29] find much

later the smectic and nematic phases do not become stable until a shape anisotropy of 3.1 and 3.7, respectively. Hence, Vieillard-Baron falsely concludes that the hard spherocylinder model, in spite of its apparent simplicity, is hardly an useful reference system for the study of the nematic phase. The attempt to study a system of 2392 molecules with a shape anisotropy of five has to be abandoned due to the inadequate computational requirements. In a later work Frenkel [84] remark that the simulations of Vieillard-Baron may be plagued by critical slowing-down effects due to the vicinity of both, the isotropic-nematic and the nematic-smectic phase transitions. This may explain the extremely long preparatory runs mentioned by Vieillard-Baron which are required to generate an equilibrated fluid configuration when starting from the crystalline solid.

One way to circumvent the problem of limited computational power is to use simplified models. One of these simplifications is the use of parallel hard spherocylinders. In this model the polymers are represented by hard spherocylinders which are not allowed to rotate. A theory of ordered phases for these systems is developed by Taylor et al. [255] while Somoza and Tarazona [240] use a density functional approximation to investigate a phase diagram which is illustrated in Figure (2.2a). The Molecular Dynamics simulations of Veerman and Frenkel [271] concentrate on the nucleation process of the parallel hard spherocylinder system. In a later simulational study Costa et al. [54] take a deeper look at the nematic-smectic phase transition of parallel hard spherocylinders.

With increasing computer power and the investigation of more sophisticated models the former restrictions may be bypassed. Frenkel [84] is the first to use freely rotating hard spherocylinders in simulations and to find ordered, liquid crystalline phases in those systems. A few years earlier Shashidhar et al. [237] experimentally observe a N-SmA-SmC multicritical point in a single component liquid-crystal system. Several groups investigate the phase transitions [158, 205, 232] and provide phase diagrams [241, 272] for the hard spherocylinder model. Figure (2.2) shows four phase diagrams for hard spherocylinders. Somoza and Tarazona [239] investigate the nematic-smectic A-smectic C phase transitions in systems of parallel hard spherocylinders. The nematic-smectic A transition is illustrated in Figure (2.2a). The same transition is displayed in Figure (2.2b) as studied by Hołyst and Poniewierski [113] for perfectly aligned hard spherocylinders. Figure (2.2c) shows a more detailed phase diagram for hard rods with full translational and orientational freedom as obtained from a density functional theory [206, 207]. In Figure (2.2d) the isotropic-nematic transition lines for different approaches are compared at which the computer simulation data are obtained by a density functional theory [51].

In the simulational study Bolhuis and Frenkel [29] obtain a very detailed phase diagram for hard spherocylinders with variable length-to-width ratios $L/D$. Two phase diagrams for different ranges of length-to-width ratios are displayed in Figures (2.3a) and (2.3b). Note that the smectic phase is not stable for length-to-width ratios below 3.1 and the nematic phase does not become stable until a value of 3.7 is reached. Figure (2.3c) compares these results with the density field theory study of Graf and Löwen [92]. Finally, Figure (2.3d) shows a phase diagram obtained from Monte-Carlo simulations by McGrother et al. [177] for shape anisotropies between three and five.

Close to the melting point of the smectic A phase transverse interlayer particles are predicted for hard rods in a theoretical and numerical study with fixed box shape [269]. These particles are located between the two layers and roughly perpendicular to the director. Transverse interlayer particles are also observed in simulations of hard sphero-

cylinders without [267] and with [266, 268] flexible end groups. In these simulations a variable box shape with constant volume is used. A significant amount of transverse interlayer particles is only expected for short rods, that is, $L/D < 5$.

In recent years, more complex models have been explored. In their Dissipative Particle Dynamics simulations of lyotropic rigid polymers Zhao and Wang [298] find smectic A, smectic B, nematic and isotropic phases. The attractive, hard spherocylinders studied by Wu et al. [292] using perturbation theory exhibit isotropic and nematic phases. They summarize that the incorporation of an attractive potential leads to an increased orientational order at high densities compared to an athermal system and, thus, to a stabilization of the nematic state.

**Figure 2.2** Different phase diagrams for hard spherocylinder models. For all diagrams the $x$-axis is characterized by the length $L$ and the diameter $D$ of the spherocylinder. The $y$-axis is always the density of the system, which may be rescaled by a given factor. $\rho_{\mathrm{cp}}$ is the density of close packing. (a) Nematic-smectic A transition in a system of parallel hard spherocylinders. The upper part of the plot shows the critical wavelength, while the lower part displays the critical density $\rho^* = \rho/\rho_{\mathrm{cp}}$. From [239]. (b) The solid line shows the N-SmA transition for the theory presented in the paper. The dashed line is a comparison to another study. From [113]. (c) Phase diagram including the isotropic, nematic and smectic phase. The shaded area corresponds to the N-I two-phase region. There is a tricritical point at $L/D = 2.99$ and $v_0$ is the volume of the hard rod. From [207]. (d) Comparison of the isotropic-nematic transition line for different approaches. The reduced density $\rho^*$ is $\rho/\rho_{\mathrm{cp}}$. From [51].

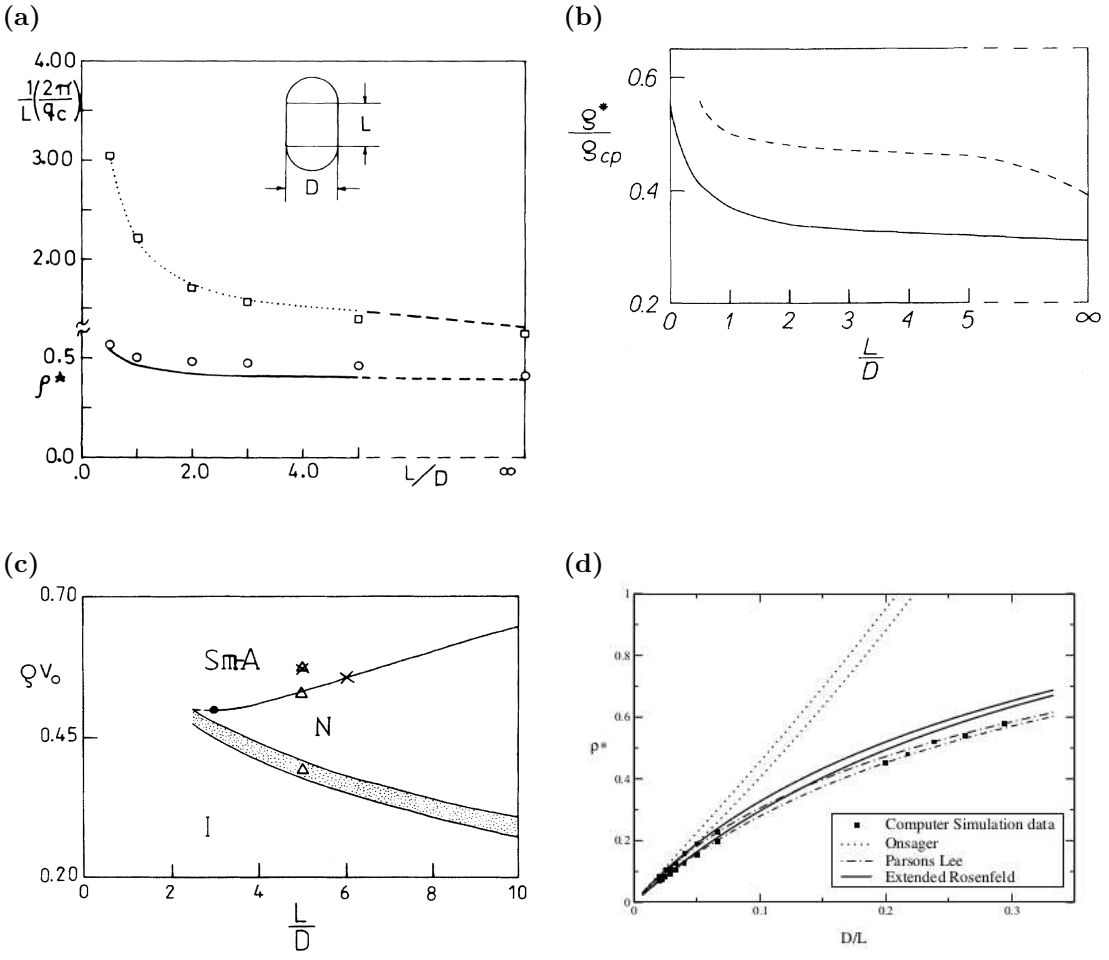

**Figure 2.3** Detailed phase diagrams for hard spherocylinders. $L$ and $D$ are the length and the diameter of the spherocylinder, respectively. The reduced density $\rho^* = \rho/\rho_{\mathrm{cp}}$ is related to the density of close packing $\rho_{\mathrm{cp}}$. (a) Phase diagram for the range $0 < L/D < 5$ including the isotropic (I), nematic (N), smectic (Sm) , plastic (P) and solid (S) phase. (b) Phase diagram for a $L/D$ ratio of up to 100. AAA and ABC represent different stackings of the solid phase. Both from [29]. (c) Comparison with results of a Density Field Theory study (dark gray area) with $p = L/D$. From [92]. (d) In this phase diagram the packing fraction is labeled $\eta$ and the solid phase K. From [177].

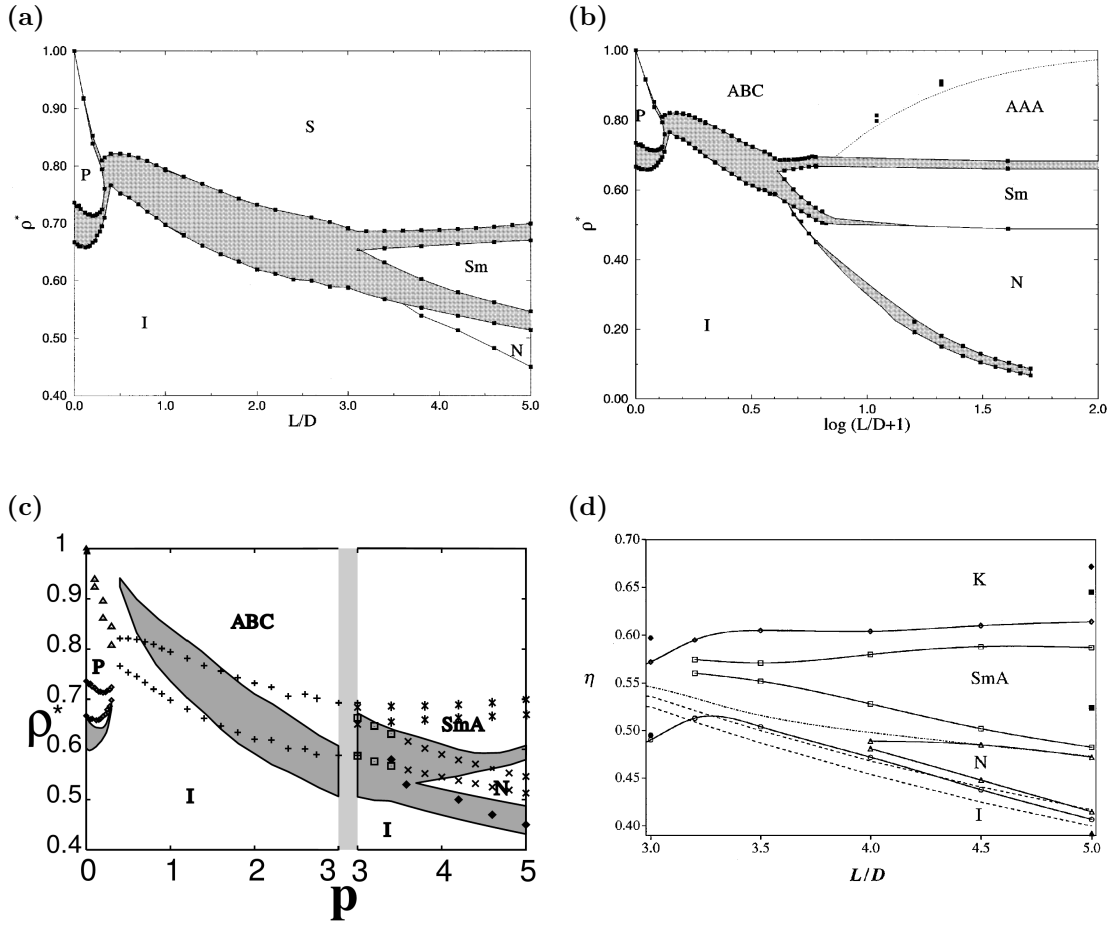

## 2.3 Rod/coil mixtures

Finally, we briefly mention some results for mixtures of rod and coil polymers. Mixtures of coil and rod homopolymers behave differently than systems with only one of the components or with rod-coil diblock copolymers. The addition of coils to a rod polymer system dramatically changes the phase behavior. But since the two components are not connected to each other they may still separate at a macroscopic scale.

The most prominent theory explaining the phenomenon that the addition of non-adsorbing polymers to a suspension of colloidal particles may induce a phase separation into a colloid-poor and colloid-rich phase is developed by Asakura and Oosawa [14, 15]. If the distance between two colloidal particles becomes smaller than the diameter of the polymers an excluded volume not accessible to the polymers arises. The resulting depletion interaction leads to an attractive force between the colloidal particles. Along with the Alexander-de Gennes model for polymer brushes (see page 123) we use the Asakura-Oosawa model to derive the interactions between tetrapods and excess polymer in the second part of this thesis.

The phase separation of mixtures containing rod-like and coil-like polymers is closely related to the model described by Asakura and Oosawa [142]. An isotropic-nematic phase transition for an athermal system due to an entropy effect is theoretically predicted by Flory [80]. With their simulations Bolhuis et al. [30] examine the influence of attractive interactions on the phase behavior of their hard spherocylinder model mentioned earlier in this chapter. The attraction is introduced by the addition of non-adsorbing polymers causing a depletion force. The computed phase diagrams are displayed in Figure (2.4) for different diameter ratios $q$ between spherocylinders and polymers. The phase diagrams comprise isotropic, nematic, smectic and solid phases. The fugacity $z$ in Figure (2.4a) is related to the osmotic pressure which causes the depletion force. The polymer concentration in Figure (2.4b) is expressed by the parameter $\varepsilon$. They argue that the hard spherocylinder model is the simplest realistic reference model available for many lyotropic liquid crystalline materials.

**Figure 2.4** Phase diagrams for a system of spherocylinders with $L/D = 5$ mixed with polymers. The parameter $q$ is the diameter ratio of these polymers, proportional to the radius of gyration $R_g$ and a measure for the interaction range. $\rho^*$ is the reduced density of the spherocylinders. (a) As predicted by thermodynamic perturbation theory. Here $z$ is the fugacity which is related to the osmotic pressure. (b) Simulated with an attractive generalized square-well potential. The parameter $\varepsilon$ is proportional to the polymer concentration. Both from [30].

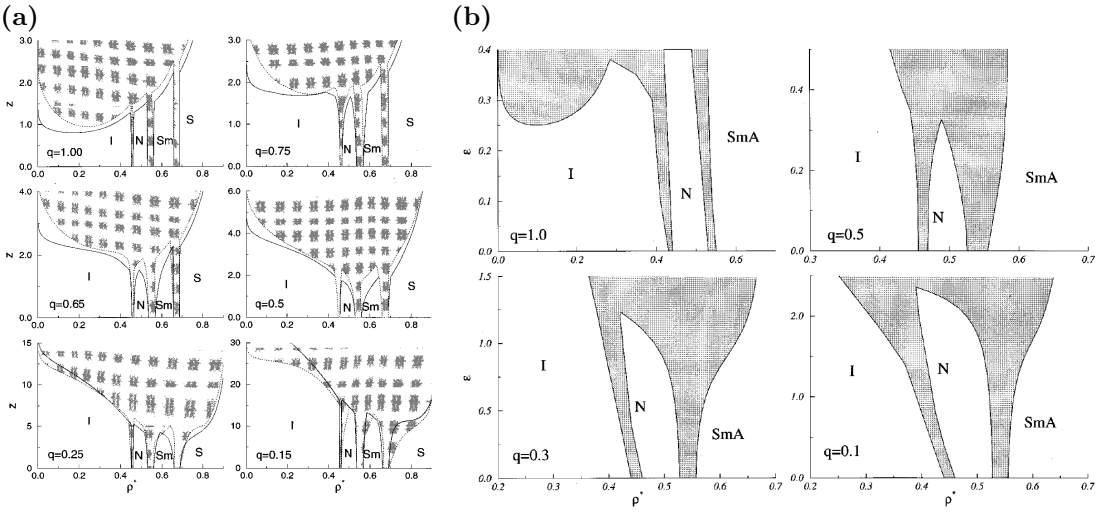


## 2.4 Rod-coil block copolymers

In this section we introduce significant results from the field of rod-coil block copolymers. We also refer to a few results of more complex systems such as triblock copolymers. There are some helpful reviews on rod-coil block copolymers [131, 141, 157, 190]. Beside the studies mentioned in this section, there are further theoretical [3, 74, 83, 110, 124, 130, 132, 172, 191, 208, 213, 248, 256], experimental [123, 154, 189, 256, 262, 263] and some simulational works [11, 12, 50, 58, 59, 103, 115, 116, 119, 156, 180, 288].

Some exemplary phases for rod-coil block copolymers are illustrated in Figure (1.6) on page 14. An exemplary phase diagram is shown in Figure (1.7) on page 15. A theoretical description of the nematic and smectic A phases is firstly proposed by Semenov and Vasilenko [233] in 1986. Williams and Fredrickson [286] predict the so-called hockey puck phase for high coil volume fraction in 1992. To our knowledge this phase has not been observed in experiments so far. But self-consistent field theory calculations [294] and Brownian Molecular Dynamics simulations [153] validate the existence of this phase. Figure (2.5) displays four snapshots of the simulated rod-coil copolymers, consisting of six rod and nine coil beads. The bonds between rod beads are rigid, but flexible between coil beads. Lin et al. label the phases disc and string phase. They may be associated with the hockey puck phase and the needle phase predicted by Raphael and de Gennes [212]. In another study, which is based on the Maier-Saupe wormlike chain model, Williams and Halperin [287] also find lamellar, cylindrical and spherical structures.

**Figure 2.5** Snapshots of rod-coil copolymers ($R_6C_9$) with different rod interaction parameters $\epsilon_{RR}$. (a) Disc or hockey puck phase (b) String phase. From [153].

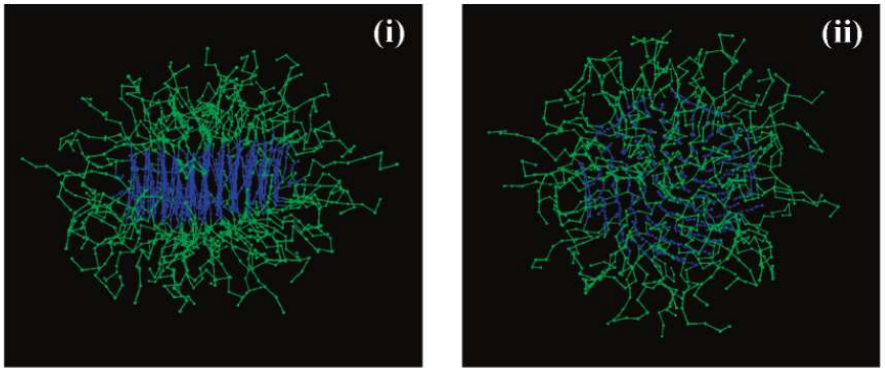


(a) $\varepsilon_{RR} = 3.1$ (i: side view perpendicular to the rod axis; ii: top view along the rod axis)

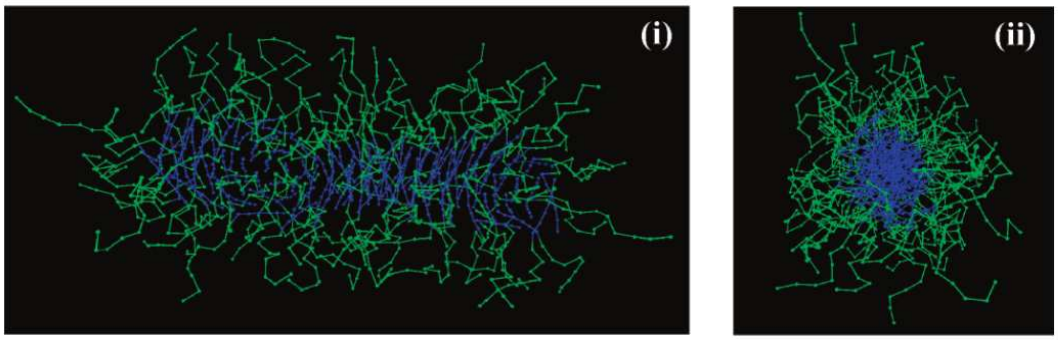


(b) $\varepsilon_{RR} = 2.6$ (i: top view perpendicular to the string axis; ii: side view along the string axis)

Beside the wavy lamellar phase displayed in Figure (2.6b,A) Chen et al. [44, 45] observe zigzag and arrowhead phases (see Figure (1.6) on page 14) for rod-coil block copolymers. In their experimental study they also include a theoretical explanation for the formation of the zigzag morphology. They emphasize the role of the solvent and distinguish three different types of the zigzag morphology. The morphologies range from well ordered zigzags to highly fragmented zigzags which are randomly oriented in the plane of the film. The transmission electron microscopy images in Figure (2.6a) show fragmented and short zigzags, whereas the zigzags in Figure (2.6b,B and C) are well ordered. In the zigzag phase the rods are oriented parallel to each other along the director **n** but the layer normals, indicated by the vectors **p**, have an angle of approximately 88° towards each other. As marked in Figure (2.6a, D and E) the layer normal **p** points in the same direction for all layers in the arrowhead phase. The directors **n** of the layers have the eponymous shape of an arrowhead.

The zigzag phase is also observed in experiments with polydisperse $\alpha$-helical polypeptides which act as rod-like mesogens [226]. In their coarse-grained simulations of rod-coil multiblock copolymers Lintuvuori and Wilson [156] find evidence for metastable chevron-like structures. Self-consistent field theory calculations [208, 294] confirm that the zigzag

**Figure 2.6** TEM images of the zigzag phase. The dark parts represent the rods and the light domains the coil part of the polymer. (a) Fragmented zigzag phase (top) and short zigzags (bottom). From [44]. (b) Wavy lamellar (A), zigzag lamellar (B and C) and arrowhead (D and E) phase. **n** is the rod chain axis and **p** the layer normal. From [45]

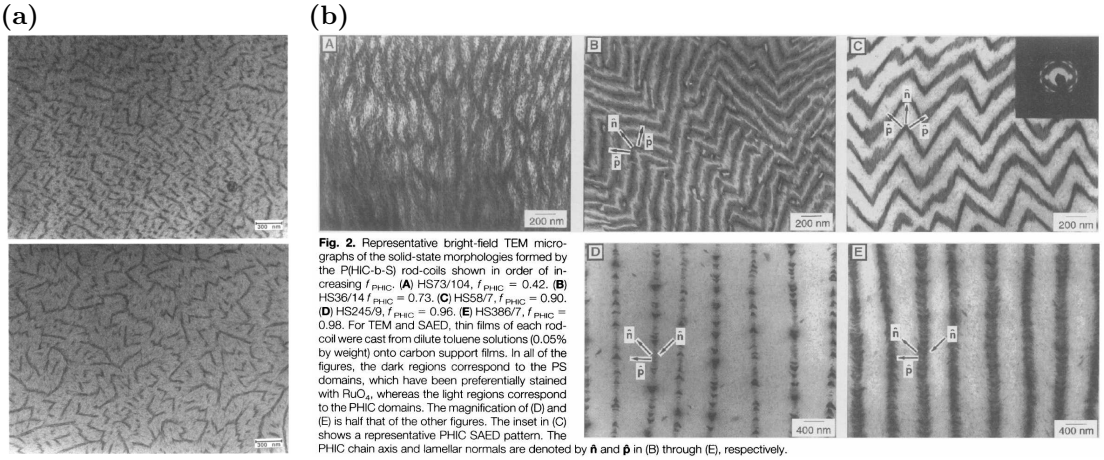


**Fig. 2.** Representative bright-field TEM micrographs of the solid-state morphologies formed by the P(HIC-b-S) rod-coils shown in order of increasing $f_{PHIC}$. (**A**) HS73/104, $f_{PHIC} = 0.42$. (**B**) HS36/14 $f_{PHIC} = 0.73$. (**C**) HS58/7, $f_{PHIC} = 0.90$. (**D**) HS245/9, $f_{PHIC} = 0.96$. (**E**) HS386/7, $f_{PHIC} = 0.98$. For TEM and SAED, thin films of each rod-coil were cast from dilute toluene solutions (0.05% by weight) onto carbon support films. In all of the figures, the dark regions correspond to the PS domains, which have been preferentially stained with $RuO_4$, whereas the light regions correspond to the PHIC domains. The magnification of (D) and (E) is half that of the other figures. The inset in (C) shows a representative PHIC SAED pattern. The PHIC chain axis and lamellar normals are denoted by $\hat{\mathbf{n}}$ and $\hat{\mathbf{p}}$ in (B) through (E), respectively.

phase has a higher free energy than the smectic C phase and is, therefore, metastable with respect to a defect free smectic C structure.

Among other phases the tethered nanorods simulated by Horsch et al. [115] using Brownian Dynamics form a tetragonally perforated lamellar and the honeycomb phase. Both structures are not predicted by any available theory but have been found in experiments [62, 140, 187, 218, 256]. They further predict a new phase comprised of chiral cylinders. The polymers are modeled as a series of beads which are connected rigidly if they represent rods or by a flexible spring potential for coils. In this study both components consist of five beads. The resulting phase diagram and snapshots of the observed phases for tethered rods are illustrated in Figures (2.7a) and (2.7c). For comparison Figure (2.7b) displays a phase diagram of flexible block copolymers. It demonstrates that the phase behavior for tethered rods is much richer. In both phase diagrams the inverse temperature $1/T^*$ is plotted against the volume fraction of the tethered rods $\phi$. Optical transmission, atomic force microscopy (AFM), fluorescence and scanning electron microscopy (SEM) images of a honeycomb structured film observed by de Boer et al. [62] are shown in Figure (2.7d). The inset in the SEM images demonstrates the open surface structure of the polymer film with hole diameters between two and three microns and spherical cavities with a diameter of three to five microns. Recent studies reveal that condensation of small water droplets on the surface of the polymer solution is driving the formation mechanism of the honeycomb structures [126, 203, 204].

In a further study Horsch et al. [116] focus on the role of rod aspect ratio and tether length on the self-assembly of end-tethered nanorods in solution. They distinguish between moderate and low aspect ratio rods, with aspect ratios greater or less than five to one, respectively. The distinction is made at this aspect ratio since former works have shown that only hard rod systems with an aspect ratio greater than five form a nematic phase [29]. They find that the simulated tethered rods with low aspect ratios

**Figure 2.7** (a) Phase diagram plotting the inverse temperature $1/T^*$ versus the volume fraction $\phi$ of tethered rods. The cubic micelle (C), long micelle (LM), hexagonal cylinder (H), tetragonally perforated lamellar (TPL), honeycomb (HC) and lamellar (L) morphologies are indicated.(b) Phase diagram of flexible block copolymers for comparison. The region between H and L is expected to be the gyroid phase. (c) Predicted morphologies for the tethered rods. The labels are the same as in (a). (L) is a smectic C phase and ($H_I$) the hexagonal chiral cylinder phase while ($H_{II}$) shows individual chiral cylinders from the hexagonal cylinder phase. All three images are from [115]. (d) Optical transmission and AFM (top), fluorescence and SEM (bottom) images of a honeycomb structured film. From [62].

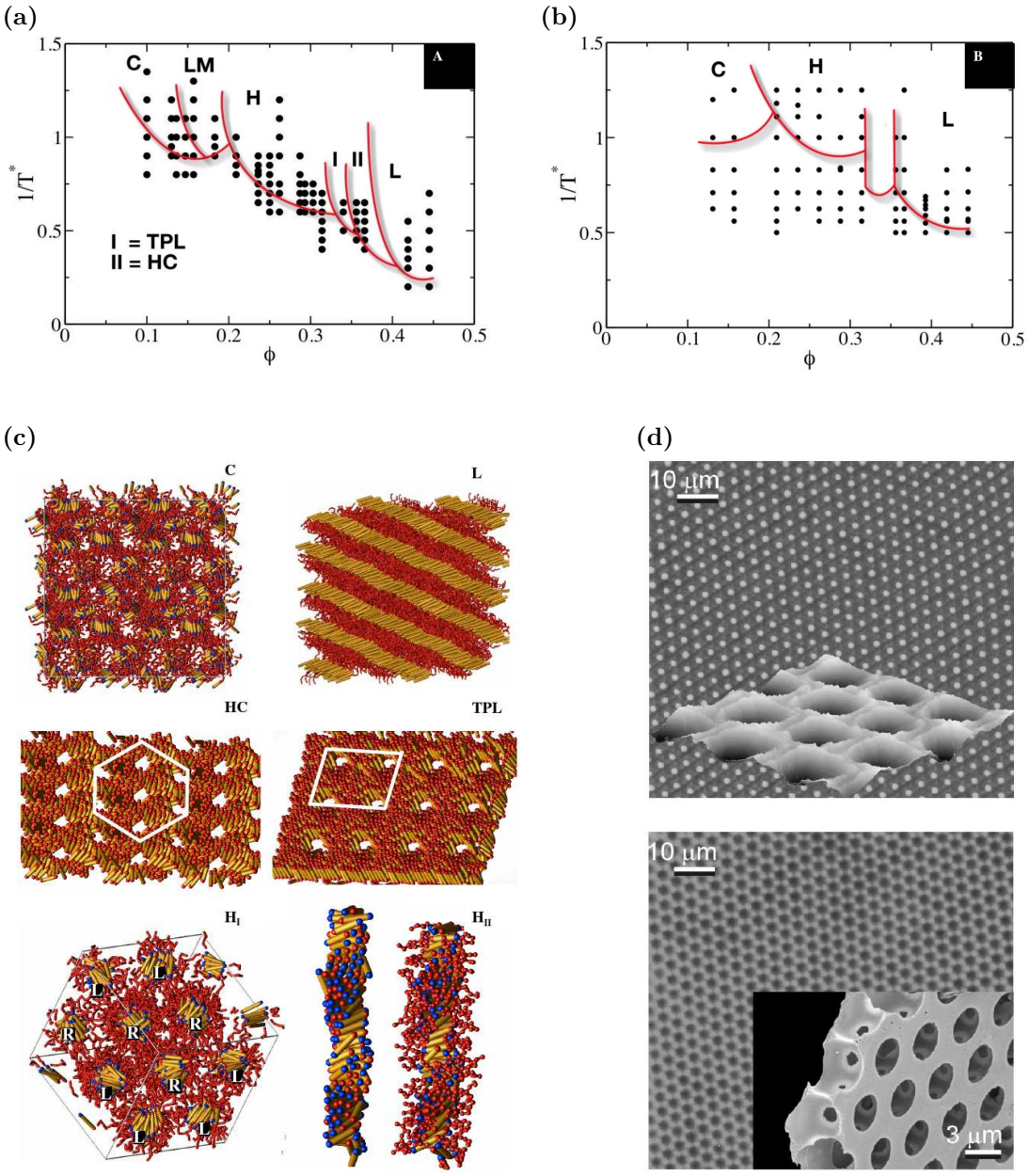

show a less extensive phase behavior. Another focus of this second study is on the influence of tether length on the final structure and especially on its curvature. So they demonstrate that it becomes increasingly more difficult for rods to pack parallel to each other as the tether length increases. This results in an increase in interfacial curvature with increasing tether length. The formation of structures with less and less curvature with decreasing tether length provides further evidence that the rod-rod interactions and their desire to form flat interfaces dominates for short tether lengths. Hence, they conclude that the tethers are driving the observed curvature effects.

Several groups observe a stabilization of the smectic phase at expense of the nematic phase with increasing coil fraction for rod-coil block copolymers [11, 12, 156, 176, 243]. In their theoretical and simulational study of polymer tethered rods Wilson et al. [288] show that the stability of the nematic phase first increases and then decreases with increasing chain length until the nematic phase is suppressed altogether. Jiang and Wu [125] investigate the influence of coil fraction in an athermal solution of rod-coil copolymers on the isotropic-nematic transition. For this purpose, they propose a hybrid model that combines the scaled particle theory with Monte-Carlo simulations. They emphasize that a formation of the nematic phase is hindered by the addition of coils. The polymers consist of $m_\mathrm{r}$ rigidly and $m_\mathrm{f}$ flexibly connected hard spheres with a bond of length $L^*$ between each sphere. Two phase diagrams which show the isotropic-nematic phase transition in dependence of the coil fraction are plotted in Figure (2.8). The plots point out that the nematic phase vanishes for $m_\mathrm{r}$ smaller than eight at constant $m = m_\mathrm{r} + m_\mathrm{f} = 15$ (Figure 2.8a) and for $m_\mathrm{f} \geq 35$ with fixed $m_\mathrm{r} = 30$ (Figure 2.8b).

**Figure 2.8** Phase diagrams for rod-coil block copolymers showing the isotropic-nematic phase transition demonstrating that an increase in coil fraction destabilizes the nematic phase. $\eta$ is the packing fraction, $L^*$ the bond length. Each copolymer consists of $m = m_\mathrm{r} + m_\mathrm{f}$ hard spheres where $m_\mathrm{r}$ spheres build the rigid block and $m_\mathrm{f}$ spheres the flexible block. (a) For constant $m = 15$. The nematic phase does not emerge for $m_\mathrm{r} < 8$. (b) The length of the rigid block $m_\mathrm{r}$ is fixed to 30. The nematic phase ceases at $m_\mathrm{f} = 35$. Both from [125].

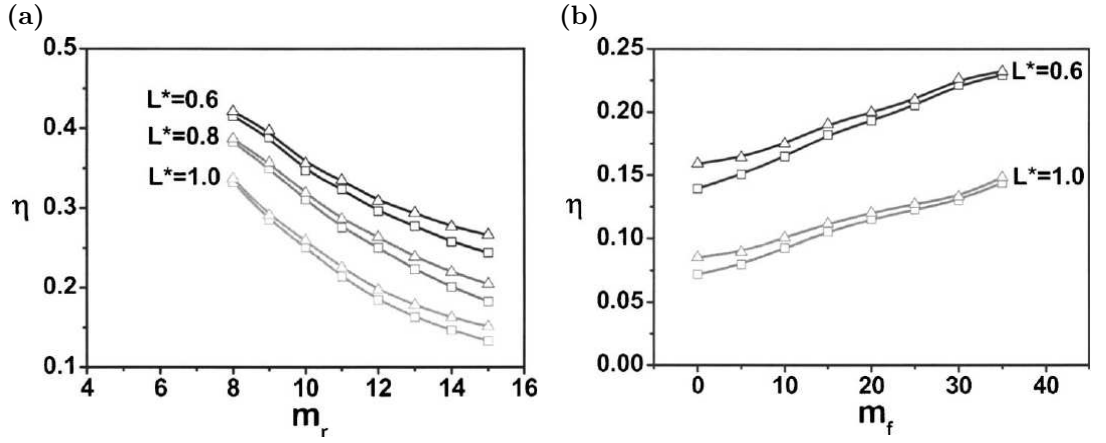

Figure (2.9) shows two phase diagrams for rod-coil diblock copolymers obtained by self-consistent field theory. In both cases the rod polymers fraction $f$ is plotted against a parameter $C = G = L^2 D\rho$, which is proportional to the average number density of copolymers $\rho$. Here, $L$ and $D$ are the total contour length and diameter characterizing the polymers in the worm-like models. Both studies demonstrate that the addition of coil polymers to rod-like polymers stabilizes the smectic phase with respect to the nematic phase. The phase diagram in Figure 2.9a comprises an isotropic, nematic and smectic phase. Using a self-consistent field theory approach Düchs and Sullivan [74] determine that the nematic phase is not entirely suppressed with respect to the isotropic and smectic phases. This result is in contradiction with other studies [5, 12, 175, 268]. The phase diagram in Figure 2.9b from Song et al. [242] shows comparable results but additionally distinguishes between the smectic A and the smectic C phase. For their study they use a more sophisticated implementation of the self-consistent field theory. They summarize that the nematic phase disappears for high coil fraction after a triple point is reached.

**Figure 2.9** Phase diagrams for rod-coil diblock copolymers. $C$ and $G$ are proportional to the average polymer number density $\rho$ and $f$ is the rod fraction. (a) The nematic phase is not entirely suppressed. From [74]. (b) The smectic A and C phases are differentiated and the nematic phase vanishes for high coil fraction. From [242].

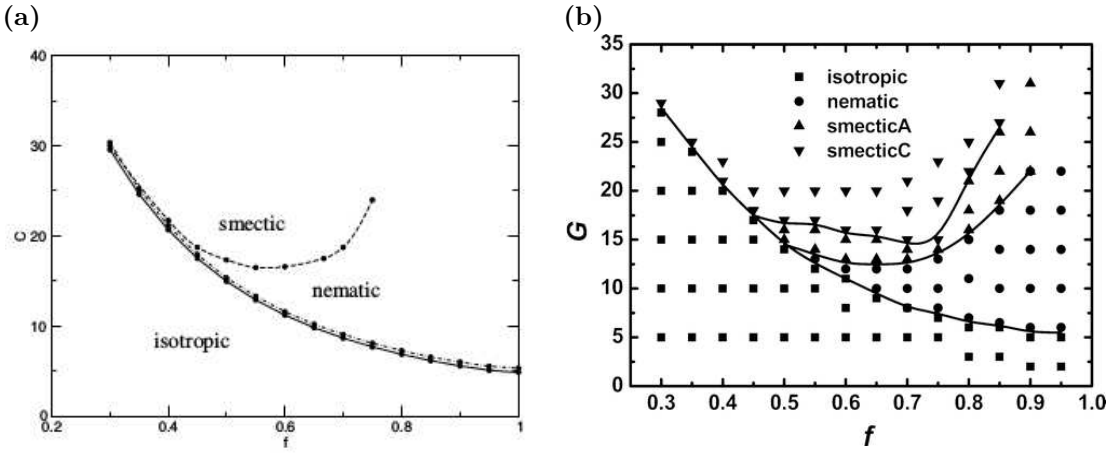


Similar results are found in Monte-Carlo simulations of systems containing hard spherocylinders with flexible tails attached to each end and without coils [266]. Figure (2.10) illustrates the nematic order parameter $S$ of the studied systems with and without tails using filled and open symbols, respectively. One can see that the addition of coils stabilizes the smectic A phase at a lower pressure and the nematic phase disappears. Furthermore, they determine that the layers in the smectic A and crystal phase are further apart when tails are added, whereas the ordering of the rods within the layers does not change much.

**Figure 2.10** Nematic order parameter $S$ for hard spherocylinders without coils (open symbols) and with two coil chains (filled symbols). Circles represent the isotropic, triangles the nematic, squares the smectic A and diamonds the crystal phase. It is visible that the addition of coils suppresses the nematic phase and stabilizes the smectic phase at a lower pressure $P^*$. From [266].

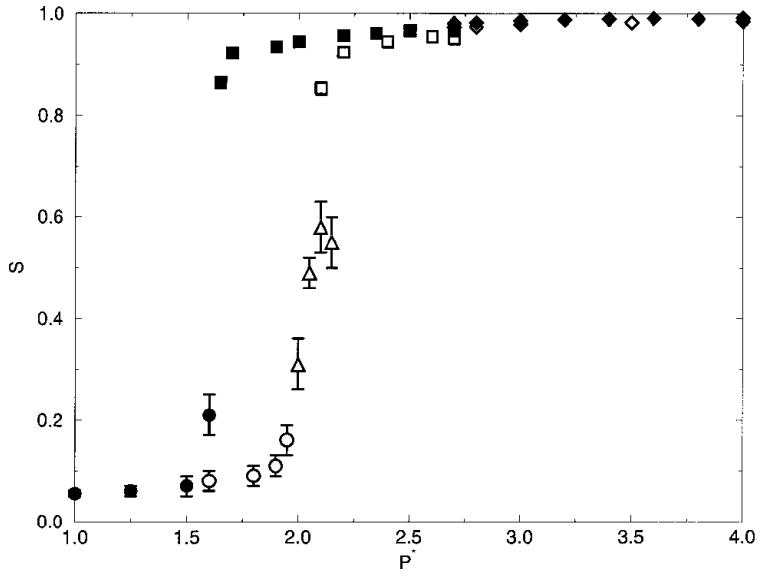


Reenders and ten Brinke [213] investigate the phase behavior of monodisperse rod-coil diblocks with an attractive Maier-Saupe attraction between the rod blocks and a Flory-Huggins interaction to model the incompatibility of rod and coil blocks. They observe isotropic, nematic and smectic C phases for high rod fraction and spherical, hexagonal and lamellar phases for low rod fraction. Phase diagrams for different interaction parameters are shown in Figure (2.11). Note that in contrast to the phase diagram of coil-coil diblock copolymers (see Figure (1.3) on page 11) the resulting phase diagram, displayed in Figure (2.11a), is asymmetric. In this figure the Maier-Saupe interaction parameter $\omega$ is zero. The phase diagram in Figure (2.11b), where $\omega$ is eight times the Flory-Huggings parameter $\chi$, looks very different. As in Figure (2.9a) the nematic phase is not suppressed completely for high coil fractions.

Lin et al. [155] study polymersomes formed by rod-coil diblock copolymers in selective solvents with the Dissipative Particle Dynamics method. The morphological phase diagram in dependence of rod and coil length is displayed in Figure (2.12a). Here, x and y are the number of spheres representing the rod and coil block, respectively. In their experimental study Olsen and Segalman [188] observe a series of transitions from lamellar to nematic and finally to isotropic upon heating symmetric diblock copolymers. As they note, the nematic-isotropic transition temperature decreases with increasing coil fraction. For high coil fractions the system only exhibits an isotropic phase. The experimental phase diagram is shown in Figure (2.12b). They also mention that the lamellar region in their phase diagram may potentially contain smectic-like regions not investigated further in their study. Finally, Figure (2.12c) shows four more phase diagrams for rod-coil block copolymers obtained by different models.

**Figure 2.11** Phase diagrams for rod-coil diblocks with $N = 40$ each. (a) Phase diagram with Maier-Saupe interaction parameter $\omega = 0$. There is a critical point at $f_{\mathrm{rod}} \approx 0.73$ and a triple point at $f_{\mathrm{rod}} \approx 0.42$. (b) Phase diagram with Maier-Saupe interaction parameter $\omega = 8\chi$. There are no triple points. Both from [213].

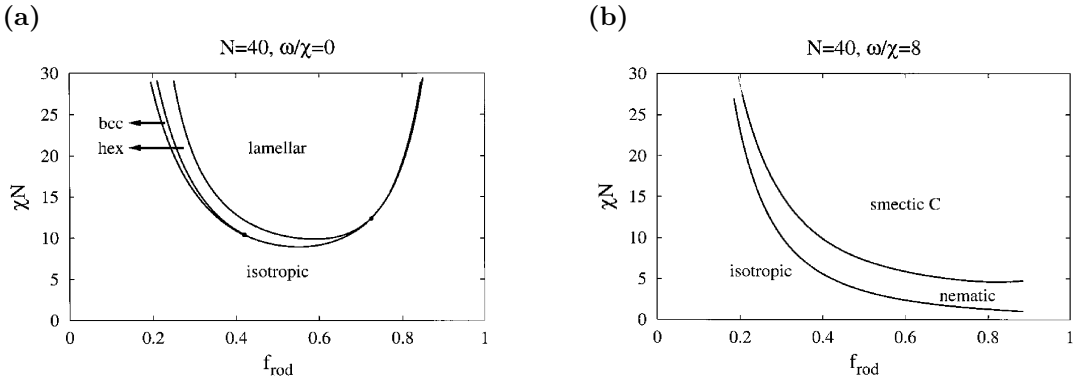


In their Dissipative Particle Dynamics simulations He et al. [105] compare the phase behavior of linear and cyclic rod-coil block copolymers. Beside different morphologies the cyclic polymers have a higher order-disorder transition point and a more symmetric phase diagram than linear polymers. The resulting phase diagrams for cyclic and linear rod-coil block copolymers are displayed in Figure (2.13).

Beside cyclic rod-coil block copolymers there are also a lot of other interesting, slightly more complex systems. The Monte-Carlo simulations of McGrother et al. [178] demonstrate that the range of stability of the nematic phase is increased at the expense of the smectic A phase when a terminal dipole is added to a hard spherocylinder. On the other hand, it is well known that the smectic A phase is little affected by the addition of flexible coils to hard spherocylinders, while the nematic phase is suppressed. The interplay of these two effects is investigated by van Duijneveldt et al. [268]. They propose a simple model to simulate hard spherocylinders with an attached coil and an optional terminal dipole. They not only observe that the nematic phase is suppressed when coils are attached and that the transitions from disordered to ordered states and finally to crystalline states occur at lower densities. They also find that all four phases survive if a terminal dipole is added. Using self-consistent field theory Song et al. [243] study binary mixtures of rod-coil block copolymer systems with rod or coil-homopolymers and find that the addition of coil-homopolymers stabilizes the smectic phases. Additionally, an enhancement in stability of ordered phases is observed when rods are added as they strongly affect the orientation ordering of the system.

**Figure 2.12** (a) Morphological phase diagram of $R_xC_y$ rod-coil copolymers. From [155]. (b) Phase diagram for rod-coil diblock copolymers plotting temperature against coil fraction as achieved from experiments. From [188]. (c) Phase diagrams from (A) mean field predictions [208], (B) Landau predictions [114] and (C,D) a weakly segregated PPV-*b*-PI system in term of the Flory-Huggins interaction $\chi N$ (C) and the Maier-Saupe interaction $\mu N$ (D) [191]. From [296].

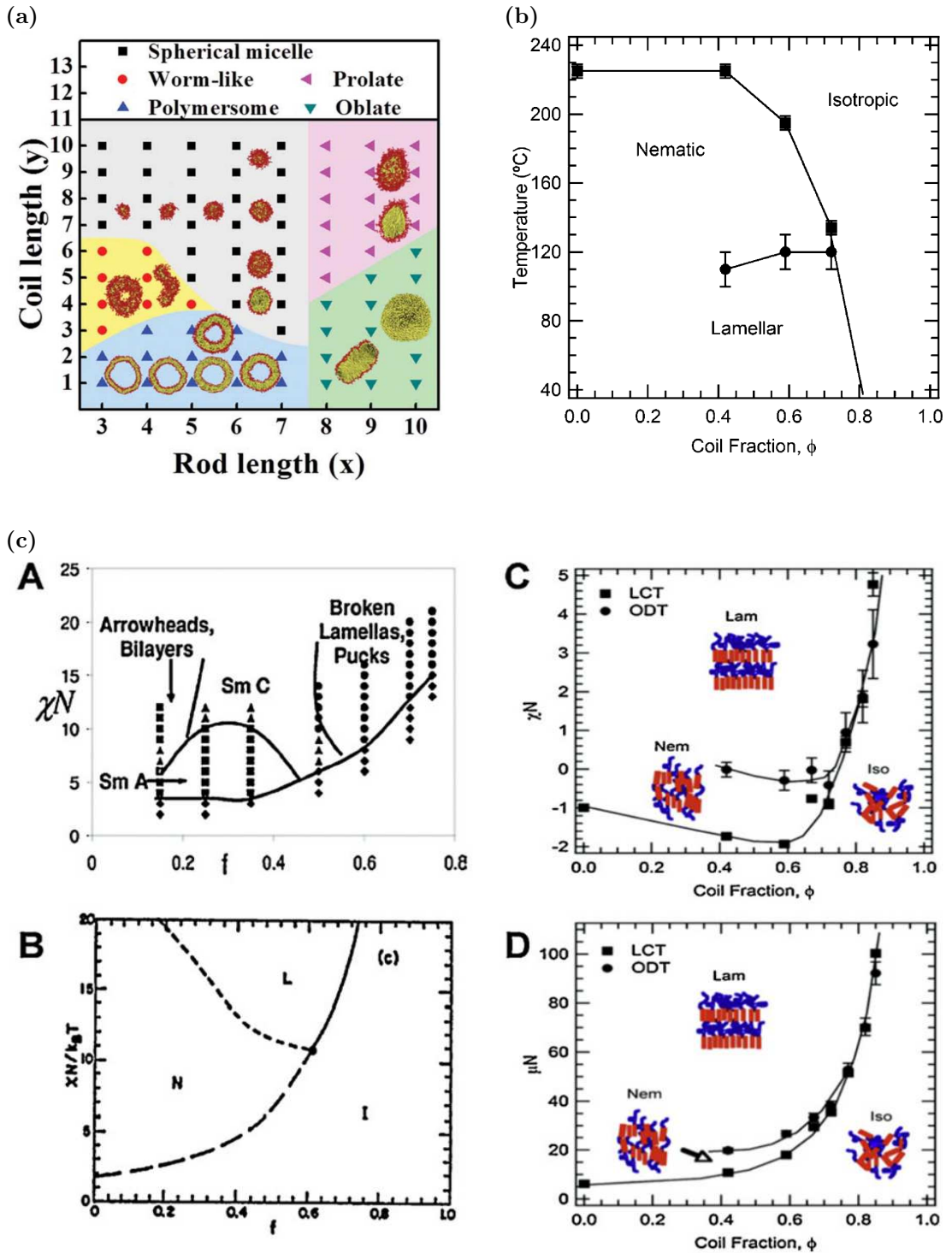

**Figure 2.13** Phases diagrams for cyclic and linear rod-coil block copolymers. The Flory-Huggins parameter $\chi N$ is plotted against the rod fraction $f_{\mathrm{rod}}$. The shown morphologies are micelles (△,▲), hexagonal cylinders (○,●), gyroid (☆,★), perforated lamellae (⊟), lamellae (□) and liquid-crystalline lamellar (■) phases. From [105]

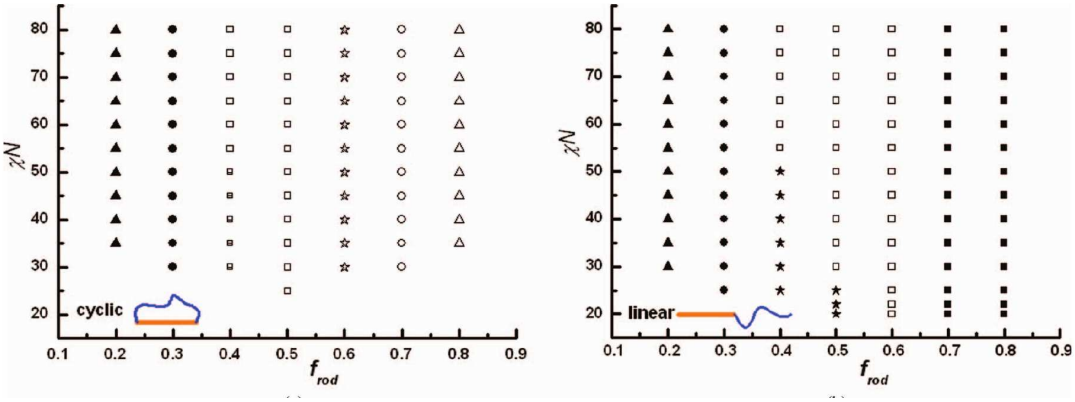


## 2.5 Photovoltaic applications

In this section we present some applications of rod-coil block copolymer systems with a focus on optoelectronics. There are a number of good reviews [96, 122, 231, 258, 296] dealing with conjugated block copolymers and their use for organic optoelectronic devices.

In a combined experimental and simulational investigation Chang et al. [42] study surface morphologies of $\pi$-conjugated rod-coil block copolymers films. Depending on temperature and grafting density they find small, hemispherical domains, transforming to isolated islands and finally wormlike structures or even networklike morphologies. As they emphasize the photophysical properties of the polymers is highly correlated to the surface morphologies.

In a comprehensive study Shah and Ganesan [236] investigate the correlations between morphologies and photovoltaic properties of rod-coil block copolymers. For this purpose, they use a self-consistent field theory to generate structures in confined situations, which are used as input for a drift-diffusion model. This way they analyze different morphologies and the effect of domain orientation on the current-voltage ($J$-$V$) response curves. The resulting curves and corresponding density profiles for donor and acceptor phases are summarized in Figure (2.14). In all schematics the rods make up the donor phase which is colored in blue. The acceptor phase is colored in red and represents the coil polymers. In Figure (2.14a) parallel and perpendicular bilayer phases are compared. It is obvious that the efficiency is higher for bilayers perpendicular to the electrode surfaces. The examination of electron densities shows that the short-circuit current is higher due to the fact that electrons and holes are generated continuously throughout the device with perpendicular domain orientation but not for devices with parallel domain orientation. The difference is even stronger for lamellae domains as illustrated in Figure (2.14b). The efficiency of the parallel lamellae morphology does not differ much from the parallel bilayer structure. Smaller domain areas and a larger donor-acceptor interface of the perpendicular lamellae morphology on the contrary result

in a much higher efficiency. Figure (2.14c) shows puck morphology and its $J$-$V$ curve compared to the curves of the parallel and perpendicular lamellae phases. One may expect a higher efficiency because of the much larger interfacial area leading to a higher production of free charges. Unfortunately, the absence of continuous pathways for holes to reach the anodes results in a merely moderate performance. As the highest efficiency is found for the perpendicular lamellae phase further optimizations are tested for this phase. The effect of domain spacing on the short-circuit current density for different exciton lifetimes is printed in Figure (2.14d). Note that the exciton diffusion length is proportional to the square root of the diffusion time. From the results one can conclude that the optimal domain size is of the order of the exciton diffusion length. In summary, they find that a perpendicularly orientated lamellar morphology with an optimal domain spacing around the exciton diffusion length is most desirable to obtain high photocurrents and efficiencies.

It is not only important to receive such structures for an arbitrary rod-block copolymer in a controllable manner. The single polymers also need to comply with the requirements of an optoelectronic device. For this purpose, several new production techniques are continuously developed. One way to achieve such morphologies for the desired polymers is to pattern active material into ordered nanostructures. An example for this method is displayed in Figure (2.15). In their study Botiz and Darling [32] use block copolymers consisting of P3HT and biodegradable PLLA blocks which form the desired lamellae morphology oriented perpendicular to the substrate. After removing the PLLA blocks $C_{60}$ molecules are added as acceptor material. The result is a highly ordered morphology with P3HT donor domains and $C_{60}$ acceptor domains which have the desirable properties for efficient photovoltaic devices. Simply blending P3HT donor homopolymers and $C_{60}$ acceptors leads to less ordered morphologies which are additionally harder to control.

In the last few years the use of more complex polymers, such as CdSe tetrapods, led to a further improvement in the transport of electrons perpendicular to the plane of the film and hence to higher efficiencies [250]. The application of tetrapods in optoelectronic devices is discussed in detail in Chapter 6.

**Figure 2.14** Schematics for different morphologies and corresponding $J$-$V$ curves. The current density $J$ is in units of $\mathrm{Am}^{-2}$ and the voltage $V$ in volts. The donorphase (rods) is colored in blue and the acceptor layer (coils) in red. (a) Parallel and perpendicular bilayer morphology. (b) Parallel lamellae and perpendicular lamellae. (c) Puck phase. (d) Perpendicular multilayer morphology and the effect of domain spacing $D$ on the short-circuit current density $|J_{sc}|$ for different exciton lifetimes. From [236].

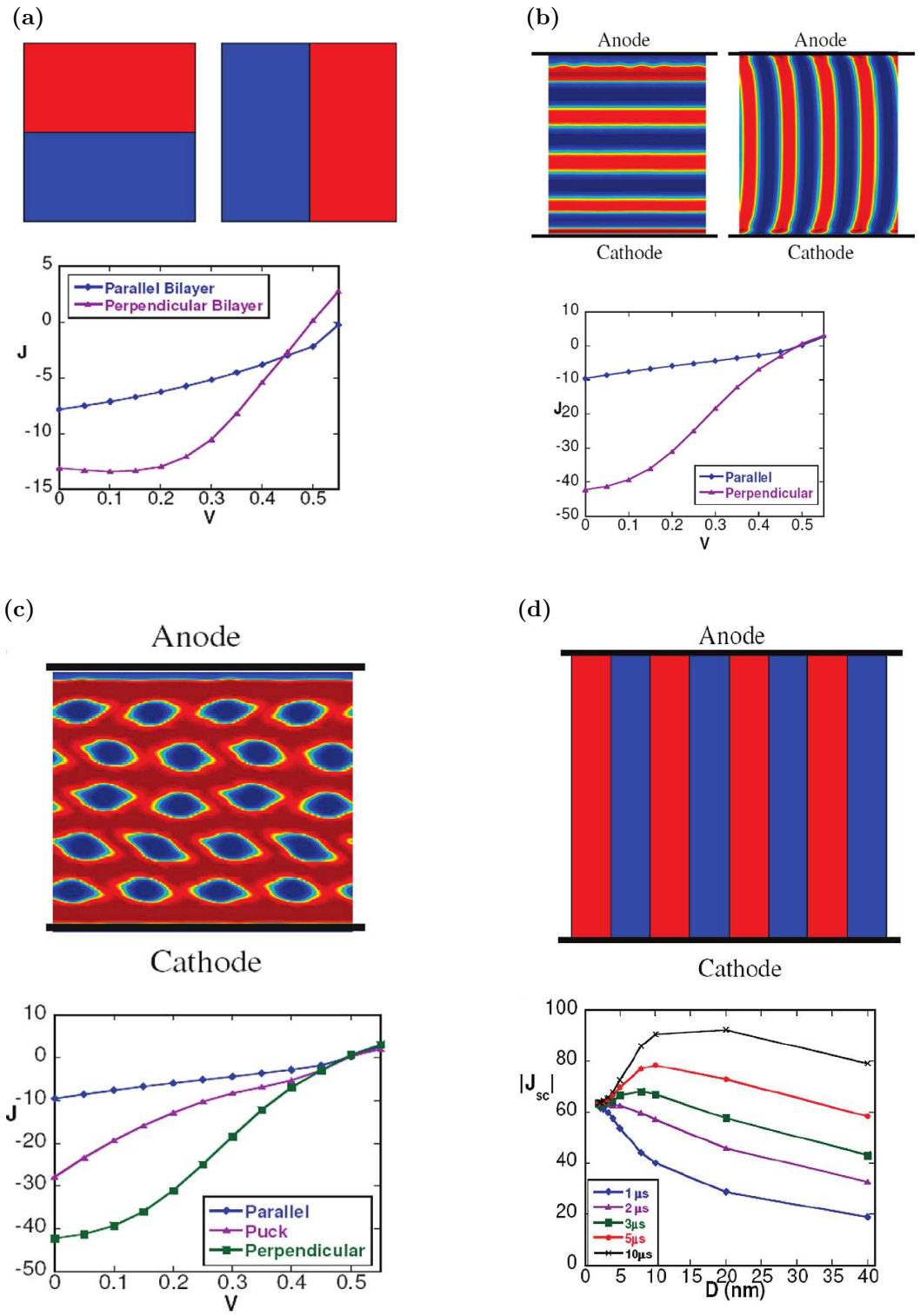

**Figure 2.15** (a) Chemical structure of P3HT-*b*-PLLA and its schematic representation. (b) Ordered nanoscale morphology composed of lamellae oriented perpendicular to the substrate. (c) Ordered P3HT donor domains of molecular dimension after removal of biodegradable PLLA block. (d) Ordered nanoscale morphology with P3HT donor domains separated by $C_{60}$ acceptor domains. (e) Less ordered morphology obtained when simply blending P3HT donor homopolymer and $C_{60}$ acceptors as comparison to (d). From [32].

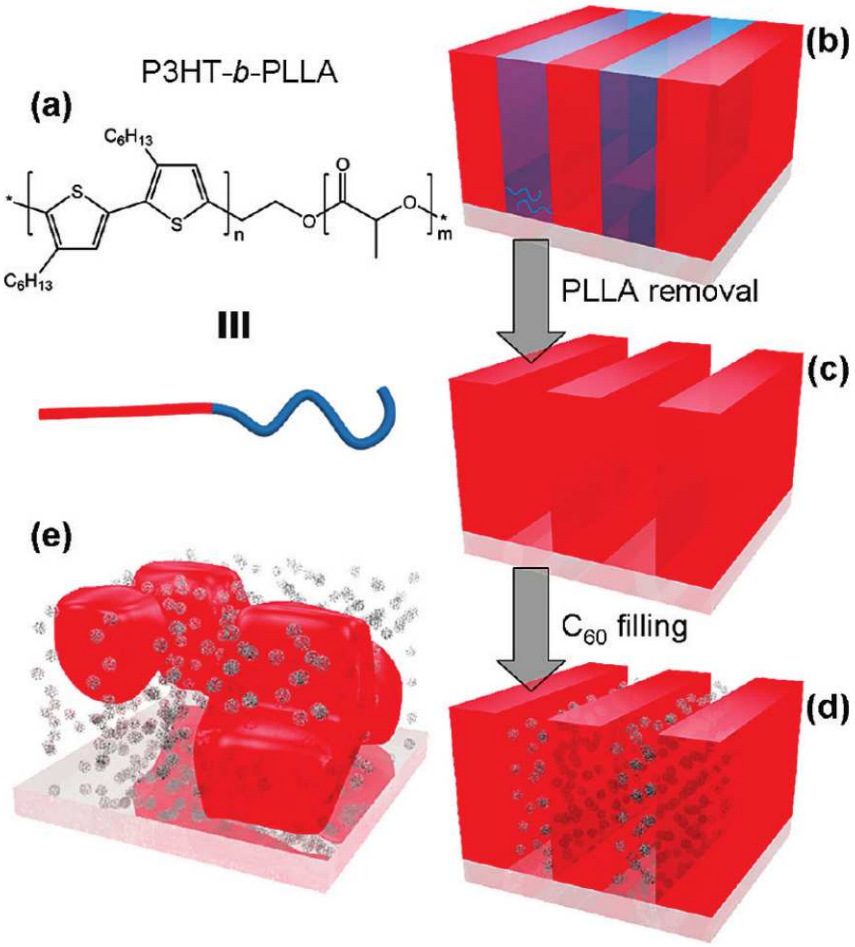

Chapter 3

# Description of the Model

**Contents**



In this chapter we introduce our polymer model and some simulation details. In the first section we introduce our model for the polymers. After presenting the properties of the simulation box in the second section we give a brief introduction to Monte-Carlo simulations in the third section. In the fourth section we discuss how the polymers interact with each other. In the last section we introduce the observables we have used to analyze our simulations.

## 3.1 Polymers

The goal of this work is to simulate rod-coil block copolymers. In this section we show how these polymers are represented in our model. First, we mention the properties of hard spherocylinders which are used to model the stiff rod polymers. The flexible coil polymers are simulated using a bead-spring model. Then we show how these two polymers are combined to rod-coil block copolymers.

### 3.1.1 Rod polymers

The rigid rod polymers in our model are represented by hard spherocylinders. They consist of a cylinder of length $L$ and diameter $D$ capped on both sides with hemispheres with the same diameter as the cylinder. The orientation is given by an unit vector $\hat{\mathbf{u}}$ whose origin is placed at the rods center of mass. A sketch of a spherocylinder is drawn in Figure (3.1).

For the limiting case $L$ equals zero we obtain hard spheres. Because of its simplicity the hard-sphere model is a very well studied model and, therefore, often used as reference. The limit $D = 0$ results in line segments. This model is often referred to as hard rod model. Other well studied models are the parallel hard spherocylinder model in which all unit vectors $\hat{\mathbf{u}}$ show in the same direction and the parallel rod model for which, additionally, $D$ is zero. For the extreme case $L/D \to \infty$ we recover the Onsager limit [192] of infinitely long rods, which are known to exhibit a nematic phase.

**Figure 3.1** Spherocylinder of length $L$ and diameter $D$ and an unit vector $\hat{\mathbf{u}}$.

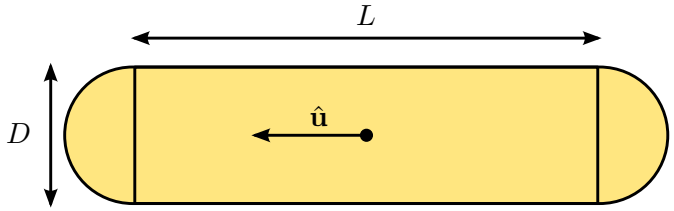


The total length $\lambda$ of a spherocylinder is defined as

$$\lambda = L + D. \tag{3.1}$$

In most simulations in this work the diameter $D$ is set to one. Consequently, the radius $r = D/2$ is equal to 0.5 in these cases. With this restriction the often used spherocylinder shape anisotropy or nonsphericity

$$p = \frac{L}{D} \tag{3.2}$$

becomes $L$ and the length-to-width ratio

$$q = \frac{\lambda}{D} = \frac{L + D}{D} = \frac{L}{D} + 1 = p + 1 \tag{3.3}$$

reduces to $L + 1$. For a sphere with $L = 0$ the shape anisotropy $p$ becomes zero and the length-to-width ratio $q$ reaches its minimal value of one.

For most simulations in this work we use a shape anisotropy of $L/D = 5$. Prior studies [29, 30, 84, 115, 158, 177, 207, 268, 272, 288] have shown that a pure spherocylinder system should exhibit an isotropic, nematic, smectic and solid phase for this value (see Figure (2.3)) and it is known that $p$ is between 3 and 5 for most thermotropic liquid crystals [84].

The rod number density

$$\rho_{\text{Rods}} = \frac{N_{\text{Rods}}}{V_{\text{Box}}} \tag{3.4}$$

is given by the ratio of the number of rods $N_{\text{Rods}}$ in the system and the systems volume $V_{\text{Box}}$, which will be introduced in the next section. Here the volume of the rods and their packing fraction is not taken into account. With the density of regular close packing for spherocylinders

$$\rho_{\text{cp}} = \frac{2}{\sqrt{2} + \sqrt{3}p} \tag{3.5}$$

we define the reduced density

$$\rho^* = \frac{\rho_{\text{Rods}}}{\rho_{\text{cp}}}. \tag{3.6}$$

The volume of a single rod is given by

$$V_{\text{Rod}} = \frac{4\pi}{3}r^3 + \pi r^2 L \tag{3.7}$$

$$= \frac{\pi}{4}D^3\left(\frac{2}{3} + p\right). \tag{3.8}$$

With this we can define a fill factor for the rods

$$F_{\text{Rods}} = \rho_{\text{Rods}} \cdot V_{\text{Rod}}. \tag{3.9}$$

The excluded volume of two spherocylinders [51, 113, 192, 276, 278], which have an angle $\theta$ with respect to each other, is

$$V_{\text{excl}} = \frac{4\pi}{3}D^3 + 2\pi D^2 L + 2DL^2\sin(\theta). \tag{3.10}$$

The sine term may be treated in different ways. Onsager [192] computes the average over all directions and gets

$$\int \frac{\mathrm{d}\Omega}{4\pi}\,\sin(\theta) = \frac{\pi}{4} \tag{3.11}$$

which results in an excluded volume

$$V_{\text{excl}} = 2B_2 = \frac{4\pi}{3}D^3 + 2\pi D^2 L + \frac{\pi}{2}DL^2 \tag{3.12}$$

where $B_2$ is the second virial coefficient. Some works which focus on highly ordered phases take advantage of the fact that the angles between the spherocylinders are very small for these phases. Hence, also the sine term becomes very small and can be neglected so one gets

$$V_{\text{excl}} = \frac{4\pi}{3}D^3 + 2\pi D^2 L. \tag{3.13}$$

Our rods are monodisperse, so all spherocylinders in a simulation run have equal size parameters $L$ and $D$ and, therefore, equal volume and shape anisotropy $p$. Finally, we introduce a formula to compute the surface of a spherocylinder

$$S_{\text{Rod}} = 2\pi r\left(2r + L\right) = \pi D^2\left(1 + p\right). \tag{3.14}$$

### 3.1.2 Coils

The coil polymers are linear chains modeled by a bead-spring model. Each polymer chain consists of $m$ point-like monomers connected by $m-1$ Gaussian springs. Therefore, the coils have no real volume. We treat them as ideal chains. So the monomers may overlap and the chains have crossable bonds, hence, there are no entanglements. The number of coil beads is $N_{\text{Coils}}$. For the simulations of rod-coil block copolymers each rod is connected to one chain, therefore, the number of coil beads $N_{\text{Coils}}$ is equal to the number of rods $N_{\text{Rods}}$. In these cases we will simply label them as $N(= N_{\text{Rods}} = N_{\text{Coils}})$ and only differentiate between $N_{\text{Coils}}$ and $N_{\text{Rods}}$ when needed. The total number of monomers in the system is given by

$$M = m \cdot N_{\text{Coils}}. \tag{3.15}$$

In analogy to the rod number density, we define the coil number density as

$$\rho_{\text{Coils}} = \frac{N_{\text{Coils}}}{V_{\text{Box}}}. \tag{3.16}$$

Figure (3.2) shows a sketch of a coil chain with $m$ beads and $m-1$ Gaussian chains. For Gaussian chains the probability $P(r)$ to have a distance $r$ between the ends of a chain obeys the distribution

$$P(r) = \frac{4\pi r^2}{(2/3\ \pi \langle R_{\text{e}}^2 \rangle)^{3/2}}\ e^{-\frac{3r^2}{2\langle R_{\text{e}}^2 \rangle}} \tag{3.17}$$

where $\sqrt{\langle R_{\text{e}}^2 \rangle}$ is the average end-to-end distance of the chain. The value of $\sqrt{\langle R_{\text{e}}^2 \rangle}$, and therefore the expansion of the coil chain, depends on the interaction parameters, which are introduced in Section 3.4.

**Figure 3.2** Bead-spring model of a single coil polymer consisting of $m$ monomers connected by $m-1$ Gaussian springs.

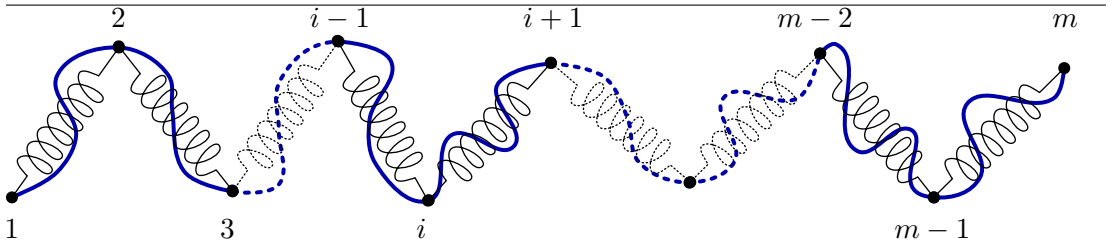


### 3.1.3 Rod-coil block copolymers

For the simulation of rod-coil diblock copolymers we combine the rod and coil homopolymers described above. Therefore, we always attach exactly one coil to each rod. The first coil bead is connected to the bottom position of its dedicated spherocylinder by a Gaussian spring. This spring has the same characteristics as those connecting the monomers of the coils. Since no monomer is added at the connection point the number of monomers per coil $m$ stays constant, while the number of springs per polymer increases from $m-1$ to $m$. The additional bead with index 0 in Figure (3.3) is just a 'virtual' monomer and not treated as a monomer for the interactions in Section 3.4.

**Figure 3.3** Cartoon of a rod-coil block copolymer in our system. The first bead of the coil polymer with $m$ monomers is attached to the bottom position of a rod-like polymer of length $L$, diameter $D$ and unit vector $\hat{\mathbf{u}}$.

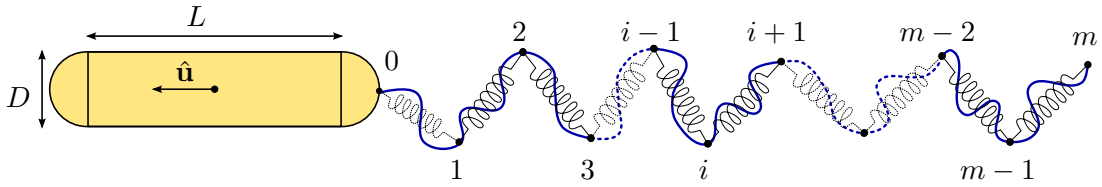


Rod and coil blocks must share an interfacial area. Their size mismatch leads to a packing frustration which is parametrized by the geometrical asymmetry $\nu$ [231]. This parameter is defined as the ratio between the coil radius of gyration $R_g$ (see Section 3.5) and the rod length $L$

$$\nu = \frac{R_g}{L}. \tag{3.18}$$

## 3.2 Simulation box and system

In this section we present the parameters which define the simulation box. We simulate different types of polymers in this work. In most cases this are rod-coil block copolymers. For some comparisons we also simulate systems containing only rod or coil polymers. For other tests we use non-connected rod and coil polymers in a mixture. But we always use the same simulation box and methods. This is also true for the tetrapod/polymer mixtures simulated in the second part of this thesis. In all of our models we use the Monte-Carlo method to simulate the system of interest. During each simulation run the number of particles as well as shape and volume of the simulation box is kept constant.

In general, a simulation box contains $N_{\text{Rods}}$ rod polymers and $N_{\text{Coils}}$ coil chains. In most simulations we have rod-coil block copolymers. For these polymers each rod has a coil chain attached to its end and the number of coil chains is equal to the number of rods. Therefore, we will usually just mention the total number of polymers

$$N = N_{\text{Coils}} = N_{\text{Rods}}. \tag{3.19}$$

All simulations are performed in a rectangular box with periodic boundary conditions in all three directions. The box sizes in the three directions are given by $L_x, L_y$ and $L_z$, which are constant but may differ from each other. Thus, the volume can be calculated as

$$V_{\text{Box}} = L_x \cdot L_y \cdot L_z. \tag{3.20}$$

The developed model is an off-lattice model. This means the polymers can move through the simulation box in a continuous way. Nevertheless, we introduce a grid to subdivide our simulation box. As we will see in Section 3.4 some of the interactions in our model are based on local densities. To calculate these densities we have to subdivide our simulation box into small cubical boxes of size $\delta_i$ with $\delta_x = \delta_y = \delta_z := \delta$. The cells have to be cubic to guarantee that the interactions are isotropic. The volume of each cell is given by

$$V_{\text{Cell}} = \delta_x \cdot \delta_y \cdot \delta_z = \delta^3. \tag{3.21}$$

Hence, the simulation box can take any rectangular shape composable from cubical cells. This also introduces a restriction to the lengths of the simulation box, since each length $L_i$ has to be the $n_i$-th multiple of the associated cell size $\delta_i$. With this the box volume may also be expressed as

$$V_{\text{Box}} = n_x\delta_x \cdot n_y\delta_y \cdot n_z\delta_z = n_x \cdot n_y \cdot n_z \cdot \delta^3 = N_{\text{Cells}} \cdot V_{\text{Cell}} \tag{3.22}$$

where $N_{\text{Cells}}$ is the total number of cells.

A sketch of a simulation box with $4 \times 3 \times 3$ cells is shown in Figure (3.4). One of the 36 cells with volume $\delta^3$ is highlighted. Just like for the simulation box the shape and the size of all cells are kept constant during the simulation. The cell size $\delta$ has to be chosen very carefully. As we will see later in Section 3.4 the cell size $\delta$ determines the interaction range of most interactions in our model. Therefore, the cell size must not be smaller than the mean distance between the monomers, otherwise the polymers would barely interact. On the other hand, the cell size should not be too large, since in this case the ability to resolve an inhomogeneous density distribution will be lost [69]. In most runs we have chosen a cell size of $\delta$ equal to 1.5. The motivation for the selection of this cell size will be discussed in Section 4.1.

**Figure 3.4** Simulation box with a volume $L_x \cdot L_y \cdot L_z$. The box is divided into $4 \times 3 \times 3$ cells. The yellow highlighted cell has a volume of $\delta^3$.

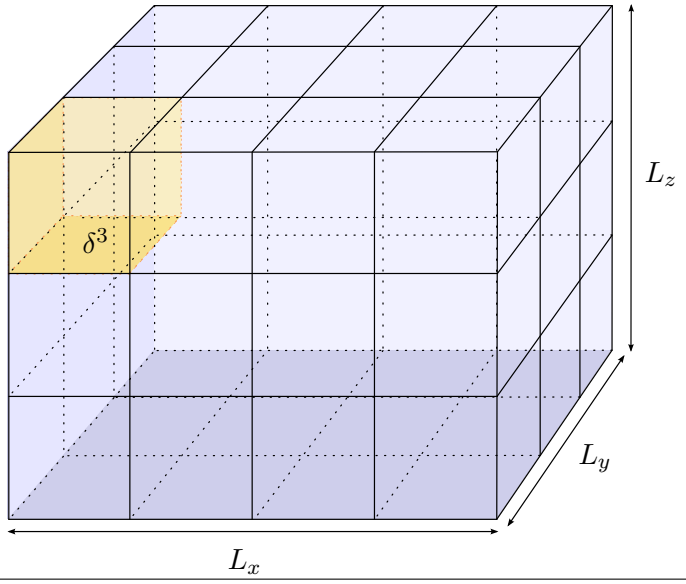


We use periodic boundary conditions in all three dimensions. This means each particle leaving the simulation box reenters the box on the opposite site of the box. A sketch of a two-dimensional system with periodic boundary conditions is shown in Figure (3.5). The central gray box and the polymers in intense color represent the main simulation box and the central images of the polymers. For simplicity we only show eight neighboring boxes. The phantom images of the polymers are displayed in lighter color. The central image of a polymer can interact with the phantom image of a polymer. To prevent an interaction of an particle with its own image directly or via only one bridging polymer the box size is chosen to be a least three times the total length $\lambda$ of a rod in all three directions.

**Figure 3.5** Cartoon of the periodic boundary conditions in our system. The images shows a projection onto the two-dimensional plane. The central gray box is the simulation box containing rod-coil block copolymers. The surrounding lighter boxes and polymers are periodic images of the system.

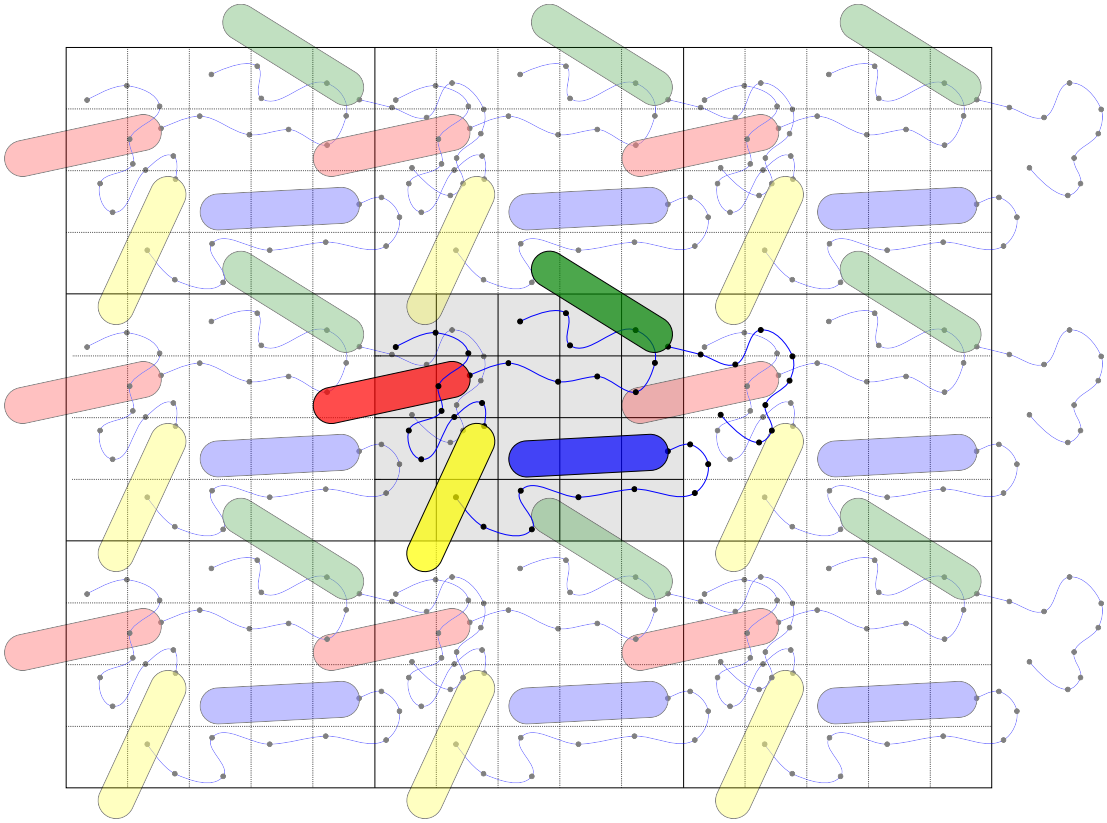

Whenever we do not start our simulation from a prior configuration we have to set up our system artificially. To this end, we have several options. There are no constraints for the placement of the monomers since they have no volume, are allowed to penetrate the rod polymers and the chains are crossable. The hard spherocylinders representing the rod polymers have a volume and are impenetrable. Hence, especially for high densities, primarily the placement of the rods is critical and, therefore, done before the coil chains are attached to the bottoms of the spherocylinders.

The first possibility to set up the rods is in a completely ordered manner. Depending on the box size and the length $L$ and the diameter $D$ of the spherocylinders we place the rods on a simple orthorhombic lattice in several layers. The layers are filled row by row. The rods are either all aligned along the positive $z$-axis or, with a tunable ratio, randomly along the positive and negative $z$-axis. The second way is very similar. Instead of placing the spherocylinders next to each other in a fixed sequence, we calculate all possible positions in advance and then place them randomly at a free position. For these two methods it is possible to move all rods randomly for several thousand steps with hard-body interactions only, before the coil beads are added.

Alternatively, we may set up the system completely random. Here, all spherocylinders are placed randomly in the simulation box with a random orientation. For dense systems it takes a very long time to set up a random configuration. For these systems we increase the size of the simulation box and place all rods in the box randomly. Afterwards, we reduce the size of the box in small steps. After each step we check if the new size is compatible with the periodic boundary conditions. If there is an overlap of the rods the old box size is restored. After randomly moving all rods several times a new attempt to reduce the box size is started. This is repeated until the desired box size is reached.

Before the main simulation is started we perform a prerun. During the prerun the move ranges of the polymers are adapted every few steps until an average acceptance rate of about 33% is reached. These move ranges are used as starting values for the main simulation. Based on the measured acceptance rates the move ranges may also be changed during the simulation run. This is usually done after an adjustable number of simulation sweeps.

## 3.3 Monte-Carlo simulations

In this section we briefly describe the Monte-Carlo method [9, 10, 85, 135] used for all simulations in this work. The basic idea of Monte-Carlo simulations is to make trial moves for the particles and accept or reject them depending on a given criterion. This criterion is related to the energy change of the system during the trial move. The concrete energies for our system of rod-coil block copolymers will be introduced in the following section. For now we will use a general energy $\beta\mathcal{H}$, which is replaced later by the expression in Equation (3.25).

At the beginning of each Monte-Carlo step the total energy of the current system is calculated and saved as $\beta\mathcal{H}_{\text{old}}$. Then a random particle is chosen and moved. Depending on the move range $\kappa$ associated with the type of movement the monomer or rod is translated or the rod is rotated by a random amount. After the move the new energy $\beta\mathcal{H}_{\text{new}}$ is computed. The move will be accepted with a probability

$$acc(\text{old}\rightarrow\text{new}) = \min\left(1, \exp(-\{\beta\mathcal{H}_{\text{new}} - \beta\mathcal{H}_{\text{old}}]\})\right). \tag{3.23}$$

This means, if the new configuration has a lower energy the move is always accepted. In case the total energy increases the acceptance rate diminishes with increasing energy difference. If a move is rejected the old configuration is restored. For coil moves this algorithm is repeated $M$ times and for both possible rod moves $N_{\text{Rods}}$ times. So on average every monomer is moved and every rod is translated and rotated once per Monte-Carlo step.

The Monte-Carlo method is unsuitable to investigate dynamic properties of a system, as time is not an involved variable [2]. In order to achieve correct results the simulations must be ergodic. This means that all possible configurations in phase space should be attainable if the algorithm would run for an infinite amount of time. As it is unfeasible to run a simulation infinitely long, it is not possible to prove that an algorithm is ergodic. Usually, a system is assumed to be ergodic, if it fulfills detailed balance. The detailed

balance condition states that for each transition between two states there has to be a reverse transition with a non-zero probability. It is given by

$$P_i W_{ij} = P_j W_{ji} \tag{3.24}$$

where $P_\alpha$ is the probability of the system being in state $\alpha$ and $W_{\alpha\beta}$ is the transition rate from state $\alpha$ to $\beta$. A process satisfying the detailed balance condition is called a reversible Markov chain. A Markov chain is a stochastic, memoryless process. This means that a future state of the system solely depends on the current state and not on previous states.

To avoid systematic errors it is essential to use good random number generators with a high periodicity in computer simulations [135]. Therefore, to provide a fast generation of high-quality pseudo-random numbers, we use the *C++11* uniform real distribution class template with the 64-bit implementation *mt19937_64* of the Mersenne twister engine [174, 186].

## 3.4 Interactions

In this section we describe how the polymers, we introduced in Section 3.1, interact with each other. First we give a general overview of all interactions in our system. Then we discuss each single contribution. For some interactions we first introduce a general expression and then show how they are calculated in the different models we use.

To decide if a Monte-Carlo move is accepted or rejected we have to calculate the energy difference between the old and the new configuration. Therefore, we need an expression for the total energy of the system. The total Hamiltonian $\mathcal{H}$ comprises four different contributions

$$\beta\mathcal{H} = \beta\mathcal{H}_{\mathrm{RR}} + \beta\mathcal{H}_{\mathrm{G}} + \beta\mathcal{H}_{\mathrm{CC}} + \beta\mathcal{H}_{\mathrm{CR}} \tag{3.25}$$

where $\beta$ denotes the inverse temperature, that is, $\beta = 1/k_{\mathrm{B}}T$ with $k_{\mathrm{B}}$ being the Boltzmann constant. $\beta\mathcal{H}_{\mathrm{RR}}$ is the rod-rod interaction and $\beta\mathcal{H}_{\mathrm{G}}$ the interaction energy of the Gaussian polymer chains. The interaction between monomers $\beta\mathcal{H}_{\mathrm{CC}}$ and the rod-coil interaction $\beta\mathcal{H}_{\mathrm{CR}}$ are both based on local densities. The particular contributions are described in detail in the following sections.

For the temperature range of interest the chemical bonds, which provide the connectivity, are basically unbreakable. The interaction strengths of the terms $\beta\mathcal{H}_{\mathrm{CC}}$ and $\beta\mathcal{H}_{\mathrm{CR}}$ dependent on effective parameters $\chi_{\mathrm{CC}}$ and $\chi_{\mathrm{CR}}$, respectively. These $\chi$-parameters stem from integrating out microscopic degrees of freedom. We assume that their temperature dependence is weak in the range of interest. Consequently, we investigate the phase behavior in dependence of these $\chi$-parameters instead of looking explicitly at the temperature.

### 3.4.1 Rod-rod interaction

As described in Section 3.1.1 we use impenetrable spherocylinders to model the rod polymers. They are characterized by their orientation, which is described by the unit vector $\hat{\mathbf{u}}$ and the two parameters length $L$ and diameter $D$ or, alternatively, their aspect ratio $p$. The interaction between the rods is a pure hard-body interaction preventing an

overlap of the rods. For a system with $N_{\text{Rods}}$ rods in a volume $V_{\text{Box}}$ this interaction can be written as

$$\beta\mathcal{H}_{\text{RR}}(d) = \begin{cases} \infty & : \text{rods overlap} \\ 0 & : \text{otherwise} \end{cases} \tag{3.26}$$

where the scalar parameter $d$ is the shortest distance between two rods. Figure (3.6) shows a system with four rods. Note that the drawn cells are nonessential since $\beta\mathcal{H}_{\text{RR}}$ is only related to the distance between the rods and in no way to the cells. To check if two rods overlap we need to calculate the shortest distance between the two spherocylinders. As long as this distance is bigger than the diameter $D$ of the spherocylinders the potential is zero. For smaller distances the potential is infinite, prohibiting an overlap of the rods.

**Figure 3.6** Two-dimensional sketch of a system with $5 \times 4$ cubic cells and four rods.

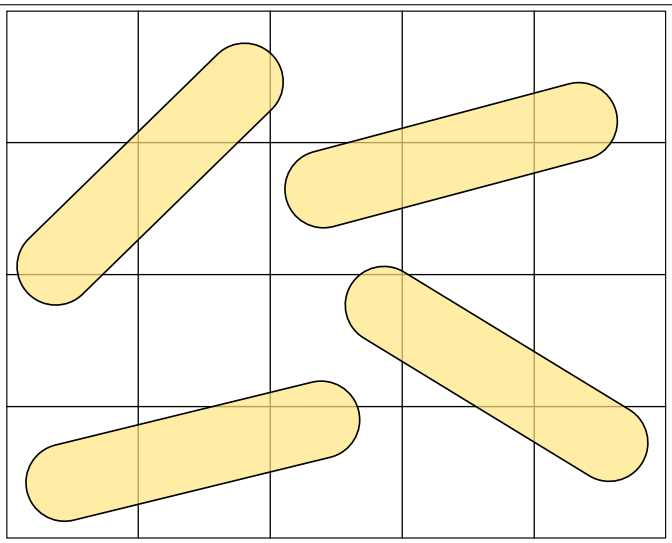

The overlap detection between spherocylinders is much more complicated than for spheres. A fast algorithm to evaluate the shortest distance between rods is published by Vega and Lago [273]. This algorithm is used and improved by several other groups [2, 19, 39, 166]. We also use a revised version of the original algorithm. This algorithm can further be optimized and used for the distance calculation between spherocylinders and spheres, which are spherocylinders with $L = 0$, or monomers, which are spheres with a radius of zero, that is, $L = D = 0$.

In this algorithm we treat the spherocylinders as finite line segments of length $L$. Any point on the line segments can be described parametrically by

$$\mathbf{t}_i = \mathbf{r}_i + \mu_i \hat{\mathbf{u}}_i \tag{3.27}$$

where $\mathbf{r}_i$ and $\hat{\mathbf{u}}_i$ are the position and unit vector of the $i$-th rod, respectively, and $\mu_i$ is a parameter in the interval $[-L/2, L/2]$. If $\mathbf{r}_{ij}$ is the distance vector connecting the centers of two rods $i$ and $j$

$$\mathbf{r}_{ij} = \mathbf{r}_j - \mathbf{r}_i \tag{3.28}$$

the distance vector $\mathbf{d}_{ij}$ between two points on the line segments reads

$$\mathbf{d}_{ij}(\mu_i, \mu_j) = \mathbf{r}_{ij} + \mu_j \hat{\mathbf{u}}_j - \mu_i \hat{\mathbf{u}}_i. \tag{3.29}$$

Figure (3.7) illustrates the calculation of the shortest distance between two spherocylinders. The basic idea is to adapt both $\mu$-parameters, by which the parametrized points $\mathbf{t}_1$ and $\mathbf{t}_2$ move along the line segments, until the distance between these two points is minimized. Instead of actually varying the $\mu$-parameters we can compute them and, thus, the shortest distance between the rods.

**Figure 3.7** Calculation of the shortest distance $\mathbf{d}_{12}$ (red) between two rods 1 and 2, with unit vectors $\hat{\mathbf{u}}_1$ and $\hat{\mathbf{u}}_2$. The two line segments of length $L$ are highlighted in blue and green. The shortest distance is achieved by varying the parameters $\mu_1$ and $\mu_2$, thus shifting the points $\mathbf{t}_1$ and $\mathbf{t}_2$ along the line segments until the distance between these points is minimized.

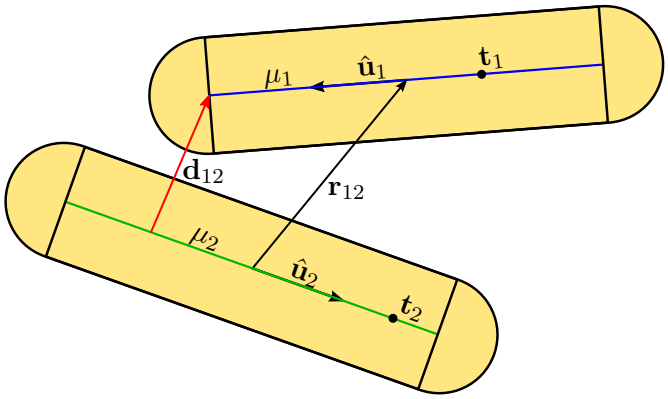


In computer simulations it is more convenient to deal with squared distances to avoid the expensive calculation of square roots. Hence, we use the squared distance

$$\mathbf{d}_{ij}^2 = \mathbf{r}_{ij}^2 + 2\mu_j \hat{\mathbf{u}}_j \cdot \mathbf{r}_{ij} - 2\mu_i \hat{\mathbf{u}}_i \cdot \mathbf{r}_{ij} - 2\mu_i \mu_j \hat{\mathbf{u}}_i \cdot \hat{\mathbf{u}}_j + \mu_i^2 + \mu_j^2. \tag{3.30}$$

To obtain the shortest distance we have to minimize this equation with respect to both $\mu_i$ and $\mu_j$. This way we get the primed $\mu$-parameters

$$\mu_i' = \frac{\hat{\mathbf{u}}_i \cdot \mathbf{r}_{ij} - (\hat{\mathbf{u}}_i \cdot \hat{\mathbf{u}}_j)(\hat{\mathbf{u}}_j \cdot \mathbf{r}_{ij})}{1 - (\hat{\mathbf{u}}_i \cdot \hat{\mathbf{u}}_j)^2} \tag{3.31}$$

$$\mu_j' = \frac{(\hat{\mathbf{u}}_i \cdot \hat{\mathbf{u}}_j)(\hat{\mathbf{u}}_i \cdot \mathbf{r}_{ij}) - \hat{\mathbf{u}}_j \cdot \mathbf{r}_{ij}}{1 - (\hat{\mathbf{u}}_i \cdot \hat{\mathbf{u}}_j)^2} \tag{3.32}$$

which minimize Equation (3.30). If they exceed the interval $[-L/2, L/2]$ the parameters are set to $-L/2$ or $L/2$ depending on whether the negative or positive bound is exceeded. As they only depend on known or easily computable parameters, they can be calculated directly. Substituting these values into Equation (3.30) gives the shortest squared distance between the line segments. If this squared distance is smaller than $D^2$ the spherocylinders are overlapping.

To speed up the overlap detection special cases like parallel or perpendicular rods are treated separately. Additionally, it is useful to calculate the distance between the centers of the rods $\mathbf{r}_{ij}^2$ beforehand, as it is needed anyway to receive the shortest distance in Equation (3.30). If the centers have a larger distance than the total length of a spherocylinder $\lambda = L + D$, these rods can not overlap. Therefore, we can skip the rest of the computation, as our interactions do not depend on the numerical value of the

distance. For these calculations it is important to apply periodic boundary conditions correctly, since the distance between a central image and a periodic image may be shorter than the distance between the central images of both rods. Another approach we tried to speed up the computation is to implement lists which save if a spherocylinder overlaps with a cell. Then we only have to check the rods for overlap if they have a common cell in their lists.

### 3.4.2 Coil-coil interactions

Beside the interaction with the rods, the coils have two different types of interactions. The first contribution is a pure intrachain interaction describing a Gaussian chain and provides the connectivity [72, 82]. In the continuous version of the Edwards model [25, 72, 75, 210] the conformational properties of a polymer chain with three-dimensional position vector $\mathbf{R}(i)$ in a good solvent are determined by the Hamiltonian

$$\beta\mathcal{H}_{\mathrm{G}} = \frac{3}{2b^2}\int_0^m \mathrm{d}i\,\left(\frac{d\mathbf{R}(i)}{di}\right)^2 \tag{3.33}$$

where $b$ is the average bond length. Since we do not use continuous but discrete chains the integral can be written as a sum. To get the full interaction we accumulate the contributions over all $N_{\mathrm{Coils}}$ chains and get

$$\beta\mathcal{H}_{\mathrm{G}} = \frac{k}{2}\sum_{\alpha=1}^{N_{\mathrm{Coils}}}\sum_{i=1}^{m}(\mathbf{R}_{\alpha,i-1}-\mathbf{R}_{\alpha,i})^2 \tag{3.34}$$

where $\mathbf{R}_{\alpha,i}$ is the monomer position of $i$-th monomer in the $\alpha$-th chain. The strength of the Gaussian bond energy is given by the spring constant $k$ which is related to the average bond length $b$ by

$$k = \frac{3}{b^2} \tag{3.35}$$

in three space dimensions. In our simulations we mainly use the values $k = 3, 12$ or $27$ resulting in average bond lengths $b$ of 1.0, 0.5 or $0.\overline{3}$.

The monomers at $\mathbf{R}_{\alpha,0}$ have a special role. They are virtual monomers, which are fixed to one end of the associated spherocylinder. As shown in Figure (3.3) these monomers are used to connect the polymeric chains to the rods. Therefore, merely adding a spring between monomers 0 and 1, these monomers only contribute to $\beta\mathcal{H}_{\mathrm{G}}$ in Equation (3.25) but not to the monomer density $\rho_{\mathrm{C}}$, which determines $\beta\mathcal{H}_{\mathrm{CC}}$ (see Equation (3.36) below) and $\beta\mathcal{H}_{\mathrm{CR}}$ (see Equation (3.40) in Section 3.4.3). These monomers are not moved during the monomer trial moves but during the Monte-Carlo moves of the dedicated rods. Hence, the coil related interaction $\beta\mathcal{H}_{\mathrm{G}}$ may also change during the rod moves.

The second contribution to Equation (3.25) models the excluded volume interactions of the monomers. It is given by the first term in the corresponding virial expansion

$$\beta\mathcal{H}_{\mathrm{CC}} = \frac{\chi_{\mathrm{CC}}}{2}\int_V \mathrm{d}\mathbf{r}\,(\rho_{\mathrm{C}}(\mathbf{r}))^2. \tag{3.36}$$

This contribution is based on the continuous monomer density field $\rho_{\mathrm{C}}(\mathbf{r})$ related to a given configuration [72, 82]. In order to have a stable polymer configuration the

parameter $\chi_{\mathrm{CC}}$ needs to be positive what makes $\beta\mathcal{H}_{\mathrm{CC}}$ a purely repulsive interaction. In our discrete model the continuous monomer density field $\rho_{\mathrm{C}}(\mathbf{r})$ is replaced by local densities

$$\rho_{\mathrm{C},I} = \rho_{\mathrm{C},I}\{\mathbf{R}_{\alpha,i}\} = \frac{1}{V_I} \int\limits_{\text{Cells } I} \mathrm{d}\mathbf{r} \sum_{\alpha,i} \delta(\mathbf{r} - \mathbf{R}_{\alpha,i}) \tag{3.37}$$

where $V_I$ is the volume accessible to the monomers in the $I$-th cell [25, 210]. Note that the accessible volume $V_I$ of a cell is not necessarily equal to the cell volume $V_{\mathrm{Cell}}$. In Section 3.4.4 we distinguish different models and their influence on the accessible volume. If we assume that there are $C_I$ monomers in cell $I$ the discrete densities $\rho_{\mathrm{C},I}$ can be expressed as

$$\rho_{\mathrm{C},I} = \frac{C_I}{V_I}. \tag{3.38}$$

Finally, Equation (3.36) can be written as

$$\beta\mathcal{H}_{\mathrm{CC}} = \frac{\chi_{\mathrm{CC}}}{2} \sum_I V_{\mathrm{Cell}} \left(\frac{C_I}{V_I}\right)^2. \tag{3.39}$$

Allowing us to test and compare our results to former works [25, 137, 238] we, too, set the interaction strength $\chi_{\mathrm{CC}}$ to 0.5 in nearly all our simulations.

This interaction does not distinguish whether the beads are from the same or a different chain and affects only monomers in the same cell. Hence, the cell size $\delta$ corresponds to an effective monomer size and introduces an interaction range for this interaction. As mentioned before the virtual 0-th monomers at the end of the spherocylinders do not contribute to this interaction. Since we use an off-lattice model the monomer positions can take any value in the three-dimensional volume $V_{\mathrm{Box}}$. If they are beyond the simulation box periodic boundary conditions are applied.

Figure (3.8) shows a sample configuration of four coil chains with ten monomers each. The term $\beta\mathcal{H}_{\mathrm{CC}}$ will try to spread the monomers as uniformly over all cells as possible. At the same time $\beta\mathcal{H}_{\mathrm{G}}$ will attempt to keep the monomers of one chain at an average distance $b$. The incompatibility of these two effects depends on the given system parameters.

**Figure 3.8** Two-dimensional sketch of a system with $5 \times 4$ cubic cells and four coil chains with $m = 10$ monomers.

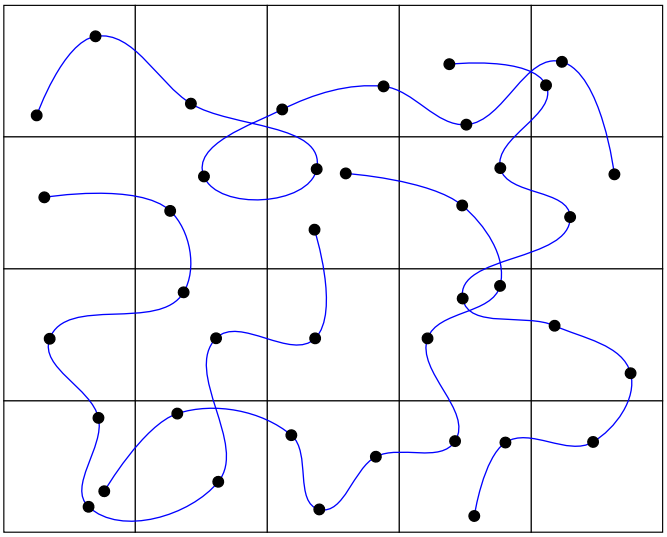

### 3.4.3 Rod-coil interaction

The last contribution to the total energy $\beta\mathcal{H}$ describes the interaction between rods and coils. Its general form is

$$\beta\mathcal{H}_{\mathrm{CR}} = \chi_{\mathrm{CR}} \int_V \mathrm{d}\mathbf{r}\, \rho_{\mathrm{C}}(\mathbf{r})\rho_{\mathrm{R}}(\mathbf{r}) \tag{3.40}$$

where the strength of the monomer-rod interaction $\chi_{\mathrm{CR}}$ is a non negative number. As in Equation (3.36) $\rho_{\mathrm{C}}(\mathbf{r})$ is the monomer density. $\rho_{\mathrm{R}}(\mathbf{r})$ denotes the rod density. Similar to the coil density it may be written in a discretized form $\rho_{\mathrm{R},I}$, which can be interpreted as the volume fraction of the rods in cell $I$. For the sake of simplicity we will abbreviate the rod volume fraction as

$$\rho_{\mathrm{R},I} = \varphi_I. \tag{3.41}$$

Thus, Equation (3.40), expressed as discretized monomer-rod interaction, reads

$$\beta\mathcal{H}_{\mathrm{CR}} = \chi_{\mathrm{CR}} \sum_I V_{\mathrm{Cell}} \frac{C_I}{V_I} \varphi_I. \tag{3.42}$$

Please note that there is no attractive interaction in our system as this interaction is also purely repulsive. The contribution from the $I$-th cell is proportional to the product of the volume fraction of rods in this cell and the number of included monomers. Thus, the interaction may be reduced if fewer cells include a huge amount of monomers while having a big overlap with rods. So this repulsive interaction can be seen as a separation strength trying to push rods and monomers into unequal cells. The interaction range is again limited by the cell size $\delta$. The local rod density $\rho_{\mathrm{R},I}$, or rather the volume fraction $\varphi_I$, are difficult to access. Therefore, we develop several models to obtain these values. These models are described in the following section.

If $\chi_{\mathrm{CR}}$ is equal to zero there is no interaction between rods and coils. At first glance, there is no difference for the rods to a system without coils. But since the coils stay attached to the rods and still interact with each other they can not move entirely free.

So this may not be directly comparable with a system without coils. In Figure (3.9) a system with four rod-coil block copolymers in a simulation box of five times four cubic cells is illustrated.

**Figure 3.9** Two-dimensional sketch of a system with $5 \times 4$ cubic cells and four rod-coil block copolymers with $m = 10$ monomers.

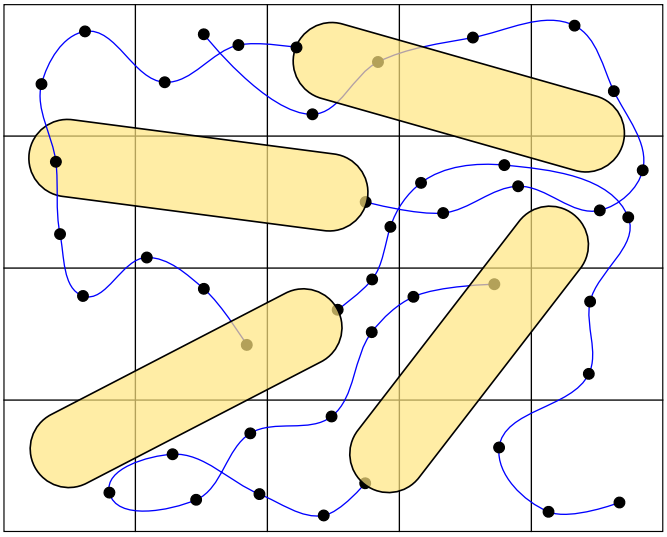

### 3.4.4 Different models

#### Monte-Carlo integration

In our first approach we model the rod-coil interaction by hard-body constraints. This means a monomer may not enter a spherocylinder. Additionally, we have a density-dependent interaction which describes soft interactions of longer range.

$$\beta\mathcal{H}_{\mathrm{CR}} = \begin{cases} \infty & : \text{monomers enter rods} \\ \chi_{\mathrm{CR}} \int\limits_V \mathrm{d}\mathbf{r}\, \rho_{\mathrm{C}}(\mathbf{r})\rho_{\mathrm{R}}(\mathbf{r}) & : \text{otherwise} \end{cases} \tag{3.43}$$

So, whenever a trial move would end in a situation in which a monomer is inside a rod this move is rejected. Otherwise we get the contribution already known from Equation (3.40). To check if a monomers is inside a spherocylinder we use the same shortest distance algorithm as for the rods. Since a monomer can be expressed as a spherocylinder of length and diameter equal to zero this algorithm can be simplified dramatically and is much faster.

As the monomers are not allowed to enter the spherocylinders the volume $V_I$ accessible to the monomers in a cell $I$ is reduced by the space occupied by the rods and may, therefore, be smaller than the volume $V_{\mathrm{Cell}}$ of the cells. For a given rod volume fraction $\varphi_I$ the reduced volume can be calculated as

$$V_I = (1 - \varphi_I)\, V_{\mathrm{Cell}}. \tag{3.44}$$

Using this relation Equation (3.39) and Equation (3.42) become

$$\beta\mathcal{H}_{\mathrm{CC}} = \frac{\chi_{\mathrm{CC}}}{2} \sum_I \frac{1}{V_{\mathrm{Cell}}} \left( \frac{C_I}{1-\varphi_I} \right)^2 \tag{3.45}$$

$$\beta\mathcal{H}_{\mathrm{CR}} = \chi_{\mathrm{CR}} \sum_I \frac{C_I}{1-\varphi_I} \varphi_I. \tag{3.46}$$

The rod volume fraction $\varphi_I$ is determined in means of a Monte-Carlo integration scheme. To this end a fixed number of $\Omega$ random positions are generated in cell $I$. Then we count the number $\omega_I$ of positions which are inside of rods. The rod volume fraction $\varphi_I$ can then be approximated as

$$\varphi_I = \rho_{\mathrm{R},I} = \frac{V_{\mathrm{R},I}}{V_{\mathrm{Cell}}} \approx \frac{\omega_I}{\Omega} \tag{3.47}$$

where $V_{\mathrm{R},I}$ is the total volume occupied by rods in cell $I$. With this the reduced volume accessible to the monomers and the contributions $\beta\mathcal{H}_{\mathrm{CC}}$ and $\beta\mathcal{H}_{\mathrm{CR}}$ can be expressed as

$$V_I = \left(1 - \frac{\omega_I}{\Omega}\right) V_{\mathrm{Cell}} \tag{3.48}$$

$$\beta\mathcal{H}_{\mathrm{CC}} = \frac{\chi_{\mathrm{CC}}}{2} \sum_I \frac{1}{V_{\mathrm{Cell}}} \left( \frac{C_I}{1-\frac{\omega_I}{\Omega}} \right)^2 \tag{3.49}$$

$$\beta\mathcal{H}_{\mathrm{CR}} = \chi_{\mathrm{CR}} \sum_I \frac{C_I}{1-\frac{\omega_I}{\Omega}} \frac{\omega_I}{\Omega}. \tag{3.50}$$

For a sufficient accuracy a lot of random positions are needed. As the same positions have to be used for the calculation of the old and the new energy during a Monte-Carlo step, all positions must be saved. This may become very memory consuming. There is no need to generate a new distribution of random positions for each Monte-Carlo step. However, it has to be regenerated regularly to avoid artifacts. Results obtained with this model are published in reference [73].

#### Monte-Carlo integration using a pool of random number cells

The random numbers for the positions, needed to calculate the rod densities, have to be reshuffled from time to time of course. Saving all the random numbers does not only consume a lot of memory but the generation also takes a lot of time.

Hence, we improve the model by using a pool of cells filled with random numbers. Figure (3.10) shows a pool of $p$ cubic cells filled with $\omega$ random positions. For each cell only the relative positions to the center position $\mathbf{r}_{\mathrm{c}}$ of the $\omega$ random numbers are saved. As we save the central positions of all $I$ cells this allows us to easily place each of the $p$ cells at any cell $I$ of the simulation box and calculate the random positions. For each cell of our simulation box one of these $p$ cells is randomly chosen. After a give number of steps the cells are redistributed randomly. This way we need to save much less random numbers, which have to be generated only once.

This model needs less memory and is much faster but the performance is still not satisfying. In addition, the rods are nearly immobile at higher monomer concentrations because of the hard core interaction between monomers and spherocylinders. Thus we develop a completely different approach.

**Figure 3.10** Pool of $p$ cells filled with $\omega$ random positions, denoted by red points, relative to the center position $\mathbf{r}_c$ of the cell.

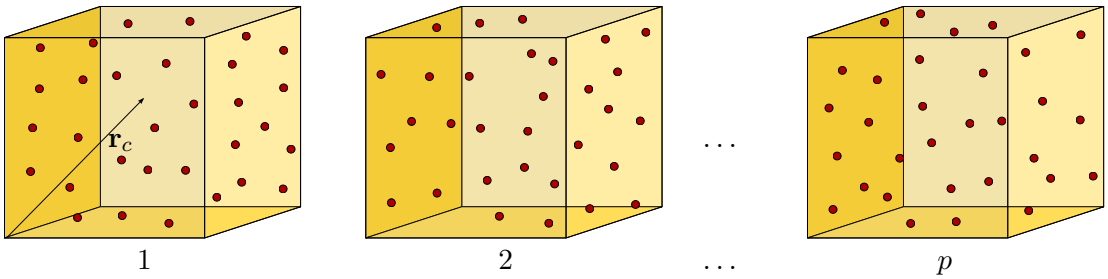


### Surface approximation method

The calculation of the rod densities takes a lot of time. Since the monomers are not allowed to penetrate the rods we have to check if the rods and monomers overlap after each rod and monomer Monte-Carlo step. After each of both possible rod moves the rod volume fractions $\varphi_I$ for all cells $I$ which are in contact with the moved rod have to be recomputed. As the accessible volume $V_I$ depends on $\varphi_I$ these values also change and the coil-coil interactions $\beta\mathcal{H}_{\mathrm{CC}}$ in all affected cells have to be recalculated, too. This huge amount of computations dramatically slows down the simulation.

Therefore, we now allow the monomers to enter the spherocylinders. In addition, we change the way how the rod densities are approximated. In this model we place virtual dots on the surface of the spherocylinders, which are used to approximate the rods densities. Figure (3.11a) shows a rod-coil block copolymer with these points added to the surface. We add a point at the top and bottom of each spherocylinder and rings of six points each. The point at the bottom position is the same point as the 0-th virtual monomer. The first ring is placed at the center of the spherocylinder. Then rings at distances of half the rod diameter are added along the cylindrical core. Figure (3.11b) illustrates a rendered image of a rod-coil block copolymer with 56 surface points.

For convenience, we use spherocylinders with a diameter equal to one. This way we can do all the expensive sine and cosine calculations needed to place the points on the rings beforehand. Additionally, by using six points per ring, we can ensure that the distance between each neighboring point is half the rod diameter and, thus, the same value as the distance between the rings. This is important to assess the accuracy of this approximation and to decide how big the cell size should be. Later we will show that the cell size $\delta$ should not be smaller than the distance between the points. The total number of surface points for each rod only depends on the length and can be calculated as

$$\gamma = 6(2L + 1) + 2. \tag{3.51}$$

It is pretty easy and fast to determine the number $\Phi_I$ of surface points in cell $I$. With this we can define the rod density in the $I$-th cell as

$$\varphi_I = \rho_{\mathrm{R},I} = \frac{V_{\mathrm{Rod}}\,\Phi_I/\gamma}{V_{\mathrm{Cell}}} \approx \frac{V_{\mathrm{R},I}}{V_{\mathrm{Cell}}} \tag{3.52}$$

**Figure 3.11** (a) Rod-coil block copolymer with surface points. Each circle consists of six points resulting in an angle of 60° between each point. The first circle is centered at the origin of the unit vector $\hat{\mathbf{u}}$. The distance between the circles is $D/2$. Additionally, there is a point at the top and bottom positions of the rods. The latter one is used as connection point to the coil chain. (b) A rendered image of a rod-coil block copolymer with $L = 4$, $D = 1$, $m = 24$ monomers and $\gamma = 56$ surface points.

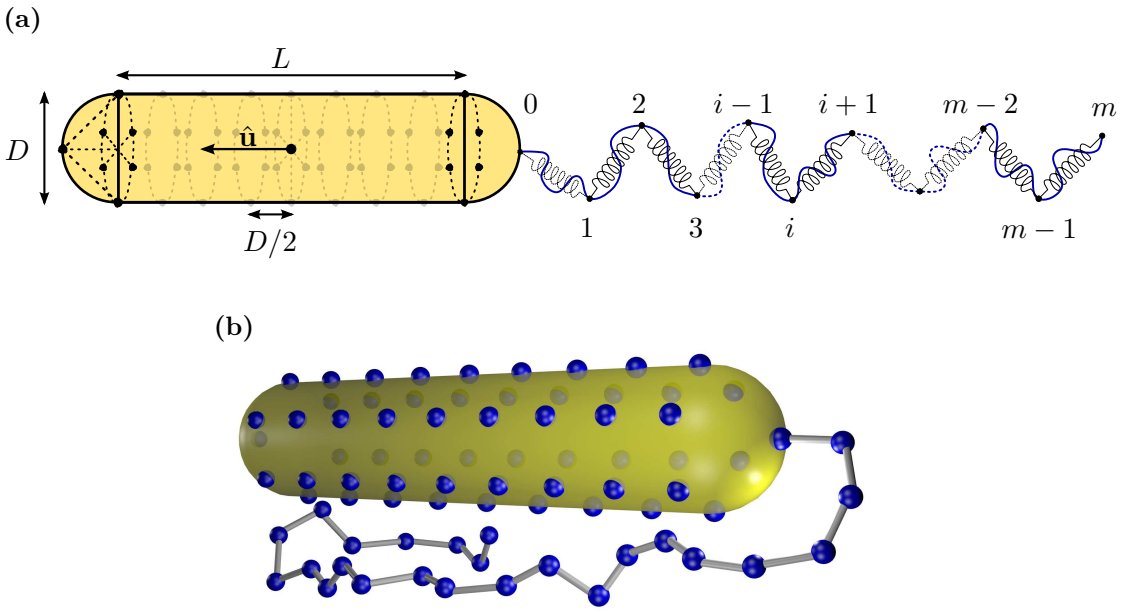


where $V_{\text{Rod}}$ is the volume of a spherocylinder and $V_{\text{R},I}$ is the rod volume fraction in cell $I$. This allows us to express the rod-coil interaction from Equation (3.42) as

$$\beta\mathcal{H}_{\text{CR}} = \chi_{\text{CR}} \sum_I V_{\text{Cell}} \frac{C_I}{V_I} \frac{V_{\text{Rod}}\, \Phi_I/\gamma}{V_{\text{Cell}}} = \chi^*_{\text{CR}} \sum_I C_I\, \Phi_I \tag{3.53}$$

where all constant values are condensed in $\chi^*_{\text{CR}}$. As the monomers are allowed to penetrate the rods the volume accessible to the monomers and the cell volume do not differ anymore and Equation (3.39) can also be simplified. Again summarizing all constant values to an interaction parameter $\chi^*_{\text{CC}}$ we get

$$\beta\mathcal{H}_{\text{CC}} = \frac{\chi_{\text{CC}}}{2} \sum_I V_{\text{Cell}} \left(\frac{C_I}{V_I}\right)^2 = \chi^*_{\text{CC}} \sum_I C_I^2. \tag{3.54}$$

In this model we do not have to distinguish different accessible volumes anymore and an increase or decrease in density always adds or removes the same contribution. Thus, we do not only save time to calculate the reduced volume for each cell but we also need less memory and can benefit from fewer memory accesses. To calculate the interactions $\beta\mathcal{H}_{\text{CC}}$ and $\beta\mathcal{H}_{\text{CR}}$ we only have to determine $C_I$ and $\Phi_I$. Both values can be implemented as integer values, which need less memory and can benefit from the much faster prefix increment and decrement operators. This way the densities and interactions can be computed very efficiently. A further benefit may be that instead of

using neighbor lists, we can swiftly check if the surface points of a spherocylinder are in a cell and only check spherocylinders for overlap if they have common cells.

## 3.5 Observables

In this section we introduce the observables and methods we use to analyze our simulations and characterize the phases.

A very common way to describe the dimension of a polymer chain is its radius of gyration $R_g$. Experimentally it is accessible via static light, small-angle neutron and x-ray scattering. Therefore, the radius of gyration is frequently used to compare theoretical results with measurements. It is defined as the root mean square distance of the collection of monomers from their common center of mass. Thus, the mean square radius of gyration [72] for a chain of $m$ monomers is given by

$$R_g^2 = \frac{1}{m}\sum_{i=1}^{m}\left\langle (\mathbf{R}_i - \mathbf{R}_{CM})^2 \right\rangle \tag{3.55}$$

where $\mathbf{R}_{CM}$ is the the center-of-mass vector

$$\mathbf{R}_{CM} = \frac{1}{m}\sum_{i'=1}^{m}\mathbf{R}_{i'}. \tag{3.56}$$

Given a number of beads per coil $m$ with an average distance $b$ between each bead the average squared radius of gyration of a Gaussian chain fulfills the relation

$$\left\langle R_g^2 \right\rangle = \frac{1}{6}mb^2 = \frac{m}{2k}. \tag{3.57}$$

Another length characterizing a polymer chain is the end-to-end distance

$$\mathbf{R}_e = (\mathbf{R}_{Last} - \mathbf{R}_{First}) \tag{3.58}$$

The end-to-end distance is simply calculated as the difference vector between the last and the first bead of a polymer chain. It is prevalent to use the average squared end-to-end distance. For a Gaussian chain it follows the relation

$$\left\langle R_e^2 \right\rangle = mb^2 = \frac{3m}{k} \tag{3.59}$$

The value $mb$ is often denoted as contour length, which is the maximal chain length for fully stretched or stiff connections. The ratio between the average squared values of the radius of gyration and the end-to-end distance for Gaussian chains is

$$\frac{\left\langle R_e^2 \right\rangle}{\left\langle R_g^2 \right\rangle} = 6. \tag{3.60}$$

With the mean end-to-end distance we may define the invariant degree of polymerization

$$\tilde{N} = \left(\rho_0 \frac{R_e^3}{M}\right)^2 \tag{3.61}$$

where $\rho_0$ is the monomer density. The square root of this quantity provides an estimate for the number of molecules inside the volume of a reference chain and, thus, the degree of interdigitation of the molecules [183]. In a dense three-dimensional melt it is proportional to the molecular weight [69].

The alignment is an important measure to characterize a phase. Spherocylinders have a shape anisotropy $p$ which is only zero for spheres. For all other cases the rods have an elongated shape and, therefore, an orientation. This allows us to calculate order parameters depending on the orientations of the spherocylinders.

The nematic order parameter is a simple and widely used way to define such an order parameter. A general definition is

$$S = \langle P_2(\cos\theta)\rangle = \left\langle \frac{3\cos^2\theta - 1}{2} \right\rangle \tag{3.62}$$

where the brackets denote the average over the complete ensemble, $P_2$ is the second Legendre polynomial and $\theta$ is the angle between the axis of a rod and the director $\mathbf{n}$. The director $\mathbf{n}$ describes the preferred direction of the elongated polymers in the system.

In the isotropic phase $S$ is zero and in the nematic phase $S$ is greater than zero but smaller than one. Experimental values of $S$ in nematics are typically in the range from 0.4 to 0.7 [22, 23, 109, 134, 144]. The Maier-Saupe theory predicts a phase transition at a value of 0.43 for the order parameter $S$ [163, 164, 165].

Instead of calculating the director every time it is often sufficient to specify one axis as director. So we get three order parameters $S_x, S_y$ and $S_z$, which measure the alignment of the rods with the given axis. Hence, averaging over all $i$ polymers using the $\alpha$-th component of the unit vectors $\hat{\mathbf{u}}_i$ with $\alpha = x, y, z$, we can define the order parameter

$$S_\alpha = \left\langle \frac{3}{2} u_i^\alpha u_i^\alpha - \frac{1}{2} \right\rangle. \tag{3.63}$$

These values can be combined to a further order parameter

$$\tilde{S} = S_x^4 + S_y^4 + S_z^4 - \frac{3}{5}. \tag{3.64}$$

If there is no alignment all three cubed $S_\alpha$ values cancel out and the minimal value of $-0.6$ is reached. For complete alignment along one axis the associated $S_\alpha$ value will become one and the two other values will equal zero. So $\tilde{S}$ will sum up to its maximal value of 0.4.

For a more accurate calculation of the nematic order parameter, including the director $\mathbf{n}$, we have to use the nematic order tensor denoted as

$$S_{\alpha\beta} = \frac{1}{N} \sum_{i=1}^{N} \left\langle \frac{3}{2} u_i^\alpha u_i^\beta - \frac{1}{2} \delta_{\alpha\beta} \right\rangle \tag{3.65}$$

with $\alpha$ and $\beta$ taking the values $x, y$ or $z$. The tensor $S_{\alpha\beta}$ is a symmetric and traceless second order tensor. Hence, it has three real eigenvalues and corresponding orthogonal eigenvectors. After diagonalizing $S_{\alpha\beta}$ we get three eigenvalues $\lambda_+, \lambda_0$ and $\lambda_-$ with $\lambda_+ > \lambda_0 \geq \lambda_-$ and $\lambda_+ + \lambda_0 + \lambda_- = 0$. The eigenvector of the biggest eigenvalue $\lambda_+$, which is commonly used as order parameter, is the systems director $\mathbf{n}$.

In general, these eigenvalues also contain a biaxiality $\eta$ and can be written as $\frac{2}{3}S$, $-\frac{1}{3}S+\eta$ and $-\frac{1}{3}S-\eta$ [27, 159]. Here $S$ is the order parameter defined in Equation (3.62) and $0 \leq \eta \leq S$. This way the nematic order tensor can be expresses as

$$\mathbf{S} = \begin{pmatrix} -\frac{1}{3}S - \eta & 0 & 0 \\ 0 & -\frac{1}{3}S + \eta & 0 \\ 0 & 0 & \frac{2}{3}S \end{pmatrix} = \begin{pmatrix} \lambda_- & 0 & 0 \\ 0 & \lambda_0 & 0 \\ 0 & 0 & \lambda_+ \end{pmatrix}. \tag{3.66}$$

With this the order parameter $S$ and the biaxiality of the molecular distribution $\eta$ can be calculated as

$$S = \lambda_+ - \frac{1}{2}(\lambda_0 + \lambda_-) \tag{3.67}$$

$$\eta = -\frac{1}{2}(\lambda_- - \lambda_0). \tag{3.68}$$

For unaxial phases $\eta$ equals zero and, thus, $\lambda_0$ equals $\lambda_-$. Figure (3.12) shows several liquid-crystalline phases including exemplary uniaxial and biaxial nematic order tensors for the smectic C, smectic A and nematic phases.

**Figure 3.12** Liquid-crystalline phases in dependence on the temperature $T$. For the smectic phases and the nematic phase the nematic order tensor $S_{\alpha\beta}$ is specified. Here the eigenvalues are labeled $\varepsilon$. The layer normal and director are denoted by $\mathbf{k}$ and $\mathbf{n}$, respectively. From [134]

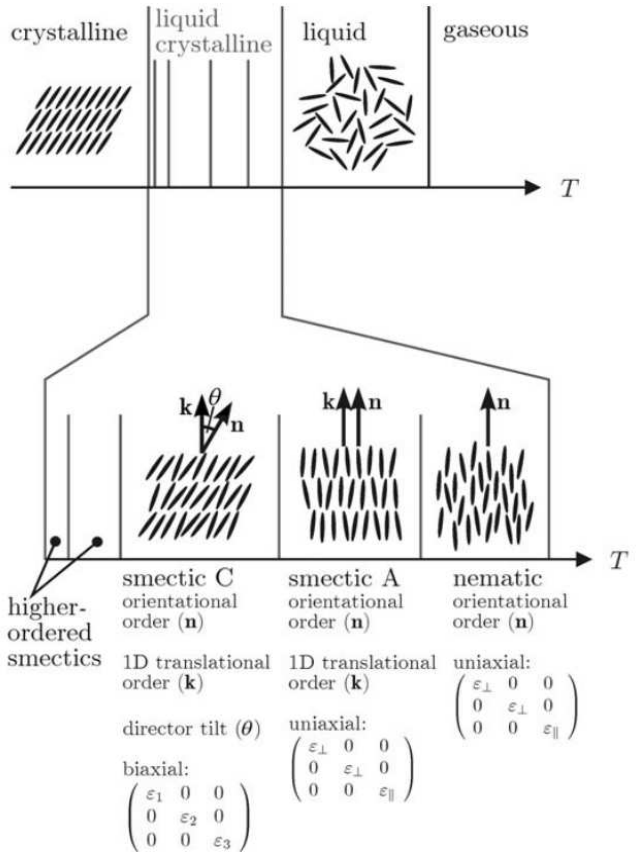

Other important observables are the pair correlation function $g(r)$ and the orientational correlation function $g_2(r)$. The pair correlation function $g(r)$ gives a probability to find a particle in a volume element $\mathrm{d}\mathbf{r}$ located at position $\mathbf{r}$ if another particle is at $\mathbf{r} = 0$. For a system of $N$ particles and a number density $\rho_0$ the radial correlation function can be defined as

$$g(r) = \frac{1}{4\pi N r^2 \rho_0} \sum_{j=1}^{N} \sum_{\substack{i=1 \\ i \neq j}}^{N} \delta\left(r - r_{ij}\right) = \frac{1}{2\pi N r^2 \rho_0} \sum_{j=1}^{N} \sum_{i>j}^{N} \delta\left(r - r_{ij}\right) \tag{3.69}$$

where $\delta\left(r - r_{ij}\right)$ is the delta distribution, which becomes one if the distance $r_{ij} = r_i - r_j$ between two particles $i$ and $j$ equals $r$ and is zero otherwise. Correlation functions can be calculated up to a distance $r_{\max}$ that should not be larger than half the size of the simulation box.

Another common version, using the radial correlation function $g(r)$, is the radial distribution function, which reads

$$R(r) = 4\pi r^2 \rho_0 \, g(r). \tag{3.70}$$

The pair correlation function $g(r)$ can be obtained by Fourier transformation of the structure factor, which can be measures in neutron and x-ray scattering experiments.

Depending on the order of the system the correlation function decays with increasing distance. The decay for various types of order are illustrated in Figure (3.13). For true long-range order there is no decay. For systems with quasi-long-range order, such as smectic liquid crystals, the decay of the correlation function follows a power law which is characterized by a positive and often small constant $\eta$. The value of $\eta$ also depends on the exhibited phase. For nematic liquid crystals or fluids, which only have short-range order, $g(r)$ decays exponentially. The constant $\xi$ is the so-called correlation length.

For anisotropic particles an orientational correlation function can be defined. It is a measure for the correlation of the rod orientations and is given by

$$g_2(r) = \langle P_2(\hat{\mathbf{u}}(0)\hat{\mathbf{u}}(r)) \rangle \tag{3.71}$$

where the brackets indicate ensemble averaging, $P_2$ is the second Legendre polynomial (see Equation (3.62)) and the unit vectors $\hat{\mathbf{u}}$ characterize the orientation of particles at the origin and $r$, respectively. Sometimes also correlation functions based on Legendre polynomials of higher order, for example, $P_4$ or $P_6$, are used.

**Figure 3.13** Decay of the correlation function $g(r)$. Here, $a$ is the monomer size. For a system with long-range order $g(r)$ remains constant, while its decay is described by a power law for systems with quasi-long-range order. The positive constant $\eta$ varies for different systems. For systems with short-range order $g(r)$ shows an exponential decay, where $\xi$ is the correlation length.

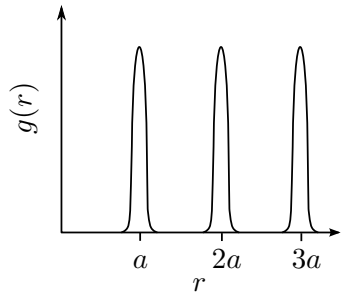


Ideal solid lattice
Long-range order

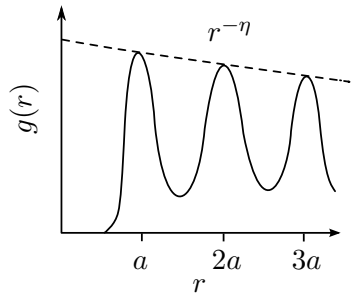


Smectic liquid crystal
Quasi-long-range order

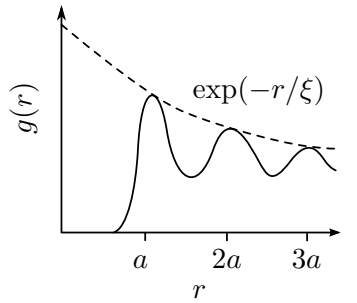


Nematic liquid crystal or fluid
Short-range order

Chapter 4

# Influence of model parameters

**Contents**



Before we can investigate the phase behavior of rod-coil block copolymers in our model we have to understand the influence and interplay of the model parameters. In Appendix A we show some preparatory work reflecting the single steps in the development of the program. In Appendix A.1 we investigate a basic phase diagram for pure rod systems while Appendix A.2 summarizes our findings for rod/coil mixtures. In this chapter we present several results which demonstrate the influence of the model parameters. At first we investigate the role of the cell size in systems of rod-coil block copolymers. Then we compare the three different methods we use to compute the interactions between rods and coils. Afterwards, we study the influence of the number of monomers per coil and, finally, the spring constant $k$ on the phase behavior.

## 4.1 Choosing the correct cell size

After we have tested the implementation of pure rod systems in Appendix A.1 and rod/coil mixtures in Appendix A.2 we connect the coils and rods to form rod-coil block copolymers. With the introduction of the coils and their interactions we also add a discretization of the simulation box into multiple, cubical cells. Therefore, we have to set a cell size at the beginning of each simulation. We have already mentioned that the choice of the correct cell size is crucial. A wrong choice may lead to undesirable behavior. In this section we discuss one of these unwanted effects and motivate our choice of the cell size.

As a first attempt we simply set the cell size $\delta$ to one and, therefore, equal to the diameter $D$ of the spherocylinders in the simulations. For this case, especially in dilute systems, we observe an alignment of the spherocylinders along the cell structure. To investigate the influence of the cell size on the arrangement of the rods we start several test simulations. To get comparable results the diameter of the spherocylinders is chosen to be equal to one while their length equals five in all simulations discussed in this section.

Our first attempt to solve the problem that the rods align along the cell structure is to change the cell size. In a first test we investigate systems with five different cell sizes $\delta$ equal to 0.1, 0.5, 1.0, 1.5 and 2.0. We only use thirty spherocylinders with extremely long coil chains consisting of 500 monomers each. This way we can very likely prevent empty cells. Thus, there should always be an interaction between a rod and the surrounding coils while the order effect of the spherocylinders among each other is reduced. The interaction parameters are set to $\chi_{\mathrm{CR}} = \chi_{\mathrm{CC}} = 0.5$ and $k = 27$. The cubic simulation box has a side length of sixteen for a cell size of two and fifteen for all other cell sizes, which results in a reduced density $\rho^*$ around 0.04 for the runs.

Snapshots of the final configurations for all five systems are displayed in Figure (4.1). It is clearly visible that orientations along the axes are preferred if the cell size $\delta$ equals the rod diameter $D$ as illustrated in Figure (4.1c). If the cell size is reduced to a value smaller than the diameter of the spherocylinders the alignment along the cell structure vanishes. This is noticeable in Figures (4.1a) and (4.1b) for cell sizes 0.1 and 0.5, respectively. If the cell size is increased to 1.5 or 2.0 the alignment is not reduced distinctly. Another effect is that the rods affiliate to small clusters of three and two or even four adjacent, parallel rods to match the cell structure. Figure (4.1d) shows the final configuration for a system with a cell size of 1.5 and illustrates that the rods try to pack in triplets. The snapshot in Figure (4.1e) indicates that an arrangement in pairs of two or four spherocylinders is favorable for a cell size of two.

As a first result we can conclude that the cell size should not be equal to the spherocylinder diameter. Systems with smaller cell sizes show the expected phase behavior but have the drawback that they may not fit our model. As already mentioned the cell size must not be smaller than the mean distance between the monomers. In case we use the surface approximation method to estimate the rod densities the cell size is additionally limited by the distance between the points on the surface of the spherocylinders. Bigger cell sizes should be treated with caution as well. Especially, if they are multiples of the diameter as they may not sufficiently reduce the alignment along the cell structure without further adjustments. Furthermore, if the cell size becomes to large the ability to resolve an inhomogeneous density distribution of the monomers

will be lost [69]. Although it is not prohibited it is cumbersome to choose odd cell sizes such as 1/3 or 1.6. In order to choose a suitable cell size we have to compare further properties of our simulations.

**Figure 4.1** Snapshots of a dilute system with different cell sizes $\delta$ demonstrating the alignment of the spherocylinders along the cell structure for improper parameters. The spherocylinders have a length of five and a diameter $D$ equal to one.The interaction parameters $\chi_{CR}$ and $\chi_{CC}$ are both equal to 0.5. For cell sizes below $D$ no alignment is visible ((a) $\delta = 0.1$ and (b) $\delta = 0.5$). If the cell size equals the rods diameter ((c) $\delta = 1.0 = D$) an alignment along the cell structure is clearly visible. For systems with bigger cell sizes than the diameter we also observe a high alignment. In addition, several spherocylinders (three for (d) $\delta = 1.5$ and two or even four for (e) $\delta = 2.0$) affiliate to fit the cell structure. All images are cropped to facilitate a focus on the essential region.

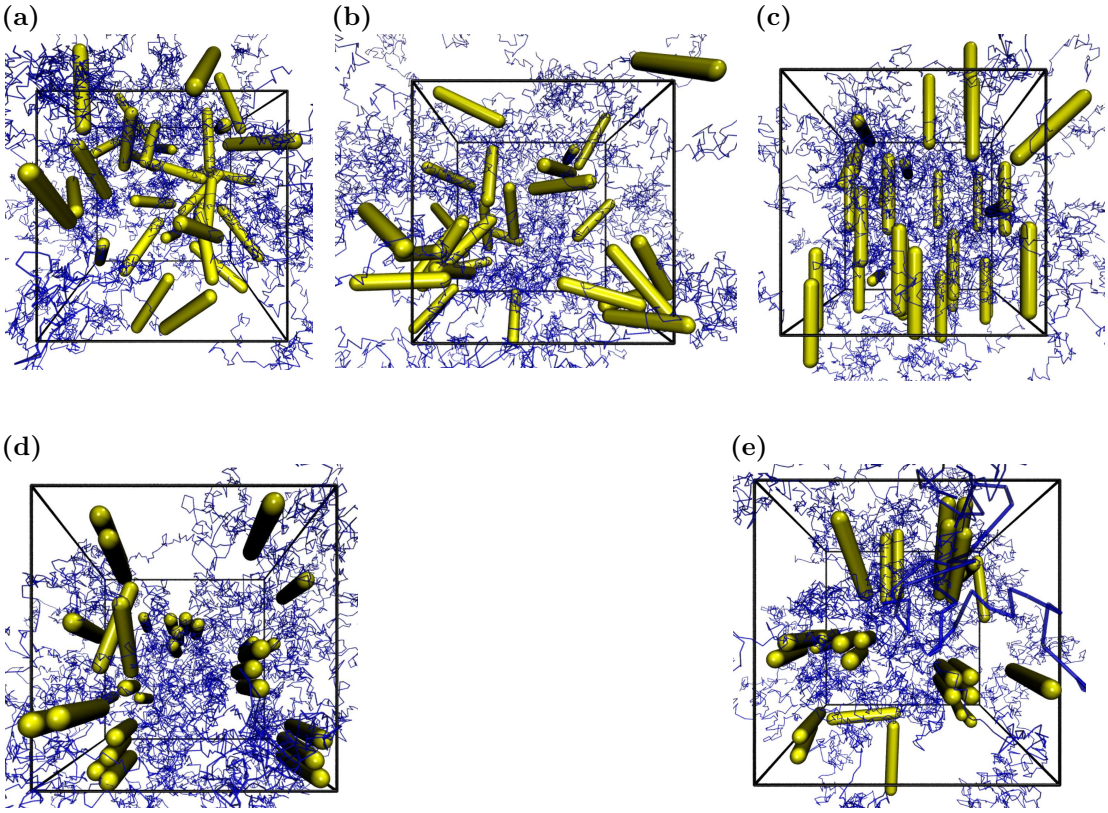


For this purpose, we start two more simulations with the same parameters as before but with a smaller rod-coil interaction parameter $\chi_{CR}$ equal to 0.2. Figure (4.2) shows two plots for the five different cell sizes and all three different simulation runs. The simulations discussed above are displayed by the blue line while the two simulations with smaller $\chi_{CR}$ values are illustrated by the red and orange colored lines. The first plot in Figure (4.2a) displays the biggest eigenvalue of the nematic order tensor $\lambda_+$, which is used as order parameter. We see that all configurations are isotropic, that is, $\lambda_+$ is smaller than 0.4, for small cell sizes of 0.1 and 0.5. For a cell size of $\delta = D = 1$ the order significantly increases for all three systems. The rods align along the cell structure. For

bigger cell sizes the results differ. As we have seen in the snapshots in Figure (4.1) the spherocylinders in a system with a big rod-coil interaction parameter align along the cell structure. In this case, illustrated by the blue line, the order parameter $\lambda_+$ increases. The red and orange line for the new simulations demonstrate that the alignment is reduced if the rod-coil interaction parameter $\chi_{CR}$ has a smaller value. This further demonstrates that the formation of different phases can be controlled by altering the rod-coil interaction parameter for these cell sizes. This is of great importance as we aim to investigate the phase behavior of the rod-coil block copolymers in dependence of the interaction strength between rods and coils.

The second plot in Figure (4.2b) shows the average time the program needs for 100000 steps in seconds. As expected systems with more cells need more time. Remember, that the box size for the runs with $\delta$ equal to two is increased from fifteen to sixteen. This may lead to a small slowdown of the simulations. Nevertheless, the values for $\delta$ equal to 1, 1.5 and 2 do not differ much. The simulations with smaller cell sizes need perceptibly longer. For the two smallest cell sizes we see that the runs with a cell size of 0.1 are much slower than those with a cell size of 0.5. As one of our goals is to achieve an efficient program the cell size should not become to small.

**Figure 4.2** Plots of average values for five different cell sizes $\delta$. (a) The biggest eigenvalue $\lambda_+$ is used as order parameter. The blue line indicates a simulation with $\chi_{CR} = 0.5$. The red and orange lines simulations with a smaller value of 0.2. In both cases $\chi_{CC}$ equals 0.5. (b) Average time of the three simulations for 100000 steps in seconds.

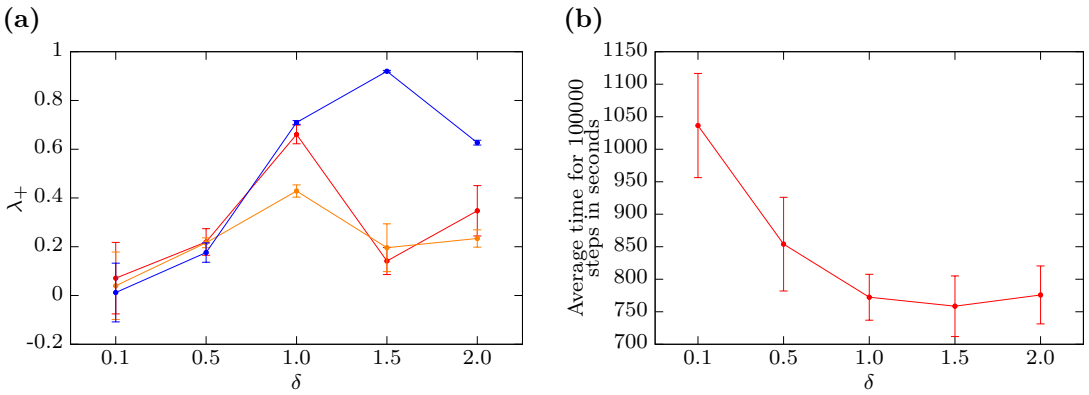


Another possibility to avoid an alignment along the cell structure may be to reduce the rod-coil interaction. In the following, we want to further examine the relation of the rod-coil interaction parameter on the observed effect. For this purpose, we simulate fifty rods with a length of $L = 5$ in a simulation box of size $15 \times 15 \times 15$. The cell size is chosen to be equal to the diameter of the spherocylinders $\delta = D = 1.0$. We attach a coil with 400 monomers each to one end of each rod. We start from an ordered configuration and after 200000 steps the simulations are stopped. The coil-coil interaction parameter $\chi_{CC}$ is set to 0.5 and the spring constant $k$ equals 27. Each of the four runs has another value for the rod-coil interaction parameter $\chi_{CR}$. Snapshots of the final configurations for values 0.05, 0.1, 0.2 and 0.3 for $\chi_{CR}$ are displayed in Figure (4.3). From previous runs we already know that the system exhibits an isotropic phase at this density if the

interactions between rods and coils are turned off. As demonstrated at the beginning of this section we further know that the spherocylinders strongly align along the cell structure for an interaction parameter of $\chi_{CR}$ equal to 0.5 in a comparable system.

**Figure 4.3** Snapshots of the final configurations with a cell size of $\delta = 1.0 = D$ and $\chi_{CC} = 0.5$. For small coil-rod interaction parameters ((a) $\chi_{CR} = 0.05$ and (b) $\chi_{CR} = 0.1$) the systems are isotropic. For higher interaction parameters ((c) $\chi_{CR} = 0.2$ and (d) $\chi_{CR} = 0.3$) the alignment increases.

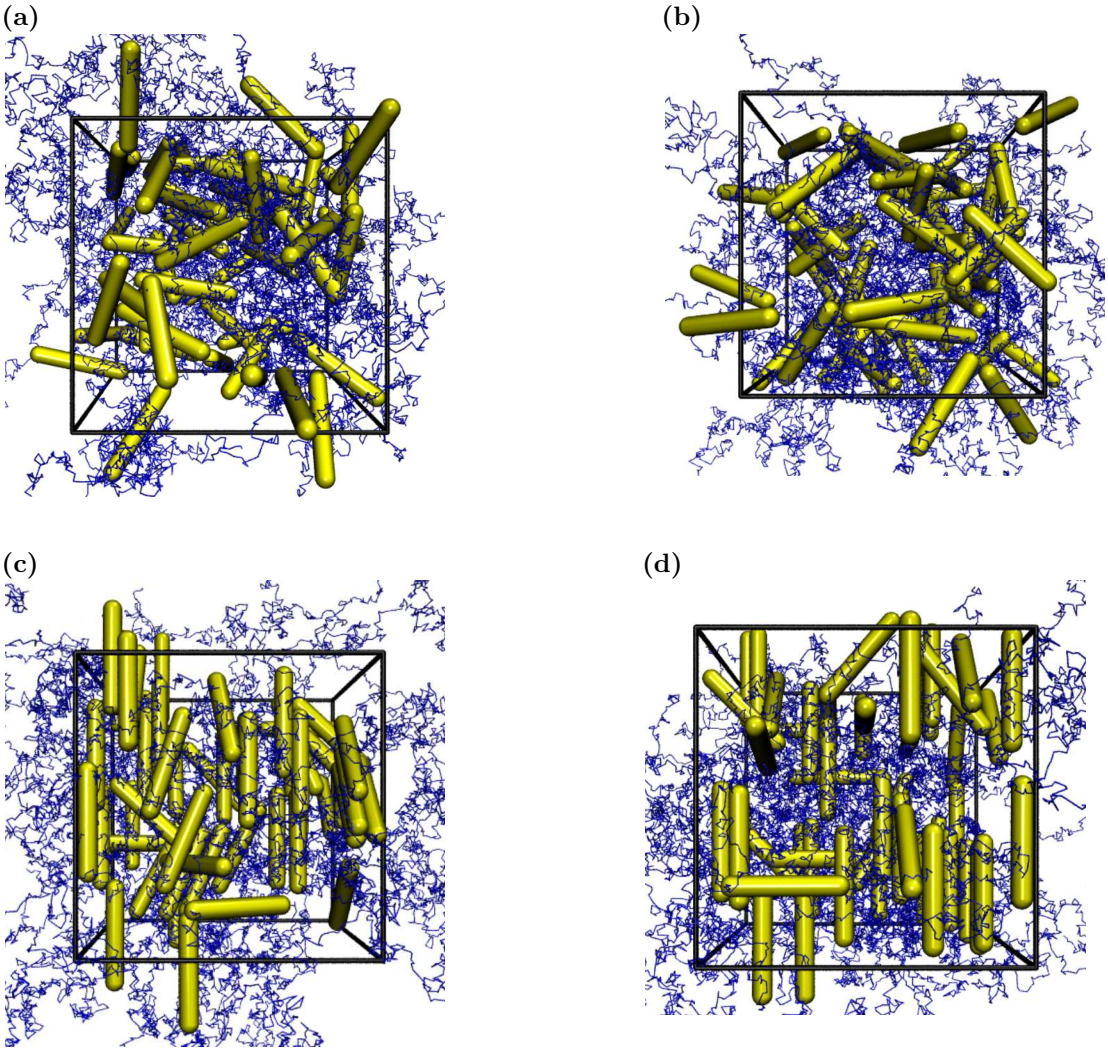


We clearly see that there is no alignment of the spherocylinders in Figures (4.3a) and (4.3b) with very small rod-coil interaction parameters $\chi_{CR}$ of 0.05 and 0.1, respectively. If we increase the interaction parameter to 0.2 the rods have a clear tendency to align along the cell structure, as displayed in Figure (4.3c). For even higher values of $\chi_{CR}$ this effect becomes stronger as Figure (4.3d) demonstrates for a $\chi_{CR}$ value of 0.3. Thus, we can affirm that the minimization of the repulsive interaction between rods and coils causes the arrangement of the spherocylinders along the cell structure. The use of a smaller interaction parameter reduces the alignment of the rods along the cell structure,

even if the cell size is equal to the diameter of the spherocylinders. Choosing a too low interaction parameter for the rod-coil interaction may be problematic as this interaction is essential for the stabilization of higher ordered phases.

To conclude we find that the cell size should under no circumstances be equal to the diameter of the rods as this strengthens the alignment of the spherocylinders along the cell structure. In our case this is a cell size equal to one. For this cell size the rod-coil interaction parameter would have to be set to a very small value to avoid an alignment at all. Simulations with a very small cell size of 0.1 are far too slow and do not fulfill the requirements of our model. A cell size of $\delta$ equal to 0.5 also results in long simulation times and may still conflict with our model. For a cell size of two we find that two or four spherocylinders may affiliate in order to fit the cell structure. Such a big cell size may already be too large to allow an sufficient inhomogeneous density distribution of the monomers. As the alignment along the cell structure can not be prevented this cell size and other multiples of the diameter $D$ should be avoided, too.

Hence, we set the cell size $\delta$ to 1.5 for nearly all simulations as this value is easy to handle, not an integral multiple of the diameter and guarantees adequate simulation times. Further, we can finely tune the phase behavior by changing the rod-coil interaction parameter $\chi_{\mathrm{CR}}$ for this cell size.

The solution to adapt the cell size is suitable for the calculation of the interactions in all three models introduced in Section 3.4.4. We have already mentioned that the cell size should not be smaller than the distance between the monomers in a coil and the surface points if we use the surface approximation method. For all simulations in this thesis the value of the spring constant $k$ is chosen to result in an average distance $b$ between the monomers smaller than the chosen cell size of 1.5. For the chosen number of surface points in this thesis the distance between neighboring points equals 0.5 and, therefore, is the lower limit of the cell size for this method. Accordingly, the chosen cell size of 1.5 is compatible with the requirements for our model.

If we use the surface approximation method to estimate the rod densities there are further solutions to reduce the alignment along the cell structure. It is possible to rearrange the surface points from time to time, for example, by rotating the spherocylinder along its unit vector. In this case we either have to save all surface point positions for all rods or a rotation angle or rotation vector for each spherocylinder and recompute all points every time they are needed. The implemented algorithm, therefore, needs more memory and is much slower. Nevertheless, for a cell size equal to one we find that the rods are not oriented along the axes anymore if we rearrange the surface points every 100th step. A further disadvantage of this method is that we have to recalculate the rod-coil interaction energy every time we rearrange the points. This does not only slow down the simulations but there are also undesired jumps in the energy. One method to control these energy jumps is to implement the rearrangement as a Monte-Carlo move. This method is not implemented and tested as other solutions are much easier and faster.

## 4.2 Comparison of the three different models

During the development of the program we regularly profile the code in order to find bottlenecks and provide efficient code. On this occasion we find that the speed of the

program drastically depends on the chosen underlying model. In this section we compare the three different models we have introduced in Section 3.4.4.

As far as we can say from the examined runs the three models give comparable results. The first and second model are closely related to each other and should give very similar results anyway. The third model uses a different approach. In order to get the desired behavior we have to adjust the interaction parameters. This makes a direct comparison between the models difficult. Results obtained with the first model are published in reference [73]. The findings in this publication are in accordance with the results we obtain with the second and third model. The most remarkable difference between the three models is the CPU time needed for a given number of steps.

To test the speed of the models we set up 10 different systems with 50 to 250 rods and 3 to 162 monomers per rod for all three models. The size of the simulation box is $15 \times 15 \times 19$ for all simulations with a cell size $\delta$ equal to one. We let the simulations run for 10000 steps and then compare the simulation times.

The first model uses a simple Monte-Carlo integration scheme to determine the rod densities. In this model the monomers are not allowed to penetrate the rods. Therefore, the accessible volume for the monomers in each cell has to be calculated repeatedly after each Monte-Carlo move of a spherocylinder. To approximate the rod volume fraction in a cell and, thus, the rod densities we draw a given number of random numbers per cell and count the amount of points inside and outside of spherocylinders in each cell. Even though this model is giving reasonable results it is pretty slow.

A first improvement is to implement a Monte-Carlo integration method that uses a pool of random number cells. Each of these cells contains a fixed quantity of random numbers and is associated with one cell of the simulation box. After several steps the random number cells are rearranged. This way we have to generate much less random numbers and need less memory. In a few tests we find that this method is 5 to 10 times faster than the simple Monte-Carlo integration method.

Even with this improvment the method is still not efficient enough. Another big drawback is the excluded volume interaction between rods and coils as it results in very immobile rods. This can be bypassed by using soft interactions. For this reason we introduce the much more efficient surface approximation method. In this model the monomers may penetrate the spherocylinders. But the sharing of a common cell for monomers and rod surface points is penalized. This way we can skip the expensive overlap detection between monomers and rods and, furthermore, we do not have to calculate the accessible volume for the monomers after every rod move. Thus, this method is significantly faster. In the test runs we find that the simulations are between 400 to 16000 times faster than the second model.

We may also calculate the average time each method needs for one step per spherocylinder and per monomer. On average the first method needs around $36 \cdot 10^{-5}$ seconds per rod and monomer for one step. The second model still requires approximately $6 \cdot 10^{-5}$ seconds per step, whereas the surface approximation method on average merely needs about $13 \cdot 10^{-9}$ seconds.

Thus, most results in this thesis are obtained with the surface approximation method as the two other methods would be much to slow to achieve meaningful results in a reasonable time.

## 4.3 Influence of the coil length

After combining the coils and rods to rod-coil block copolymers we start to add some further features to the program. In this section we present one of these features. It allows us to alter the length of the coils when starting from another configuration. If the new coil chains are shorter than the old ones we remove the rearmost monomers until the new length is reached. In case the new chains are longer than before we add monomers at random positions close to the endmost monomer position of the current chain until the desired length is achieved.

We use this algorithm to demonstrate the metastability of the zigzag phase in the following chapter. Here we discuss the results of a system for which we decrease the number of monomers from 162 to 3 in four steps. We start from an old, highly ordered configuration at which each coil consists of 162 monomers. To show that this configuration is fully equilibrated we do not change the number of monomers for the first 500000 steps. Then we gradually decrease the number of monomers every 500000 steps to 108, 54, 18 and finally 3 monomers. Note that we do not wait for the systems to equilibrate completely in this case as we only want to demonstrate the applicability of the algorithm and show the basic behavior of the systems with changing coil length.

The size of the simulation box for all simulations is $48 \times 30 \times 36$ with a cell size of 1.5. The spherocylinders have a length $L$ of five and a diameter $D$ of one. The interaction parameters for all runs are $\chi_{\mathrm{CC}} = 0.5$, $\chi_{\mathrm{CR}} = 0.5$ and $k = 12$. The simulations are performed at five different densities $\rho^* = 0.1$, 0.15, 0.2, 0.25 and 0.3, whereas the densities are adjusted by using different numbers of rod-coil block copolymers.

In Figure (4.4) we see the development of the order parameter $S_z$ along the $z$ direction for different densities. In the first and second region the number of monomers per coil is 162 and 108, respectively. All systems are highly ordered. In the third region the number of monomers is reduced to 54. For the lowest density, represented by the red line, we observe a phase transition to an isotropic phase at this point, while the values for the other systems merely change insignificantly. In the fourth region each coil only consists of 18 monomers and the order decreases even for systems with higher densities. In the last region the number of monomers per coil is reduced to 3 and all systems converge to an isotropic state.

We can conclude that the order decreases with shrinking coil length. With these simulations we also demonstrate that a phase transition can be driven by changing the number of monomers per coil. This effect is studied in the following chapter in more detail where it is used to investigate a phase diagram for rod-coil block copolymers in dependence of the number of monomers per coil.

**Figure 4.4** Order parameter $S_z$ for different reduced densities $\rho^* = 0.1$ (red), 0.15 (green), 0.2 (blue), 0.25 (magenta) and 0.3 (orange). Every 500000 steps the number of monomers per coil $m$ is reduced. Starting from an ordered state with 162 monomers per coil all systems converge to an isotropic state if $m$ is reduced to 3. In all simulations $\chi_{CC}$ and $\chi_{CR}$ are equal to 0.5 and $k$ is 12.

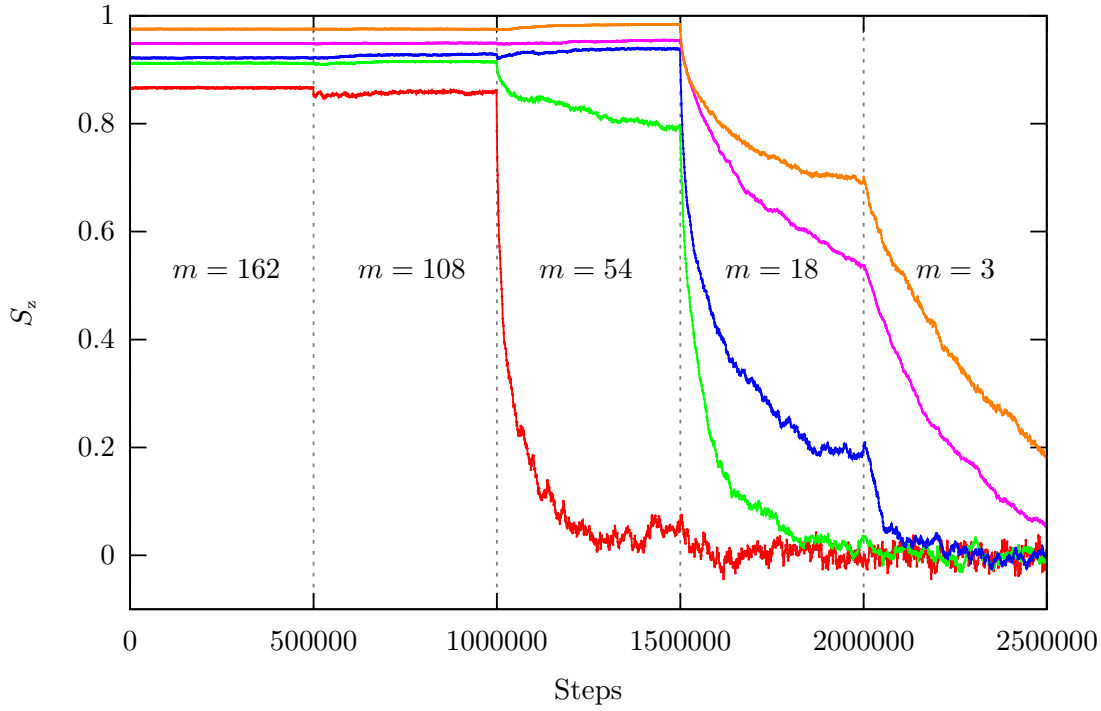


## 4.4 Influence of the spring constant

Beside the number of monomers per coil the spring constant $k$ is another parameter affecting the length of the coils in our systems. This value controls the intrachain interaction of the coils. As it is related to the average distance $b$ between the monomers it is especially a measure for the total length of the coils. Remember that $k$ equals $3/b^2$ for a Gaussian chain and the total contour length of a coil with $m$ monomers is given by $bm$.

In this section we check the influence of $k$ on some sample systems. For this purpose, we set up a system with 300 rods with a length-to-width ratio $L/D$ of 5/1. Choosing a simulation box of size $15 \times 15 \times 19$ results in a reduced density of $\rho^*$ around 0.353. The cell size $\delta$ is equal to one in all runs. The rod-coil interaction parameter $\chi_{CR}$ is chosen to be 0.2 and each coil consists of 50 monomers. The values of the coil-coil interchain interaction parameter $\chi_{CC}$ can take the values 0.1, 0.2, 0.5, 1.0, 2.0, 4.5 and 10.0. For the intrachain interaction parameter $k$ we use the values 3, 12 and 27 leading to average monomer distances of 1, 1/2 and 1/3, respectively.

Figure (4.5) demonstrates how both parameters, namely $\chi_{CC}$ and $k$, influence the phase behavior. The plot shows the order parameter $S_z$ along the $z$-axis against $k$ for different values of $\chi_{CC}$. It illustrates that the order slightly decreases with increasing

$k$ value if the coil-coil interaction is small. Snapshots of the final configuration for $\chi_{CC} = 0.1$ are displayed in Figure (4.6). For moderate $\chi_{CC}$ equal to 0.5 the order is hardly influenced by $k$. An increase in $k$ leads to a higher order for higher $\chi_{CC}$ values. For a value of $\chi_{CC}$ of one this effect is almost sufficient to drive a transition from an isotropic phase, for values of $k$ equal to 3 and 12, to a nematic phase, for a value of 27 for $k$. This is also visible in the snapshots of the simulations in Figure (4.7).

**Figure 4.5** Order parameter $S_z$ along the $z$-axis for different values of $k$ and $\chi_{CC}$. The value of $\chi_{CR}$ is 0.2 for all simulation runs. For small values of $\chi_{CC}$ (0.1 (red) and 0.2 (green)) the order decreases with increasing $k$. For a moderate $\chi_{CC}$ value of 0.5 (blue) the order only changes insignificantly. For high $\chi_{CC}$ values (1.0 (magenta), 2.0 (orange), 4.5 (grey) and 10.0 (purple)) the order increases for larger $k$ values.

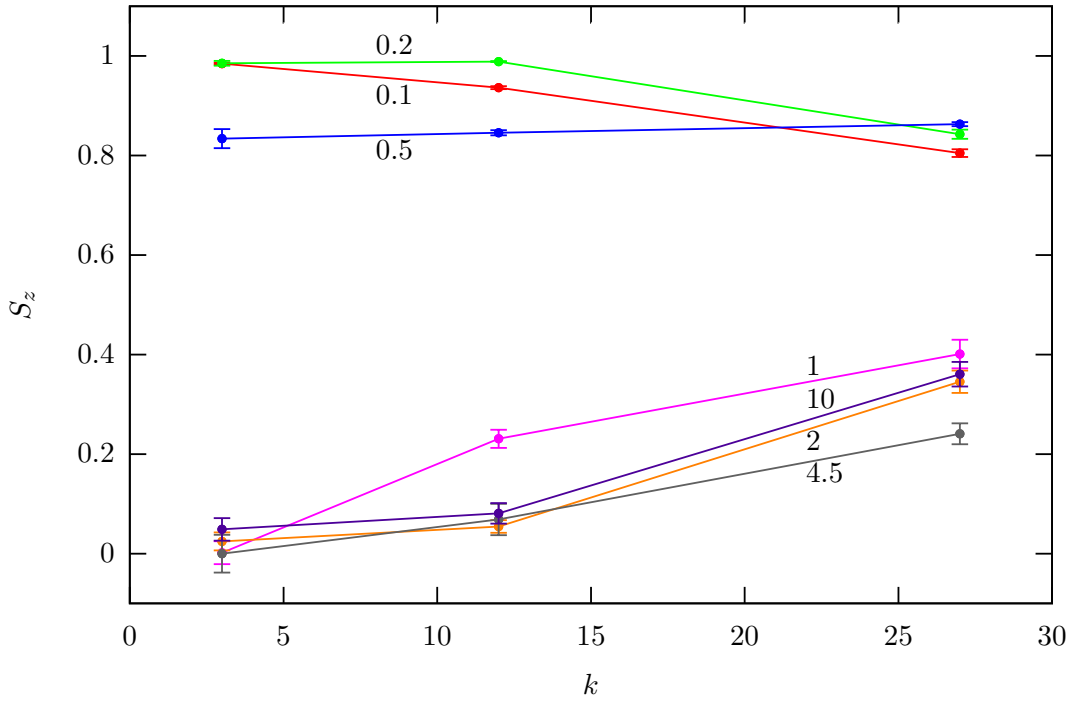


For small values of $\chi_{CC}$ the repulsion between the monomers is low. Thus, they have a lower tendency to spread equally over the whole box as the energy penalty for regions with a high local monomer density is small. Further, when $\chi_{CC}$ is smaller than $\chi_{CR}$, the repulsion between the monomers and the spherocylinders is more dominant. A penetration of the monomers into rod-rich regions is, therefore, hindered.

For small values of $k$ the coils are longer, occupy more cells and, thus, make a mixing of rod and coil-rich regions more difficult. With increasing $k$ the chains are getting shorter and occupy less space. Because of this the number of influenced cells decreases and there are more cells with a low coil density. This allows the spherocylinders to move more freely and, thus, the order is reduced. Hence, an increase in $k$ decreases the order for small $\chi_{CC}$ values.

**Figure 4.6** Snapshots of the final configurations for three runs with $\chi_{CR} = 0.2$, $\chi_{CC} = 0.1$ and different $k$ values. The order decreases with increasing $k$. (a) $k = 3$. (b) $k = 12$. (c) $k = 27$.

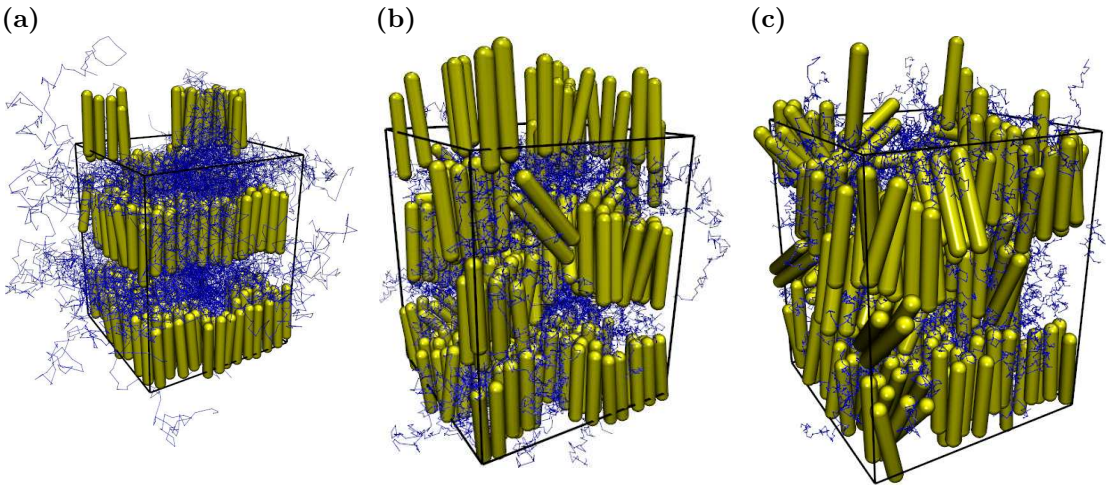


For high coil-coil interaction parameters $\chi_{CC}$ the systems behave contrariwise. Here the rod-coil interaction is less dominant and the monomers are hardly expelled from rod-rich regions. As the energy penalty for a high local monomer density is much higher in this case the monomers try to distribute evenly and occupy more cells.

For small $k$ values this is not hindered and the chains are widely spread. Therefore, there is a more or less equal monomer density in all cells. This leads to a mostly uniform coil-coil and rod-coil interaction in all cells. The resulting systems are in an isotropic state.

For a high value of $k$ the chains are much shorter and the probability to have more monomers is one cell is much higher. This leads to higher local monomer densities and, thus, the repulsion between rods and coils is increased. The resulting formation of coil and rod-rich regions leads to a stabilization of ordered phases. Hence, an increase in $k$ increases the order for big $\chi_{CC}$ values.

**Figure 4.7** Snapshots of the final configurations for three runs with $\chi_{\mathrm{CR}} = 0.2$, $\chi_{\mathrm{CC}} = 1.0$ and different $k$ values. An increase in $k$ leads to higher order. For small values of $k$ ((a) $k = 3$ and (b) $k = 12$) the system exhibits an isotropic phase. (c) For a higher value of $k = 27$ the system is at the transition point to the nematic phase.

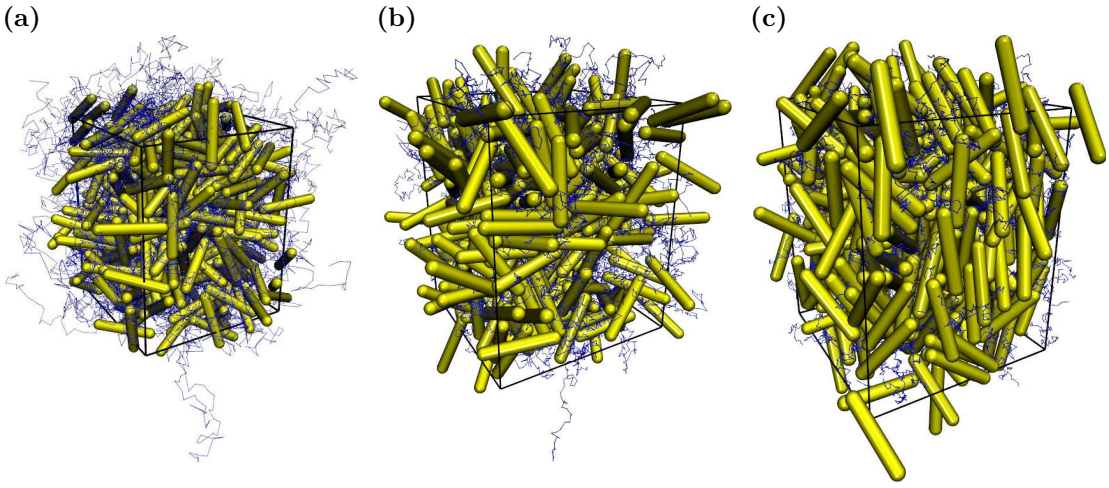

Chapter 5

# Phases in dilute systems

Contents



In this chapter we show the results of a detailed series of simulations and the resulting phase diagram for rod-coil block copolymers in our model. Then we emphasize the stabilization of the smectic phase in our systems of rod-coil block copolymers compared to pure rod systems. Additionally, we present some outstanding phases and demonstrate the metastability of the zigzag phase in our model.

## 5.1 Phase diagram

A main goal of this thesis is to study the phase behavior of rod-coil block copolymers. In this section we present the main results of a detailed series of simulation runs including a phase diagram characterizing the phase behavior of rod-coil block copolymers in our model in dependence of the number of monomers per coil $m$ and the interaction parameter $\chi_{\mathrm{CR}}$ between rods and coils.

In order to identify the phase transition points for the rod-coil block copolymers we investigate a lot of different systems. For all systems in this section the spherocylinders have a length $L$ of five and a diameter $D$ of one. The size of the simulation box is set to $48 \times 30 \times 36$. This is eight, five and six times the total length $\lambda$ of a spherocylinder in $x$, $y$ and $z$-direction, respectively. The cell size $\delta$ is fixed to 1.5 to reduce an alignment of the rods along the cell structure as discussed in Section 4.1. The coil-coil interaction parameter $\chi_{\mathrm{CC}}$ is set to 0.5 and the spring constant $k$ equals 12, thus, the average distance $b$ between the monomers is 0.5. The simulations are set up to run for 7000000 steps.

The systems contain 100 to 6000 spherocylinders in increments of 100. This corresponds to a range of 0.0097 to 0.5830 for the reduced density of the spherocylinders $\rho^*$ in steps of 0.0097. We simulate all of these systems with five different numbers of monomers per coil $m$. This way we can determine the dependence of the phase transition on the coil length. The shortest chains contain 3 monomers per coil. For the next longer chains $m$ equals 18 and 54. The longest coils consist of 108 and 162 monomers per chain.

All runs are started twice. Once they start from an ordered system and once from a random configuration. For each number of monomers per coil up to five runs with different rod-coil interaction parameters are started. For all sets interaction parameters $\chi_{\mathrm{CR}}$ equal to 0, 0.5 and 1.0 are investigated. For the systems which start from an ordered configuration additional runs with values of 0.1 and 0.25 for $\chi_{\mathrm{CR}}$ are examined.

Figure (5.1) illustrates several plots of the average values over the last 100000 steps for the biggest eigenvalue $\lambda_+$ of the nematic order tensor, which is used as order parameter, against the reduced density $\rho^*$. Remember, that the order parameter varies between zero for an isotropic phase and one for a perfectly aligned crystal phase. While some groups use a value of 0.4 [29], a phase transition from the isotropic to the nematic phase is predicted for a value of 0.43 by the Maier-Saupe theory [163, 164, 165]. Experimental values for nematics are normally in the range from 0.4 to 0.7 [22, 23, 109, 134, 144]. For bigger values higher ordered phases such as the smectic phases are found. For a smectic the value of the order parameter is usually between 0.8 and 0.9 [102, 211].

The first plot in Figure (5.1a) shows the results of randomly set up systems with three monomers per coil and rod-coil interaction parameters with values equal to 0.0, 0.5 and 1.0. All other plots show results for systems that are initiated in an ordered manner and include plots for additional rod-coil interaction parameters with values of 0.1 and 0.25. The comparison of the results for $m = 3$ for the two different setup methods demonstrates that the results are in good agreement. Thus, we only show the graphs for the systems we set up in an ordered manner for all other values of $m$ as they also contain the results of the additional rod-coil interaction parameters.

The only mentionable difference between the graphs for three monomers per coil is the dip at densities around 0.39 in Figure (5.1a) for a value of $\chi_{\mathrm{CR}}$ equal to one. This

dip neither occurs for an rod-coil interaction parameter equal to 0.5 nor if we start from an ordered configuration as Figure (5.1b) illustrates. The reason for this dip is a somewhat random effect displayed in the snapshot of the two affected systems in Figure (5.2). When we start from a random configuration it may happen during the order process that the final, ordered layer structures are perpendicular to each other. This reduces the value of the order parameter. Nevertheless, both regions are highly ordered. For other densities and interaction parameters this seems to be unfavorable or is at least not observed in our simulations.

In Figure (5.1b) we clearly see that the phase transition point does not only depend on the length of the coils but also on the interaction parameter between rods and coils. In comparison to all other graphs in Figure (5.1) this dependence is most visible in this plot. Whereas the transition points for $\chi_{\mathrm{CR}}$ equal to zero and 0.1 do not differ it is distinctly visible that the phase transition is shifted to lower reduced densities if the rod-coil interaction parameter is increased.

For the simulations containing 18 monomers per coil there are strong fluctuations for reduced densities approximately between 0.29 and 0.39 as can be seen in Figure (5.1c). In this region we observe the wavy lamellar state which we will discuss in Section 5.3. The layers in this phase have a moderate to high curvature. In some cases the curvature becomes so high that the layers break. From this several ordered regions, which are perpendicular to each other, may emerge. This process is shown in Figure (5.3) for a rod-coil interaction parameter $\chi_{\mathrm{CR}}$ equal to 0.25. For a reduced density of 0.292 we observe a wavy lamellar state as illustrated in Figure (5.3a). As Figure (5.3b) shows the curved layers start to twist against each other for a slightly higher reduced density of 0.311. If we further increase the density the single layers start to overlap as displayed in Figure (5.3c). From the tearing apart the perpendicular, ordered regions shown in Figure (5.3d) arise at a reduced density of 0.340. Depending on how disintegrated the layers are the order parameter may vary in a wide range in this region.

In Figures (5.1d) to (5.1f) we display the results for $m$ equal to 54, 108 and 162, respectively. We clearly see that the order increases with growing coil length and the phase transition points are shifted towards lower densities. Further, we determine that the distance between the phase transition points shrinks with increasing coil length. For $m$ equal to 54 we still can clearly distinguish between the phase transition point for $\chi_{\mathrm{CR}} = 0.25$ and the indistinguishable points for 0.5 and 1. For 162 monomers per coil the phase transition is hardly dependent on the value of $\chi_{\mathrm{CR}}$ anymore.

From the results of our simulations plotted in Figure (5.1) we can obtain a phase diagram for rod-coil block copolymers in our model. If we assume that a phase transition between a disordered and an ordered state occurs if $\lambda_+$ exceeds a value of 0.43 [163, 164, 165] we can plot the number of monomers per coil $m$ against the reduced densities $\rho^*$ of the phase transition points. The resulting phase diagram for all five rod-coil interaction parameters is displayed in Figure (5.4) whereas we use the same colors to distinguish the interaction parameters as in Figure (5.1). The turquoise colored shapes indicate the location of special phases we discuss in the following sections. Figure (5.4a) shows the phase diagram in linear scaling while the plot in Figure (5.4b) uses a logarithmic scale on the $y$-axis for the number of monomers per coil $m$. We clearly see that the transition lines for interaction parameters equal to 0 and 0.1 are not distinguishable. The phase transition for these interaction parameters is located at a reduced density around 0.466 for all values of $m$. This is the same reduced density where we find the isotropic to

**Figure 5.1** Plots of the biggest eigenvalue $\lambda_+$ of the nematic order tensor against the reduced density $\rho^*$. The differently colored lines represent different rod-coil interaction parameters $\chi_{\mathrm{CR}}$ with the values 0.0 (red), 0.1 (orange), 0.25 (green), 0.5 (blue) and 1.0 (magenta). (a) 3 monomers per coil. Random setup. (b) 3 monomers per coil. (c) 18 monomers per coil. (d) 54 monomers per coil. (e) 108 monomers per coil. (f) 162 monomers per coil.

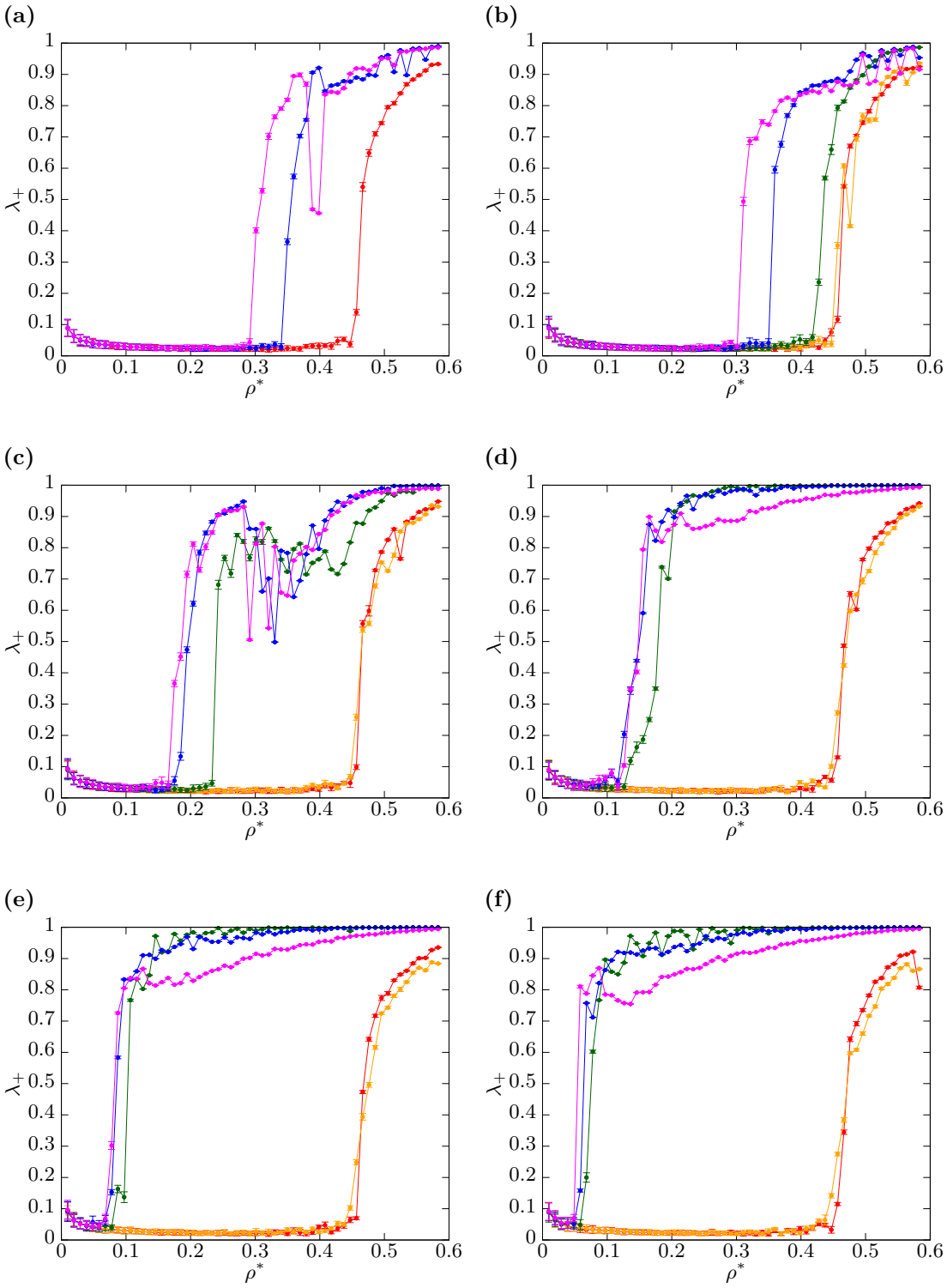

**Figure 5.2** Snapshots of the final configurations of two systems which start from a random setup. The value of $\chi_{CR}$ is one and $\chi_{CR}$ equals 0.5. (a) and (b) show the top and side view of the system with 4000 spherocylinders at a reduced density of 0.389. The systems in (c) and (d) contain 4100 rods which corresponds to a reduced density of 0.398.

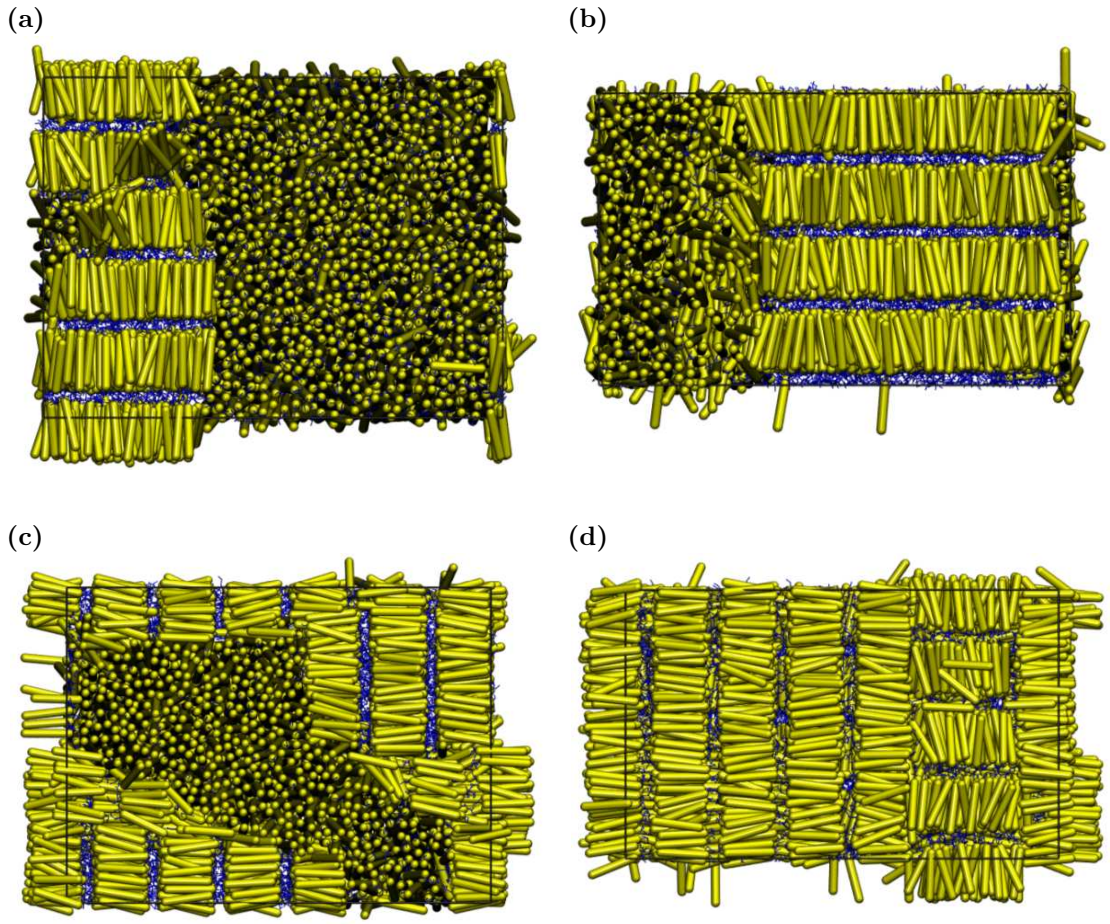


nematic phase transition for a pure rod system (see Appendix A.1). This shows that the additional coils only have a stabilizing effect on the rod-coil block copolymers if the rod-coil interaction parameter exceeds a certain threshold. In these simulations this limit lies between 0.1 and 0.25.

For $\chi_{CR}$ equal to 0.25 we find the phase transition to occur at perceptibly higher densities than for the two highest interaction parameters. The lines for the two highest rod-coil interaction parameters run close to each other. For most values of $m$ the transition points are located at a higher density for the smaller value of 0.5. For 54 and 108 monomers per coil the transition points are found at the same reduced densities. We also see that the transition points for different interaction parameters move closer together with increasing number of monomers per coil.

**Figure 5.3** Snapshots of the wavy lamellar phase for rod-coil block copolymer systems with 18 monomers per coil and a rod-coil interaction parameter $\chi_{CR} = 0.25$. The value of $\chi_{CC}$ is 0.5. (a) $\rho^* = 0.292$. The layers have a strong curvature. (b) $\rho^* = 0.311$. The single layers are twisted against each other. (c) $\rho^* = 0.321$. The curvature is too high and the layers start to overlap. (d) $\rho^* = 0.340$. The layer structure breaks and perpendicular, ordered regions occur.

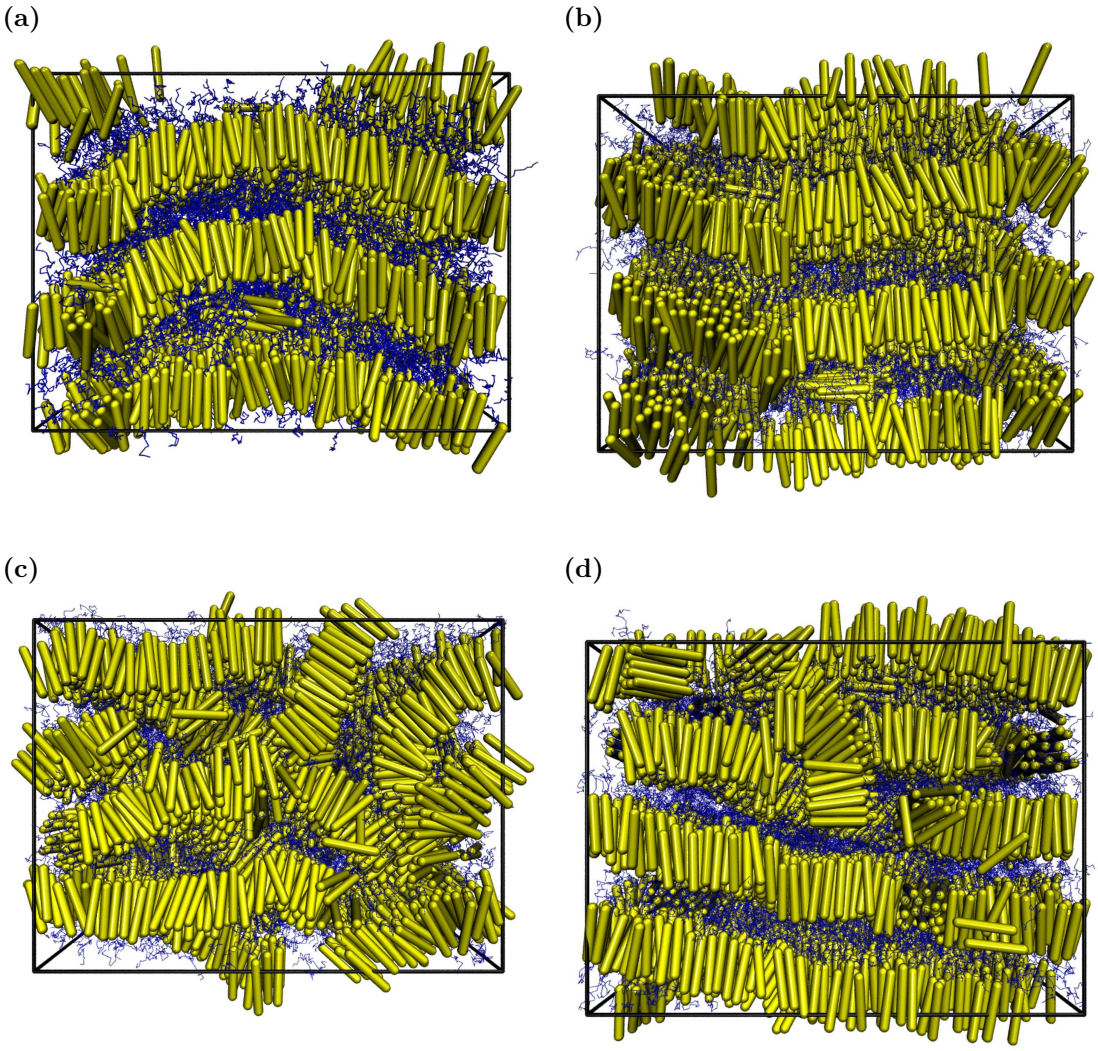


The logarithmic plot in Figure (5.4b) suggests that there is a logarithmic relation for the phase transition line. If we perform a linear regression we get the three equations

$$\ln(m) \approx -10.9\rho^* + 5.9 \qquad \text{for } \chi_{CR} = 0.25 \tag{5.1}$$

$$\ln(m) \approx -13.7\rho^* + 5.9 \qquad \text{for } \chi_{CR} = 0.5 \tag{5.2}$$

$$\ln(m) \approx -16.1\rho^* + 6.1 \qquad \text{for } \chi_{CR} = 1.0. \tag{5.3}$$

**Figure 5.4** Final phase diagram plotting the number of monomers per coil $m$ against the reduced density of rods $\rho^*$, that is, the rod number density $\rho_{\text{Rods}}$ divided by the density of regular close packing for spherocylinder $\rho_{\text{cp}}$. The coil-coil interaction parameter $\chi_{\text{CC}}$ is set to 0.5. The differently colored lines are only added to guide the eye and represent different rod-coil interaction parameters $\chi_{\text{CR}}$ with the values 0.0 (red), 0.1 (orange, dashed), 0.25 (green), 0.5 (blue) and 1.0 (magenta). All systems to the left of these lines are in a disordered state while systems on the right side of a line are in an ordered state. The turquoise shapes indicate special points in the phase diagram we refer to in the following sections. The circle indicates a wavy lamellar state (see Section 5.3) with $\chi_{\text{CR}} = 0.5$, the diamond clusters (see Section 5.4) with $\chi_{\text{CR}} = 1$ and the square percolating structures (see Section 5.5) with $\chi_{\text{CR}} = 1$. (a) Linear scale on both axes. (b) Logarithmic scale on the $y$-axis.

**(a)**

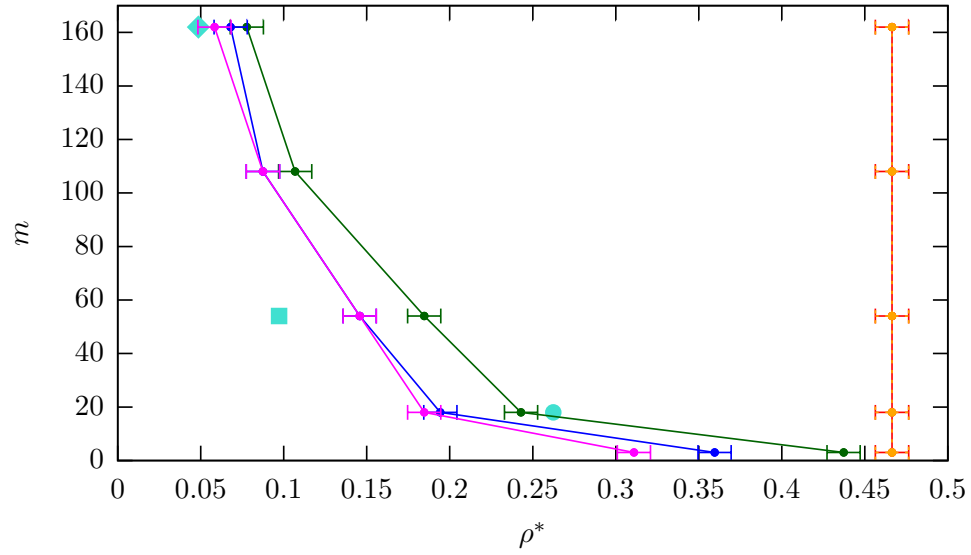


**(b)**

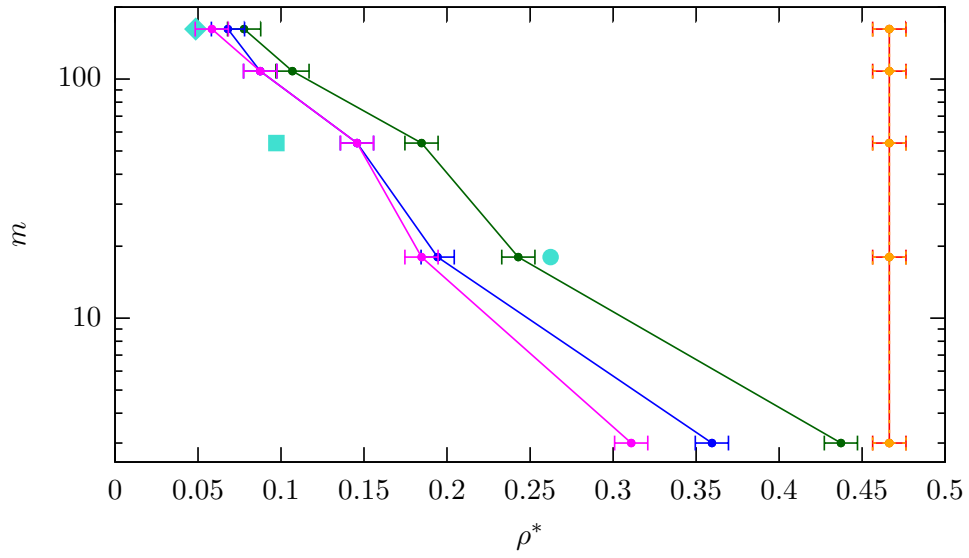

These equations also reflect the finding that for a given number of monomers per coil a lower reduced density is needed for a phase transition if the rod-coil interaction parameter increases.

Remember that the monomers of the coils have no volume. Nevertheless, the number of monomers per coil can be associated with the expansion of the coils in three-dimensional space. At sufficient high values of $\chi_{\mathrm{CR}}$ the monomers repel the rods. This may be represented by an effective volume fraction $\phi$, which scales with $m$. This way we can connect the effective volume fraction $\phi$ of the coils with the free energy $\mathcal{F}$ via the relation

$$\mathcal{F} \sim ln(\phi) \sim ln(m). \tag{5.4}$$

For a system with fixed reduced density the free energy of the coils would, thus, decrease with increasing rod-coil interaction. To see how the free energy of a coil depends on its expansion we calculate the free energy of an ideal chain. The free energy $\mathcal{F}_{\mathrm{ic}}(r)$ of an ideal chain with a distance $r$ between its ends is related to the Gaussian distribution $P(r)$ via

$$\mathcal{F}_{\mathrm{ic}}(r) = -k_{\mathrm{B}}T \ln P(r). \tag{5.5}$$

Using the probability function $P(r)$ as given in Equation (3.17) and the relation for the end-to-end distance $R_{\mathrm{e}}$ from Equation (3.59) we can compute the free energy of an ideal chain as

$$\mathcal{F}_{\mathrm{ic}}(r) = \frac{3k_{\mathrm{B}}T}{2mb^2}r^2 + \mathcal{F}_0 \tag{5.6}$$

where $\mathcal{F}_0$ is a constant. To minimize its free energy a coil needs to reduce the distance $r$ between its ends.

In summary, we find that the free energy decreases with increasing interaction parameter $\chi_{\mathrm{CR}}$. This decrease is related to a shorter distance between the ends of the coils and, thus, a smaller effective volume fraction, which scales with the number of monomers per coil. If $m$ decreases the free energy also decreases and a higher reduced density or a higher rod-coil interaction is needed for the phase transition.

## 5.2 Stabilization of the smectic phase

As discussed in Section 2.4 several groups observe a stabilization of the smectic phase at expense of the nematic phase with increasing coil fraction for rod-coil block copolymers. In our simulations we have strong first-order phase transitions, that is, there are coexisting states [46]. For pure rods with a shape anisotropy $L/D = 5$ (see Appendix A.1) and rod-coil block copolymers with rod-coil interaction parameters $\chi_{\mathrm{CR}}$ equal to 0 and 0.1 we find nematic phases. For higher rod-coil interaction parameters $\chi_{\mathrm{CR}}$ we observe first-order transitions directly into a smectic state, omitting the nematic phase. With increasing coil length a further stabilization of the smectic phase can be ascertained. In this section we illustrate this effect by comparing the biaxiality $\eta$ for different coil lengths and rod-coil interaction parameters.

The prior results show that the ordered phases occur at a significantly lower density when coils with a sufficient rod-coil interaction are present. It is also obvious that the order increases with growing coil length. To demonstrate the stabilization of the smectic phase we need some further observables. Using Equations (3.67) and (3.68) we calculate the order parameter $S$ and the biaxiality $\eta$ from the three eigenvalues $\lambda_-$, $\lambda_0$ and $\lambda_+$ of the nematic order tensor, which we compute during the simulations. The plots in this section are generated from the simulation runs presented in the last section which started from an ordered state.

The resulting plots of the biaxiality $\eta$ against the order parameter $S$ for different values of $m$ are illustrated in Figures (5.5) to (5.9) at which we only show the relevant range of 0.4 to one for the order parameter $S$. For the biaxiality on the $y$-axis we use a logarithmic scale.

In all figures we clearly see that only very few systems have an order parameter greater than 0.4 for rod-coil interaction parameters equal to zero and 0.1. In most cases the biaxiality shows strong fluctuations for these interaction parameters. For these parameters we also find the systems with the highest values for $\eta$. For higher rod-coil interaction parameters the biaxiality does not exceed a value of 0.1.

As Figure (5.5) demonstrates the addition of coils with three monomers leads to a stabilization for sufficiently high rod-coil interaction. We see that the number of systems in the range of 0.4 to one for $S$ increases with increasing value of $\chi_{\mathrm{CR}}$. Further, we find that the fluctuations in most systems are reduced and the biaxiality exhibits smaller values. The same observations can be made in Figure (5.6) for systems with 18 monomers per coil.

For values of $m$ equal to 54 and higher the effect becomes much more distinct. In Figure (5.7), (5.8) and (5.9) for 54, 108 and 162 monomers per coil, respectively, we clearly see that much more systems have a higher order parameter $S$ if $\chi_{\mathrm{CR}}$ increases. Furthermore, we find that the biaxiality is reduced for these systems and decreases with increasing values of $S$.

In summary we find that we only observe a nematic phase for pure rod systems and rod-coil block copolymers with rod-coil interaction parameters equal to and below 0.1. For higher values of $\chi_{\mathrm{CR}}$ we observe a first-order transition into a smectic phase. The stabilization of the smectic phase further increases if more monomers are added to the coils.

**Figure 5.5** Plots of the biaxiality $\eta$ in a logarithmic scale against the order parameter $S$ for rod-coil block copolymers with 3 monomers per coil. The rod-coil interaction parameter has the values (a) $\chi_{CR} = 0$, (b) $\chi_{CR} = 0.1$, (c) $\chi_{CR} = 0.25$, (d) $\chi_{CR} = 0.5$ and (e) $\chi_{CR} = 1$.

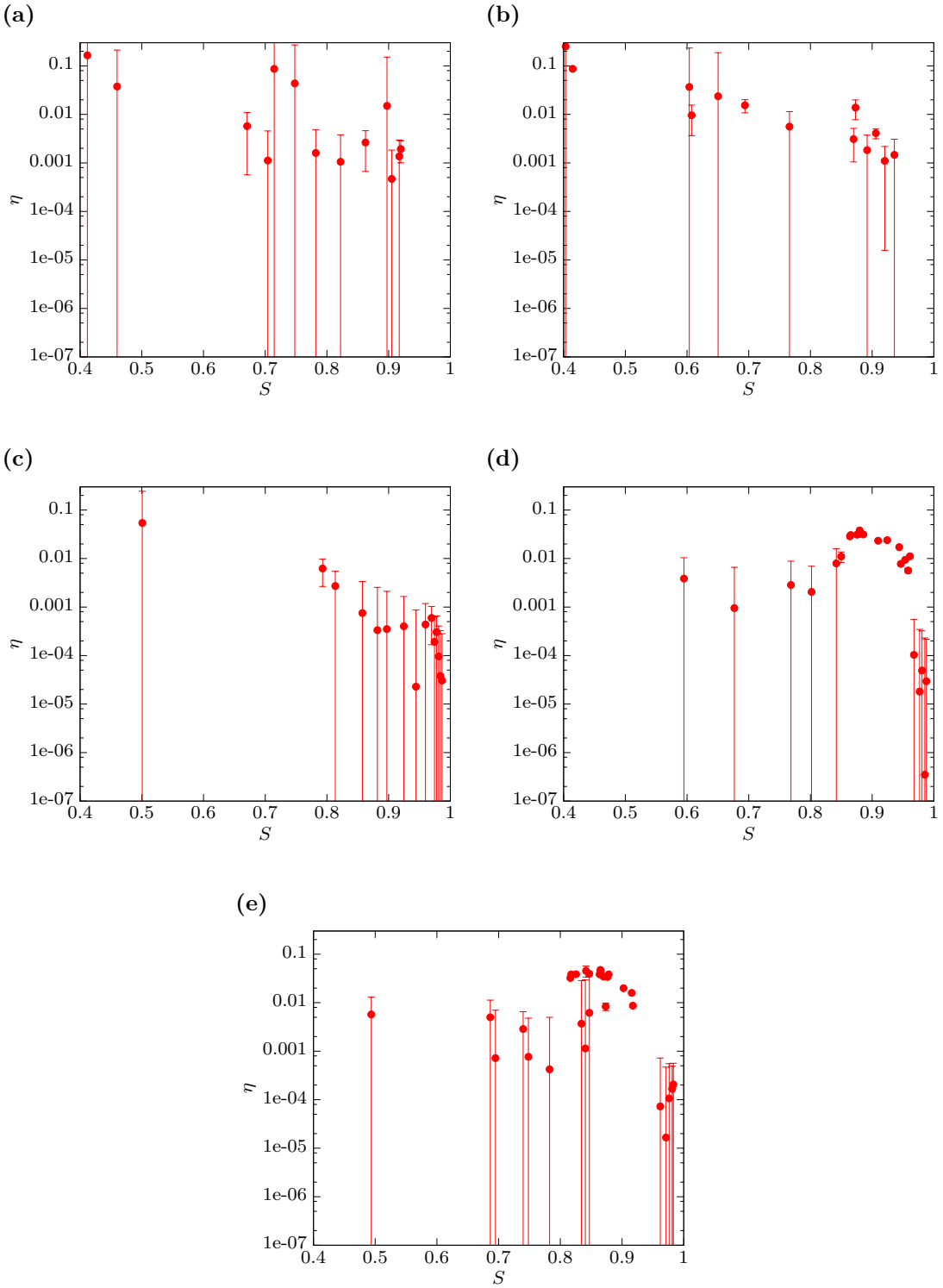

**Figure 5.6** Plots of the biaxiality $\eta$ in a logarithmic scale against the order parameter $S$ for rod-coil block copolymers with 18 monomers per coil. The rod-coil interaction parameter has the values (a) $\chi_{CR} = 0$, (b) $\chi_{CR} = 0.1$, (c) $\chi_{CR} = 0.25$, (d) $\chi_{CR} = 0.5$ and (e) $\chi_{CR} = 1$.

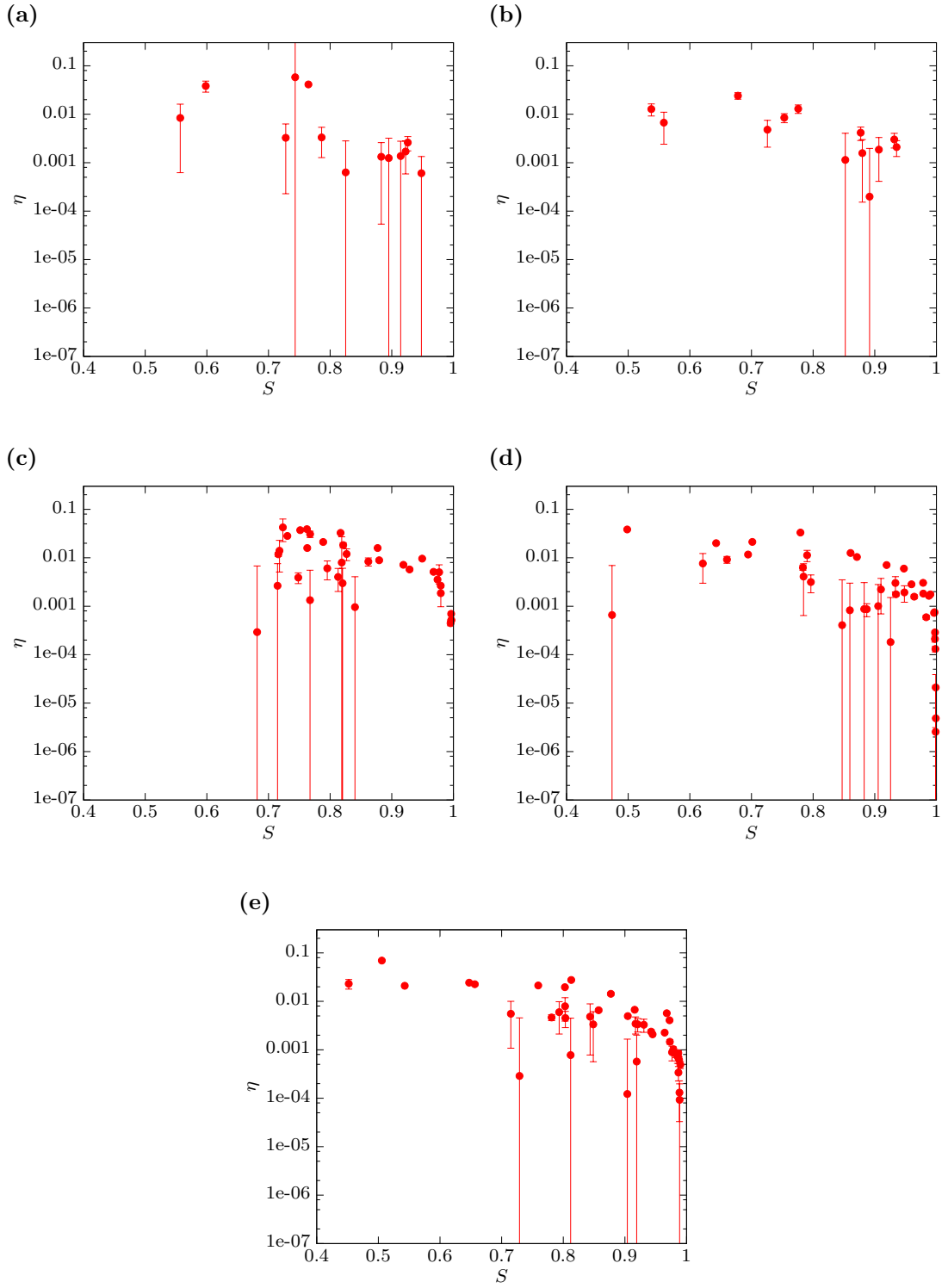

**Figure 5.7** Plots of the biaxiality $\eta$ in a logarithmic scale against the order parameter $S$ for rod-coil block copolymers with 54 monomers per coil. The rod-coil interaction parameter has the values (a) $\chi_{CR} = 0$, (b) $\chi_{CR} = 0.1$, (c) $\chi_{CR} = 0.25$, (d) $\chi_{CR} = 0.5$ and (e) $\chi_{CR} = 1$.

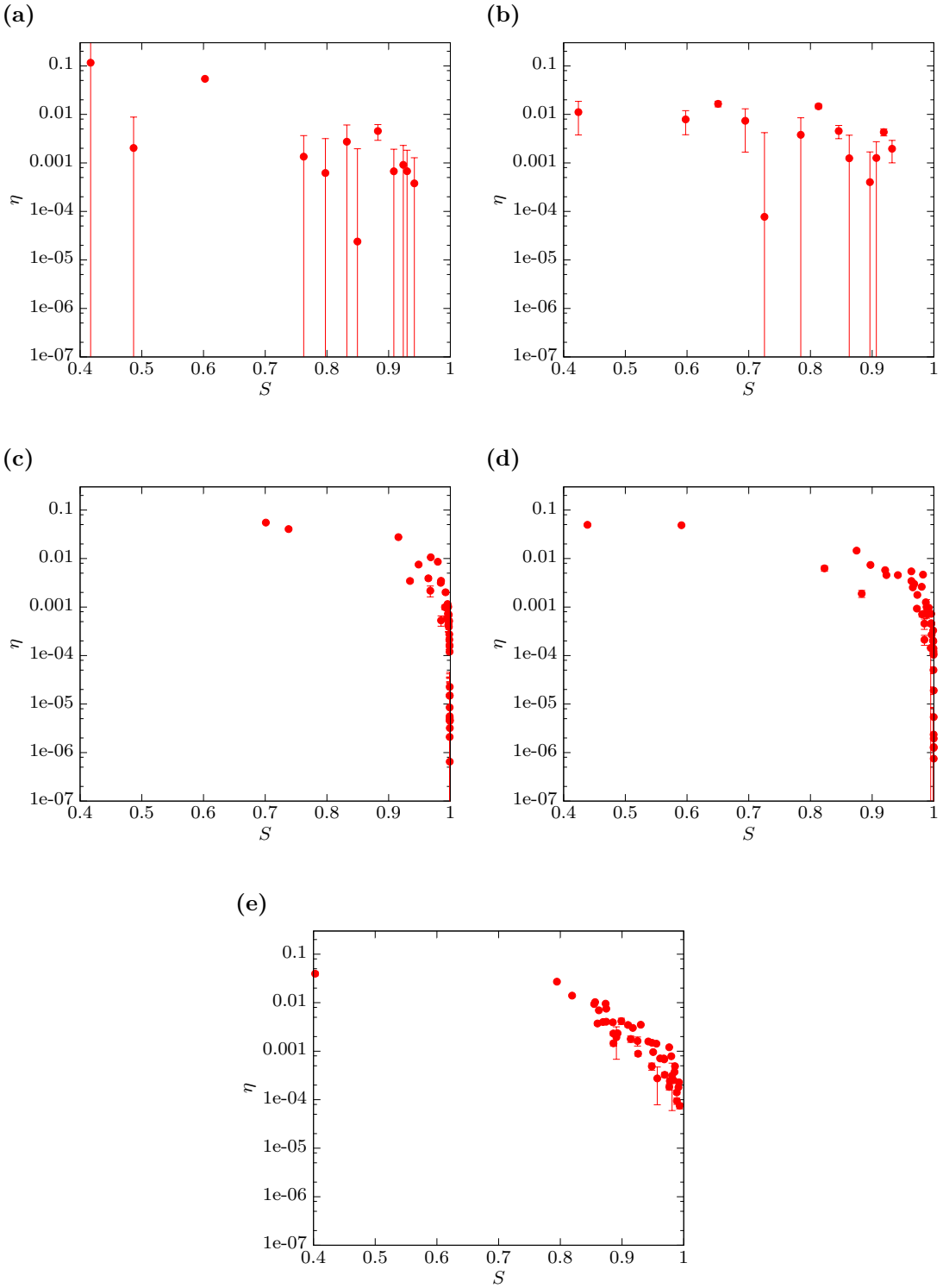

**Figure 5.8** Plots of the biaxiality $\eta$ in a logarithmic scale against the order parameter $S$ for rod-coil block copolymers with 108 monomers per coil. The rod-coil interaction parameter has the values (a) $\chi_{CR} = 0$, (b) $\chi_{CR} = 0.1$, (c) $\chi_{CR} = 0.25$, (d) $\chi_{CR} = 0.5$ and (e) $\chi_{CR} = 1$.

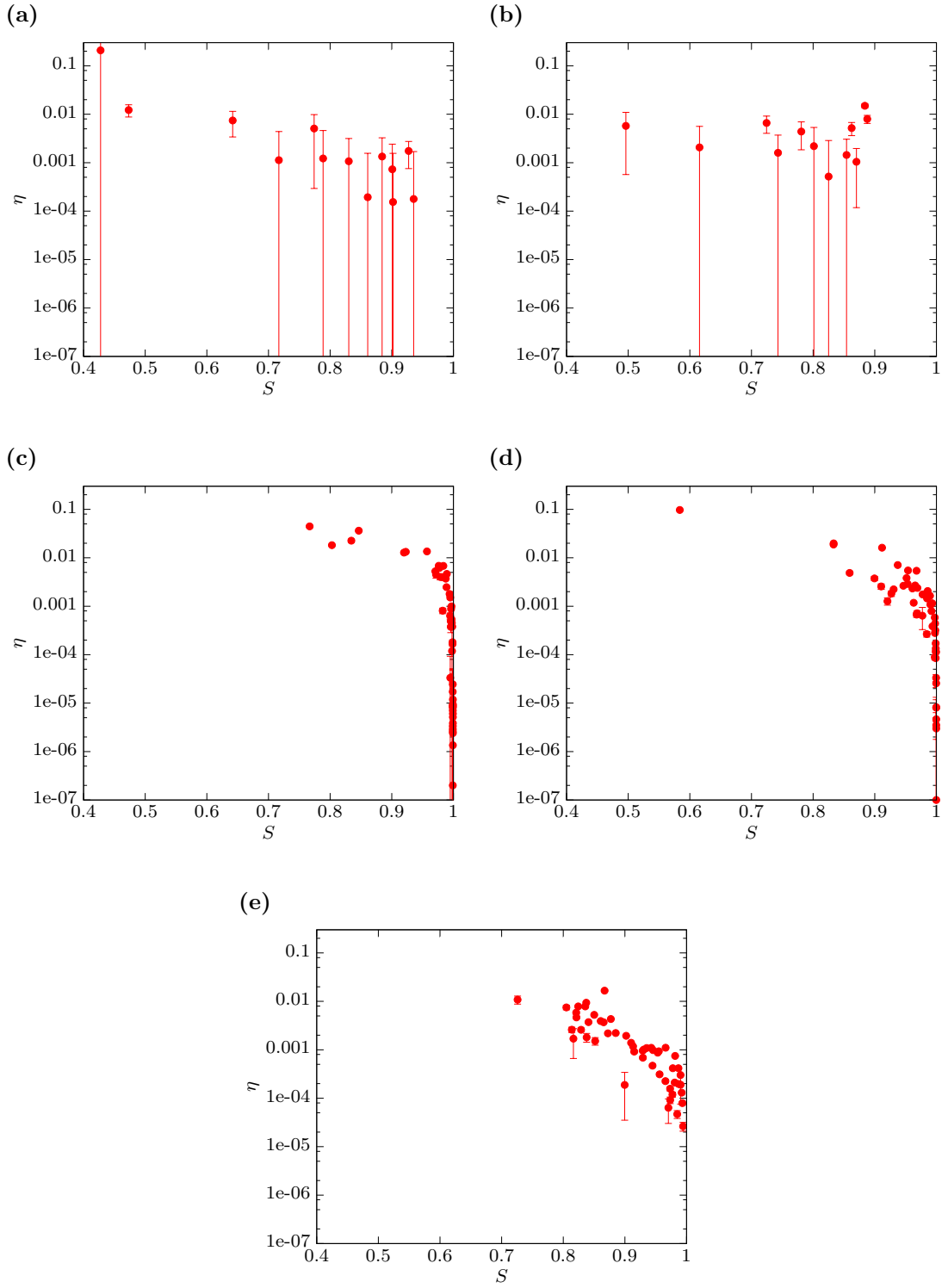

**Figure 5.9** Plots of the biaxiality $\eta$ in a logarithmic scale against the order parameter $S$ for rod-coil block copolymers with 162 monomers per coil. The rod-coil interaction parameter has the values (a) $\chi_{CR} = 0$, (b) $\chi_{CR} = 0.1$, (c) $\chi_{CR} = 0.25$, (d) $\chi_{CR} = 0.5$ and (e) $\chi_{CR} = 1$.

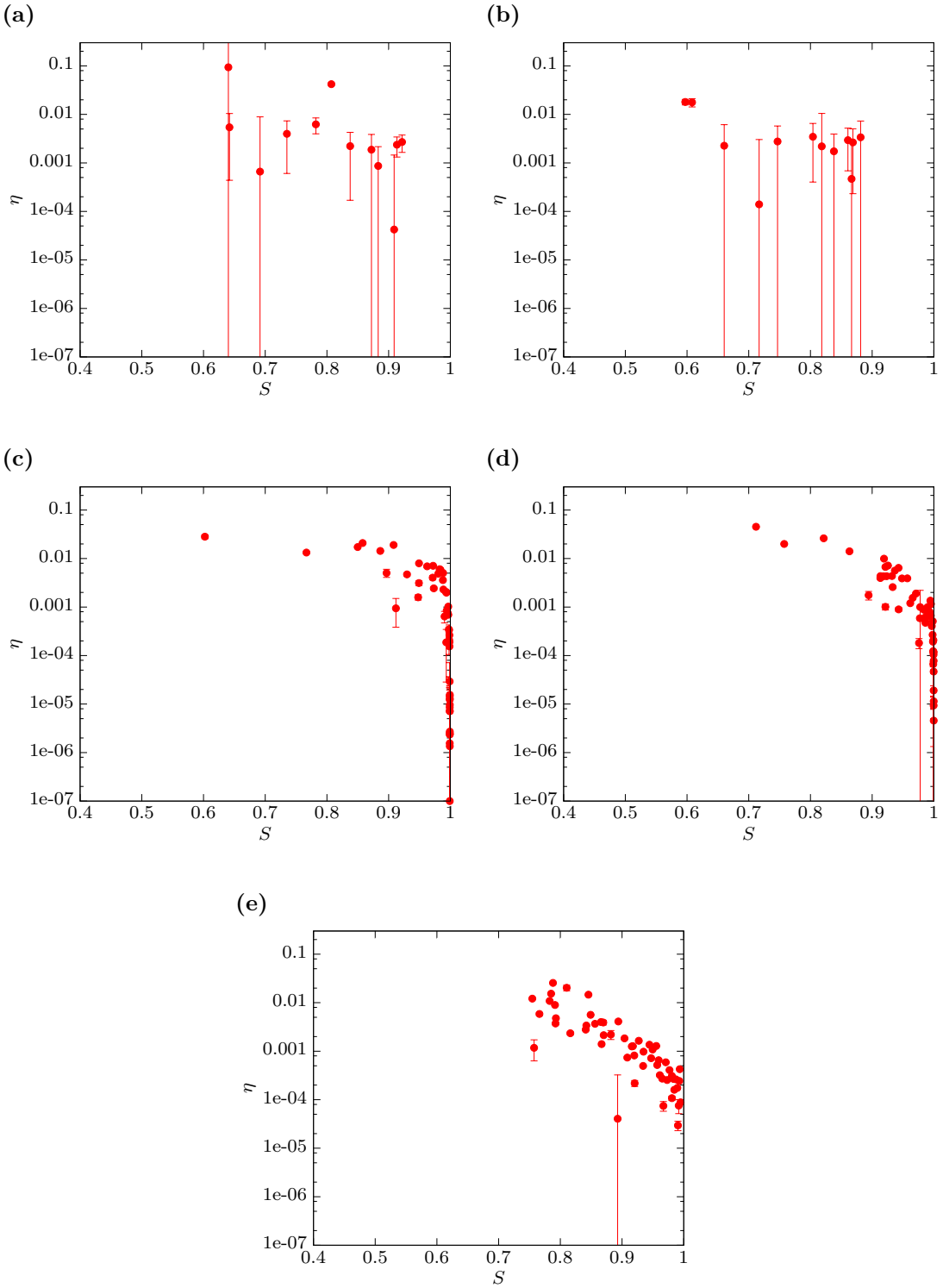

## 5.3 Wavy lamellar state

In Figure (5.3) we have already illustrated how the wavy lamellar state leads to big fluctuations in the order parameter $\lambda_+$ in Figure (5.1c). Figure (5.10) shows two more snapshots of systems that exhibit a wavy lamellar state. Both snapshots are taken from simulations performed to obtain the phase diagram presented in Section 5.1 with 18 monomers per coil. The first configuration in Figure (5.10a) has a very low curvature. Its reduced density is approximately 0.282 and the rod-coil interaction parameter $\chi_{\mathrm{CR}}$ is set to one. For a slightly lower value of $\rho^*$ around 0.262 and $\chi_{\mathrm{CR}}$ equal to 0.5 the curvature is much higher as Figure (5.10b) demonstrates. The second configuration is indicated by the turquoise circle in the phase diagram in Figure (5.4).

**Figure 5.10** Wavy lamellar state for two different reduced densities and rod-coil interaction parameters. (a) The system with $\chi_{\mathrm{CR}}$ equal to one and a reduced density $\rho^* \approx 0.282$ has a low curvature. (b) The system with a slightly lower reduced density around 0.262 and a lower rod-coil interaction parameter of $\chi_{\mathrm{CR}} = 0.5$ shows a high curvature. In both cases $\chi_{\mathrm{CC}}$ equals 0.5.

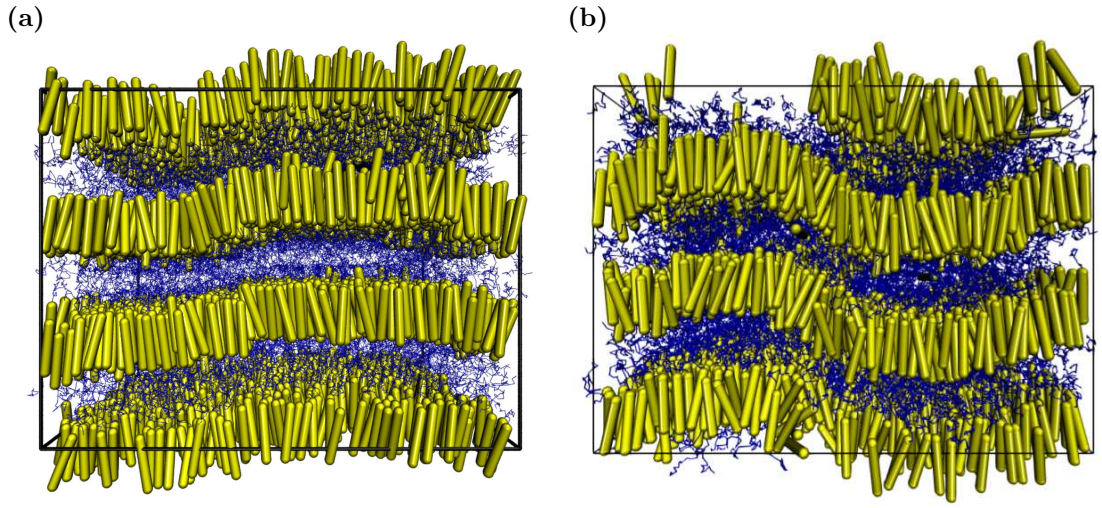


## 5.4 Cluster

For systems with a very low reduced density $\rho^*$ for the spherocylinders and a high volume fraction of coils we observe clusters. Figure (5.11) shows a sample configuration for a system at a reduced density around 0.049 and 162 monomers per coil and $\chi_{\mathrm{CR}}$ equal to one. The parameter $\chi_{\mathrm{CC}}$ is equal to 0.5. This configuration is marked by the turquoise diamond in Figure (5.4). Even though we do not observe a hockey puck phase explicitly we presume that it, if at all, may occur in this region. In tests with much higher rod-coil interaction parameters $\chi_{\mathrm{CR}}$ equal to two, five and ten clusters are also observed for systems at the same density and 162 monomers per coil.

**Figure 5.11** Cluster phase for a system with very low reduced density $\rho^*$ around 0.049 and high coil volume fraction. Each coil consists of 162 monomers. $\chi_{CC}$ is set to 0.5 while $\chi_{CR}$ equals one.

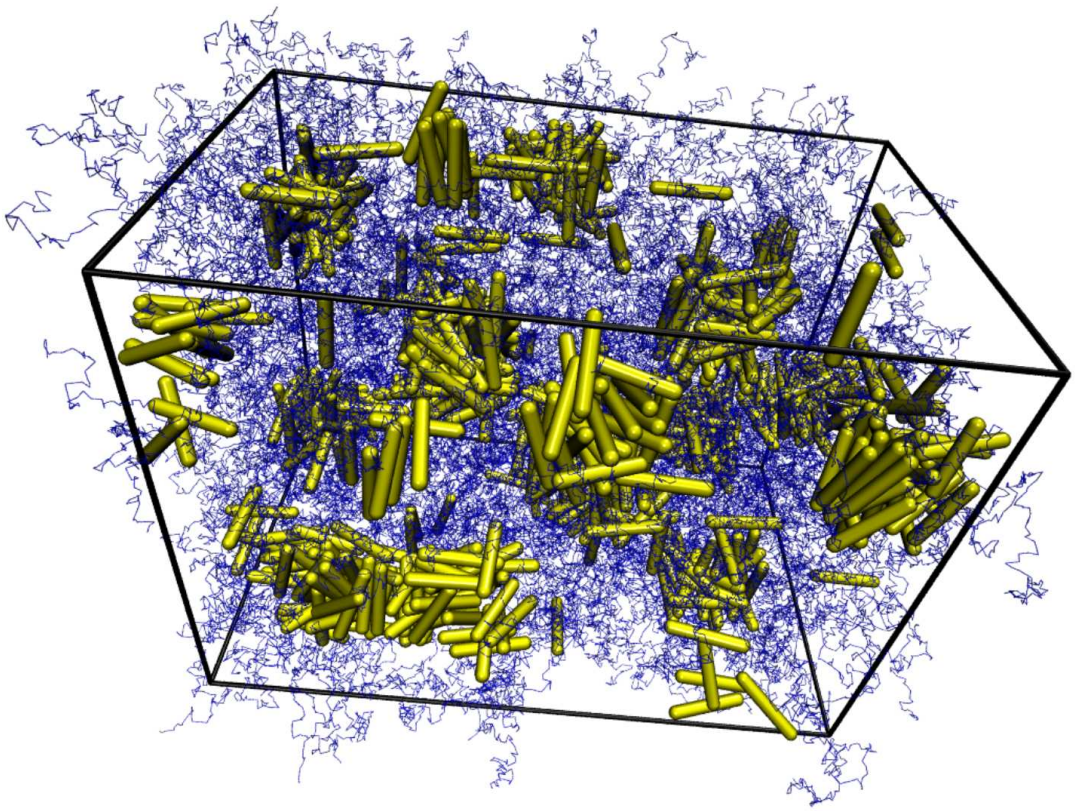

## 5.5 Percolating structures

Another class of interesting structures we find in our simulations are percolating structures. Beside highly ordered structures these structures may be of interest for the development of highly efficient organic solar cells. We observe percolating structures for slightly higher reduced densities and shorter coils than the clusters described in the previous section.

The snapshot shown in Figure (5.12) is taken from a simulation used to investigate the phase diagram in Section 5.1. The coils in the illustrated run consist of 54 monomers and have an interaction parameter $\chi_{CC}$ equal to 0.5. The reduced density for the rods is around 0.097. The rod-coil interaction parameter $\chi_{CR}$ is equal to one. This configuration is marked by the turquoise square in Figure (5.4).

**Figure 5.12** Snapshot of a configuration that exhibits a percolating structure. The reduced density $\rho^*$ is about 0.097 and $m$ equals 54. The interaction parameters $\chi_{CC}$ and $\chi_{CR}$ are set to 0.5 and one, respectively.

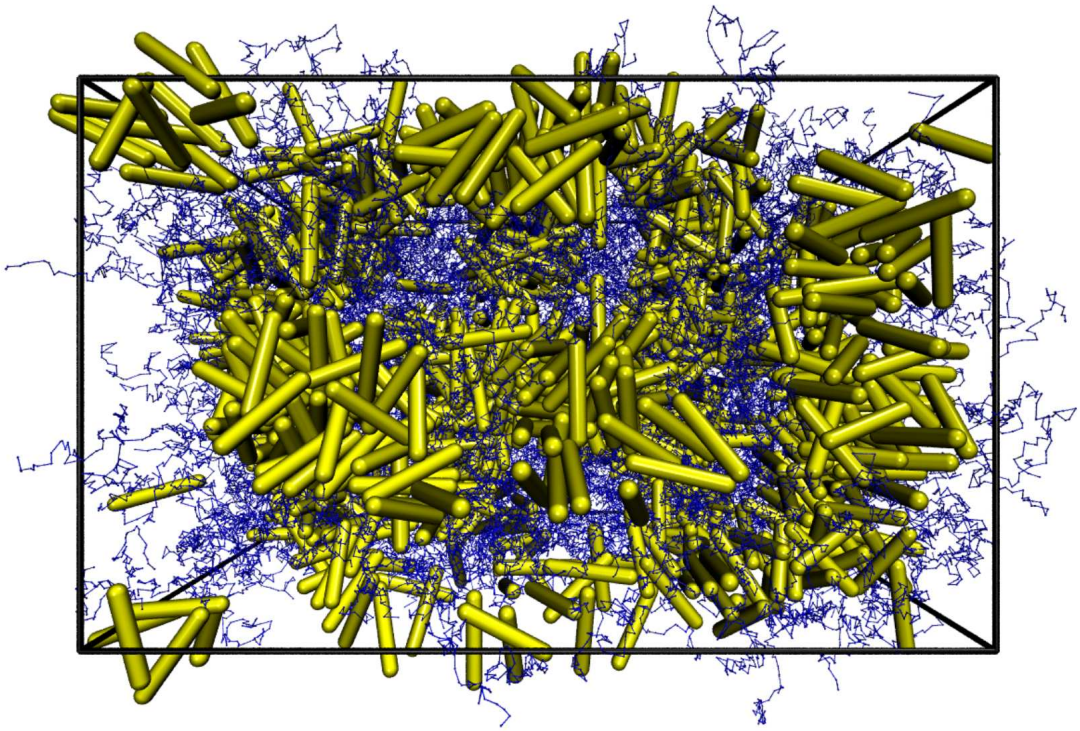

## 5.6 Zigzag phase

In a few simulations we observe a zigzag phase. As already mentioned in Chapter 2 this phase is believed to be metastable. In this section we check if the zigzag phase is also metastable in our model.

Figure (5.13) illustrates two snapshots of simulations that end in a zigzag phase. Both runs start from an ordered configuration in a cubic simulation box that has a length of 26 in all three directions and a cell size of one. The spherocylinders have a length $L$ of five, a diameter $D$ equal to one and the attached coils consist of 50 monomers. The spring constant $k$ is set to 27 and the interaction parameters $\chi_{CC}$ and $\chi_{CR}$ are both equal to 0.1. Note that the values of the interaction parameters differ from the ones we have used for the simulations in order to obtain the phase diagram in Section 5.1. The configuration in Figure (5.13a) contains 1790 spherocylinders which results in a reduced density of 0.513. The configuration in Figure (5.13b), with 1752 rods and a reduced density around 0.502, is used as initial configuration for the test runs in this section. Based on our findings so far we would expect a smectic phase in this region. As the snapshots demonstrate the layers are deformed into a zigzag structure.

The zigzag phase may be metastable. It may, for example, only occur due to the misfit of the sizes of the simulation box and the block copolymers. One possibility to check if the zigzag phase is metastable would be to vary the size of the simulation box. We choose a different approach and change the length of the coils, or more precisely the

**Figure 5.13** Snapshots of two final configurations that exhibit a zigzag phase. The two systems only differ in the number of rods. For both configurations $\chi_{CC}$ and $\chi_{CR}$ are equal to 0.1. (a) $N = 1790$ and $\rho^* \approx 0.513$. (b) $N = 1752$ and $\rho^* \approx 0.502$.

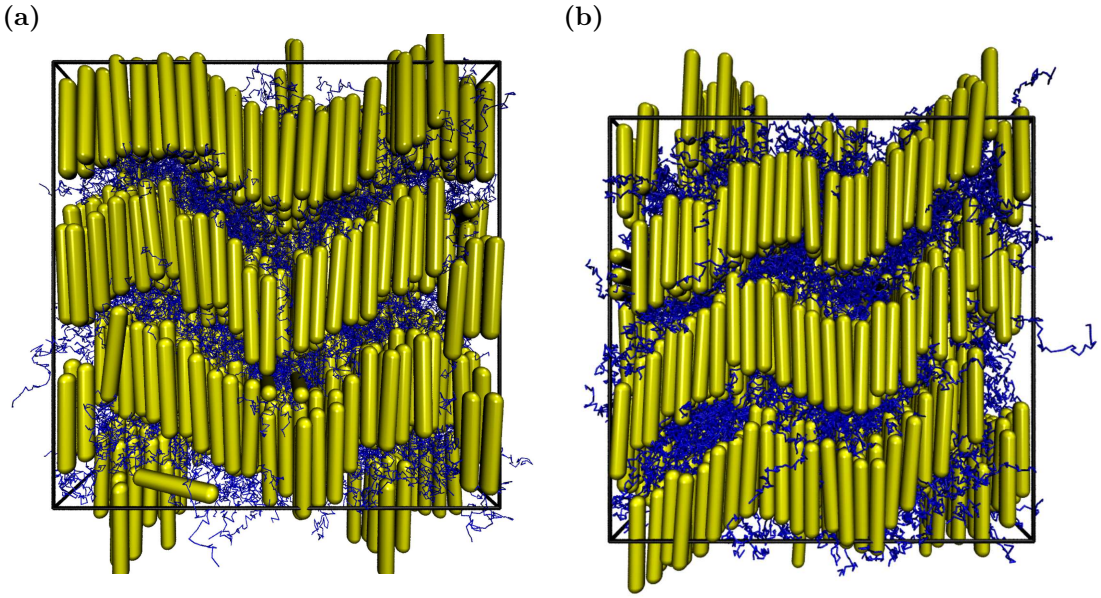


number of monomers per coil $m$, using the algorithm introduced in Section 4.3, thereby modifying the freedom of movement for the rods. For this purpose, we use the final configuration of a prior simulation that exhibits a zigzag phase as initial configuration for new simulations. Then we extend or shorten the coil length and restart the simulations. After these systems are equilibrated we take the final configurations and reset the number of monomers to the old value before the simulations are started again. All other parameters are the same as in the initial simulation.

The snapshots in Figure (5.14) show the final configurations for the simulations with modified coil lengths. The configuration shown in Figure (5.14a) merely contains ten monomers per coil. It can be clearly seen that the three layer zigzag structure vanishes and four ordered layers form. The tilt of these layers is an indicator that there is a mismatch between the simulation box size and the expansion of the block copolymers. For slightly longer coils, consisting of 25 monomers, we also observe ordered layers. However, this configuration does not tilt and only three layers occur as Figure (5.14b) demonstrates. The shorter coil length just lead to a smoothing out of the zigzag structure but do not allow a rearrangement of the rod-coil block copolymers. The configuration with $m$ equal to 40 behaves similar. With the exception that the layers run obliquely as illustrated in Figure (5.14c). The snapshot in Figure (5.14d) shows the final configuration of the simulation for which the old value of 50 for $m$ is retained. We see that the zigzag structure remains for this coil length. In Figure (5.14e) we see the final configuration for coils with 75 monomers. The zigzag structure is still clearly visible and only marginally smoothed out. For the longest coils with 100 monomers the zigzag structure vanishes completely and three ordered layers that run obliquely form as Figure (5.14f) illustrates.

**Figure 5.14** Snapshots of final configurations for systems starting from a zigzag structure with altered coil lengths. The coils in the former configuration consist of 50 monomers and $\chi_{CC} = \chi_{CR} = 0.1$. (a) $m = 10$. Four layers form and the system rotates. (b) $m = 25$. Ordered layers. (c) $m = 40$. Ordered layers that run obliquely. (d) $m = 50$. For an unchanged coil length the zigzag structures remains stable. (e) $m = 75$. The zigzag structure is slightly smoothed out. (f) $m = 100$. Ordered layers that run obliquely form.

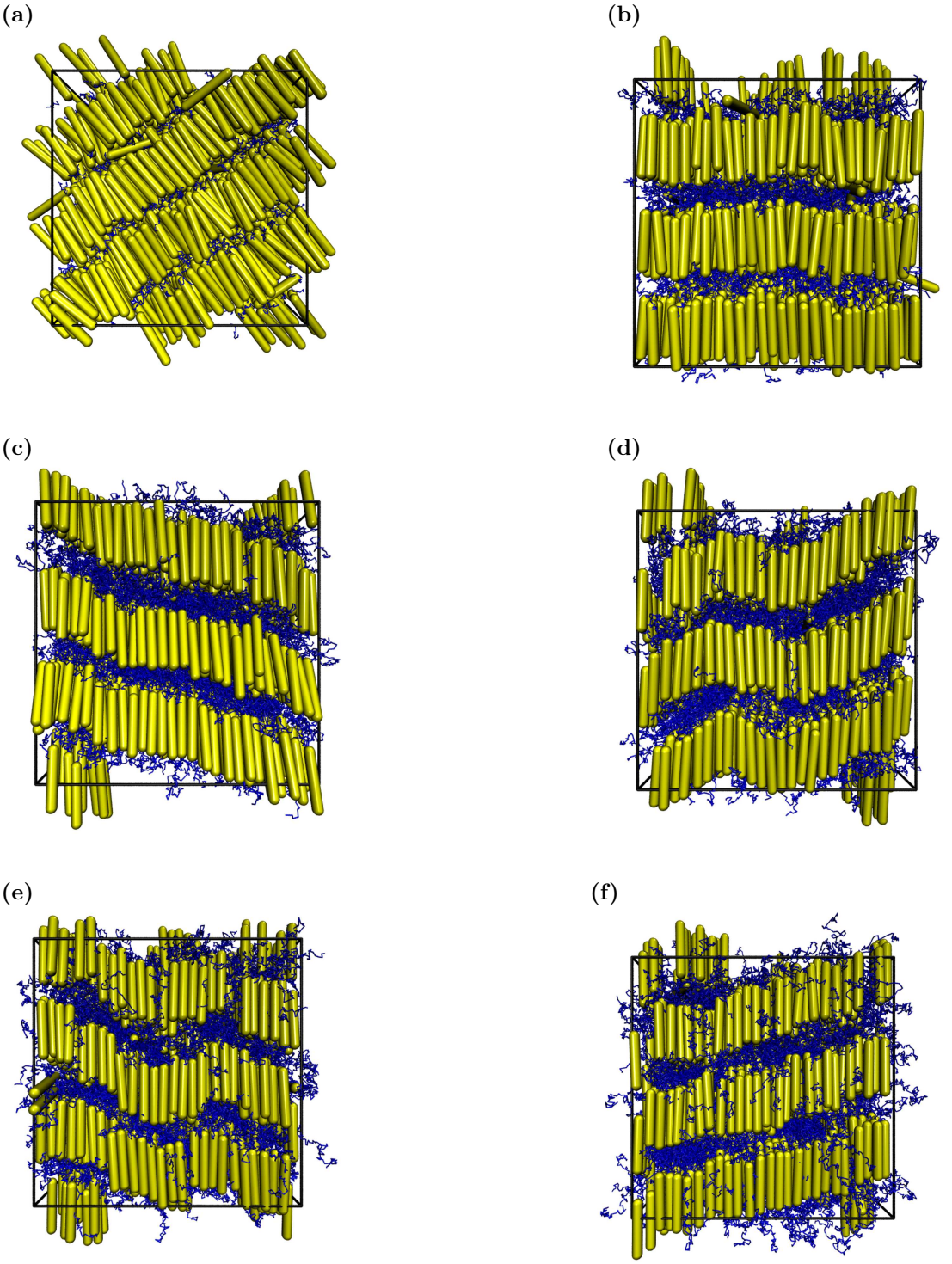

After the evaluation of the systems with altered coil lengths we reset the number of monomers to 50 for all runs and restart the simulations using the configurations from Figure (5.14) as initial configurations. If the zigzag phase is not metastable the simulations should end in a zigzag structure again. But this is not the case as the snapshots of the final configurations in Figure (5.15) demonstrate. The system whose coils consisted of ten monomers in the prior runs the distance between the layers increases as Figure (5.15a) illustrates. For the configuration which had 25 monomers per coil in the previous runs shown in Figure (5.15b) alternately tilted layers form. As the size of the simulation box does not allow the formation of four layers in $y$-direction this is not a real arrowhead phase. We presume that such a phase may occur for a different box size. The system with $m$ equal to 40 exhibited layers that run obliquely. The final configuration after reseting the coil length is displayed in Figure (5.15c). We see that all layers are now at the same level and slightly tilted. For the two configurations shown in Figures (5.15d) and (5.15e) the zigzag structure is indeed more clearly visible for the unmodified run but still recognizable for the run with 75 monomers in the previous simulation. As Figure (5.15f) demonstrates the obliquely running layer structure remains for the run that was altered to 100 monomers per coil before.

From these results we can conclude that the zigzag phase is metastable in our model.

**Figure 5.15** Final configurations of the simualtions starting from the configurations in Figure (5.14) after the number of monomers per coil is reset to 50 monomers. The interaction parameters $\chi_{CC}$ and $\chi_{CR}$ are set to 0.1. (a) Reset from $m = 10$. Three ordered layers form. (b) Reset from $m = 25$. Alternately tilted layers. (c) Reset from $m = 40$. Layers are tilted in the same direction. (d) Reset from $m = 50$. The initial zigzag structure remains. (e) Reset from $m = 75$. The zigzag structure is still identifiable. (f) Reset from $m = 100$. Obliquely running, ordered layers.

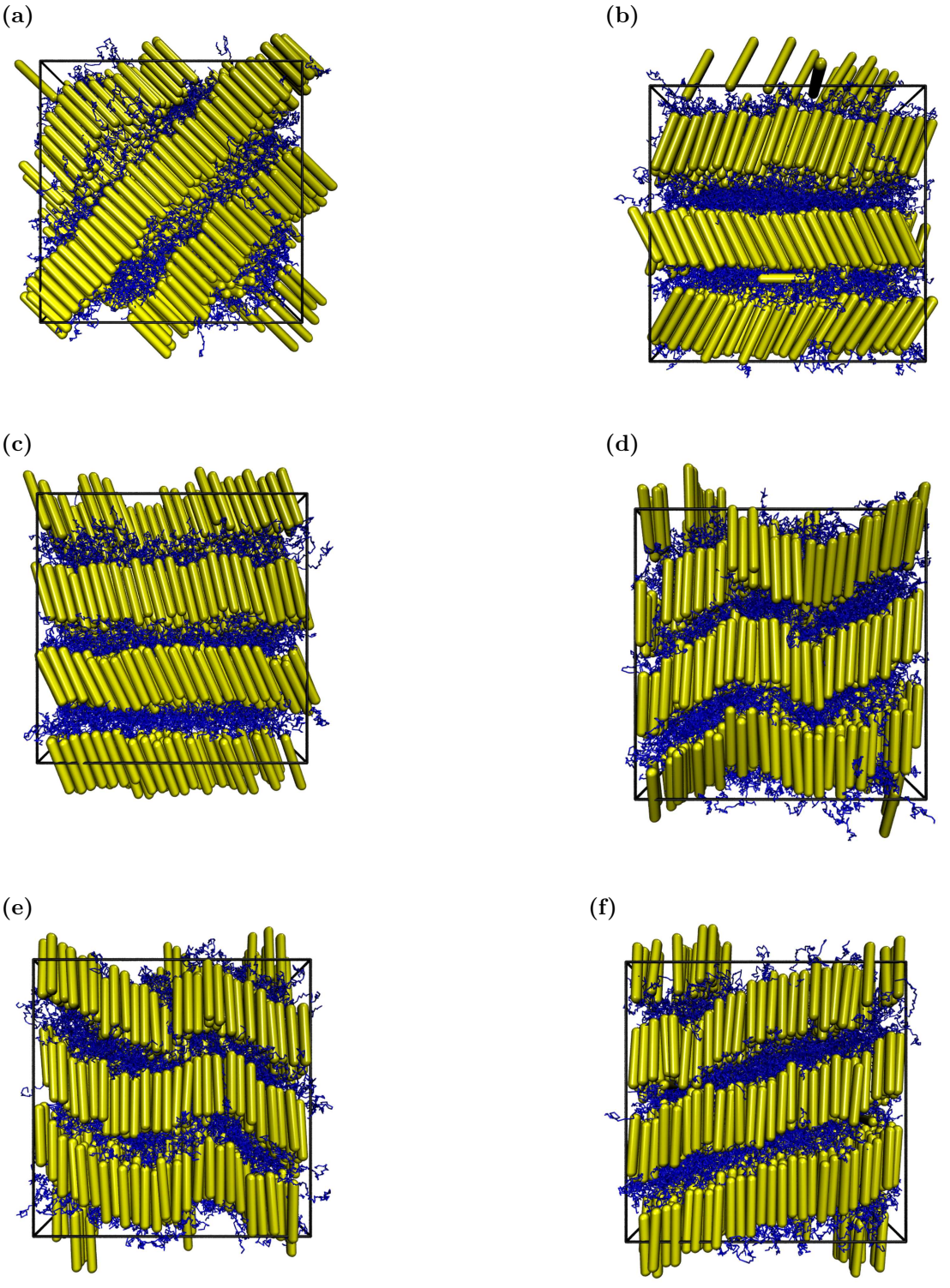

# Part II

# Computer simulation of tetrapod/polymer mixtures

Chapter 6

# Tetrapods

Contents



In this chapter we give a brief introduction to tetrapods and an overview over research on tetrapods so far. Then we give a motivation outlining why we study these systems and mention some further works which are related to the derivation of our simulation model in the following chapter.

## 6.1 Introduction

The research of tetrapods is of great interest as their three-dimensional character may potentially pave the way for interesting optical, electrical and mechanical properties. Tetrapods consist of four arms branching out from the core at tetrahedral angles of 109.5°. Their branched shape prevents a dense packing as it is observed for other anisotropic particles, such as spherocylinders. Additionally, unlike rods, their structure prohibits them to lie flat on the plane. This may improve the electron transport perpendicular to the plane. The three-dimensional shape of tetrapods also facilitates charge transport in all spatial directions independent of their orientation. Furthermore, the porous structure of tetrapods provides large interfacial areas and percolating pathways for electrons. Thus, a higher fraction of excitons are able to diffuse to the interface and the charges can be transported efficiently to the electrodes. For these reasons they are considered as a promising candidate to achieve more efficient, stable and inexpensive solar cells.

A lot of effort is put into the examination of better methods to control and optimize the morphology in order to achieve efficient devices. There are many parameters that may influence the aggregation of tetrapods. Not only the way of device fabrication, the used materials for the tetrapods and the solvent are of great importance for the morphology. Also a highly controllable growth of the tetrapods is indispensable. A recent work demonstrates that tetrapods with grafted polymers have a significantly better film quality than bare tetrapods [151].

## 6.2 Research review

In this section we present some assorted results with a focus on tetrapods and the advantage of their use for hybrid organic-inorganic photovoltaic devices. A good review on recent developments in synthesis and controlled assembly of colloidal branched nanocrystals is given by Li et al. [145].

Already in 1987 Hasegawa et al. [104] observe highly ordered three-dimensional networks of structural units for polystyrene-polyisoprene diblock copolymers, which they identify as tetrapods via electron microscopy. They emphasize that there are only three three-dimensional continuous structures possible for these structural units. This are the wurtzite, the single-diamond and the double-diamond structure, whereas they suggest that the last one is the most probable one. These three structures are shown in Figure (6.1) each one viewed from four different directions. They also mention that the tetrapod-network structure can be changed into lamellar, cylindrical and spherical microdomain morphologies by using another casting solvent.

If the tetrapods are molecular units, instead of structural units in a morphology, more phases are possible. In their theoretical study Blaak et al. [28] predict an uniaxial nematic and a cubatic phase, which is a special case of the biaxial nematic phase and has not yet been observed in experiments, for a system of tetrapods. But these results are solely correct in the Onsager limit of infinite aspect ratios only taking hard-core interactions into account.

**Figure 6.1** Characteristic views of different lattice models for the tetrapod units from different directions. (a) Wurtzite lattice model. (b) Single-diamond lattice model.(c) Double-diamond lattice model. From [104]

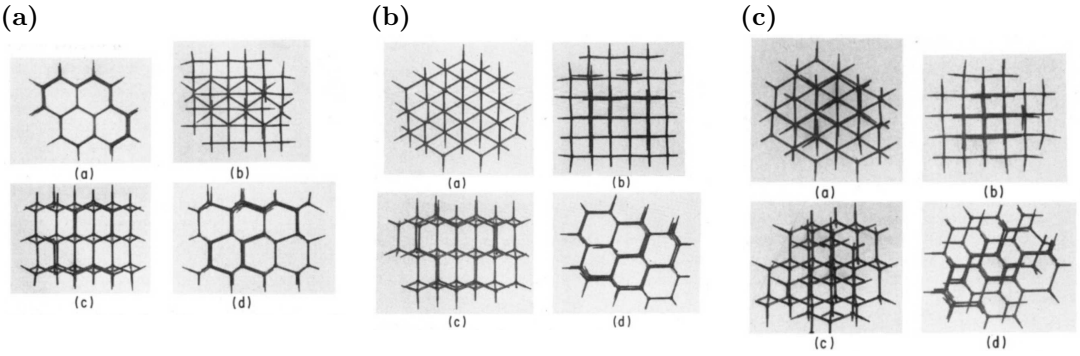


The optical and electrical properties of a system strongly depend on the shape and size of the polymers. Therefore, a well controlled synthesis [161] is a crucial factor allowing to tune the properties of the device. Nowadays it is possible to synthesize polymers with extreme properties. For example, Manna et al. [167] obtain CdSe nanorods exceeding 100 nm in length and aspect ratios of over 30:1, as well as arrow-, teardrop-, tetrapod and branched tetrapod-shaped nanocrystals. In a later work [168] they concentrate on the independent control of the width and length of the four arms of CdTe tetrapods. They also mention a higher degree of solubility for tetrapod nanocrystals compared to separate rods of the same length and diameter as the tetrapod arms. The reason is that it is easier for two rods to achieve a large contact area with each other what may lead to aggregation.

Likewise Choi et al. [49] investigate the properties of CdSe/CdS core/shell tetrapods with different arm lengths. But also more complex structures are feasible and show very interesting properties. Milliron et al. [180] fabricate anisotropic colloidal nanocrystal heterostructures with linear and branched topology as illustrated in Figure (6.2). They couple colloidal quantum dots and rods while still being able to control branching and composition. Thus, it is possible to tune the nature of the interactions and the properties of each component independently. One example are branched tetrapods with CdSe central tetrapods and terminal CdTe branches (d in Figure (6.2)) which have unusual charge-separating properties making them attractive for photovoltaic energy conversion.

Further, the internal structure of tetrapods is investigated. The high-resolution transmission electron microscopy analysis of tetrapod-shaped CdSe nanocrystals by Pang et al. [197] demonstrates that the core of these tetrapods has a zinc blende crystal structure while the four arms have a wurtzite crystal structure. This is also discussed in the study of Asokan et al. [16] which reveals that the usage of quaternary ammonium surfactant ligands results in CdSe tetrapods with high shape and dimensional uniformity. But this is only true for CdSe, CdS, CdTe and ZnO tetrapods and not for ZnS tetrapods. Zhu et al. [300] find that the branches of their ZnS tetrapods exhibit a zinc blende phase and not a wurtzite phase like the aforementioned tetrapods.

**Figure 6.2** Colloidal nanocrystal heterostructures with linear and branched topology. (a and b) Back branching. (c) Extended tetrapods. (d) Structural isomers in branched tetrapods. From [180].

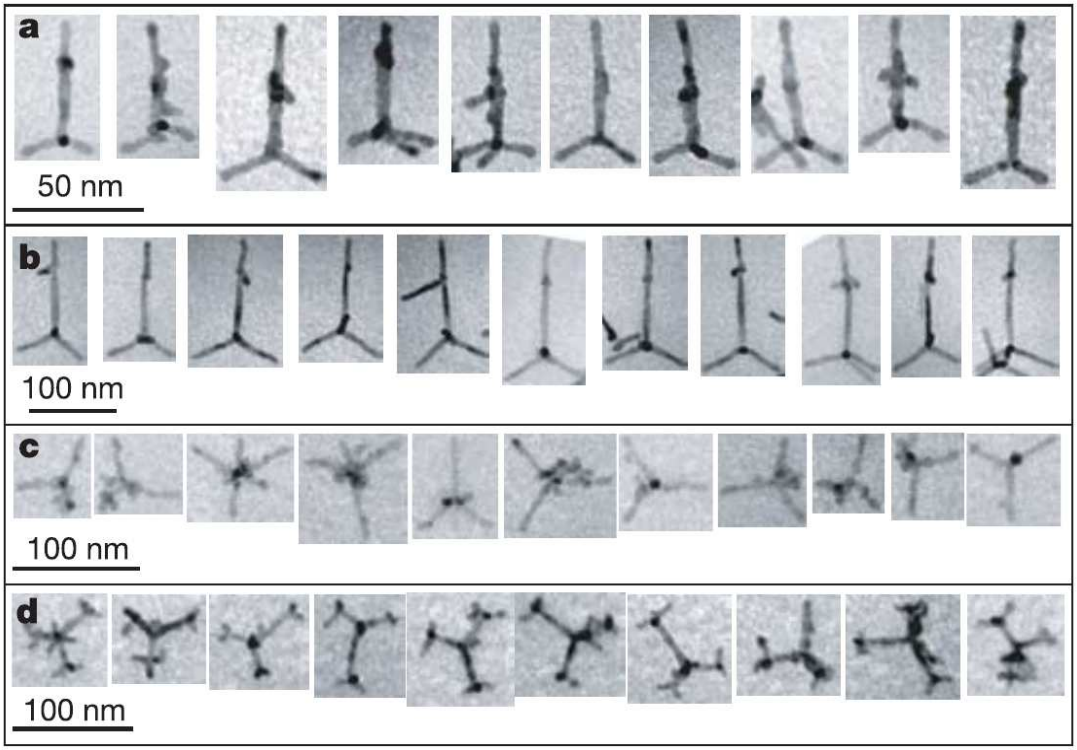


Tetrapods can form various networks which influence the systems properties. For instance, Franchini et al. [81] investigate the phototransport in tip-to-tip networks of CdSe/CdTe tetrapods. Zanella et al. [297] present various types of superlattices of nanorods and three-dimensional networks of octapod/tetrapod-shaped nanocrystals fabricated by depletion attraction. Figure (6.3) shows transmission electron microscopy images and sketches of three aggregation patterns for ZnTe/CdTe tetrapods. The images show fragments of treeing and interlacing and honeycomb-like two-dimensional networks. They also emphasize that the network of interlaced polymers could be beneficial for photovoltaic devices, if the used polymers are semiconducting.

Due to their geometry tetrapods and octapods tend to self-align on a substrate making them interesting for solar cells [145]. The importance of tetrapods for optoelectronic devices is underlined by several studies. Sun et al. [250] show that their devices based on CdSe tetrapods have high efficiencies due to the good electron transport perpendicular to the plane of the film. They demonstrate that device performance of branched particles like tetrapods is better than for both nanorods and quantum dots when blended with polymers. Based on a low band gap conjugated polymer and CdSe tetrapods Dayal et al. [61] fabricate a highly efficient bulk heterojunction solar cell. In most devices tetrapods with a CdSe core and CdTe arms act as electron-acceptors. Li et al. [149] introduce a new hybrid heterostructure with improved photovoltaic performance using electron-conducting fullerene (C60) as interlayer material, making the CdSe/CdTe tetrapods act as electron-donor.

**Figure 6.3** Three different aggregation patterns observed for ZnTe/CdTe tetrapods. (a,d-a) Treeing. (b,d-b) Honeycomb-like networks. (c,d-c) Interlacing. From [297]

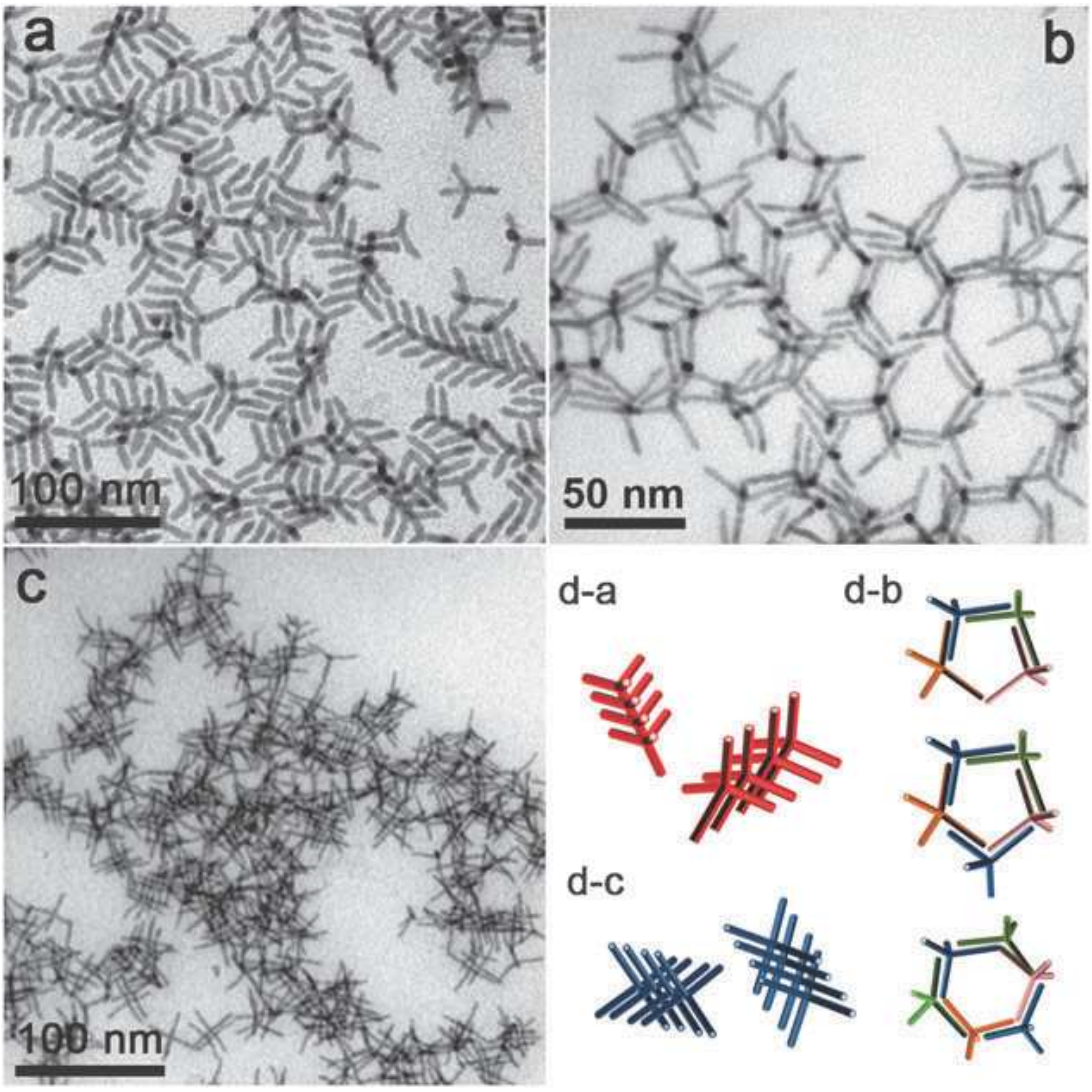


Finally, we would like to put a special focus on the work of Lim, zur Borg, Char and Zentel [151]. The model we introduce in the next chapter is designed to fit to their inorganic/organic hybrid systems. In cooperation with both experimental groups we have been able to reproduce the key results of their experiments.

In a first paper Lim et al. [150] explain their method for a controlled synthesis of highly uniform CdSe tetrapods. A schematic illustration of their continuous precursor injection approach and transmission electron microscopy images at different time steps are shown in Figure (6.4).

They also demonstrate the capability of this method to produce tetrapods in a controllable manner. The transmission electron microscopy images in Figure (6.5) show arm-length and diameter-controlled tetrapods as well as tetrapods with stepwise-varying diameter.

**Figure 6.4** The continuous precursor injection (CPI) approach. (a) Schematic illustration of the CGI approach. (b-g) Transmission electron microscopy images after (b) 0 (c) 10 (d) 20 (e) 30 (f) 40 (g) 50 minutes. Reproduced from [150]

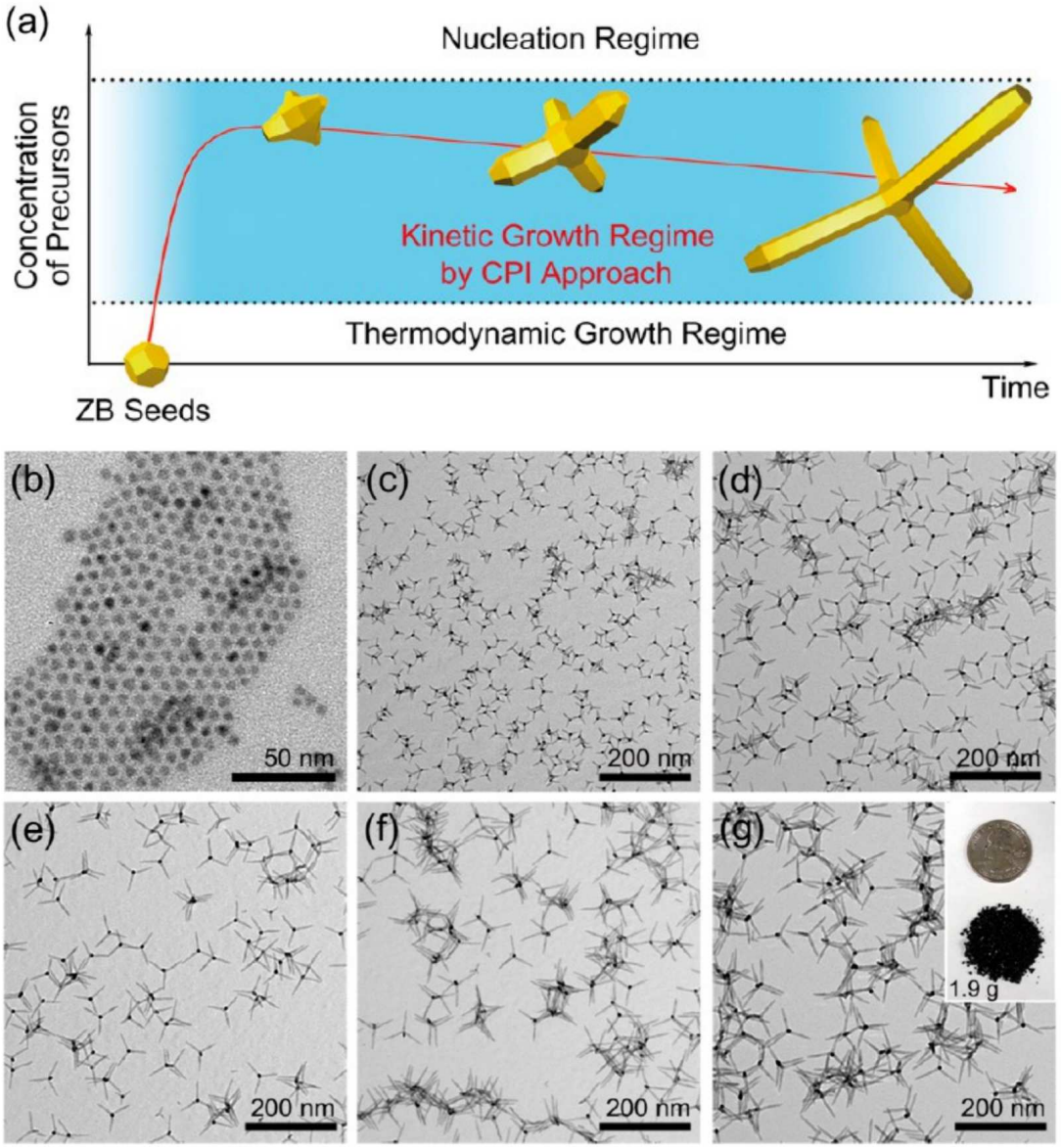


In a later paper of the group they demonstrate that grafted tetrapods show much better film qualities [151]. The systems consists of monodisperse CdSe tetrapods dispersed in a polymer matrix. We label these homopolymer-tetrapod mixtures "blends". Additionally, it is possible to graft semiconducting block copolymers of the same type as the excess polymers to the surface of the tetrapods. These block copolymer-tetrapod mixtures are referred to as "hybrids". Figure (6.6) shows a detailed overview over the system. The basic finding of the experiments is that the blends tend to form clusters in the matrix of excess polymers. For the hybrid systems the clustering is significantly reduced as the transmission electron microscopy images in Figure (6.7) show.

**Figure 6.5** Transmission electron microscopy images showing (a) arm-length controlled and (b) diameter-controlled tetrapods. (c) Stepwise-varying diameter. From [150]

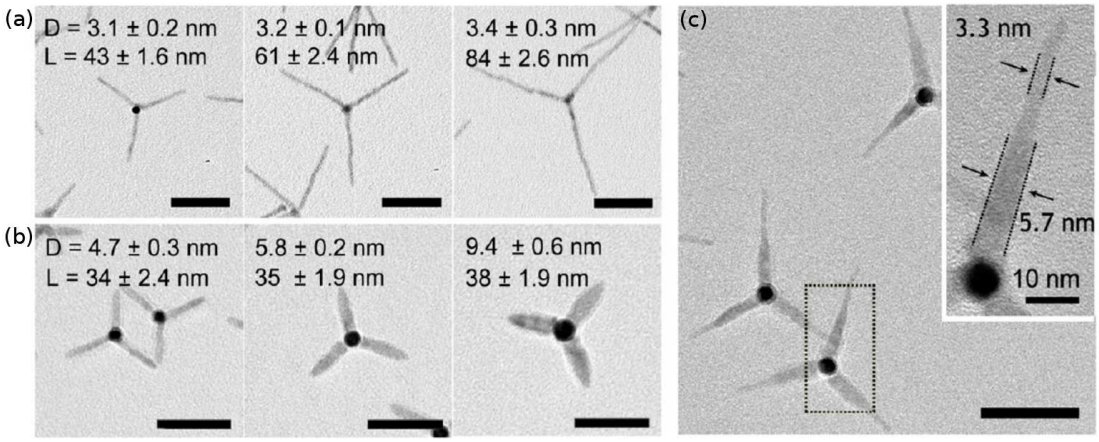


**Figure 6.6** CdSe tetrapods (yellow) and excess polymer poly(TPDF-b-SSMe) (green with anchor group in red). Using the "Grafting-to" method one gets the "hybrid" model. The tetrapods are dispersed in a polymer matrix.

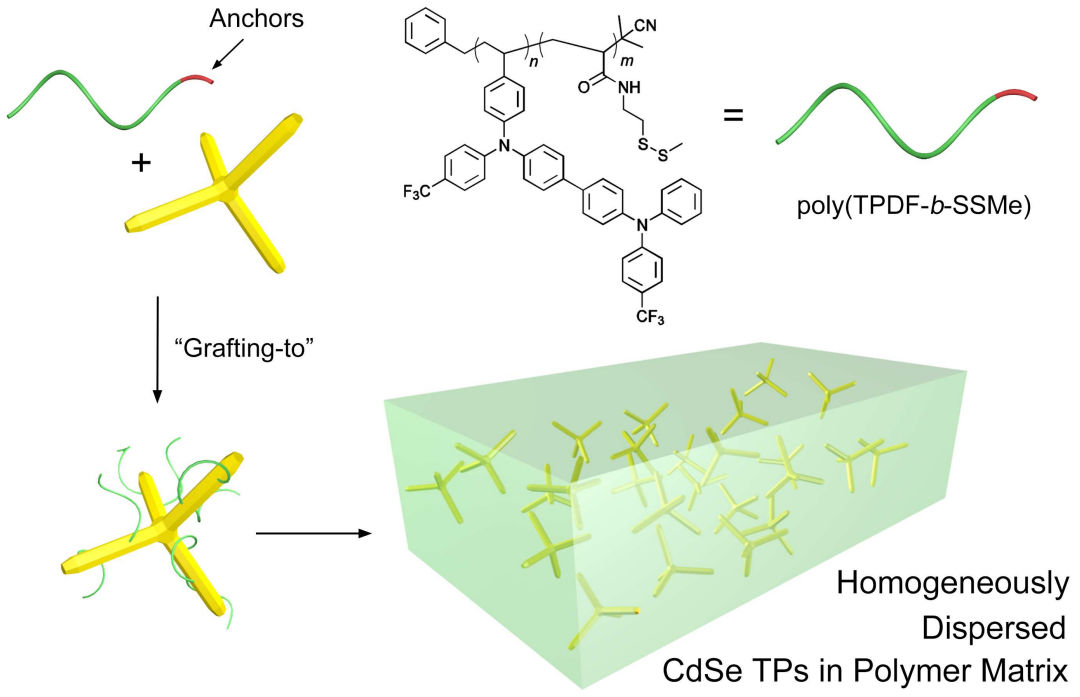

**Figure 6.7** Transmission electron microscopy images of a blend and a hybrid system. It is clearly recognizable that the clustering is reduced in the hybrid system.

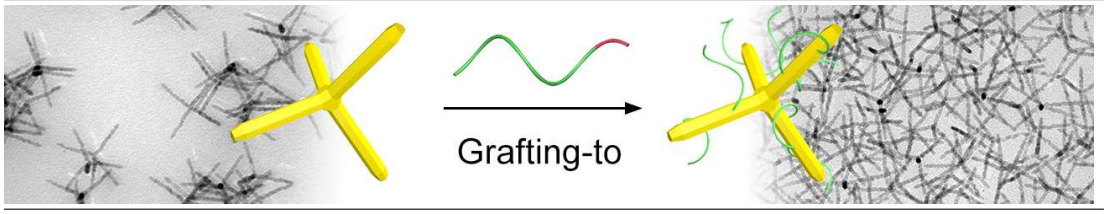


The measurements are performed for different tetrapod arm length and amounts of polymer loading to find the ideal morphology for hybrid solar cells. Figures (6.8), (6.9) and (6.10) show transmission electron microscopy images with arm length of 40, 70 and 100 nanometers, respectively. The top rows (a, c, e) are the hybrid samples and the bottom rows (b, d, f) the blend samples. The columns represent different polymer/tetrapod ratios (wt%). In the first column (a, b) this ratio is 50:50 and in the last one (e, f) 90:10. The middle column (c, d), with a wt% of 70:30, also includes an inset showing a magnified view. It is obvious that the film quality for the hybrids is much better, while the blends have a strong tendency to form clusters. This can already be observed for tetrapods with short arms. With increasing arm length the clustering becomes predominant. For tetrapods with moderate arm length the hybrid system is still relatively homogeneous. In the samples with the longest arms the effect of the attached polymers is still conspicuous, but, especially for a polymer/tetrapod ratio of 50:50, the hybrid sample shows inhomogeneities. Here a limit of this approach seems to be reached.

**Figure 6.8** Transmission electron microscopy images of tetrapods dispersed in a polymer matrix at different ratios. The tetrapod arm length is 40 nm. The top row shows the hybrid samples and the bottom row the blend samples. The polymer/tetrapod ratio (wt%) is 50:50 for a and b, 70:30 for c and d (insets show magnified view) and 90:10 for e and f. Scale bars represent 0.5 $\mu$m and 100 nm in the insets. From [151].

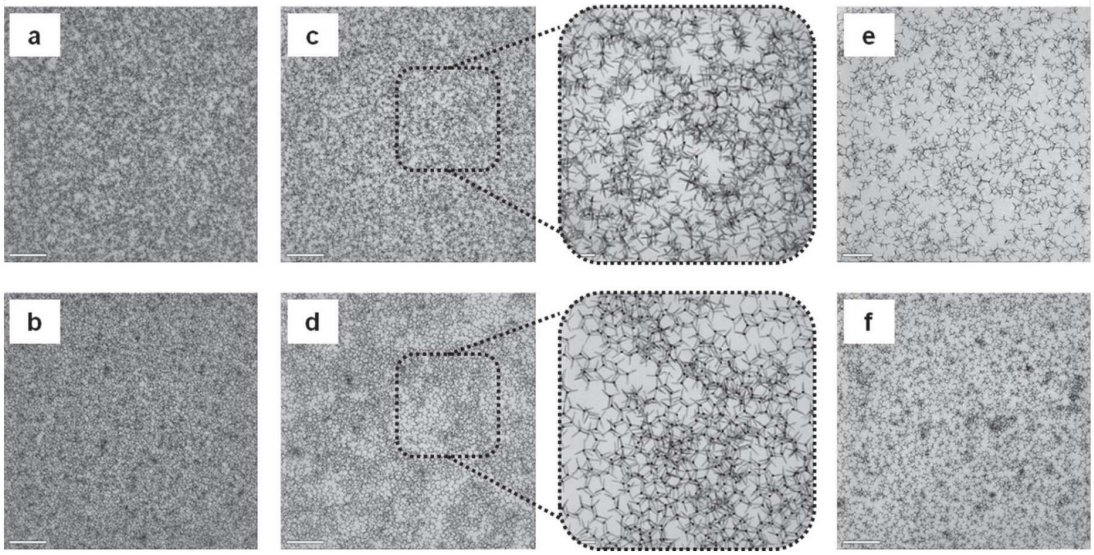

**Figure 6.9** Transmission electron microscopy images of tetrapods dispersed in a polymer matrix at different ratios. The tetrapod arm length is 70 nm. The top row shows the hybrid samples and the bottom row the blend samples. The polymer/tetrapod ratio (wt%) is 50:50 for a and b, 70:30 for c and d (insets show magnified view) and 90:10 for e and f. Scale bars represent 0.5 $\mu$m and 100 nm in the insets. From [151].

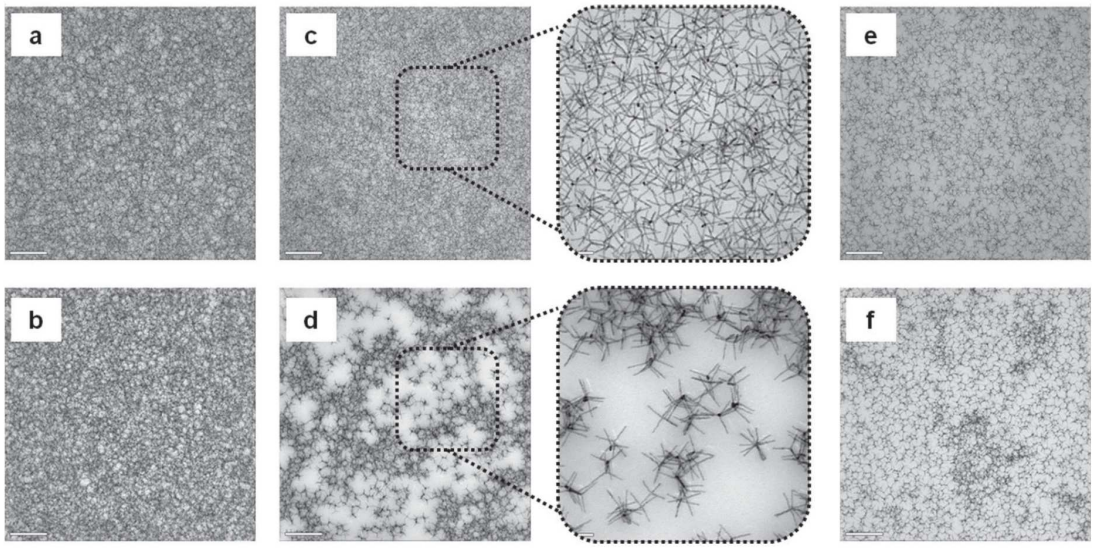


**Figure 6.10** Transmission electron microscopy images of tetrapods dispersed in a polymer matrix at different ratios. The tetrapod arm length is 100 nm. The top row shows the hybrid samples and the bottom row the blend samples. The polymer/tetrapod ratio (wt%) is 50:50 for a and b, 70:30 for c and d (insets show magnified view) and 90:10 for e and f. Scale bars represent 0.5 $\mu$m and 100 nm in the insets. From [151].

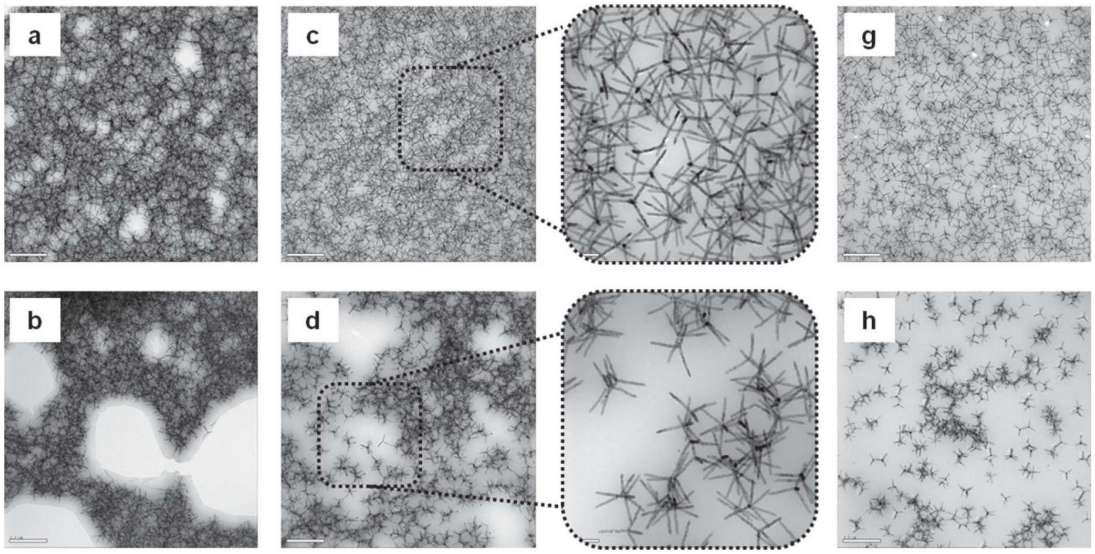

## 6.3 Further related work

In the next chapter we develop a model to simulate these polymer grafted tetrapods. Therefore, we derive a potential which represents the interaction induced by the polymer brushes attached to the surface of the tetrapods. Here, we present some related works. A comparison of several models for colloid-polymer mixtures can be found in reference [252].

At first, we take a look at bottlebrush polymers. This are macromolecules with polymeric side chains. For bottlebrush polymers with high backbone stiffness lyotropic liquid crystal phases are observed [148, 245, 261, 289]. Besides this fact, there are numerous studies on bottlebrush polymers with a flexible backbone [37, 38, 87, 137, 238, 257, 259, 283].

An even closer related system are hairy rod polymers. They consist of flexible side chains grafted onto a stiff macromolecular backbone. These side chains may have a crucial effect on the solubility of the polymers.

While Subbotin et al. [248] only find a lamellar and two hexagonal microphases in their theoretically study, Knaapila et al. [132] observe isotropic, nematic, lamellar, square and oblique lattice structures, but no simple hexagonal phase. Beside Molecular Dynamics simulations [152] there are also Dissipative Dynamics simulations [48] to study the phase behavior of hairy-rod polymers. In the latter study the polymers exhibit a lamellar phase for dense side chains which becomes an inverted cylindrical phase for lower side chain densities. But the experimentally observed nematic phase is not found.

Chapter 7

# Model

**Contents**



In this chapter we introduce the model used for the simulation of the tetrapod polymers. We give a short introduction to quaternions which are used to rotate the tetrapods. Then we derive the potential which represents the interactions for the tetrapods and the additional polymer brushes grafted onto their surface. Further, we introduce an algorithm which allows the simulation of systems with fluctuating volume. A test of this algorithm can be found in Appendix B.1. Finally, we present some model parameters and observables.

## 7.1 Model

In this chapter we mainly concentrate on the examination of the inorganic/organic hybrid system studied by Lim, zur Borg, Char and Zentel. Their experimental findings and our simulation results are published in a joint paper [151].

The program we use for the simulation of rod-coil block copolymers may easily be modified to simulate tetrapods. For this purpose four spherocylinders are arranged around a common center with an tetrahedral angle of 109.5 degree between each other. The coil chains are removed and all density based interactions are replaced by effective potentials. Therefore, there is no need to subdivide the system into cells anymore.

In principle it would have been possible to use the density based interactions introduced in the rod-coil copolymer model in Part I of this work. Then the coils could be used as not connected polymer chains to simulate the excess polymer and we could connect coils to the surface points of the spherocylinders to represent the brushes. In practice this system would not have been tractable because of the size ratios in the experiments. The excess and brush polymers are much smaller than the tetrapod diameter. Therefore, we would need a very fine grid which is computationally expensive. Additionally, we would need a huge amount of surface points to graft the brushes densely to the surface of the tetrapods and to satisfy the prerequisite that the cell size has to be bigger than the distance of the surface points in order to get a reasonable approximation for the rod density. With each rotation all these points would have to be recomputed, what would slow down the simulations dramatically. Furthermore, the dissimilar sizes would result in move ranges of very unequal order for the brush polymers and the tetrapods. Since the brush polymers are much shorter than the diameter of the tetrapods, the explicit structure of the brush polymers is not of interest anyway and can be replaced by an effective potential.

For these reasons we develop a coarse-grained model including the effects of polymers in an implicit manner by effective interactions. For ease rotations are done using quaternions. In the following we will explain the model used for the tetrapod simulations in detail.

## 7.2 Tetrapods

In this section we describe how a tetrapod is characterized and motivate the choice of our model. A tetrapod is made out of four arms which have a common central point. For our model we assume that all of these arms are of equal length $L$ and have a constant diameter $D$. This is reasonable as the group of Lim et al. [150] demonstrates that they can fabricate tetrapods with highly uniform arm length and diameter (see Figure (6.5)). The central angle between all four arms is identical and known as the tetrahedral angle

$$\theta_{\mathrm{T}} = \arccos\left(-\frac{1}{3}\right) = 2\arctan(\sqrt{2}) \approx 109.47°. \tag{7.1}$$

In our model each arm is represented by a hard spherocylinder of length $L$ and diameter $D$. A snapshot of a tetrapod is displayed in Figure (7.1). For the rod-coil block copolymers in Part I we place the unit vectors $\hat{\mathbf{u}}$ of the spherocylinders at their center of mass. For the tetrapods we locate the origin of the unit vectors $\hat{\mathbf{u}}_{\mathrm{T}}$ at the common central point. If the unit vector $\hat{\mathbf{u}}$ at the center of mass is needed for an algorithm, for

example, the shortest distance algorithm for spherocylinders introduced in Section 3.4.1, it can easily be calculated by shifting the tetrapod unit vectors $\hat{\mathbf{u}}_{\mathrm{T}}$ by $L/2 + D$ along its direction. The advantage of this method is that it is much easier to rotate the tetrapods this way using quaternions.

**Figure 7.1** Snapshot of a tetrapod as used in our simulations. The four unit vectors $\hat{\mathbf{u}}_{\mathrm{T},i}$ are located at the central point of the tetrapod. The angel $\theta_{\mathrm{T}}$ between the arms is the tetrahedral angle.

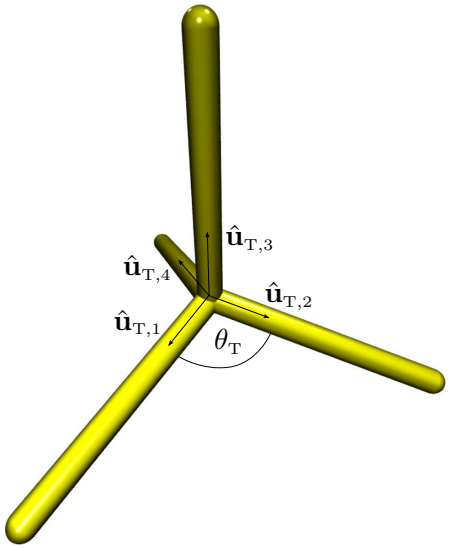


## 7.3 Rotations using quaternions

For the rotation of the tetrapods we use quaternions. Compared to the use of rotation matrices this parameterization has some advantages. Quaternions are numerically more stable than Euler angles, less susceptible to round-off errors, need less memory and are often computationally faster than rotation matrices.

There are numerous ways to express a rotation. When rotating a rigid body in three dimensions rotation matrices are most commonly used. Any rotation can be achieved by composing three sequential rotations by the Euler angles $\varphi$, $\vartheta$ and $\psi$. Since matrix multiplication is noncommutative the order in which multiple rotations are performed is crucial. Additionally, with each rotation the coordinate system is rotated. Hence each following rotation is done in the rotated coordinate system. This is not only counterintuitive but also a possible source of errors. Euler angles also have the disadvantage that singularities may occur. When the middle rotation aligns the axes of the first and last rotation a singular alignment, also known as gimbal lock, occurs. These singularities are characteristic of Euler angles but not rotation matrices as such. They can be avoided by choosing other representations for the rotation.

Another common representation is to use an angle and an axis. In a three-dimensional space a rotation matrix has three degrees of freedom. Instead of using three Euler angles to represent these degrees of freedom one may also use one angle $\theta$ and a fixed axis $\mathbf{a}$ to

characterize a rotation. For the simple case that this axis is described by an unit vector, that is, $\mathbf{a} = \hat{\mathbf{u}} = \begin{bmatrix} u_x & u_y & u_z \end{bmatrix}^{\mathrm{T}}$, the rotation matrix $R(\theta, \hat{\mathbf{u}})$ can be written as

$$R(\theta, \hat{\mathbf{u}}) = \begin{bmatrix} 1 + \Phi(\theta)\left(u_x^2 - 1\right) & u_x u_y \Phi(\theta) - u_z \sin\theta & u_x u_z \Phi(\theta) + u_y \sin\theta \\ u_y u_x \Phi(\theta) + u_z \sin\theta & 1 + \Phi(\theta)\left(u_y^2 - 1\right) & u_y u_z \Phi(\theta) - u_x \sin\theta \\ u_z u_x \Phi(\theta) - u_y \sin\theta & u_z u_y \Phi(\theta) + u_x \sin\theta & 1 + \Phi(\theta)\left(u_z^2 - 1\right) \end{bmatrix} \tag{7.2}$$

with $\Phi(\theta) = 1 - \cos\theta$. The matrix $R(\theta, \hat{\mathbf{u}})$ rotates a vector $\mathbf{p}$ by an angle $\theta$ towards an unit vector $\hat{\mathbf{u}}$. The rotated vector $\mathbf{p}'$ can be expressed as

$$\mathbf{p}' = R(\theta, \hat{\mathbf{u}})\mathbf{p} \tag{7.3}$$

But using this representation is very inefficient since a lot of expensive calculations have to be performed. To overcome this drawback and the singularities of Euler angles we decide to use quaternions in our simulations.

Quaternions are first described by William Rowan Hamilton [100] in 1847. They form a four-dimensional vector-space over the real numbers commonly named $\mathbb{H}$ for Hamilton. A quaternion $q$ is fully characterized by four real numbers $a$, $b$, $c$ and $d$ or a real scalar $s$ and a purely imaginary vector $\mathbf{v}$

$$q = a1 + bi + cj + dk = s + \mathbf{v} = (s, \mathbf{v}). \tag{7.4}$$

Here we use the most common basis 1, $i$, $j$ and $k$ where 1 is the identity element of $\mathbb{H}$ and $i$, $j$ and $k$ are hypercomplex numbers with

$$i^2 = j^2 = k^2 = ijk = -1. \tag{7.5}$$

By multiplying hypercomplex numbers from the left or right further relations, such as $ij = k$ and $ji = -k$, can be derived. The hypercomplex numbers $i$, $j$ and $k$ are imaginary basis vectors of $\mathbb{H}$ as well as a basis for $\mathbb{R}^3$. So any vector $\mathbf{p}$ may be represented by a quaternion $p = (0, \mathbf{p})$. The conjugate $q^*$ of a quaternion $q$ is given by

$$q^* = -\frac{1}{2}\left(q + iqi + jqj + kqk\right) \tag{7.6}$$

$$= a1 - bi - cj - dk = s - \mathbf{v} = (s, -\mathbf{v}) \tag{7.7}$$

and its reciprocal $q^{-1}$ by

$$q^{-1} = \frac{q^*}{\|q\|^2} \tag{7.8}$$

where

$$\|q\| = \sqrt{qq^*} = \sqrt{q^*q} = \sqrt{a^2 + b^2 + c^2 + d^2} \tag{7.9}$$

is the quaternion norm. The multiplication of two quaternions $g$ and $h$ is noncommutative and given by

$$g \cdot h = (s_1, \mathbf{v}_1) \cdot (s_2, \mathbf{v}_2) \tag{7.10}$$

$$= (s_1 s_2 - \mathbf{v}_1 \cdot \mathbf{v}_2, s_1\mathbf{v}_2 + s_2\mathbf{v}_1 + \mathbf{v}_1 \times \mathbf{v}_2). \tag{7.11}$$

Conventionally, normalized quaternions, that is, $\|q\| = 1$, are used to represent rotations in three dimensions. Those unit quaternions are called versors. It is easy to

see that in this case the reciprocal $q^{-1}$ is equal to the conjugate $q^*$. With the Euler axis $\hat{\mathbf{a}}$ and the angle $\theta$ a quaternion $q$ and its inverse $q^{-1}$ can be written as

$$q = \exp\left(\frac{\theta}{2}\hat{\mathbf{a}}\right) = \cos\frac{\theta}{2} + \hat{\mathbf{a}}\sin\frac{\theta}{2} = s + \mathbf{v} \tag{7.12}$$

$$q^{-1} = \exp\left(-\frac{\theta}{2}\hat{\mathbf{a}}\right) = \cos\frac{\theta}{2} - \hat{\mathbf{a}}\sin\frac{\theta}{2} = s - \mathbf{v}. \tag{7.13}$$

With these equations the rotation of a vector $\mathbf{p}$, represented by the quaternion $p = (0, \mathbf{p})$, about an axis $\hat{\mathbf{a}}$ by an angle $\theta$ can be expressed as

$$p' = qpq^{-1} = qpq^* \tag{7.14}$$

$$= \left(\cos\frac{\theta}{2} + \hat{\mathbf{a}}\sin\frac{\theta}{2}\right) p \left(\cos\frac{\theta}{2} - \hat{\mathbf{a}}\sin\frac{\theta}{2}\right) \tag{7.15}$$

where the quaternion $p'$ is equal to $(0, \mathbf{p}')$ at which $\mathbf{p}'$ is the position of the vector $\mathbf{p}$ after the rotation. As $q$ is a versor it is easily possible to calculate the orthogonal rotation matrix $Q(q)$ if desired.

$$Q(q) = \begin{bmatrix} 1-2(c^2+d^2) & 2(bc-ad) & 2(bd+ac) \\ 2(bc+ad) & 1-2(b^2+d^2) & 2(cd-ab) \\ 2(bd-ac) & 2(cd+ab) & 1-2(b^2+c^2) \end{bmatrix} \tag{7.16}$$

## 7.4 Interactions

In this section we derive the potentials used in our simulations and motivate their choice. Before we begin with the derivation of the potentials we have to make some assumptions. For a more realistic model these effects should be taken into account.

For the derivation of the interactions we use a coarse-grained model for the polymer brushes. The coarse-graining is done by replacing the polymer chains by a series of blobs containing a given number of monomers. To this end, our first assumption is that the investigated polymer brushes can be described with this model at all.

In the used model each blob has a diameter $\xi$. For a curved surface one would observe a swelling of the blob diameter $\xi(\mathbf{r})$ with increasing distance $\mathbf{r}$ to the center of the spherocylinder. The effect of distance dependent swelling is illustrated in Figure (7.2) and, for example, evaluated in detail for different solvent qualities by Daoud and Cotton [60].

In our second assumption we presume that the diameter of the blobs is constant. In other words, the diameter $\xi(\mathbf{r})$ does not depend on the distance $\mathbf{r}$ and can simply be written as $\xi$. This assumption is reasonable if the length of the brush polymers is much shorter than the diameter of the spherocylinders. This is true in our system as we know from the experimental values. As a further consequence of this assumption we find that the local curvature of the surface can be neglected and, therefore, we can treat the curved surfaces as planar walls locally. Figure (7.3) shows the cross-section of a tetrapod arm with short, attached brush polymers which are represented by blobs with constant diameter $\xi$. The enlarged region demonstrates that the local curvature is negligibly low, as the diameter of the tetrapod arms is much bigger than the length of the polymer brushes. The bending of a polymer brush depending on the curvature for the blob model is, for example, examined by Sevick and Williams [234].

**Figure 7.2** Top view on a spherocylinder with diameter $D$ representing one arm of a tetrapod. The brush polymers are enclosed in blobs of diameter $\xi(\mathbf{r})$ depending on the distance $\mathbf{r}$ to the center of the spherocylinder. For brushes much shorter than $D$ the dependence on the distance $\mathbf{r}$ can be neglected and $\xi$ is constant.

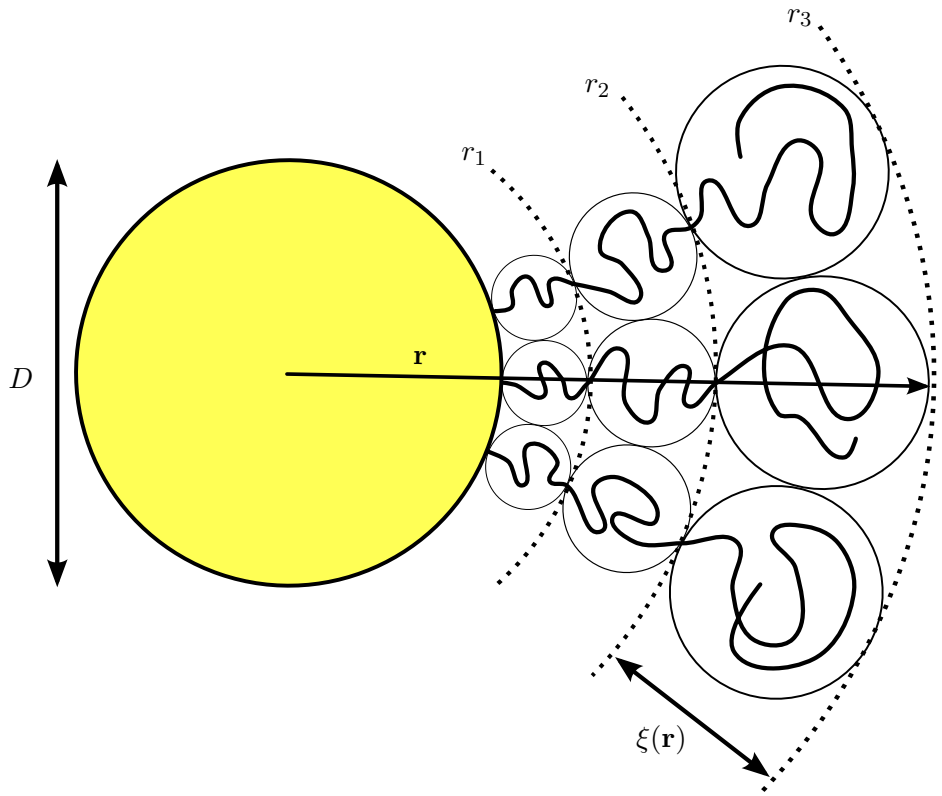


**Figure 7.3** Cross-section of a spherocylinder of diameter $D$ with grafted brush polymers. The blobs have a constant diameter $\xi$. The right side shows a magnification of the dashed lined area. For very short brushes the local curvature can be neglected.

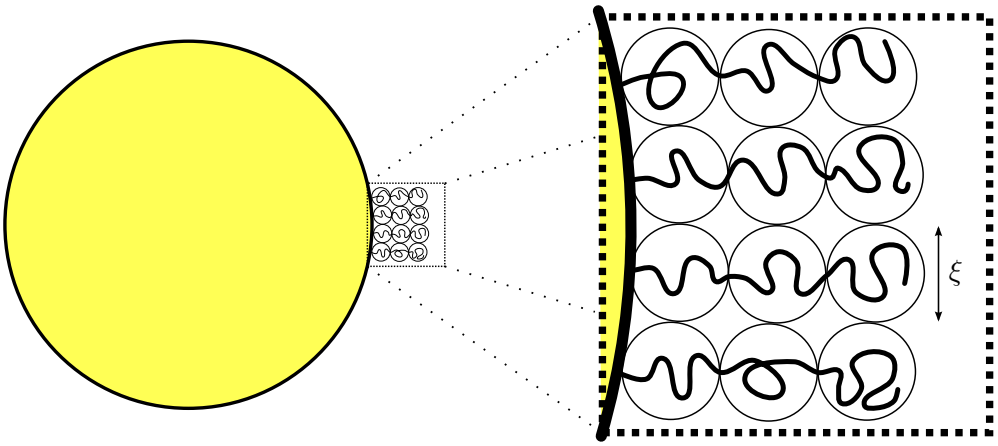

In the last step of the derivation we include the excess polymer. The use of a compressible polymer is possible but much more complicated and more assumptions and approximations are needed. Therefore, mainly to simplify the calculation, one assumption is that excess polymers between two brushes are not compressed but expelled. The excess polymers can then be characterized by their radius of gyration $R_g$. Another important assumption is that the excess polymer can be treated as dilute polymer solution. Otherwise, the used radius of gyration $R_g$ would have to be replaced by the correlation length $\xi_{corr}$ in the polymer system.

### 7.4.1 Alexander-de Gennes model

In the first step we describe the properties of two brushes attached to opposite, plane walls. In the Alexander-de Gennes [8, 64, 65, 66, 67] model for polymer brushes the chains of the brushes are represented by a series of blobs. To calculate the interaction between two tetrapod arms with grafted semiconducting block copolymers we first look at a system of two hard walls separated by a distance $D$. The polymers are grafted to the walls. The grafting points have a distance $d$ which is related to the grafting density $\sigma = 1/d^2$. The distance $d$ between the grafting points is much smaller than the radius of gyration of the polymers so all chains are completely stretched. Each brush polymer in total consists of $N$ monomers and has a height $h_0$ which is a multiple of the constant blob diameter $\xi$. Figure (7.4) shows a sketch of the system. Here the thickly drawn walls represent the surfaces of the tetrapod arms.

The number of blobs in one row is given by

$$n = D/\xi. \tag{7.17}$$

Each blob contains $m$ monomers and the blob diameter $\xi$ scales as

$$\xi = m^{\nu} \tag{7.18}$$

where the exponent $\nu$ equals 3/5, 1/2 or 1/3 for good, $\Theta$ and poor solvent, respectively.

The number of monomers per area can, thus, be expressed in two different ways. Firstly, it can be written as the total number of monomers of two chains $2N$ divided by the squared distance between two grafting points $d^2 = 1/\sigma$. Secondly, it is equal to the number of blobs $n$ times the number of monomers in a blob $m$ over the squared blob diameter $\xi^2$. These two equations have to be equal

$$\frac{2N}{d^2} = 2N\sigma \stackrel{!}{=} \frac{nm}{\xi^2}. \tag{7.19}$$

With Equations (7.17) and (7.18) we get

$$2N\sigma = \frac{nm}{\xi^2} = \frac{D}{m^{\nu}}\frac{m}{m^{2\nu}} = Dm^{1-3\nu}. \tag{7.20}$$

**Figure 7.4** System of polymer brushes attached to two plane walls. The walls are separated by a distance $D$. The polymers are characterized by their height $h_0$, the constant blob diameter $\xi$ and the grafting density $\sigma$.

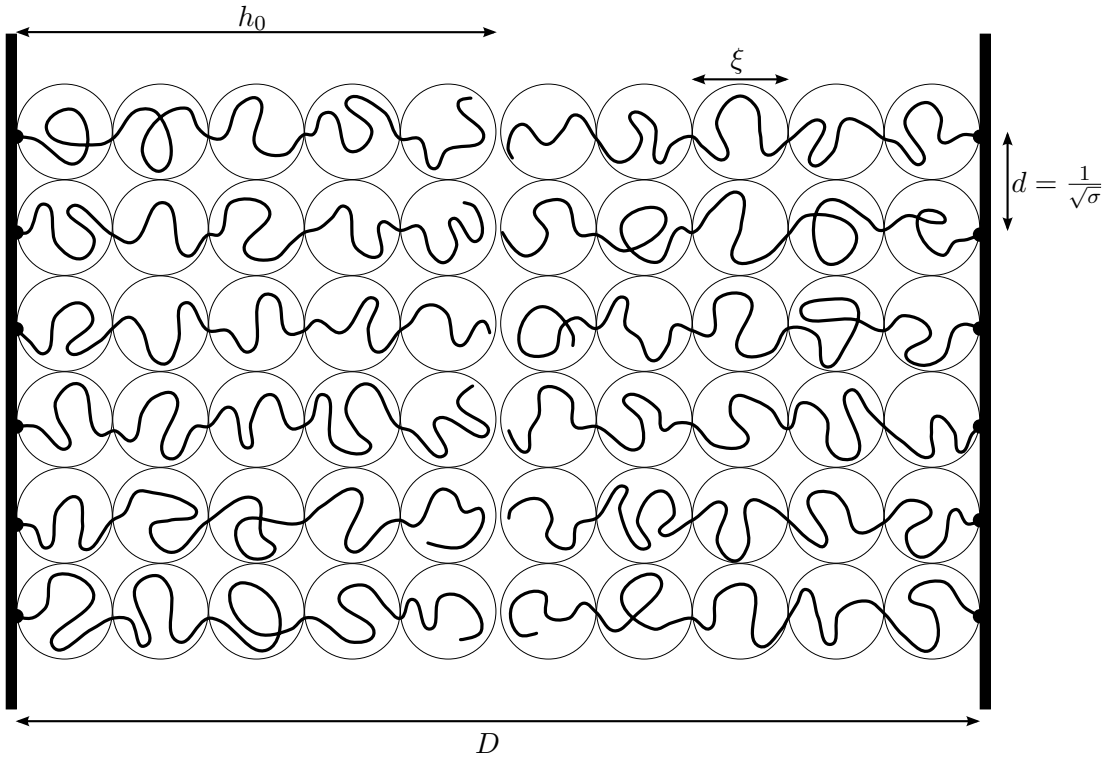


With this the number of monomers per blob $m$, the blob size $\xi$ and the number of blobs $n$ may be written as

$$m = \left(\frac{2N\sigma}{D}\right)^{\frac{1}{1-3\nu}} \tag{7.21}$$

$$\xi = \left(\frac{2N\sigma}{D}\right)^{\frac{\nu}{1-3\nu}} \tag{7.22}$$

$$n = D\left(\frac{2N\sigma}{D}\right)^{\frac{-\nu}{1-3\nu}}. \tag{7.23}$$

The free energy per blob is given by $1/\beta$ where $\beta = 1/k_\mathrm{B}T$ is the inverse temperature and $k_\mathrm{B}$ the Boltzmann constant. The free energy of the system of two brushes per area $A = \xi^2$ can then be calculated as

$$\frac{\beta\mathcal{F}_\mathrm{Brush}}{A} = \frac{n}{\xi^2} \tag{7.24}$$

$$= D\left(\frac{2N\sigma}{D}\right)^{\frac{-3\nu}{1-3\nu}}. \tag{7.25}$$

For a $\Theta$-solvent $\nu$ is $\frac{1}{2}$ and we get

$$\frac{\beta \mathcal{F}_{\text{Brush}}}{A} = D \left( \frac{2N\sigma}{D} \right)^3 \tag{7.26}$$

$$= (2N\sigma)^3 \frac{1}{D^2}. \tag{7.27}$$

With the definition that the force $F$ is the negative derivation of the free energy by the distance, one may compute the pressure $P$ as the force per area as

$$P = \frac{F}{A} = -\frac{\partial}{\partial D} \left( \frac{\mathcal{F}_{\text{Brush}}}{A} \right) = \frac{2\,(2N\sigma)^3}{\beta} \frac{1}{D^3}. \tag{7.28}$$

For free, uncompressed brushes we can use that the distance $D$ between the walls is equal to the height of the two brushes $2h_0$. Additionally, we can assume that the distance $d$ between the densely grafted chains determines the dimension of the blobs via $\sigma = d^{-2} = \xi^{-2}$. So we can compute

$$\sigma = \frac{1}{\xi^2} = \left( \frac{2N\sigma}{2h_0} \right)^{\frac{-2\nu}{1-3\nu}} = \left( \frac{N\sigma}{h_0} \right)^2 \tag{7.29}$$

which gives

$$h_0 = N\sigma^{\frac{1}{2}}. \tag{7.30}$$

This relation is in accordance with the predictions of Moh et al. [181] who investigate the scaling law for brushes experimentally. They find that the brush height scales as $\sigma^n$ where $n$ is 1/3 for good solvent, 1/2 for $\Theta$-solvent and 4/5 for poor solvent. The proportionality of the height $h_0$ to the number of monomers $N$ validates that the brushes are stretched. Otherwise, the height would scale with $N^\nu$ as its radius of gyration $R_{\text{g}}$.

Inserting (7.30) in (7.27) we get the free energy per area

$$\frac{\beta \mathcal{F}_{\text{Brush}}}{A} = \left( 2h_0 \sigma^{\frac{1}{2}} \right)^3 \frac{1}{D^2}. \tag{7.31}$$

In this case the pressure is

$$P = \frac{F}{A} = -\frac{\partial}{\partial D} \left( \frac{\mathcal{F}_{\text{Brush}}}{A} \right) = \frac{2}{\beta} \left( \frac{2h_0\sqrt{\sigma}}{D} \right)^3. \tag{7.32}$$

### 7.4.2 Asakura-Oosawa potential for parallel walls

In the second step we take the excluded volume effect and the resulting depletion interaction into account. The depletion force is described for the first time in 1954 by Asakura and Oosawa [14, 15]. Assume a system that contains particles of different sizes. If the distance between the larger particles becomes smaller than the size of the smaller particles there is an excluded volume which is not accessible to the smaller particles anymore. Thus, for entropic reasons, the larger particles tend to reduce their distance to each other. This effect can be expressed by an effective attractive force, the depletion force.

**Figure 7.5** The walls representing the tetrapod surfaces are separated by a distance $D$. The brushes have a height $h_0$.

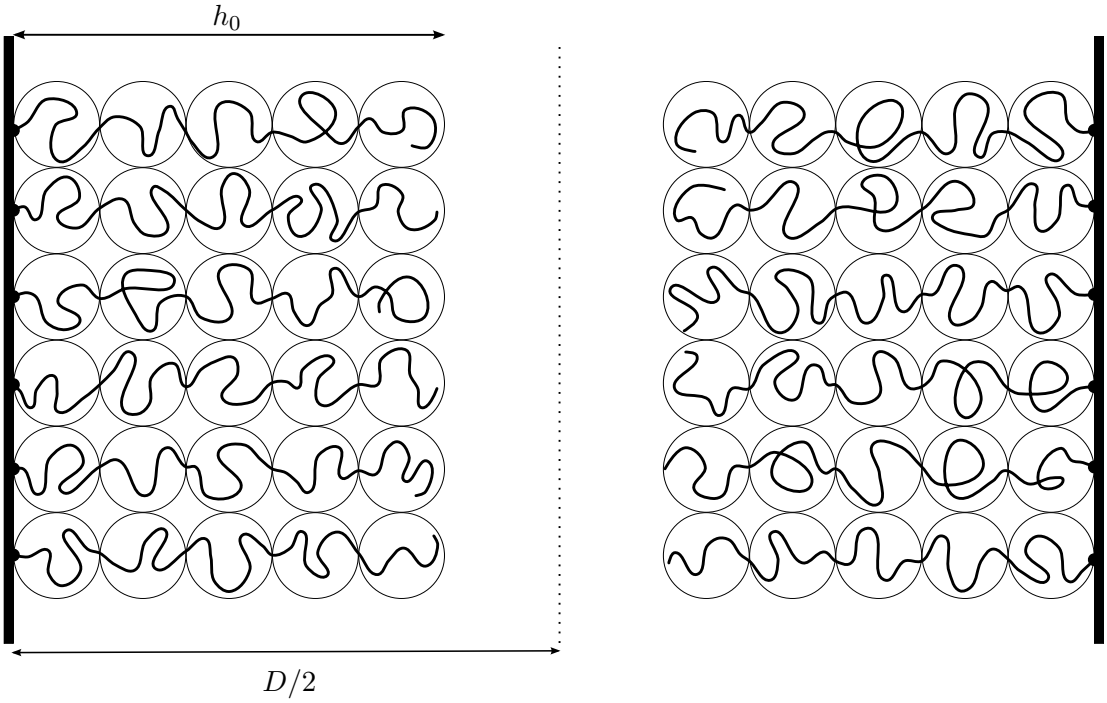


Following our assumptions we treat the surfaces of the spherocylinders as planar walls at a distance $D$. The brush polymers are fully stretched and have a height $h_0$ as displayed in Figure (7.5).

At first, we have to calculate the excluded volume for the polymer brushes. If the distance $D$ is infinite the excluded volume per area is simply

$$\frac{V_{\text{excl}}}{A} = 2h_0 \qquad \text{for } D \to \infty. \tag{7.33}$$

For a finite distance $D$ we get

$$\frac{V_{\text{excl}}}{A} = 2h_0 - 2(h_0 - D/2) = D \qquad \text{for } D > 2h_0. \tag{7.34}$$

The free energy is defined as

$$\mathcal{F}_{\text{AO}} = -k_{\text{B}}T \ln Z = -\frac{1}{\beta} \ln Z \tag{7.35}$$

where $\beta$ is the inverse temperature and $Z$ is the partition function. It is given by

$$Z = \frac{V_A^{N_{\text{P}}}}{N_{\text{P}}! \Lambda^{3N_{\text{P}}}} \tag{7.36}$$

in which $V_A$ is the volume accessible to the polymers, $N_{\text{P}}$ is the number of free polymers and $\Lambda$ is the thermal de Broglie wavelength

$$\Lambda = \frac{h}{\sqrt{2\pi m k_{\text{B}} T}} \tag{7.37}$$

where $h$ is the Planck constant. The volume accessible to the polymers $V_A$ is the difference of the systems volume $V$ and the excluded volume $V_{\text{excl}}$. So we can calculate the free energy as

$$\beta\mathcal{F}_{\text{AO}} = -\ln\left(\frac{(V - V_{\text{excl}})^{N_\text{P}}}{N_\text{P}!\Lambda^{3N_\text{P}}}\right) \tag{7.38}$$

$$= -N_\text{P}\ln\left(\frac{V - V_{\text{excl}}}{V}\right) - \ln\left(\frac{V^{N_\text{P}}}{N_\text{P}!\Lambda^{3N_\text{P}}}\right) \tag{7.39}$$

whereas the last term is the free energy of an ideal gas for $N_\text{P}$ particles

$$\mathcal{F}_{\text{ideal}} = -\frac{1}{\beta}\ln\left(\frac{V^{N_\text{P}}}{N_\text{P}!\Lambda^{3N_\text{P}}}\right). \tag{7.40}$$

In our case this contribution is constant and in particular, it does not depend on the distance $D$ between the walls. So we can write

$$\beta\mathcal{F}_{\text{AO}} = -N_\text{P}\ln\left(1 - \frac{V_{\text{excl}}}{V}\right) + \beta\mathcal{F}_{\text{ideal}}. \tag{7.41}$$

Using the relation

$$-\ln(1-x) = \sum_{k=1}^{\infty}\frac{x^k}{k} = x + \frac{x^2}{2} + \frac{x^3}{3} + \frac{x^4}{4} + \dots \tag{7.42}$$

this can be transformed to

$$\beta\mathcal{F}_{\text{AO}} = N_\text{P}\sum_{k=1}^{\infty}\frac{1}{k}\left(\frac{V_{\text{excl}}}{V}\right)^k + \beta\mathcal{F}_{\text{ideal}}. \tag{7.43}$$

Finally, we can approximate the free energy as

$$\beta\mathcal{F}_{\text{AO}} \approx \frac{N_\text{P}}{V}V_{\text{excl}} + \beta\mathcal{F}_{\text{ideal}} \tag{7.44}$$

$$= \rho_\text{P}V_{\text{excl}} + \beta\mathcal{F}_{\text{ideal}} \tag{7.45}$$

where we define the number density $\rho_\text{P}$ for the free polymers as

$$\rho_\text{P} = \frac{N_\text{P}}{V}. \tag{7.46}$$

Since we are only interested in the effective energy we can omit the constant contribution for the ideal gas and, with Equations (7.33) and (7.34), we get the effective free energy per area

$$\frac{\beta\mathcal{F}_{\text{AO}}}{A} = \begin{cases}\rho_\text{P}D & \text{for finite } D > 2h_0\\ \rho_\text{P}2h_0 & \text{for } D \to \infty\end{cases} \tag{7.47}$$

and the pressure

$$P = \frac{F}{A} = \begin{cases}-\frac{\rho_\text{P}}{\beta} & \text{for finite } D > 2h_0\\ 0 & \text{for } D \to \infty\end{cases}. \tag{7.48}$$

Note that, during the calculation of the free energy we make an approximation in Equation (7.44). Taking contributions of higher order of the series into account may increase the accuracy of the model. There are several other models which are more accurate than the Asakura-Oosawa model. For instance, Bolhuis et al. [31] specify accurate effective pair potentials for polymer solutions and Li and Ma [147] calculate the depletion interactions of two spherocylinders induced by a hard sphere fluid using Monte-Carlo simulations with the so-called acceptance ratio method. Very detailed information on the depletion interaction including the discussion of sophisticated method such as the Derjaguin approximation are given by Lekkerkerker and Tuinier [143].

### 7.4.3 Compressed brush

In this final step of the derivation we investigate the effect of the excess polymer on the polymer brush. Therefore, we allow a compression of the brush polymers but not of the excess polymers. This means that the brush height, which had a constant value of $h_0$ in the last two sections, now has a variable value labeled $h$. The excess polymers are characterized by their radius of gyration $R_\mathrm{g}$ which is assumed to be constant. A sketch of the system is shown in Figure (7.6).

**Figure 7.6** System of polymer brushes grafted to walls at distance $D$ and excess polymer. The excess polymers are incompressible and have a diameter of two times their radius of gyration $R_\mathrm{g}$. The height $h_0$ of the polymer brushes can now be reduced to a lower height $h$.

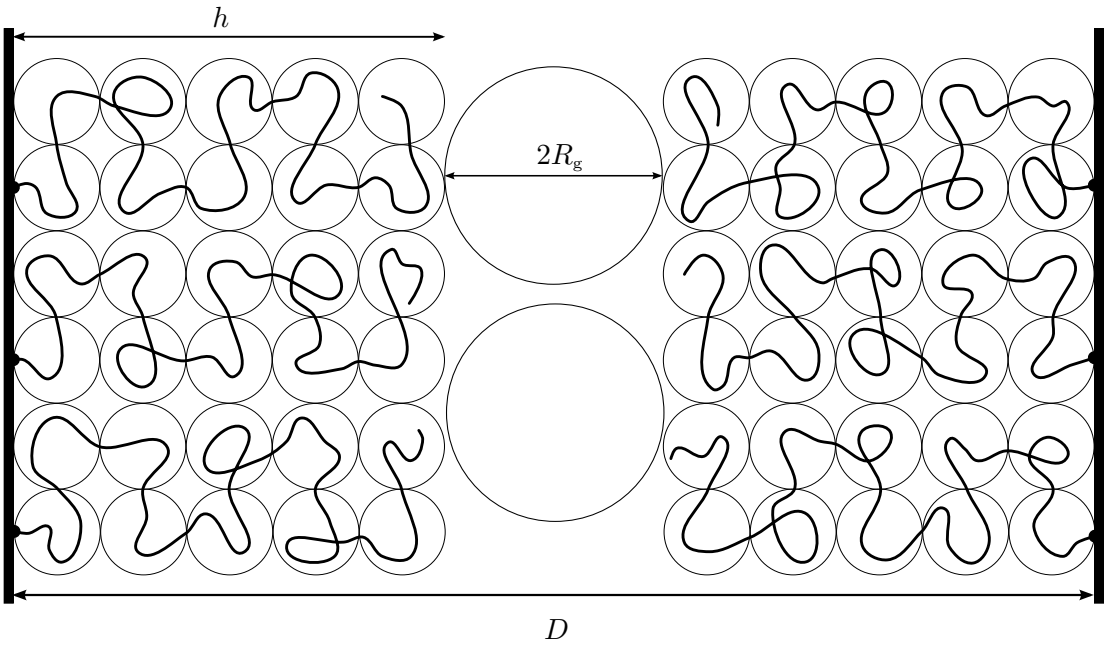

The two new parameters have to be considered in the two free energy contributions of our system. Hence, we replace $D$ with $2h$ in Equation (7.31) and include the radius of gyration $R_\mathrm{g}$ in Equation (7.47). So they become

$$\frac{\beta\mathcal{F}_\mathrm{Brush}}{A} = 2h_0\sigma^{3/2}\left(\left(\frac{h_0}{h}\right)^2 - 1\right) \text{ for } h < h_0 \tag{7.49}$$

which is adjusted to have a cutoff at $h_0$ and

$$\frac{\beta\mathcal{F}_\mathrm{AO}}{A} = \begin{cases} \rho_\mathrm{P} D & \text{for } 2h < D < 2h + 2R_\mathrm{g} \\ \rho_\mathrm{P}(2h + 2R_\mathrm{g}) & \text{for } D > 2h + 2R_\mathrm{g} \end{cases}. \tag{7.50}$$

The total free energy $\mathcal{F}_\mathrm{tot}$ is the sum of these two contributions. In the next step we have to minimize the total free energy with respect to $h$

$$\frac{\beta\mathcal{F}_\mathrm{tot}}{A} = \left.\frac{\beta\mathcal{F}_\mathrm{Brush} + \beta\mathcal{F}_\mathrm{AO}}{A}\right|_{\text{minimal for } h=h'}. \tag{7.51}$$

For this purpose, we derive the total free energy by $h$, set it to zero and evaluate it at $h = h'$. This way we get

$$\left.\frac{\partial}{\partial h}\left(\frac{\beta\mathcal{F}_\mathrm{tot}}{A}\right)\right|_{h=h'} = 0 = -4\sigma^{3/2}\left(\frac{h_0}{h'}\right)^3 + 2\rho_\mathrm{P}\begin{cases} 0 & \text{if } D < 2h' + 2R_\mathrm{g} \\ 1 & \text{if } D > 2h' + 2R_\mathrm{g} \end{cases}, \tag{7.52}$$

which can be transformed to

$$0 = -2\sigma^{3/2}\left(\frac{h_0}{h'}\right)^3 + \rho_\mathrm{P}\begin{cases} 0 & \text{if } h' > \frac{D}{2} - R_\mathrm{g} \text{ and } h' < h_0 \quad \text{(I)} \\ 1 & \text{if } h' < \frac{D}{2} - R_\mathrm{g} \text{ and } h' < h_0 \quad \text{(II)} \end{cases}. \tag{7.53}$$

If we want to solve this equation we have to distinguish between the two cases labeled (I) and (II). In the first case (I) $2h < D < 2h + 2R_\mathrm{g}$, Equation (7.53) has no solution and $h' = \min(h_0, \frac{D}{2})$. So we have to tell apart two subcases. If $D$ is smaller than $2h_0$ then $h$ equals $\frac{D}{2}$ otherwise $h$ is equal to $h_0$ and we get

$$\frac{\beta\mathcal{F}_\mathrm{tot}}{A} = \begin{cases} \rho_\mathrm{P} D + 2h_0\sigma^{3/2}\left(\left(\frac{2h_0}{D}\right)^2 - 1\right) & \text{for } D < 2h_0 \\ \rho_\mathrm{P} D & \text{for } D > 2h_0 \end{cases} \tag{7.54}$$

In the second case (II) $D$ is greater than $2h + 2R_\mathrm{g}$. Solving Equation (7.53) for this case results in

$$\rho_\mathrm{P} = 2\sigma^{3/2}\left(\frac{h_0}{h'}\right)^3 \tag{7.55}$$

which can be rewritten as

$$\left(\frac{h'}{h_0}\right)^3 = \frac{2\sigma^{3/2}}{\rho_\mathrm{P}}. \tag{7.56}$$

We define this ratio of $h'$ over $h_0$ as $\kappa$ which is related to the compression of the brush

$$\kappa := \frac{h'}{h_0} = \sqrt{\sigma}\sqrt[3]{\frac{2}{\rho_\mathrm{P}}}. \tag{7.57}$$

Since Equation (7.53) is only valid for $h' < h_0$ this ratio is smaller than one. For the case that $h'$ becomes bigger than $h_0$ we set $\kappa$ to one.

There are again two subcases. In the first case $h'$ is smaller than $h_0$ and, therefore, $\kappa$ is smaller than 1. In this case $h = \min(h_0, h') = \min(h_0, \kappa h_0) = \kappa h_0 = h'$ and the free energy reads

$$\frac{\beta \mathcal{F}_{\text{tot}}}{A} = \rho_{\text{P}} h' \left(3 - \left(\frac{h'}{h_0}\right)^2\right) + 2\rho_{\text{P}} R_{\text{g}} \tag{7.58}$$

$$= \rho_{\text{P}} \kappa h_0 \left(3 - \kappa^2\right) + 2\rho_{\text{P}} R_{\text{g}}. \tag{7.59}$$

If $h' > h_0$ the value of $\kappa$ would be bigger than one. In this case $h' = h_0$ and so $\kappa$ is equal to one and the free energy becomes

$$\frac{\beta \mathcal{F}_{\text{tot}}}{A} = 2\rho_{\text{P}} \left(h_0 + R_{\text{g}}\right). \tag{7.60}$$

With these results for different cases we can calculate the total free energy of our system for all distances. If we want to write the free energy as a function of the distance we have to distinguish between dense and dilute brushes.

For dilute brushes $h'$ is smaller than $h_0$ or in other words $\kappa$ is smaller than one. There are two subcases we have to distinguish. In the first case $h_0 < h' + R_{\text{g}}$ or $1 - \kappa < R_{\text{g}}/h_0$. In this case the total free energy per area can be expressed as

$$\frac{\beta \mathcal{F}_{\text{tot}}}{A} = \begin{cases} \rho_{\text{P}} D + 2h_0 \sigma^{3/2} \left(\left(\frac{2h_0}{D}\right)^2 - 1\right) & \text{for } D < 2h_0 \\ \rho_{\text{P}} D & \text{for } 2h_0 < D < 2h' + 2R_{\text{g}} \\ \min \begin{cases} \rho_{\text{P}} D \\ \rho_{\text{P}} h' \left(3 - \kappa^2\right) + 2\rho_{\text{P}} R_{\text{g}} \end{cases} & \text{for } D > 2h' + 2R_{\text{g}} \end{cases}. \tag{7.61}$$

If $h_0 > h' + R_{\text{g}}$ or $1 - \kappa > R_{\text{g}}/h_0$ the formula becomes slightly more complicated. In this second case the total free energy per area is

$$\frac{\beta \mathcal{F}_{\text{tot}}}{A} = \begin{cases} \rho_{\text{P}} D + 2h_0 \sigma^{3/2} \left(\left(\frac{2h_0}{D}\right)^2 - 1\right) & \text{for } D < 2h' + 2R_{\text{g}} \\ \min \begin{cases} \rho_{\text{P}} D + 2h_0 \sigma^{3/2} \left(\left(\frac{2h_0}{D}\right)^2 - 1\right) \\ \rho_{\text{P}} h' \left(3 - \kappa^2\right) + 2\rho_{\text{P}} R_{\text{g}} \end{cases} & \text{for } 2h' + 2R_{\text{g}} < D < 2h_0 \\ \min \begin{cases} \rho_{\text{P}} D \\ \rho_{\text{P}} h' \left(3 - \kappa^2\right) + 2\rho_{\text{P}} R_{\text{g}} \end{cases} & \text{for } D > 2h_0 \end{cases}. \tag{7.62}$$

Following Equation (7.56) the condition $h' < h_0$ for dilute brushes is only possible if

$$\sigma^{-\frac{3}{2}} = \xi^3 \gtrsim \frac{1}{\rho_{\text{P}}}. \tag{7.63}$$

Hence, the volume of a blob in the brush is greater than the volume per polymer in the bulk. In this case the polymers will start to penetrate the brushes and our

assumptions are not valid anymore. Therefore, we can assume that the brushes are dense, that is, $h'$ is greater than $h_0$ so we get $\kappa > 1$. Setting $\kappa$ to one gives

$$\frac{\beta \mathcal{F}_{\text{tot}}}{A} = \begin{cases} \rho_{\text{P}} D + 2h_0 \sigma^{3/2} \left( \left( \frac{2h_0}{D} \right)^2 - 1 \right) & \text{for } D < 2h_0 \\ \rho_{\text{P}} D & \text{for } 2h_0 < D < 2h_0 + 2R_{\text{g}} \\ \rho_{\text{P}} (2h_0 + 2R_{\text{g}}) & \text{for } D > 2h_0 + 2R_{\text{g}} \end{cases} . \tag{7.64}$$

With Equations (7.61), (7.62) or (7.64) we can compute the total free energy per area for systems with different brush densities and system parameters. Since we assume that the brushes are dense in the systems we investigate we use Equation (7.64) in our simulations. Nevertheless, Equations (7.61) and (7.62) for dilute brushes are also implemented. For simulations of tetrapods without polymer brushes we set the height of the polymer brushes $h_0$ to zero. Two sample effective free energies for interactions with and without polymer brushes are plotted in Figure (7.7). The parameters are chosen to be close to the values used in our simulations. Figure (7.7a) shows the free energy from Equation (7.64) with polymer brushes of height $h_0 = 2$ and a radius of gyration $R_{\text{g}}$ equal to two. The grafting density $\sigma$ is set to 0.2 and $\rho_{\text{P}}$ to 0.005. The first region for $D < 2h_0$ reflects the repulsive interaction due to the polymer brushes. The green region ends at $D = 2h_0 + 2R_{\text{g}}$ and represents the attractive depletion interaction. For greater distances the interaction is constant. All sections of the interaction are shifted by this constant so the interaction becomes zero for great distances. The second plot in Figure (7.7b) demonstrates the behavior for a system without polymer brushes, that is, for $h_0 = 0$. Therefore, the repulsive brush interaction, that is, the red part of the first plot, vanishes. For distances smaller than $2R_{\text{g}}$ the energy increases constantly. For bigger distances the energy is zero.

As mentioned before one of our assumptions is that the excess polymer is not compressed. Nevertheless, one could calculate the free energy for a system with compressible excess polymer. In this case we expect a free energy with a very similar behavior. As the division into several regions can be omitted in this case the edges at the transitions are rounded and the whole function will be much smoother. But there are a few complications in that derivation which we will not mention here in detail. Further, some more assumptions and approximations have to be made and it has to be checked if they are applicable. Anyway, this is not within the scope of this thesis and it is the task of future work to determine the behavior of a system containing compressible excess polymer exactly. We will stick to the model derived for not compressible excess polymer in this thesis.

**Figure 7.7** Plots of the total free energy per area as given in Equation (7.64). In both cases $R_g$ equals two, $\sigma$ is 0.2, $\rho_P$ is set to 0.005 and the functions are shifted by the constant (blue) value so the energy becomes zero for big distances. (a) With polymer brushes of height $2h_0 = 4$. The red part shows the repulsion of the brushes, the green line the attractive depletion interaction. (b) Without brushes, that is, $h_0 = 0$ only the attractive depletion interaction is left.

**(a)**

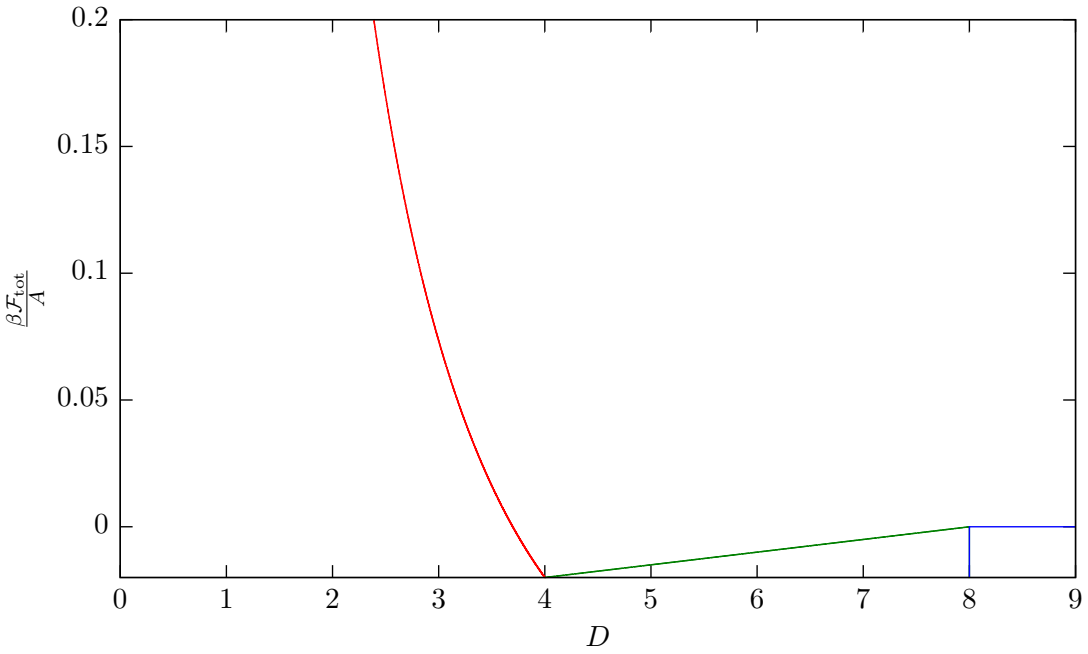


**(b)**

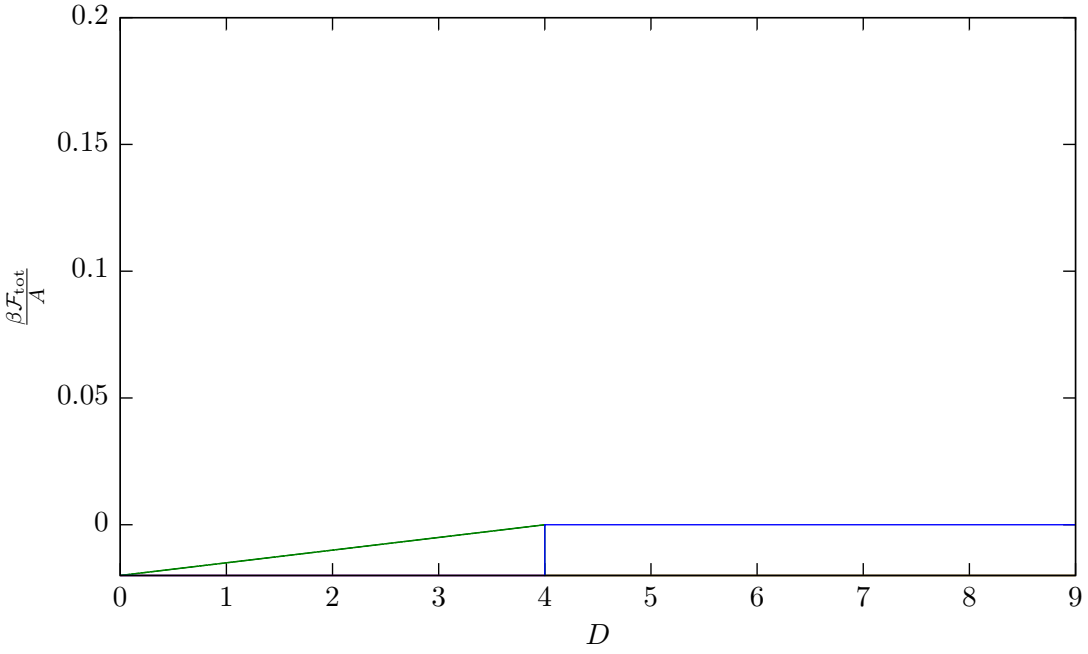

## 7.5 Fluctuating volume

So far the volume has been constant in all our systems. Now we introduce an algorithm to allow a fluctuating box volume $V_{\mathrm{Box}}$ and perform simulations in the $NPT$-Ensemble.

In order to adapt the volume of the simulation box we allow volume breath moves. These volume moves are not performed at each Monte-Carlo step but only every $k$-th step. In most cases $k$ is set to fifty in order to prevent a slowdown of the simulation due to the additional computing time this move needs.

During each volume step we rescale the simulation box by a factor $\gamma$ which may be positive or negative. The size of the simulation box is changed uniformly by the same factor in all three spatial dimensions. The length $L$ of each side of the simulation box is rescaled to $L'$ according to the relation

$$L' \to L + \gamma. \tag{7.65}$$

Further, all $i$ components of the particle positions $\mathbf{x}$ are recalculated using

$$\mathbf{x}_i' \to \frac{\mathbf{x}_i}{L} L' = \mathbf{x}_i \left(1 + \frac{\gamma}{L}\right). \tag{7.66}$$

If we vary the volume the energy of the system changes, too. The energy change with the fluctuating volume $V$ is taken into account by the volume energy

$$\mathcal{H}_{\mathrm{Volume}} = P V_{\mathrm{Box}} - N_{\mathrm{T}} T \log(V_{\mathrm{Box}}). \tag{7.67}$$

We calculate the energies of the whole system before and after each volume move. Depending on the energy change the volume move is accepted or rejected. Whenever the volume is changed we also check if the box still has its minimal size of three times the size of a tetrapod.

A test of this algorithm can be found in Appendix B.1. Note that the volume moves are not applicable to the system of rod-coil block copolymers introduced in Part I since the size of the grid must stay constant for this model. If we change the volume we also would have to rescale the grid and all related energies.

## 7.6 Parameters

Our main goal is to reproduce the results found by Lim et al. [151]. Therefore, we set the parameters to the experimental values. In this section we introduce these parameters.

At first we show how the length and diameter are obtained. Therefore, the projection length $L^*$ and the diameter $D$ are measured from transmission electron microscopy images as shown in Figure (7.8). Using simple trigonometry the arm length $L$ and the total height of the tetrapod $L'$ are calculated. The results are summarized in Table (7.1).

With the experimental values for the density and the specific volume of the CdSe tetrapods $\rho_{\mathrm{CdSe}} = 5.82\,\mathrm{g/\,cm^3}$ and $v_{\mathrm{CdSe}} = 1/\rho_{\mathrm{CdSe}} = 0.172\,\mathrm{cm^3/\,g}$, respectively, and $\rho_{\mathrm{PMMA}} = 1.190\,\mathrm{g/\,cm^3}$ and $v_{\mathrm{PMMA}} = 0.840\,\mathrm{cm^3/\,g}$ for the excess polymer, we can transform the wt% values from the experiments to a volume ratio $\alpha$. This ratio specifies how much more volume the excess polymer occupies compared to the volume of the tetrapods

$$V_{\mathrm{Polymer}} = \alpha V_{\mathrm{CdSe}}. \tag{7.68}$$

**Figure 7.8** Cartoon to show how the length and diameter for the simulations are obtained from transmission electron microscopy images. The diameter $D$ and the projection length $L^*$ can be measured directly. With this we can calculate the total height $L'$ and the arm length $L$.

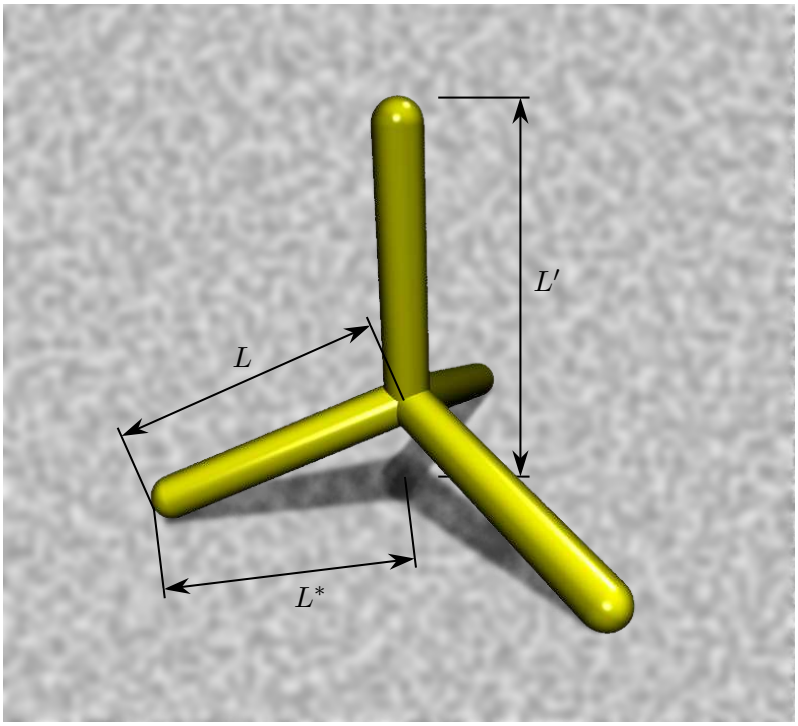


**Table 7.1** Length $L^*$ and diameter $D$ as measured from transmission electron microscopy images. The arm length $L$ and the total tetrapod height $L'$ are calculated values. All lengths are given in nanometers.

| $L^*$ | $D$ | $L$ | $L'$ |
|---|---|---|---|
| 40.0 | 6.1 | 42.4 | 56.6 |
| 67.1 | 5.8 | 71.2 | 95.0 |
| 103.0 | 10.4 | 109.3 | 145.8 |

The computed values for $\alpha$ are listed in Table (7.2). With this we can easily calculate the number density of the free polymers $\rho_{\mathrm{P}}$.

The hydrodynamic radius $R_{\mathrm{H}}$, which is closely related to the radius of gyration $R_{\mathrm{g}}$ [133], is specified to lie between 2 and 2.5 nanometers. Since the same polymer is used for the excess polymer and the brushes it is assumed that the brush height $h_0$ has approximately the same value. The grafting density $\sigma$ is estimated to be about $0.2\,\mathrm{nm}^{-2}$.

**Table 7.2** Calculated volume ratio $\alpha$ of excess polymers to tetrapods for different polymer to tetrapods ratios (wt%).

| wt% | 50:50 | 70:30 | 90:10 |
|---|---|---|---|
| $\alpha$ | 4.9 | 11.4 | 44.0 |

## 7.7 Observables

As the tetrapods have no preferred orientation we have to use alternate observables. To determine how strong the tetrapods cluster we mainly use the distances between the tetrapods. The most important distance on this occasion is the average squared minimum distance between the tetrapod arms $\langle D^2 \rangle$. For this purpose, the arms of the tetrapods are treated as spherocylinders and the individual shortest distances are computed using the shortest distance algorithm for spherocylinders introduced in Part I. The minimum distance between two arms may be small even though the centers of the tetrapods have a much greater distance. Therefore, we introduce another parameter which is the average squared minimum distance between the tetrapod centers $\langle C^2 \rangle$. This parameter may be related to the stacking of the tetrapods.

In order to compare systems with and without grafted brush polymers we need further observables. Using the average squared minimum distances defined above we can define two ratios between a hybrid and a blend system. The first one is the ratio between the average squared minimum distances between the centers

$$\mu = \frac{\langle C^2_{\text{hybrid}} \rangle}{\langle C^2_{\text{blend}} \rangle} \tag{7.69}$$

which indicates how much further the centers are from each other for the hybrid model compared to the blend model. The second ratio is

$$\nu = \frac{\langle D^2_{\text{hybrid}} \rangle}{\langle D^2_{\text{blend}} \rangle} \tag{7.70}$$

and reflects the growth of the average shortest distance between the tetrapod arms when the polymer brushes are grafted onto the tetrapod surface. Thus, these two ratios can also be used to determine the efficiency of the polymer brushes to reduce clustering.

Chapter 8

# Results

**Contents**



In this chapter we present some results for the simulations of tetrapods with and without grafted polymer brushes. We demonstrate that the aggregation of the blends is reduced for the hybrids. Further, we present some results for systems with fluctuating volume at constant pressure.

## 8.1 First simulation results

In a first test of our model we simulate 200 tetrapods in a simulation box with a size of $189 \times 379 \times 379\,\mathrm{nm}^3$ with periodic boundary conditions. The size of the box is chosen to be at least three times the total length of a tetrapod in all three spatial dimensions. In these simulations the tetrapods have an arm length of 42 nm and a diameter of 5 nm. The excess polymers have radius of gyration equal to two nanometers and a number density $\rho_\mathrm{P} = 0.0018\,\mathrm{nm}^{-3}$. The brush height is set to two nanometers and the grafting density of the brush polymers $\sigma$ is $0.23\,\mathrm{nm}^{-2}$. These values are chosen in analogy to the related experiments. The parameter $\alpha$ is set to 4.88 which is the equivalent to 50:50 wt%. The initial configuration is set up in an aligned and ordered manner. Figure (8.1) shows the result of two exemplary simulation runs. Figure (8.1a) displays the average squared minimum distance $\langle D^2 \rangle$ for the first 10000 of one million steps. In the further course the graph does not change anymore so the final steps are omitted. Starting from the same configuration, we clearly see that the distance increases for hybrids while it decreases for blends. The equilibrium distances are already reached after several hundred steps. The decrease of $\langle D^2 \rangle$ for the uncoated tetrapods indicates a clustering of the tetrapods. This is also clearly visible in the rendered image of the final configuration displayed in Figure (8.1b). Whereas the distance $\langle D^2 \rangle$ increases for the coated tetrapods which are much better dispersed as the final configuration shown in Figure (8.1c) demonstrates.

**Figure 8.1** (a) Average squared minimum distance between tetrapod arms. Only the first 10000 steps are shown on a logarithmic scale. (b) Final configuration for the uncoated system. Clusters are visible. (c) Final configuration for the coated system. The tetrapods are spread more homogeneously. In both images the tetrapods in the posterior half of the simulation box are displayed in light gray.

**(a)**

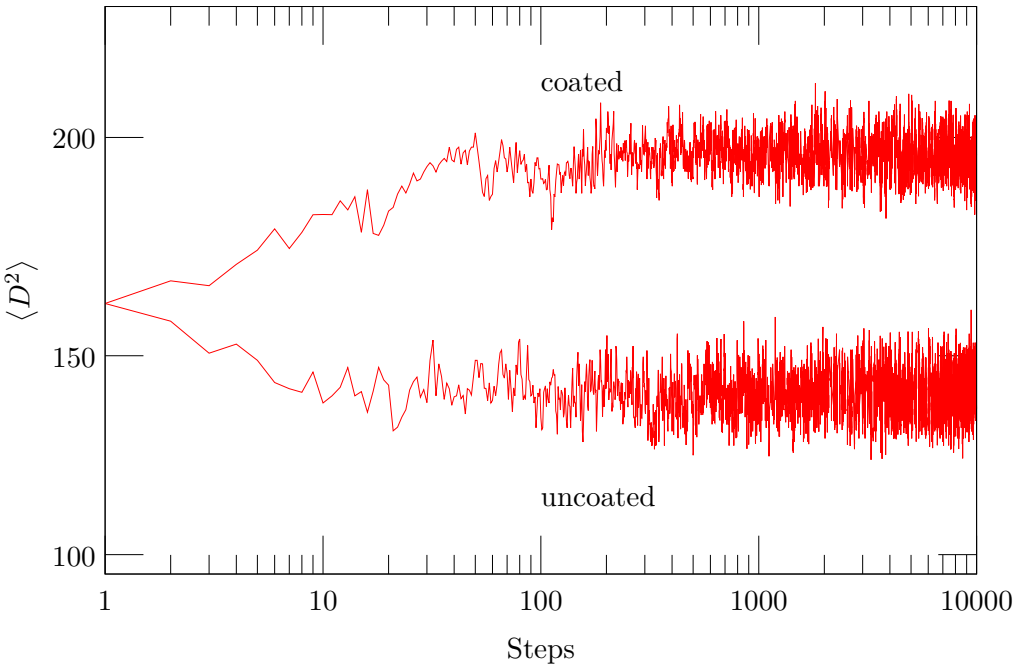


**(b)**

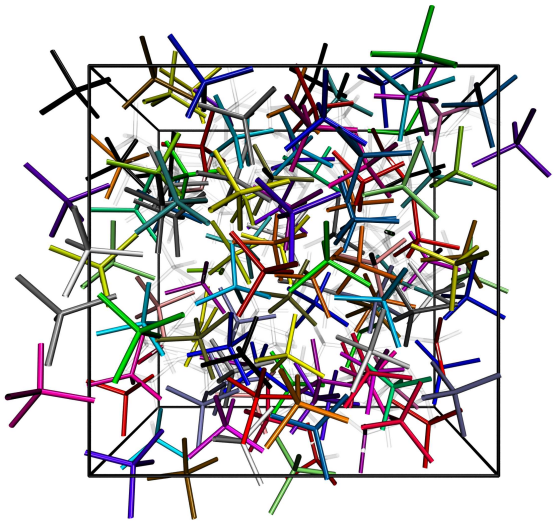

**(c)**

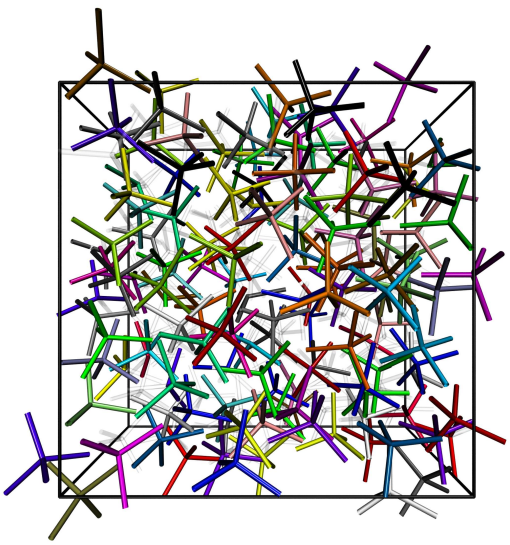

## 8.2 Further results

In the following, we present some results for different systems containing tetrapod/polymer mixtures. For the simulations we use the parameters presented in Section 7.6. All systems contain 300 tetrapods and are started once with and once without grafted polymer brushes. This way we can compare blend and hybrid systems. The initial configuration is set up in an ordered manner, that is, all tetrapods have the same orientation but their positions are chosen randomly. The simulation boxes are cubic and have side lengths between 363 and 1569.

At first we compare the ratios $\mu$ and $\nu$ for the investigated systems. Plots for both ratios are illustrated in Figure (8.2). The differently colored lines represent simulations with diverse volume ratios between excess polymers and tetrapods.

The plot of the ratio $\mu$ in Figure (8.2a) shows that the centers of the tetrapods move further apart if polymer brushes are added to the surface of the tetrapod arms. It is visible that this effect is stronger for more dilute systems. We can further observe that the effect decreases if the arm length increases.

Both observations are even more obvious in Figure (8.2b) showing the plot of the ratio $\nu$ of the average squared minimum distance between the tetrapod arms $\langle D^2 \rangle$. We clearly see that the tetrapods move further apart if brush polymers are coated. The effect again decreases with tetrapod density and arm length. Figures (8.2c) and (8.2d) show the results for two further systems with identical parameters but 200 and 400 tetrapods, respectively. We see that the effect is weaker in both cases but reflects the same tendencies. In addition, the effect is not as dominant as in the simulation shown in Figure (8.1) where slightly different parameters were used. Therefore, we may conclude that there seems to be a preferable tetrapod density for which the effect of coating is most dominant. The simulations with fluctuating volume in the following section may help to find this density.

Figures (8.3) to (8.5) show rendered snapshots of the final configurations of the simulations with 300 tetrapods. These images may be compared to the experimental results for comparable systems displayed in Figures (6.8) to (6.10). For better comparability the images in the figures are arranged in the same pattern. Note that the transmission electron microscopy images only show a thin layer of the system and our simulations use a three-dimensional simulation box with periodic boundary conditions. In order to emulate this effect without losing the additional information we get from the depth of the representation we use an orthographic projection and depth cueing when we render the images in VMD [120].

**Figure 8.2** Plots of the ratios $\mu$ and $\nu$ for systems with three different tetrapod arm lengths and three volume ratios of excess polymers to tetrapods, which are represent by the colored lines. (a) The ratio $\mu$ of the average squared minimum distances between the centers of the tetrapods decreases with increasing arm length and density. (b) For the ratio $\nu$ of the average squared minimum distances between the tetrapod arms this trend is even more dominant. (c, d) $\nu$ for systems with the same parameters as (b) but with (c) 200 and (d) 400 tetrapods.

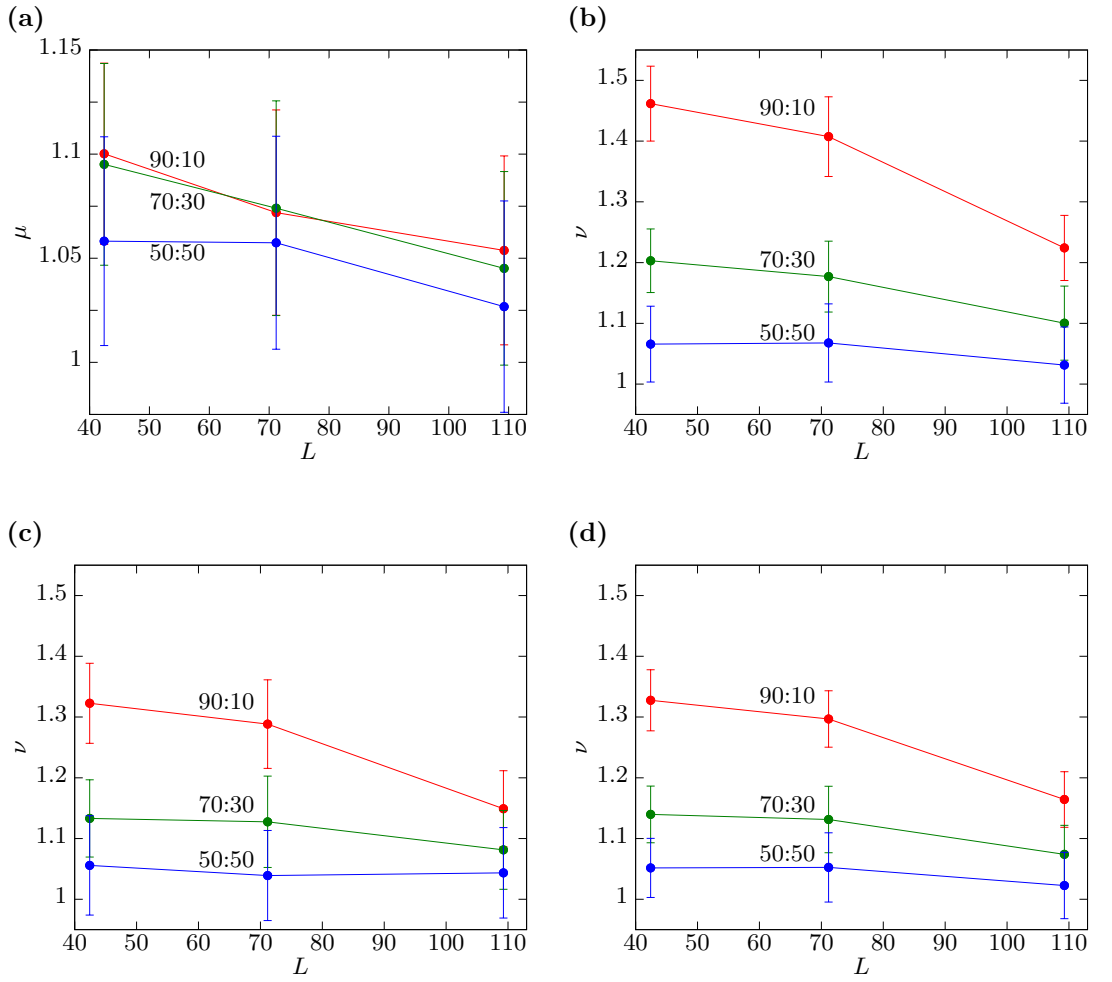

Figure (8.3) illustrates the simulation results for tetrapods with an arm length equal to 42.4 nanometers. The rendered images show hybrid and blend systems with volume ratios between the excess polymer and the tetrapods of 50:50, 70:30 and 90:10 wt%. As in the experimental images displayed in Figure (6.8) we see that the clustering is reduced if polymer brushes are added to the surface of the tetrapod arms. As for the experimental results the difference is hardly noticeable for dense systems as the comparison of Figure (8.3a) and Figure (8.3d) demonstrates. For a volume ratio of 70:30 wt% we see that the tetrapods are more equally distributed in Figure (8.3b) than in Figure (8.3e). While we see a strong clustering in Figure (8.3f) for the blend model, the addition of polymer brushes to the surface of the tetrapods leads to a more uniform distribution as illustrated in Figure (8.3c).

**Figure 8.3** Snapshots for tetrapods with an arm length of 42.4 nm. (a)-(c) show the results for the hybrid model and (d)-(f) for the blend model. The volume ratio between excess polymer and tetrapods is 50:50 for (a) and (d), 70:30 for (b) and (e) and 90:10 wt% for (c) and (f). The final configurations of the simulations can be compared to the experimentally obtained transmission electron microscopy images for matchable systems in Figure (6.8).

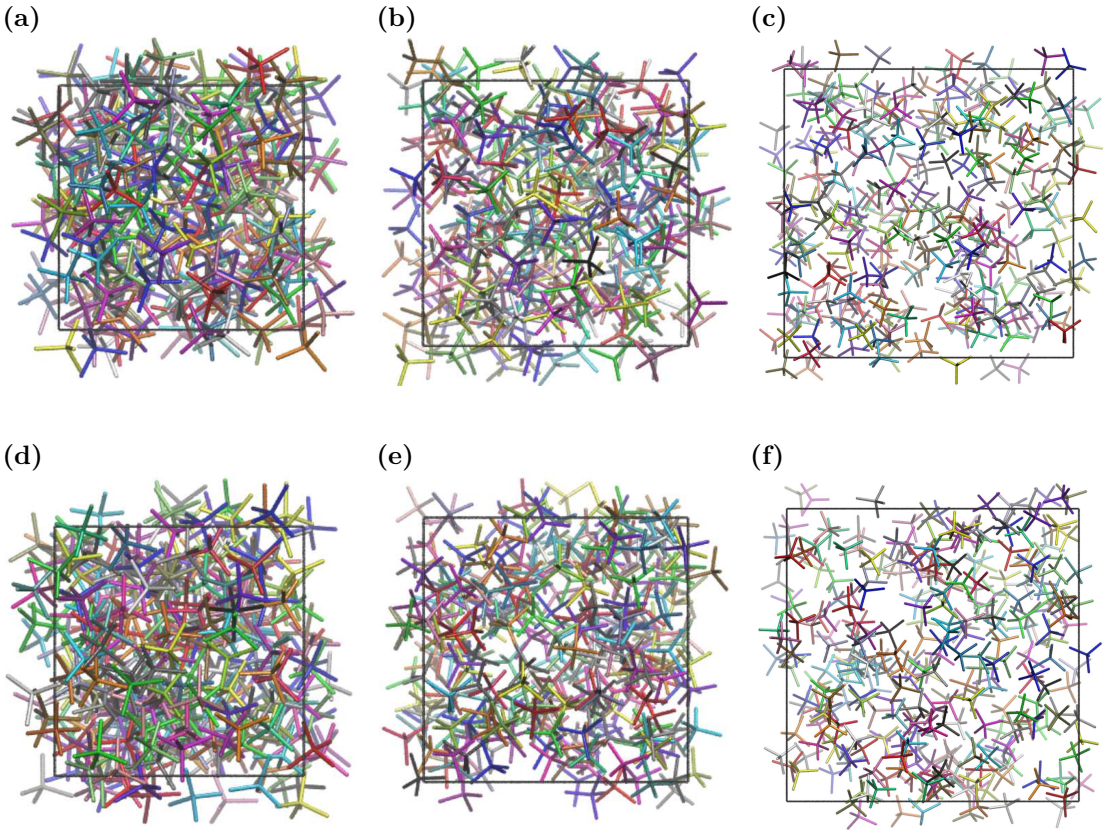

If we compare the experimental results in Figure (6.9) of tetrapods with arm lengths of 71.2 nanometers with our simulation snapshots displayed in Figure (8.4) we already notice that the clustering in our model is not as distinct as in the experimental system. Nevertheless, we still see that the effect of coating is the least noticeable for systems with a high tetrapod volume ratio as Figures (8.4a) and (8.4d) demonstrate. For a lower tetrapod volume ratio we can identify regions in Figure (8.4e) for which the tetrapods strongly interdigitate. As Figure (8.4b) illustrates this is reduced in the hybrid model. A similar effect is visible in Figures (8.4c) and (8.4f) for systems with a 90:10 volume ratio between excess polymer and tetrapods.

**Figure 8.4** Snapshots for tetrapods with an arm length of 71.2 nm. (a)-(c) show the results for the hybrid model and (d)-(f) for the blend model. The volume ratio between excess polymer and tetrapods is 50:50 for (a) and (d), 70:30 for (b) and (e) and 90:10 wt% for (c) and (f). The final configurations of the simulations can be compared to the experimentally obtained transmission electron microscopy images for matchable systems in Figure (6.9).

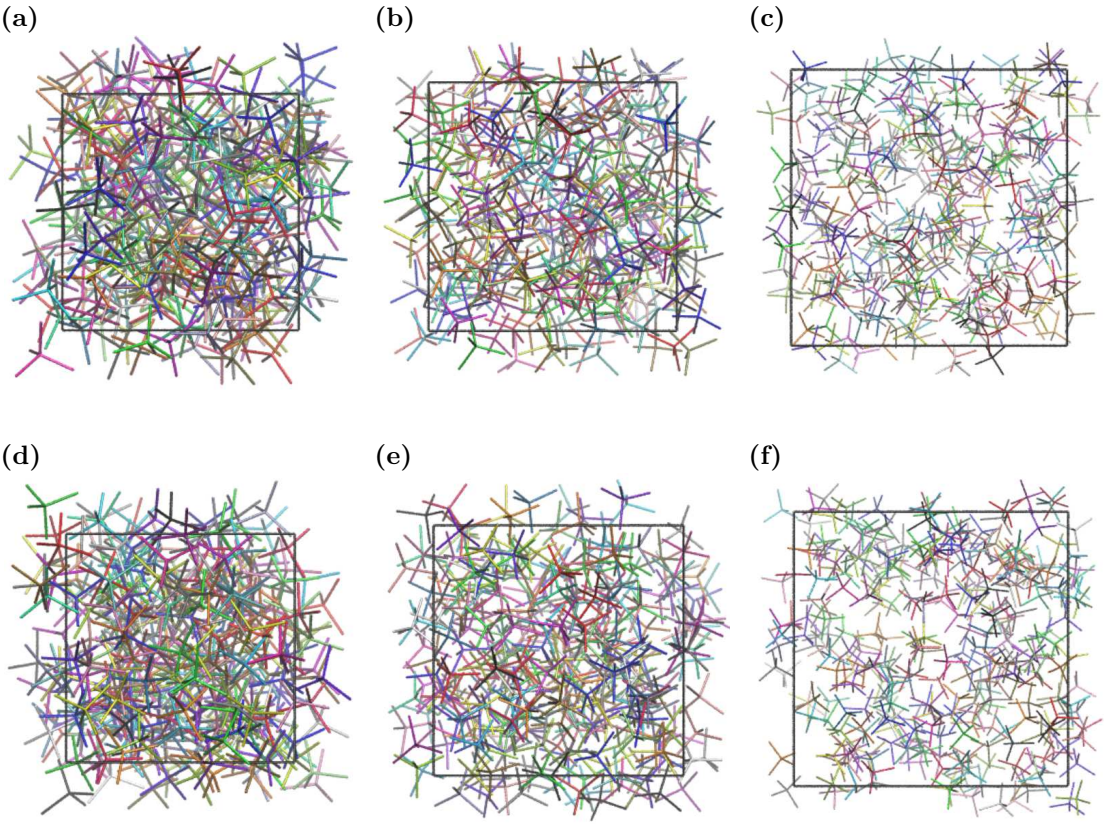

In Figure (8.5) we observe clustering for all systems with arm lengths of 109.3 nanometers. If we look at the experimental results displayed in Figure (6.10) we would expect a much stronger clustering for this arm length. We still can see that the strong clustering in Figure (8.5d) is slightly reduced in the hybrid model in Figure (8.5a) for a volume ratio of 50:50. For a lower tetrapod volume ratio the effect is somewhat more dominant as the comparison of Figures (8.5b) and (8.5e) demonstrates. While some tetrapods strongly interdigitate in the blend model as Figure (8.5f) shows, the snapshot in Figure (8.5c) illustrates that the tetrapods are distributed more equally if they are coated with polymers.

**Figure 8.5** Snapshots for tetrapods with an arm length of 109.3 nm. (a)-(c) show the results for the hybrid model and (d)-(f) for the blend model. The volume ratio between excess polymer and tetrapods is 50:50 for (a) and (d), 70:30 for (b) and (e) and 90:10 wt% for (c) and (f). The final configurations of the simulations can be compared to the experimentally obtained transmission electron microscopy images for matchable systems in Figure (6.10).

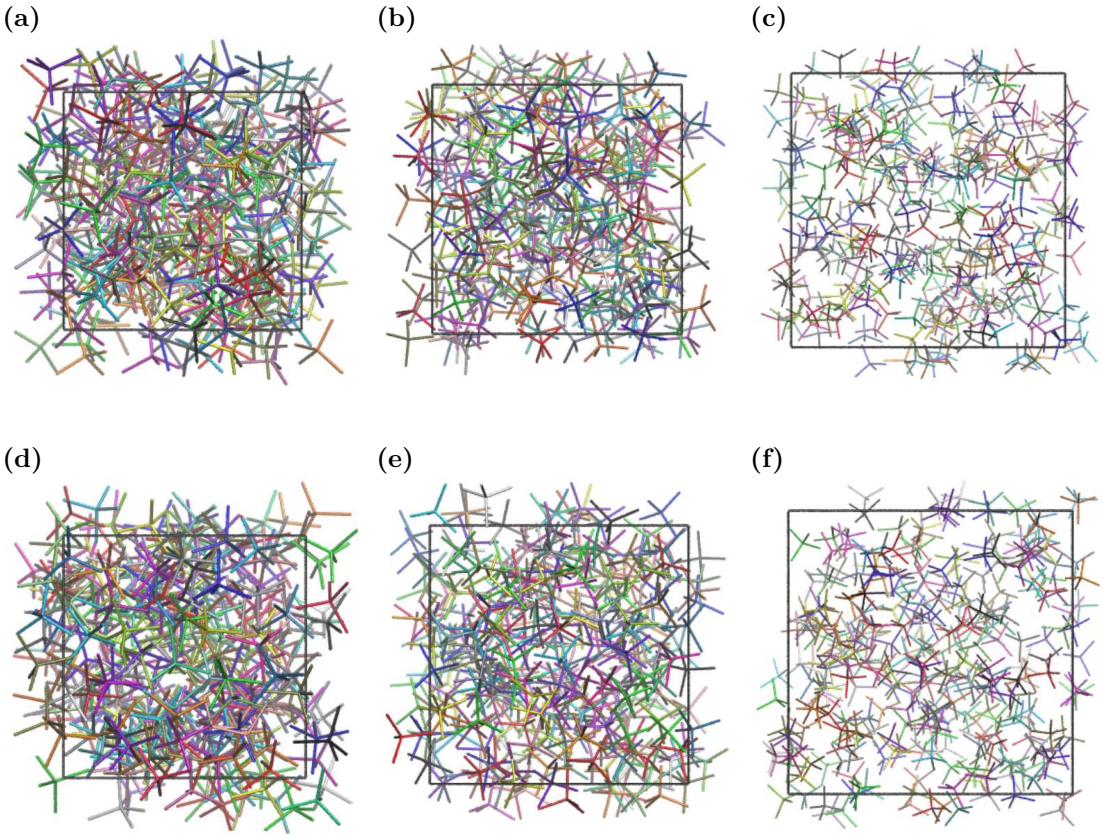

In summary, we conclude that our current model is not suitable to describe all features of the experimental system. Especially for blends a much stronger clustering is expected. This is particularly apparent for systems with tetrapod arm lengths of 109.3 nanometers. Overall the distance between the tetrapods should decrease much more with increasing arm length. We can, thus, conclude that the attraction of the tetrapods is underestimated in our model. One reason may be that our model is designed for polymer solutions and not for melts. To account for the situation in a melt more sophisticated methods, such as a self-consistent field theory, should be used. Another reason may be that there are direct attractions between the tetrapod surfaces, which are not taken into consideration in our model. The addition of such an interaction would lead to a stronger clustering and a stronger prevention, if the interaction is shielded by the brushes. The derivation of a more realistic model will be the task of future work. One step towards a more sophisticated simulation model is to allow a fluctuating box volume. This approach is discussed in the following section.

## 8.3 Simulations at constant pressure

In Section 7.5 we have introduced an algorithm for simulations with fluctuating box volume. A test of this algorithm can be found in Appendix B.1. For the simulations in this section we set the temperature $T$ to a fixed value of 1.0 and only change the pressure $P$.

To test the volume move algorithm we start several simulations at different pressures. For this first test we simulate systems containing 400 tetrapods with arm lengths equal to 42 and diameters equal to 6 nanometers. At the beginning of the simulations tetrapods with identical orientation are added at random positions in the simulation box. In all simulations in this section the volume ratio $\alpha$ of excess polymers to tetrapods is chosen to correspond to a system with 90:10 wt%. Volume moves are performed every tenth step. The pressure $P$ is varied from $1 \cdot 10^{-12}$ to 1.

Depending on the pressure we expect a different volume $V$ of the simulation box and, thus, a varying density $\rho_{\mathrm{P}}$ for the excess polymer. Ideally, it should be possible to observe an order transition driven by the pressure. As we use a constant number of tetrapods and a fixed volume ratio between tetrapods and excess polymer the density $\rho_{\mathrm{P}}$ is proportional to the inverse of the box volume $V$.

In Figure (8.6) we show the dependence of the volume $V$ divided by the number of tetrapods $N$ and the average squared minimum distances between the tetrapod arms $\langle D^2 \rangle$ and centers $\langle C^2 \rangle$ on the pressure $P$. Figure (8.6a) illustrates the values of the final volume divided by $N$ over the whole pressure range. Blends are indicated by blue lines and hybrids by red lines. In the logarithmic scaling of the plot the volume of the blends only varies slightly. We clearly see that the hybrid systems are not stable for pressures below $1 \cdot 10^{-6}$. For lower pressures the tetrapods drift apart and the volume drastically increases with decreasing pressure. In this region the system behaves roughly like an ideal gas. For pressures above $1 \cdot 10^{-6}$ the hybrids are in a liquid state. This indicates that there is a liquid-gas phase transition for hybrids. The blends are in a liquid state for all studied pressures. At this stage a phase coexistence can not be ruled out.

Figure (8.6b) shows the plot of $V/N$ for hybrids in the pressure range from $1 \cdot 10^{-6}$ to one. Here the volume hardly decreases with increasing pressure. A clear drop of the curve can only be observed at the two highest pressures. Figure (8.6c) displays the volume for blends over the full pressure range. For blends $V/N$ fluctuates around a value of $3.5 \cdot 10^5$ for pressures up to $1 \cdot 10^{-7}$. Then there is a steep leap to much lower volumes for higher pressures. For higher pressures the systems tend to have a volume per tetrapod around $2.1 \cdot 10^5$.

The instability of the hybrids for low pressures is also visible in the plots of the average squared minimum distance between the tetrapod arms and their centers shown in Figures (8.6d) and (8.6f). The comparison with Figure (8.6a) reaffirms the relation between the volume and the distances between the tetrapods. Figure (8.6e) displays the average squared minimum distance between the tetrapod arms $\langle D^2 \rangle$ in the pressure range from $1 \cdot 10^{-6}$ to one. For hybrids, just as the volume, the average squared minimum distance between the tetrapod arms only changes for high pressures.

Figure (8.7) shows snapshots of the final configurations of hybrids and blends for different pressures. For a pressure equal to $1 \cdot 10^{-7}$ we clearly see that the hybrid (Figure (8.7b)) is in a gaseous state while the blend (Figure (8.7a)) is in a liquid state. For a higher pressure of $P = 1 \cdot 10^{-6}$ both systems are in a liquid state, as Figures (8.7c) and (8.7d) demonstrate. If the pressure is increased to one the blend hardly changes as Figure (8.7e) illustrates. In Figure (8.7f) we can observe the slight decrease of the volume for hybrids, which is visible in Figure (8.6b).

From these first results we can learn that the hybrid systems are only stable for sufficient high pressures. We further find that the systems equilibrate much faster if we allow a fluctuating volume.

In the simulations in Section 8.1 the ratio $V/N$ is approximately $1.4 \cdot 10^5$ at an excess polymer to tetrapod ratio of 50:50 wt%. If we compare this with the results of this section we may conclude that the studied system is in a liquid phase. The same may apply to the simulations in Section 8.2. Deep in the liquid phase the formation of clusters is not expected. The experimental results with arm lengths of 100 nanometers (see Figure (6.10) b,d) indicate that there may possibly be an additional transition at high densities which is not taken into account by our model.

Nevertheless, more tests are needed until further predictions can be made. The investigation of a possible phase coexistence and the development of a more appropriate model will be the task of future work.

**Figure 8.6** Plots for systems of hybrids (red) and blends (blue) for different pressures $P$ allowing a fluctuation of the simulation box volume $V$. The $x$-axis is scaled logarithmically in all plots. (a) Plot of the volume $V$ divided by the number of tetrapods $N$ over the whole pressure range. (b) $V/N$ for hybrids in the pressure range from $1 \cdot 10^{-6}$ to 1. (c) $V/N$ for blends over the whole pressure range. (d) Average squared minimum distance $\langle D^2 \rangle$ for blends and hybrids. (e) $\langle D^2 \rangle$ in the pressure range from $1 \cdot 10^{-6}$ to 1. (f) Average squared minimum distance between the tetrapod centers $\langle C^2 \rangle$.

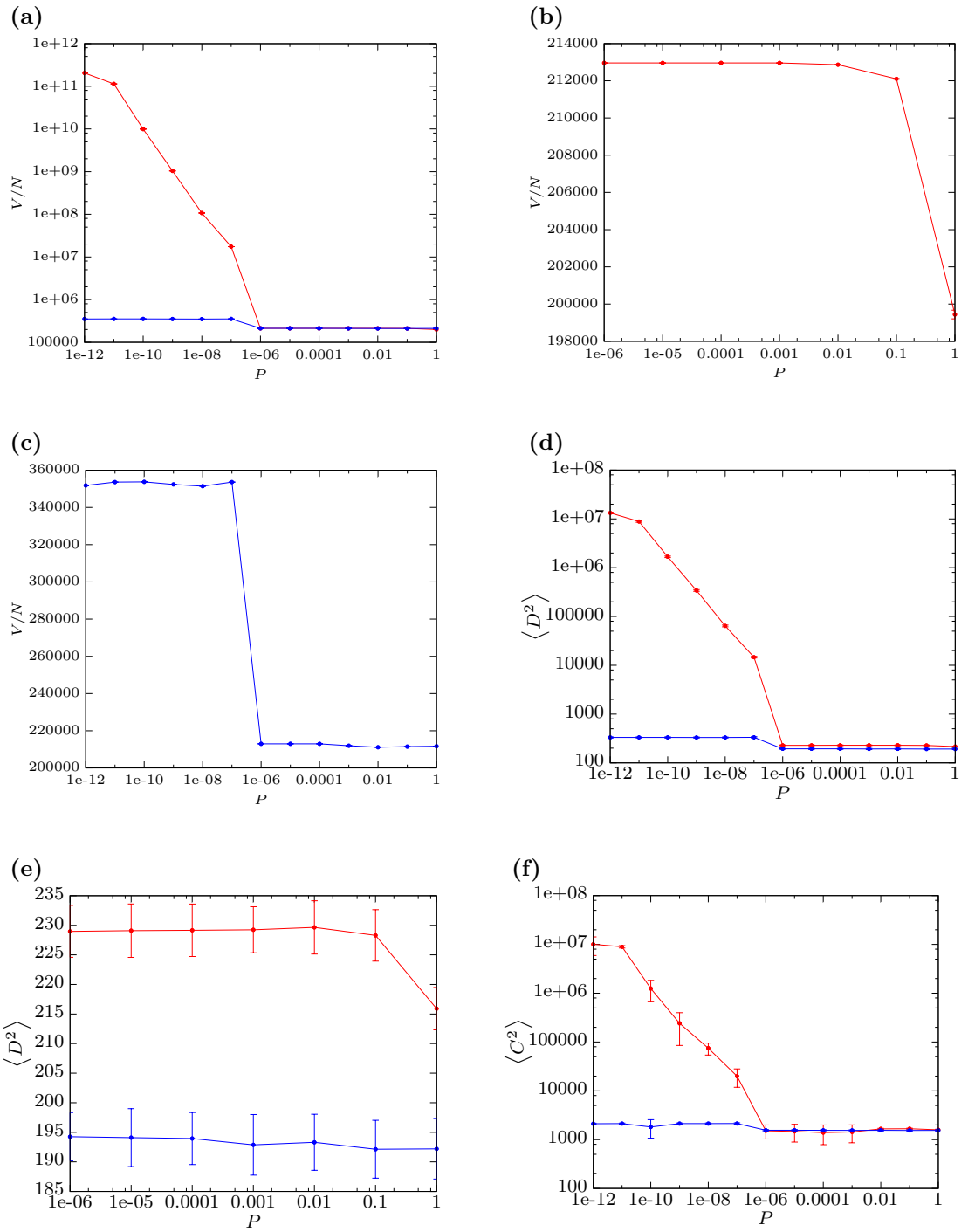

**Figure 8.7** Snapshots of the final configurations for different pressures $P$. The configurations on the left side ((a), (c), (e)) represent blends, while the systems on the right ((b), (d), (f)) are hybrids. For (a) and (b) the pressure is $1 \cdot 10^{-7}$, for (c) and (d) $P = 1 \cdot 10^{-6}$ and for (e) and (f) $P$ equals one.

**(a)**

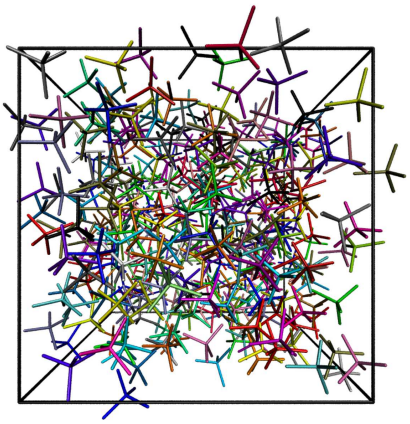

**(b)**

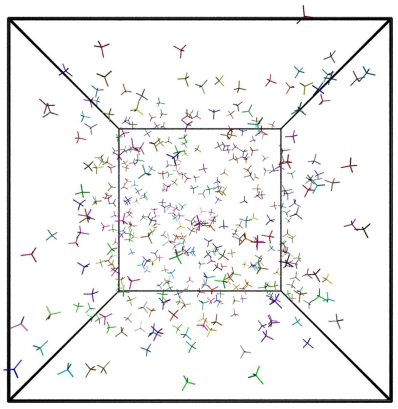

**(c)**

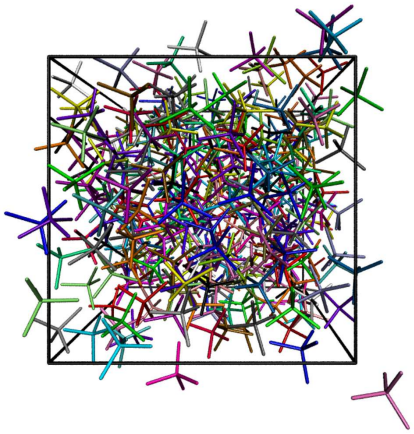

**(d)**

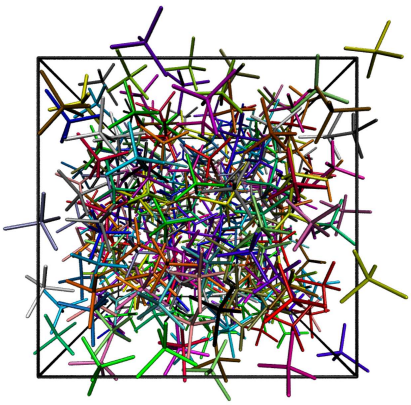

**(e)**

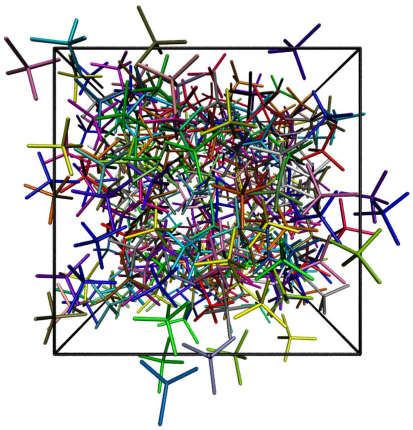

**(f)**

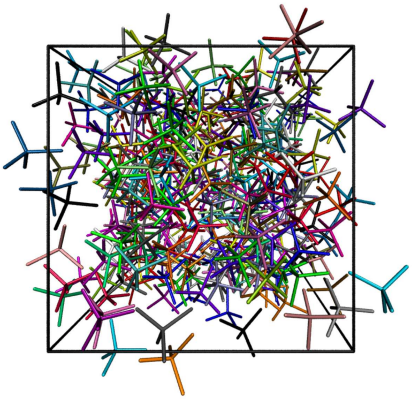

Chapter 9

# Conclusions and Outlook

Contents



In this chapter we conclude the findings of this thesis and give an outlook on possible future projects.

## 9.1 Conclusion Part I

In summary, we have introduced a new and efficient coarse-grained model system which is designed to investigate the phase behavior of rod-coil block copolymer systems on mesoscopic length scales. The interactions of the coil monomers as well as the interactions between rods and coils in this model are based on local densities whereas the packing of the rods is provided by hard core interactions. This way the conformational freedom of the flexible coils is taken into account as well as an energetic repulsion between rods and coils. In combination with the efficient numerical treatment within a Monte-Carlo simulation this model is particularly suited to study how order effects of rods for different packing fractions are altered by energetic and entropic contributions of the coils.

Based on the introduced model we have demonstrated its applicability on pure rod systems, rod/coil mixtures and systems consisting of rod-coil block copolymers. We have studied the dependence of rod-coil block copolymer systems on the different model parameters. Among them are the coil length and the interaction strength between rods and coils.

We have investigated a phase diagram for rod-coil block copolymers in our model in dependence of the number of monomers per coil and the rod-coil interaction parameter. In this connection we have found a stabilization of the smectic phase. Furthermore, we have demonstrated the capability of our model to exhibit remarkable phases such as the wavy lamellar phase, clusters and percolating structures. In addition, we have observed a zigzag phase which is found to be metastable in our model.

We hope that the results of this thesis may be helpful to understand and further examine the behavior of rod-coil block copolymers. The findings can be useful to fabricate more efficient organic solar cells or other optoelectronic devices. For this purpose, the observed highly ordered phases and percolating structures could be used to provide possible pathways for the electron transport in such devices.

In the future the program may be expanded to simulate rod-coil block copolymers with spherocylinders of unequal length and diameter. Further studies on rod/coil mixtures as well as an expansion to charged polymers or triblock copolymers may also be of interest for future projects.

## 9.2 Conclusion Part II

Motivated by an experimental study we have developed a model to simulate tetrapods in excess polymer. In addition, short polymer brushes may be added to the surface of the tetrapod arms. The interactions are represented by a potential which accounts for the repulsion of these polymer brushes as well as for the attractive depletion force due to the excess polymer. As in the associated experimental work we have found that the addition of polymer brushes to the surface of the tetrapods significantly reduces the clustering of the tetrapods. Thus, these hybrids show much better film qualities. Furthermore, we have introduced an algorithm to allow a fluctuating volume of the simulation box. This way the simulated systems equilibrate much faster and more realistic systems can be studied.

While demonstrating the applicability of the developed model we have found that it does not capture all observed features of the experimental system. In particular, our model predicts that the effect of coating goes down with increased arm length. In the experimental study the opposite is observed. Furthermore, the clustering in uncoated systems is much stronger than in our model. This suggests that the attraction of the tetrapods is underestimated. Reasons may be that our model is designed for polymer solutions, not melts. More sophisticated methods should be used to account for the situation in melts. Possibly, there is a direct attraction between the tetrapod surfaces, which are shielded by the brushes, which is not taken into account by our model.

In the future the model may be adapted to simulate more complex systems. For example, tetrapods with dissimilar arm lengths or tetrapods with charged tips. As the simulations for tetrapods use the same layout for the configuration and coordinate files as the model for rod-coil block copolymers it is also possible to use the final configurations of tetrapod simulations as initial configuration for simulations with pure rods or rod-coil block copolymers if coils are added to one end of the spherocylinders. So one could simulate the behavior of tetrapods whose central connection is chemically dissolved.

As recent results emphasize tetrapods may play an important role in the development of efficient organic solar cells. With the model illustrated in this thesis and the proposed improvements this progress may be supported.

# Appendices

Appendix A

# Appendix to Part I

## A.1 Pure rod systems

The program we use to simulate the introduced model is implemented from scratch. The development is done in several steps so every part of the code can be tested before the program is extended and new features are added. As a first step we implement a pure rod system. The results of these simulations can be compared to the findings mentioned in Section 2.2.

Remember that the spherocylinders, representing the rod-like polymers, only comprise a hard body interaction in our model. The observed phase-transitions are, therefore, purely entropy-driven. The reduced densities $\rho^*$ of pure rod systems can be adjusted by adapting the size of the simulation box, the number of spherocylinders and their size. This way comparable densities may be simulated using different system parameters.

In the simulations we present in this section the length-to-width ratio $L/D$ is varied between 0 and 30, of which we only discuss the results up to a value of five. Note that it is not the goal of this work to study this system in detail. Hence, we only investigate the order-disorder transition in a rough manner. This means that we only inspect the order parameter $S_z$ for an order-disorder transition but do not check for smectic, nematic let alone plastic phases explicitly.

Figure (A.1) shows the order-disorder transition for three sets of independent runs. The red and blue data points represent simulation runs with 10 to 9987 spherocylinders and box sizes that range from $5\times5\times5$ to $93\times93\times93$. These rods are set up in an ordered manner. The size of the simulation boxes for the green data points lies between $9\times9\times9$ and $53\times53\times53$. These systems contain 22 to 7020 rods which are arranged randomly at the beginning. In a further, more detailed test for 100 to 6800 spherocylinders with a fixed length-to-with ratio of five we use a box size of $48\times30\times36$. The rods are initiated in an ordered manner and we find a transition between the isotropic and the nematic phase at a reduced density $\rho^*$ around 0.466. This transition point is marked by a magenta colored star. In the background the phase diagram for hard spherocylinders obtained by Bolhuis and Frenkel [29] already shown in Figure (2.3) in Section 2.2 is added for comparison. We see that the obtained results of our simulations are compatible with the specified results.

We are, therefore, convinced that the chosen model and the implementation of the spherocylinders and their interaction is appropriate and we can extend the program. Further, we remark that we observe an isotropic, nematic, smectic and solid phase for a length-to-width ratio $L/D$ equal to five. For this reason we choose this length-to-width ratio for most of our simulations, especially for the investigation of the phase diagram in Section 5.1.

**Figure A.1** Order-disorder transition for pure rod systems. The red, blue and green lines with squares, circles and triangles, respectively, represent three different simulation setups. The lines between the data points are only added to guide the eye. The magenta colored star indicates the observed phase transition between the isotropic and the nematic phase. As comparison the phase diagram obtained by Bolhuis and Frenkel [29] is added in the background.

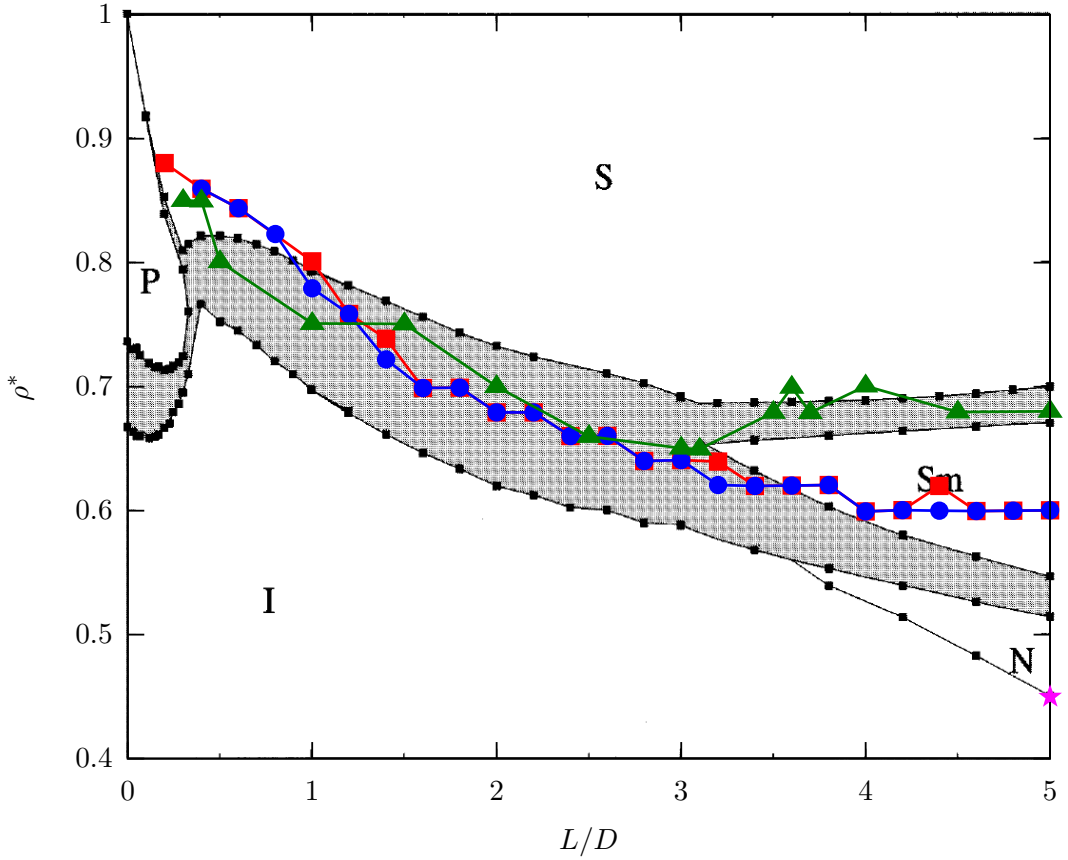

## A.2 Rod/coil mixtures

After demonstrating that the behavior of the spherocylinders is compatible with former results of pure rod systems we add coils with all associated interactions to the system. At this point the chains are not connected to the rods, yet. Thus, we have a mixture of spherocylinders and coils with all interactions mentioned in Chapter 3. Remember, that there are no attractive interactions in our model. The strength of the repulsion between the monomers and the rods and coils is controlled via the $\chi$ interaction parameters. For the runs discussed in this section we use the surface approximation method introduced in Section 3.4.4. In this model the monomers are allowed to penetrate the spherocylinders. But due to their repulsive interaction the rods and the coil monomers try to avoid sharing common cells. As the rods and coils are not connected we expect a phase separation at a macroscopic scale as already mentioned in Section 2.3.

In this section we show some exemplary structures we observe in a few test runs. Again, the investigation of this model is not a main goal of this thesis. For this reason, we solely present some exemplary results to demonstrate the basic capability of our program to simulate rod/coil mixtures. For further results more detailed and systematic studies are needed. This may be the topic of future work.

For the presented runs the size of the simulation box is set to $36 \times 36 \times 36$ and the rods, which have a length $L$ equal to five and a diameter $D$ of one, are added randomly at the beginning. The number of rods $N_{\mathrm{Rods}}$, as well as the number of chains $N_{\mathrm{Coils}}$ and the number of monomers per chain $m$ is different for each run. The values of the systems presented in this section are summarized in Table (A.1). The table also shows the total number of monomers $M$, the reduced density $\rho^*$ of the spherocylinders and the coil number density $\rho_{\mathrm{C}} = M/V_{\mathrm{Box}}$. The interaction parameters are set to $\chi_{\mathrm{CC}} = \chi_{\mathrm{CR}} = 0.5$ and $k = 12$ for all runs.

**Table A.1** Overview over the number of rods, coils, monomers per coil and total number of monomers and the densities of the systems presented in Figure (A.2).

| | $N_{\mathrm{Rods}}$ | $N_{\mathrm{Coils}}$ | $m$ | $M$ | $\rho^*$ | $\rho_{\mathrm{C}}$ |
|---|---|---|---|---|---|---|
| Figure (A.2a) | 500 | 500 | 30 | 15000 | 0.0540 | 0.3215 |
| Figure (A.2b) | 100 | 1000 | 50 | 50000 | 0.0108 | 1.0717 |

Figure (A.2) shows two structures we observe for the simulated rod/coil mixtures. If the concentration of both polymers is very low we observe a disordered system as displayed in Figure (A.2a). For systems with a small rod density but a high coil concentration we observe a microphase separation as shown in Figure (A.2b). The results of the shown simulations for rod/coil mixtures complies with the expected behavior of such a system. A more detailed investigation of this system and a more precise determination of the different structures and their properties may be the task of future work.

**Figure A.2** Structures in rod/coil polymer mixtures with the parameters listed in Table (A.1). The coils (blue) are only displayed in the simulation box, whereas the rods (yellow) are periodically repeated in positive and negative $x$ and $y$ direction. The exhibited structures include a disordered phase (a) and a macroscopic phase separation (b).

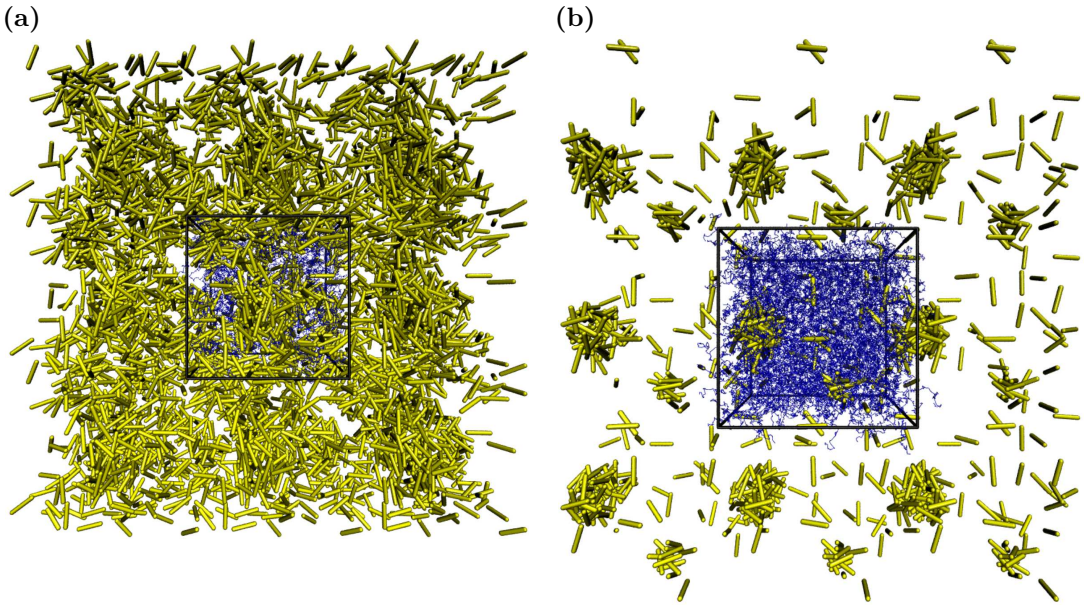

Appendix B

# Appendix to Part II

## B.1 Testing the volume moves

To check if the algorithm for the fluctuating volume is working correctly we test it, trying to reproduce the ideal gas law. For this purpose we turn off all interactions except for the volume energy introduced in Equation (7.67). Setting the Boltzmann constant $k_B$ to one the ideal gas law reads

$$PV = NT \tag{B.1}$$

and one can easily see that the volume is related to $N$ times the ratio of the temperature and the pressure

$$V = N\frac{T}{P}. \tag{B.2}$$

From this equation we can calculate the expected volume for our tests. We test four different temperature and pressure combinations which are summarized in Table (B.1).

**Table B.1** Expected volume $V$ of an ideal gas system with $N$ particles for different pressure and temperature values.

| $P$ | $T$ | $V = N\frac{T}{P}$ |
|---|---|---|
| 1.0 | 1.0 | $N$ |
| 1.0 | 2.0 | $2N$ |
| 2.0 | 1.0 | $\frac{N}{2}$ |
| 2.0 | 2.0 | $N$ |

For each combination of pressure and temperature we start runs with 100, 200 and 300 tetrapods. Volume moves are performed every 50th step and each system is set up twice, starting from a random configuration. The first system starts with a volume smaller and the second with a volume bigger than the calculated volume. So we can check if the system reaches its equilibrium value from both sides. Figure (B.1) shows the development of the volume for all simulated systems. The horizontal lines represent the expected values for the volume. The red lines are associated to systems with 100 tetrapods, the green lines to systems with 200 tetrapods and the blue lines to systems with 300 tetrapods. The plots clearly show that the expected values are reached after

several ten thousand steps and then fluctuate marginally around these values for all four combinations of temperature and pressure. We are, therefore, convinced that the volume moves are implemented correctly.

**Figure B.1** Plots of the simulation box volume $V$ versus the number of steps for the ideal gas case. Volume moves are performed every 50th step. The horizontal lines show the theoretical values the volume $V$ should reach for an ideal gas (see Table (B.1)). Red lines symbolize systems with 100, green lines systems with 200 and blue lines systems with 300 particles. We always start from one system above and one below the theoretical value. (a) $P = T = 1$. (b) $P = 1$ and $T = 2$. (c) $P = 2$ and $T = 1$. (d) $P = T = 2$.

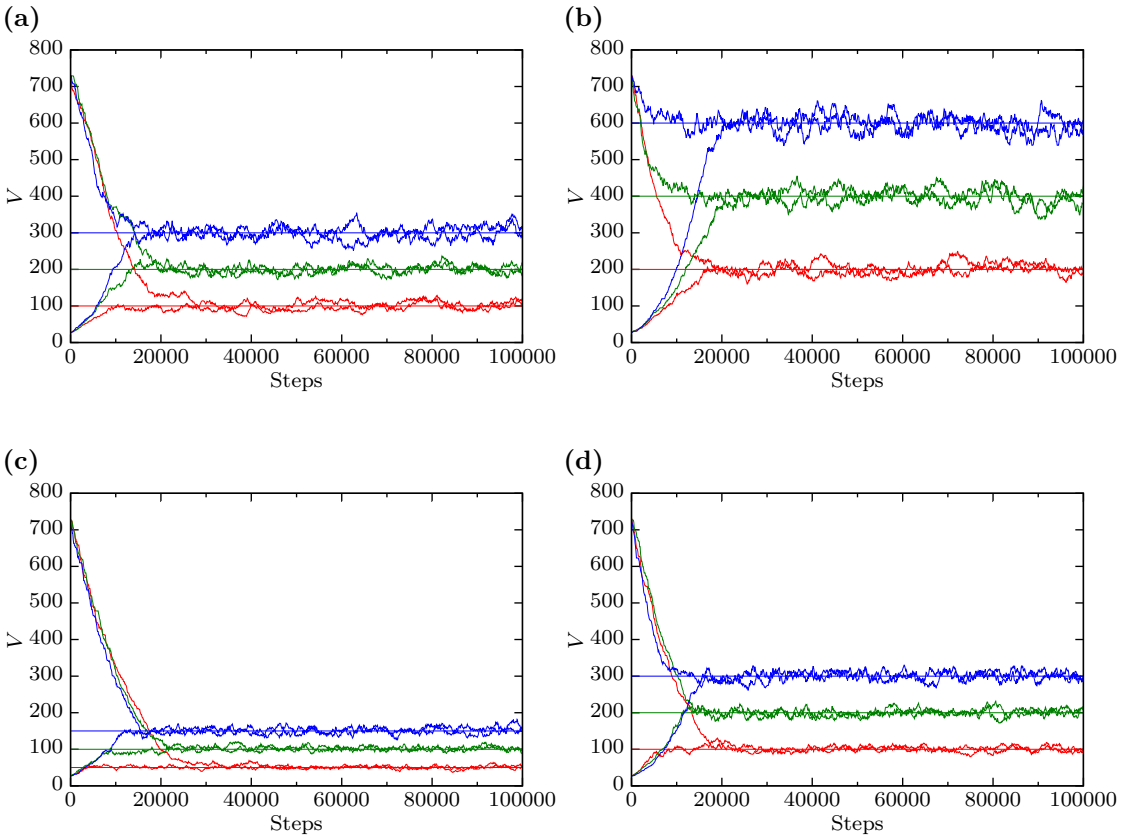

# Bibliography

[1] G. I. Ågren. End-chain flexibility and the nematic-isotropic transition in liquid crystals: A lattice model of hard particles with rigid, rodlike, central cores and semiflexible pendant segments. *The Journal of Chemical Physics*, 61(10):3959, 1974.

[2] C. R. A. Abreu, F. W. Tavares, and M. Castier. Influence of particle shape on the packing and on the segregation of spherocylinders via Monte Carlo simulations. *Powder Technology*, 134(1-2):167–180, 2003.

[3] T. Adachi, J. Brazard, P. Chokshi, J. C. Bolinger, V. Ganesan, and P. F. Barbara. Highly Ordered Single Conjugated Polymer Chain Rod Morphologies. *The Journal of Physical Chemistry C*, 114(48):20896–20902, 2010.

[4] R. Adhikari, T. A. Huy, M. Buschnakowski, G. H. Michler, and K. Knoll. Asymmetric PS- block -(PS-co-PB)- block -PS block copolymers: morphology formation and deformation behaviour. *New Journal of Physics*, 6:28–28, 2004.

[5] F. Affouard, M. Kröger, and S. Hess. Molecular dynamics of model liquid crystals composed of semiflexible molecules. *Physical Review E*, 54(5):5178–5186, 1996.

[6] N. Akino, F. Schmid, and M. P. Allen. Molecular Dynamics Study of the Nematic-Isotropic Interface. *Physical Review E*, 63(4):041706, 2001.

[7] M. Al-Barwani and M. Allen. Isotropic-nematic interface of soft spherocylinders. *Physical Review E*, 62(5 Pt B):6706–6710, 2000.

[8] S. Alexander. Adsorption of chain molecules with a polar head a scaling description. *Journal de Physique*, 38(8):983–987, 1977.

[9] M. P. Allen and D. J. Tildesley. *Computer Simulation of Liquids*. Clarendon Press, 1989.

[10] M. P. Allen and D. J. Tildesley. *Computer simulation in chemical physics*. Kluwer Academic Publishers, 1993.

[11] A. AlSunaidi, W. K. den Otter, and J. H. R. Clarke. Liquid-crystalline ordering in rod-coil diblock copolymers studied by mesoscale simulations. *Philosophical*

*transactions. Series A, Mathematical, physical, and engineering sciences*, 362 (1821):1773–81, 2004.

[12] A. AlSunaidi, W. K. den Otter, and J. H. R. Clarke. Microphase separation and liquid-crystalline ordering of rod-coil copolymers. *The Journal of chemical physics*, 130(12):124910, 2009.

[13] A. C. Arias, N. Corcoran, M. Banach, R. H. Friend, J. D. MacKenzie, and W. T. S. Huck. Vertically segregated polymer-blend photovoltaic thin-film structures through surface-mediated solution processing. *Applied Physics Letters*, 80 (10):1695, 2002.

[14] S. Asakura and F. Oosawa. On Interaction between Two Bodies Immersed in a Solution of Macromolecules. *The Journal of Chemical Physics*, 22(7):1255, 1954.

[15] S. Asakura and F. Oosawa. Interaction between particles suspended in solutions of macromolecules. *Journal of Polymer Science*, 33(126):183–192, 1958.

[16] S. Asokan, K. M. Krueger, V. L. Colvin, and M. S. Wong. Shape-controlled synthesis of CdSe tetrapods using cationic surfactant ligands. *Small (Weinheim an der Bergstrasse, Germany)*, 3(7):1164–9, 2007.

[17] J. L. Baker, A. Widmer-Cooper, M. F. Toney, P. L. Geissler, and A. P. Alivisatos. Device-scale perpendicular alignment of colloidal nanorods. *Nano letters*, 10(1): 195–201, 2010.

[18] N. Bansal, L. X. Reynolds, A. MacLachlan, T. Lutz, R. S. Ashraf, W. Zhang, C. B. Nielsen, I. McCulloch, D. G. Rebois, T. Kirchartz, M. S. Hill, K. C. Molloy, J. Nelson, and S. A. Haque. Influence of crystallinity and energetics on charge separation in polymer-inorganic nanocomposite films for solar cells. *Scientific reports*, 3:1531, 2013.

[19] M. Bargiel. Geometrical Properties of Simulated Packings of Spherocylinders. *Computational Science–ICCS 2008*, pages 126–135, 2008.

[20] F. S. Bates. Polymer-polymer phase behavior. *Science*, 251(4996):898–905, 1991.

[21] M. A. Bates and D. Frenkel. Phase behavior of two-dimensional hard rod fluids. *The Journal of Chemical Physics*, 112(22):10034, 2000.

[22] M. A. Bates and G. R. Luckhurst. Computer simulation studies of anisotropic systems. The density and temperature dependence of the second rank orientational order parameter for the nematic phase of a Gay-Berne liquid crystal. *Chemical Physics Letters*, 281(1-3):193–198, 1997.

[23] J.-F. Berret, D. Roux, and P. Lindner. Structure and rheology of concentrated wormlike micelles at the shear-induced isotropic-to-nematic transition. *The European Physical Journal B*, 5(1):67–77, 1998.

[24] G. Besold, O. Hassager, and O. G. Mouritsen. Monte Carlo simulation of diblock copolymer microphases by means of a fast off-lattice model. *Computer Physics Communications*, 121-122:542–544, 1999.

[25] G. Besold, H. Guo, and M. J. Zuckermann. Off-lattice Monte Carlo simulation of the discrete Edwards model. *Journal of Polymer Science Part B: Polymer Physics*, 38(8):1053–1068, 2000.

[26] K. Binder and M. Müller. Monte Carlo simulation of block copolymers. *Current Opinion in Colloid & Interface Science*, 5(5-6):314–322, 2000.

[27] P. Biscari, M. C. Calderer, and E. M. Terentjev. Landau-de Gennes theory of isotropic-nematic-smectic liquid crystal transitions. *Physical Review E - Statistical, Nonlinear, and Soft Matter Physics*, 75(5):051707, 2007.

[28] R. Blaak, B. M. Mulder, and D. Frenkel. Cubatic phase for tetrapods. *The Journal of chemical physics*, 120(11):5486–92, 2004.

[29] P. Bolhuis and D. Frenkel. Tracing the phase boundaries of hard spherocylinders. *The Journal of Chemical Physics*, 106(2):666–687, 1997.

[30] P. G. Bolhuis, A. Stroobants, D. Frenkel, and H. N. W. Lekkerkerker. Numerical study of the phase behavior of rodlike colloids with attractive interactions. *The Journal of Chemical Physics*, 107(5):1551, 1997.

[31] P. G. Bolhuis, A. A. Louis, J. P. Hansen, and E. J. Meijer. Accurate effective pair potentials for polymer solutions. *The Journal of Chemical Physics*, 114(9):4296, 2001.

[32] I. Botiz and S. B. Darling. Self-Assembly of Poly(3-hexylthiophene)- block - polylactide Block Copolymer and Subsequent Incorporation of Electron Acceptor Material. *Macromolecules*, 42(21):8211–8217, 2009.

[33] I. Botiz and S. B. Darling. Optoelectronics using block copolymers. *Materials Today*, 13(5):42–51, 2010.

[34] T. Boublík. Third and Fourth Virial Coefficients and the Equation of State of Hard Prolate Spherocylinders. *The Journal of Physical Chemistry B*, 108(22): 7424–7429, 2004.

[35] P. J. Camp, M. P. Allen, P. G. Bolhuis, and D. Frenkel. Demixing in hard ellipsoid rod-plate mixtures. *The Journal of Chemical Physics*, 106(22):9270, 1997.

[36] C. M. Care and D. J. Cleaver. Computer simulation of liquid crystals. *Reports on Progress in Physics*, 68(11):2665–2700, 2005.

[37] J.-M. Y. Carrillo and A. V. Dobrynin. Molecular dynamics simulations of grafted layers of bottle-brush polyelectrolytes. *Langmuir : the ACS journal of surfaces and colloids*, 26(23):18374–81, 2010.

[38] J.-M. Y. Carrillo, S. S. Sheiko, and A. V. Dobrynin. Molecular dynamics simulations of bottlebrush macromolecules in two dimensional polymeric melts under flow conditions. *Soft Matter*, 7(6):2805, 2011.

[39] A. Casey and P. Harrowell. Liquid crystal phase transitions in clusters of spherocylinders. *The Journal of Chemical Physics*, 112(1):465, 2000.

[40] S. Chandrasekhar, B. K. Sadashiva, and K. A. Suresh. Liquid crystals of disc-like molecules. *Pramana*, 9(5):471–480, 1977.

[41] S.-C. Chang, J. Liu, J. Bharathan, Y. Yang, J. Onohara, and J. Kido. Multicolor Organic Light-Emitting Diodes Processed by Hybrid Inkjet Printing. *Advanced Materials*, 11(9):734–737, 1999.

[42] W.-H. Chang, S.-H. Chou, J.-J. Lin, W.-C. Chen, and Y.-J. Sheng. Thin film morphologies of pi-conjugated rod-coil block copolymers with thermoresponsive property: a combined experimental and molecular simulation study. *The Journal of chemical physics*, 132(21):214901, 2010.

[43] C. C. Chao, T. C. Wang, R. M. Ho, P. Georgopanos, A. Avgeropoulos, and E. L. Thomas. Robust block copolymer mask for nanopatterning polymer films. *ACS Nano*, 4(4):2088–2094, 2010.

[44] J. T. Chen, E. L. Thomas, C. K. Ober, and S. S. Hwang. Zigzag Morphology of a Poly(styrene-b-hexyl isocyanate) Rod-Coil Block Copolymer. *Macromolecules*, 28 (5):1688–1697, 1995.

[45] J. T. Chen, E. L. Thomas, C. K. Ober, and G. P. Mao. Self-Assembled Smectic Phases in Rod-Coil Block Copolymers. *Science (New York, N.Y.)*, 273(5273): 343–6, 1996.

[46] A. N. Chester and S. Martellucci. *Phase Transitions in Liquid Crystals*. Springer Science & Business Media, 2013.

[47] D. L. Cheung and F. Schmid. Isotropic-nematic transition in liquid crystals confined between rough walls. *Chemical physics letters*, page 4, 2005.

[48] D. L. Cheung and A. Troisi. Molecular structure and phase behaviour of hairy-rod polymers. *Physical chemistry chemical physics : PCCP*, 11(12):2105–12, 2009.

[49] C. L. Choi, H. Li, A. C. K. Olson, P. K. Jain, S. Sivasankar, and A. P. Alivisatos. Spatially indirect emission in a luminescent nanocrystal molecule. *Nano letters*, 11(6):2358–62, 2011.

[50] S.-H. Chou, H.-K. Tsao, and Y.-J. Sheng. Structural aggregates of rod-coil copolymer solutions. *The Journal of chemical physics*, 134(3):034904, 2011.

[51] G. Cinacchi and F. Schmid. Density Functional for Anisotropic Fluids. *Journal of Physics: Condensed Matter*, 14:12223, 2002.

[52] W. R. Cooney, S. M. Thompson, and K. E. Gubbins. Virial coefficients for the hard oblate spherocylinder fluid. *Molecular Physics*, 66(6):1269–1272, 1989.

[53] M. Cosentino Lagomarsino, M. Dogterom, and M. Dijkstra. Isotropic–nematic transition of long, thin, hard spherocylinders confined in a quasi-two-dimensional planar geometry. *The Journal of Chemical Physics*, 119(6):3535, 2003.

[54] D. Costa, F. Saija, and P. V. Giaquinta. Smectic Ordering of Parallel Hard Spherocylinders: An Entropy-Based Monte Carlo Study. *The Journal of Physical Chemistry B*, 107(35):9514–9519, 2003.

[55] M. Cotter. Hard-rod fluid: Scaled particle theory revisited. *Physical Review A*, 10 (2):625–636, 1974.

[56] M. Cotter and D. Wacker. Van der Waals theory of nematogenic solutions. I. Derivation of the general equations. *Physical Review A*, 18(6):2669–2675, 1978.

[57] M. A. Cotter and D. E. Martire. Statistical Mechanics of Rodlike Particles. II. A Scaled Particle Investigation of the Aligned→Isotropic Transition in a Fluid of Rigid Spherocylinders. *The Journal of Chemical Physics*, 52(4):1909, 1970.

[58] A. Cuetos and M. Dijkstra. Kinetic Pathways for the Isotropic-Nematic Phase Transition in a System of Colloidal Hard Rods: A Simulation Study. *Physical Review Letters*, 98(9):095701, 2007.

[59] J. Cui, J. Zhu, Z. Ma, and W. Jiang. Monte Carlo simulation of the aggregation of rod–flexible triblock copolymers in a thin film. *Chemical Physics*, 321(1-2):1–9, 2006.

[60] M. Daoud and J. Cotton. Star shaped polymers : a model for the conformation and its concentration dependence. *Journal de Physique*, 43(3):531–538, 1982.

[61] S. Dayal, N. Kopidakis, D. C. Olson, D. S. Ginley, and G. Rumbles. Photovoltaic devices with a low band gap polymer and CdSe nanostructures exceeding 3% efficiency. *Nano letters*, 10(1):239–42, 2010.

[62] B. de Boer, U. Stalmach, P. F. van Hutten, C. Melzer, V. V. Krasnikov, and G. Hadziioannou. Supramolecular self-assembly and opto-electronic properties of semiconducting block copolymers. *Polymer*, 42(21):9097–9109, 2001.

[63] A. de Cuendias, R. C. Hiorns, E. Cloutet, L. Vignau, and H. Cramail. Conjugated rod-coil block copolymers and optoelectronic applications. *Polymer International*, 59(11):1452–1476, 2010.

[64] P. de Gennes. On a relation between percolation theory and the elasticity of gels. *Journal de Physique Lettres*, 37(1):1–2, 1976.

[65] P. de Gennes. *Scaling Concepts in Polymer Physics*. Cornell University Press, 1979.

[66] P. de Gennes. Polymers at an interface; a simplified view. *Advances in Colloid and Interface Science*, 27(3-4):189–209, 1987.

[67] P. de Gennes and J. Prost. *The Physics of Liquid Crystals*. Oxford University Press, 1995.

[68] C. De Michele, T. Bellini, and F. Sciortino. Self-Assembly of Bifunctional Patchy Particles with Anisotropic Shape into Polymers Chains: Theory, Simulations, and Experiments. *Macromolecules*, 45(2):1090–1106, 2012.

[69] F. A. Detcheverry, H. Kang, K. C. Daoulas, M. Müller, P. F. Nealey, and J. J. de Pablo. Monte Carlo Simulations of a Coarse Grain Model for Block Copolymers and Nanocomposites. *Macromolecules*, 41(13):4989–5001, 2008.

[70] M. Dijkstra and R. van Roij. Entropy-driven demixing in binary hard-core mixtures: From hard spherocylinders towards hard spheres. *Physical Review E*, 56(5):5594–5602, 1997.

[71] Z. Dogic and S. Fraden. *Soft Matter Vol. 2*, volume 2 of *Soft Matter*. Wiley-VCH Verlag GmbH & Co. KGaA, Weinheim, Germany, 2005.

[72] M. Doi and S. Edwards. *The Theory of Polymer Dynamics*. Clarendon Press, Oxford, 1986.

[73] S. Dolezel, H. Behringer, and F. Schmid. A model for rod-coil block copolymers. *Polymer Science Series C*, 55(1):70–73, 2013.

[74] D. Düchs and D. E. Sullivan. Entropy-induced smectic phases in rod coil copolymers. *Journal of Physics: Condensed Matter*, 14(46):12189–12202, 2002.

[75] D. Düchs, V. Ganesan, G. H. Fredrickson, and F. Schmid. Fluctuation Effects in Ternary AB + A + B Polymeric Emulsions. *Macromolecules*, 36(24):9237–9248, 2003.

[76] C. Ebner, H. R. Krishnamurthy, and R. Pandit. Density-functional theory for classical fluids and solids. *Physical Review A*, 43(8):4355–4364, 1991.

[77] A. Eliassi, H. Modarres, and G. A. Mansoori. Extension of Flory-Huggins Theory to Satisfy the Hard Sphere Limit. *Iranian Polymer Journal*, 12(5):357–366, 2003.

[78] P. J. Flory. Thermodynamics of High Polymer Solutions. *The Journal of Chemical Physics*, 10(1):51, 1942.

[79] P. J. Flory. Phase Equilibria in Solutions of Rod-Like Particles. *Proceedings of the Royal Society A: Mathematical, Physical and Engineering Sciences*, 234(1196): 73–89, 1956.

[80] P. J. Flory. Statistical Thermodynamics of Micture of Rodlike Particles. 5. Mixtures with Random Coils. *Macromolecules*, 11(6):1138–1141, 1978.

[81] I. R. Franchini, A. Cola, A. Rizzo, R. Mastria, A. Persano, R. Krahne, A. Genovese, A. Falqui, D. Baranov, G. Gigli, and L. Manna. Phototransport in networks of tetrapod-shaped colloidal semiconductor nanocrystals. *Nanoscale*, 2(10):2171–9, 2010.

[82] G. H. Fredrickson. *The equilibrium theory of inhomogeneous polymers*. Oxford University Press, 2006.

[83] G. H. Fredrickson, V. Ganesan, and F. Drolet. Field-Theoretic Computer Simulation Methods for Polymers and Complex Fluids. *Macromolecules*, 35(1):16–39, 2002.

[84] D. Frenkel. Onsager's spherocylinders revisited. *The Journal of Physical Chemistry*, 91(19):4912–4916, 1987.

[85] D. Frenkel and B. Smit. *Understanding molecular simulation: from algorithms to applications*, volume New York,. Academic Press, 2002.

[86] D. Frenkel, H. N. W. Lekkerkerker, and A. Stroobants. Thermodynamic stability of a smectic phase in a system of hard rods. *Nature*, 332(6167):822–823, 1988.

[87] N. G. Fytas and P. E. Theodorakis. Molecular dynamics simulations of single-component bottle-brush polymers with flexible backbones under poor solvent conditions. *Journal of physics. Condensed matter : an Institute of Physics journal*, 25(28):285105, 2013.

[88] J. G. Gay and B. J. Berne. Modification of the overlap potential to mimic a linear site–site potential. *The Journal of Chemical Physics*, 74(6):3316, 1981.

[89] G. Germano and F. Schmid. Nematic-Isotropic Interfaces Under Shear: A Molecular Dynamics Simulation. *The Journal of chemical physics*, pages 1–9, 2005.

[90] P. Gonnet. A simple algorithm to accelerate the computation of non-bonded interactions in cell-based molecular dynamics simulations. *Journal of computational chemistry*, 28(2):570–3, 2007.

[91] P. Gopalan, X. Li, M. Li, C. K. Ober, C. P. Gonzales, and C. J. Hawker. Rod-coil block copolymers: An iterative synthetic approach via living free-radical procedures. *Journal of Polymer Science Part A: Polymer Chemistry*, 41(22): 3640–3656, 2003.

[92] H. Graf and H. Löwen. Density functional theory for hard spherocylinders: phase transitions in the bulk and in the presence of external fields. *Journal of Physics: Condensed Matter*, 11(6):1435–1452, 1999.

[93] E. F. Gramsbergen, L. Longa, and W. H. De jeu. landau theory of the nematic isotropic phase transition. *physics reports*, 4(4):195–257, 1986.

[94] C. Groß. *A soft-tetramer model for diblock copolymer melts: structure formation and geometric characterization.* PhD thesis, Johannes Gutenberg University Mainz, 2010.

[95] C. Großand W. Paul. A soft-quadrumer model for diblock copolymers. *Soft Matter*, 6(14):3273, 2010.

[96] S. Günes, H. Neugebauer, and N. S. Sariciftci. Conjugated polymer-based organic solar cells. *Chemical Reviews*, 107(4):1324–1338, 2007.

[97] I. Gur, N. A. Fromer, M. L. Geier, and A. P. Alivisatos. Air-stable all-inorganic nanocrystal solar cells processed from solution. *Science (New York, N.Y.)*, 310 (5747):462–5, 2005.

[98] I. Gur, N. A. Fromer, C.-P. Chen, A. G. Kanaras, and A. P. Alivisatos. Hybrid solar cells with prescribed nanoscale morphologies based on hyperbranched semiconductor nanocrystals. *Nano letters*, 7(2):409–14, 2007.

[99] G. Gustafsson, Y. Cao, G. M. Treacy, F. Klavetter, N. Colaneri, and a. J. Heeger. Flexible light-emitting diodes made from soluble conducting polymers. *Nature*, 357(6378):477–479, 1992.

[100] W. R. Hamilton. LXIX. On quaternions; or on a new system of imaginaries in algebra. *Philosophical Magazine Series 3*, 30(203):458–461, 1847.

[101] M. Hamm, G. Goldbeck-Wood, A. V. Zvelindovsky, and J. G. E. M. Fraaije. Microstructure of nematic amorphous block copolymers: Dependence on the nematic volume fraction. *The Journal of Chemical Physics*, 118(20):9401, 2003.

[102] J. H. Han, J. Kim, J. K. Park, K. W. Lee, J.-I. Jin, E. Choi, and C. E. Lee. Nuclear magnetic resonance study of the smectic-cholesteric phase transition in a dimesogenic liquid crystal. *Current Applied Physics*, 14(10):1356–1359, 2014.

[103] M. Han and E. Sim. Formation of tubular scrolls with controlled internal cavity. *The journal of physical chemistry. B*, 116(6):1796–801, 2012.

[104] H. Hasegawa, H. Tanaka, K. Yamasaki, and T. Hashimoto. Bicontinuous microdomain morphology of block copolymers. 1. Tetrapod-network structure of polystyrene-polyisoprene diblock polymers. *Macromolecules*, 20(7):1651–1662, 1987.

[105] L. He, Z. Chen, R. Zhang, L. Zhang, and Z. Jiang. Self-assembly of cyclic rod-coil diblock copolymers. *The Journal of chemical physics*, 138(9):094907, 2013.

[106] X. He and F. Schmid. Spontaneous Formation of Complex Micelles from a Homogeneous Solution. *Physical Review Letters*, 100(13):15–18, 2008.

[107] T. R. Hebner, C. C. Wu, D. Marcy, M. H. Lu, and J. C. Sturm. Ink-jet printing of doped polymers for organic light emitting devices. *Applied Physics Letters*, 72 (5):519–521, 1998.

[108] T. Heiser, G. Adamopoulos, M. Brinkmann, U. Giovanella, S. Ould-Saad, C. Brochon, K. van de Wetering, and G. Hadziioannou. Nanostructure of self-assembled rod-coil block copolymer films for photovoltaic applications. *Thin Solid Films*, 511-512:219–223, 2006.

[109] W. Helfrich and G. Heppke. *Liquid Crystals of One- and Two-Dimensional Order: Proceedings of the Conference on Liquid Crystals of One- and Two-Dimensional Order and Their Applications*. Springer Science & Business Media, 2012.

[110] R. C. Hidalgo, D. E. Sullivan, and J. Z. Y. Chen. Smectic phases in rod–coil diblock copolymers. *Journal of Physics: Condensed Matter*, 19(37):376107, 2007.

[111] I. G. Hill, A. Kahn, Z. G. Soos, and R. A. Pascal, Jr. Charge-separation energy in films of $\pi$-conjugated organic molecules. *Chemical Physics Letters*, 327(3-4): 181–188, 2000.

[112] P. Hohenberg and W. Kohn. The Inhomogeneous Electron Gas. *Phys. Rev.*, 136 (3B):B864, 1964.

[113] R. Hołyst and A. Poniewierski. Nematic–smectic-A transition for perfectly aligned hard spherocylinders: Application of the smoothed-density approximation. *Physical Review A*, 39(5):2742–2744, 1989.

[114] R. Hołyst and M. Schick. Correlations in a rigid–flexible diblock copolymer system. *The Journal of Chemical Physics*, 96(1):730, 1992.

[115] M. A. Horsch, Z. Zhang, and S. C. Glotzer. Self-Assembly of Polymer-Tethered Nanorods. *Physical Review Letters*, 95(5):1–4, 2005.

[116] M. A. Horsch, Z. Zhang, and S. C. Glotzer. Simulation studies of self-assembly of end-tethered nanorods in solution and role of rod aspect ratio and tether length. *The Journal of chemical physics*, 125(18):184903, 2006.

[117] X.-D. Hu, S. E. Jenkins, B. G. Min, M. B. Polk, and S. Kumar. Rigid-Rod Polymers: Synthesis, Processing, Simulation, Structure, and Properties. *Macromolecular Materials and Engineering*, 288(11):823–843, 2003.

[118] M. L. Huggins. Solutions of Long Chain Compounds. *The Journal of Chemical Physics*, 9(5):440, 1941.

[119] Z. E. Hughes, L. M. Stimson, H. Slim, J. S. Lintuvuori, J. M. Ilnytskyi, and M. R. Wilson. An investigation of soft-core potentials for the simulation of mesogenic molecules and molecules composed of rigid and flexible segments. *Computer Physics Communications*, 178(10):724–731, 2008.

[120] W. Humphrey, A. Dalke, and K. Schulten. VMD - Visual Molecular Dynamics. *Journal of Molecular Graphics*, 14:33–38, 1996.

[121] K. Inomata, H. Shimizu, and T. Nose. Phase equilibrium studies on rod/solvent and rod/coil/solvent systems containing poly(?,L-glutamate) having oligo(ethylene glycol) side chains. *Journal of Polymer Science Part B: Polymer Physics*, 38(10): 1331–1340, 2000.

[122] R. A. J. Janssen and J. Nelson. Factors limiting device efficiency in organic photovoltaics. *Advanced materials (Deerfield Beach, Fla.)*, 25(13):1847–58, 2013.

[123] S. A. Jenekhe. Self-Assembled Aggregates of Rod-Coil Block Copolymers and Their Solubilization and Encapsulation of Fullerenes. *Science*, 279(5358):1903–1907, 1998.

[124] J. Jiang, X. Xu, J. Huang, and D. Cao. Density functional theory for rod-coil polymers with different size segments. *The Journal of chemical physics*, 135(5): 054903, 2011.

[125] T. Jiang and J. Wu. Isotropic-nematic phase transition in athermal solutions of rod-coil diblock copolymers. *The Journal of chemical physics*, 127(3):034902, 2007.

[126] O. Karthaus, N. Maruyama, X. Cieren, M. Shimomura, H. Hasegawa, and T. Hashimoto. Water-assisted formation of micrometer-size honeycomb patterns of polymers. *Langmuir*, 16(15):6071–6076, 2000.

[127] A. R. Khokhlov. Liquid-crystalline ordering in the solution of semiflexible macromolecules. *Physics Letters A*, 68(1):135–136, 1978.

[128] A. R. Khokhlov and A. N. Semenov. Liquid-crystalline ordering in the solution of long persistent chains. *Physica A: Statistical Mechanics and its Applications*, 108 (2-3):546–556, 1981.

[129] A. R. Khokhlov and A. N. Semenov. Liquid-crystalline ordering in the solution of partially flexible macromolecules. *Physica A: Statistical Mechanics and its Applications*, 112(3):605–614, 1982.

[130] L. Khounlavong, V. Pryamitsyn, and V. Ganesan. Many-body interactions and coarse-grained simulations of structure of nanoparticle-polymer melt mixtures. *The Journal of chemical physics*, 133(14):144904, 2010.

[131] H.-A. Klok and S. Lecommandoux. Supramolecular Materials via Block Copolymer Self-Assembly. *Advanced Materials*, 13(16):1217, 2001.

[132] M. Knaapila, R. Stepanyan, L. E. Horsburgh, A. P. Monkman, R. Serimaa, O. Ikkala, A. Subbotin, M. Torkkeli, and G. ten Brinke. Structure and Phase Equilibria of Polyelectrolytic Hairy-Rod Supramolecules in the Melt State. *The Journal of Physical Chemistry B*, 107(51):14199–14203, 2003.

[133] C. M. Kok and A. Rudin. Relationship between the hydrodynamic radius and the radius of gyration of a polymer in solution. *Die Makromolekulare Chemie, Rapid Communications*, 2(11):655–659, 1981.

[134] J. P. F. Lagerwall and F. Giesselmann. Current topics in smectic liquid crystal research. *Chemphyschem : a European journal of chemical physics and physical chemistry*, 7(1):20–45, 2006.

[135] D. P. Landau and K. Binder. *A guide to Monte Carlo simulations in statistical physics*. Cambridge University Press, 2009.

[136] L. Landau. The Theory of Phase Transitions. *Nature*, 138(3498):840–841, 1936.

[137] M. Laradji, H. Guo, and M. J. Zuckermann. Off-lattice Monte Carlo simulation of polymer brushes in good solvents. *Physical Review E*, 49(4):3199–3206, 1994.

[138] P. A. Lebwohl and G. Lasher. Nematic-liquid-crystal order-A Monte Carlo calculation. *Physical Review A*, 6(1):426–429, 1972.

[139] P. A. Lebwohl and G. Lasher. Nematic-Liquid-Crystal Order\char22{}A Monte Carlo Calculation. *Phys. Rev. A*, 6(6):426–429, 1972.

[140] M. Lee, B.-K. Cho, K. J. Ihn, W.-K. Lee, N.-K. Oh, and W.-C. Zin. Supramolecular Honeycomb by Self-Assembly of Molecular Rods in Rod−Coil Molecule. *Journal of the American Chemical Society*, 123(19):4647–4648, 2001.

[141] M. Lee, B.-K. Cho, and W.-C. Zin. Supramolecular Structures from Rod−Coil Block Copolymers. *Chemical Reviews*, 101(12):3869–3892, 2001.

[142] H. N. W. Lekkerkerker and A. Stroobants. Phase behaviour of rod-like colloid+flexible polymer mixtures. *Il Nuovo Cimento D*, 16(8):949–962, 1994.

[143] H. N. W. Lekkerkerker and R. Tuinier. *Colloids and the Depletion Interaction*. Springer, 2011.

[144] M. P. Lettinga, E. Barry, and Z. Dogic. Self-diffusion of rod-like viruses in the nematic phase. *Europhysics Letters (EPL)*, 71(4):7, 2005.

[145] H. Li, A. G. Kanaras, and L. Manna. Colloidal branched semiconductor nanocrystals: state of the art and perspectives. *Accounts of chemical research*, 46(7): 1387–96, 2013.

[146] J. Li, H. Zhang, and F. Qiu. Self-consistent field theory of block copolymers on a general curved surface. *The European physical journal. E, Soft matter*, 37(3):18, 2014.

[147] W. Li and H. R. Ma. Depletion interactions between two spherocylinders. *The European physical journal. E, Soft matter*, 16(2):225–31, 2005.

[148] X. Li, H. ShamsiJazeyi, S. L. Pesek, A. Agrawal, B. Hammouda, and R. Verduzco. Thermoresponsive PNIPAAM bottlebrush polymers with tailored side-chain length and end-group structure. *Soft matter*, 10(12):2008–15, 2014.

[149] Y. Li, R. Mastria, A. Fiore, C. Nobile, L. Yin, M. Biasiucci, G. Cheng, A. M. Cucolo, R. Cingolani, L. Manna, and G. Gigli. Improved Photovoltaic Performance of Heterostructured Tetrapod-Shaped CdSe/CdTe Nanocrystals Using C60 Interlayer. *Advanced Materials*, 21(44):4461–4466, 2009.

[150] J. Lim, W. K. Bae, K. U. Park, L. zur Borg, R. Zentel, S. Lee, and K. Char. Controlled Synthesis of CdSe Tetrapods with High Morphological Uniformity by the Persistent Kinetic Growth and the Halide-Mediated Phase Transformation. *Chemistry of Materials*, 25(8):1443–1449, 2012.

[151] J. Lim, L. zur Borg, S. Dolezel, F. Schmid, K. Char, and R. Zentel. Strategy for good dispersion of well-defined tetrapods in semiconducting polymer matrices. *Macromolecular rapid communications*, 35(19):1685–91, 2014.

[152] H. J. Limbach, C. Holm, and K. Kremer. Computer Simulations of the "Hairy Rod" Model. *Macromolecular Chemistry and Physics*, 206(1):77–82, 2005.

[153] S. Lin, N. Numasawa, T. Nose, and J. Lin. Brownian Molecular Dynamics Simulation on Self-Assembly Behavior of Rod−Coil Diblock Copolymers. *Macromolecules*, 40(5):1684–1692, 2007.

[154] S.-H. Lin, S.-J. Wu, C.-C. Ho, and W.-F. Su. Rational Design of Versatile Self-Assembly Morphology of Rod–Coil Block Copolymer. *Macromolecules*, 46(7): 2725–2732, 2013.

[155] Y.-L. Lin, H.-Y. Chang, Y.-J. Sheng, and H.-K. Tsao. Structural and mechanical properties of polymersomes formed by rod–coil diblock copolymers. *Soft Matter*, 9 (19):4802, 2013.

[156] J. S. Lintuvuori and M. R. Wilson. A coarse-grained simulation study of mesophase formation in a series of rod-coil multiblock copolymers. *Phys. Chem. Chem. Phys.*, 11(12):—-, 2009.

[157] C.-L. Liu, C.-H. Lin, C.-C. Kuo, S.-T. Lin, and W.-C. Chen. Conjugated rod–coil block copolymers: Synthesis, morphology, photophysical properties, and stimuli-responsive applications. *Progress in Polymer Science*, 36(5):603–637, 2011.

[158] H. Löwen. Brownian dynamics of hard spherocylinders. *Physical Review E*, 50(2): 1232–1242, 1994.

[159] G. R. Luckhurst and T. J. Sluckin. *Biaxial Nematic Liquid Crystals*. John Wiley & Sons, 2015.

[160] G. R. Luckhurst and C. Zannoni. Why is the Maier–Saupe theory of nematic liquid crystals so successful? *Nature*, 267(5610):412–414, 1977.

[161] W. Y. Lynn Ko, H. G. Bagaria, S. Asokan, K.-J. Lin, and M. S. Wong. CdSe tetrapod synthesis using cetyltrimethylammonium bromide and heat transfer fluids. *Journal of Materials Chemistry*, 20(12):2474, 2010.

[162] Y. Mai and A. Eisenberg. Self-assembly of block copolymers. *Chemical Society Reviews*, 41(18):5969, 2012.

[163] W. Maier and A. Saupe. Eine einfache molekulare Theorie des nematischen kristallinflüssigen Zustandes. *Zeitschrift Naturforschung Teil A*, 13, 1958.

[164] W. Maier and A. Saupe. Eine einfache molekularstatistische Theorie der nematischen kristallinflüssigen Phase. Teil I. *Zeitschrift Naturforschung Teil A*, 14, 1959.

[165] W. Maier and A. Saupe. Eine einfache molekularstatistische Theorie der nematischen kristallinflüssigen Phase. Teil II. *Zeitschrift Naturforschung Teil A*, 15, 1960.

[166] P. K. Maiti, A. V. Kumar, and K. G. Ayappa. Computer simulation of liquid crystals. *Journal of the Indian Institute of Science*, 2009.

[167] L. Manna, E. C. Scher, and A. P. Alivisatos. Synthesis of Soluble and Processable Rod-, Arrow-, Teardrop-, and Tetrapod-Shaped CdSe Nanocrystals. *Journal of the American Chemical Society*, 122(51):12700–12706, 2000.

[168] L. Manna, D. J. Milliron, A. Meisel, E. C. Scher, and A. P. Alivisatos. Controlled growth of tetrapod-branched inorganic nanocrystals. *Nature materials*, 2(6):382–5, 2003.

[169] F. Mathias, A. Fokina, K. Landfester, W. Tremel, F. Schmid, K. Char, and R. Zentel. Morphology Control in Biphasic Hybrid Systems of Semiconducting Materials. *Macromolecular Rapid Communications*, 36(11):959–983, 2015.

[170] M. W. Matsen. Fast and accurate SCFT calculations for periodic block-copolymer morphologies using the spectral method with Anderson mixing. *The European physical journal. E, Soft matter*, 30(4):361–9, 2009.

[171] M. W. Matsen. Strong-segregation limit of the self-consistent field theory for diblock copolymer melts. *The European physical journal. E, Soft matter*, 33(4): 297–306, 2010.

[172] M. W. Matsen and C. Barrett. Liquid-crystalline behavior of rod-coil diblock copolymers. *The Journal of Chemical Physics*, 109(10):4108, 1998.

[173] M. W. Matsen and F. S. Bates. Unifying Weak- and Strong-Segregation Block Copolymer Theories. *Macromolecules*, 29(4):1091–1098, 1996.

[174] M. Matsumoto and T. Nishimura. Mersenne twister: a 623-dimensionally equidistributed uniform pseudo-random number generator. *ACM Transactions on Modeling and Computer Simulation*, 8(1):3–30, 1998.

[175] M. Mazars, D. Levesque, and J. J. Weis. Monte Carlo study of a semiflexible liquid crystal model: The smectic phase. *The Journal of Chemical Physics*, 106 (14):6107, 1997.

[176] C. McBride, C. Vega, and L. G. MacDowell. Isotropic-nematic phase transition: Influence of intramolecular flexibility using a fused hard sphere model. *Physical review. E, Statistical, nonlinear, and soft matter physics*, 64(1):011703, 2001.

[177] S. C. McGrother, D. C. Williamson, and G. Jackson. A re-examination of the phase diagram of hard spherocylinders. *The Journal of Chemical Physics*, 104(17): 6755–6771, 1996.

[178] S. C. McGrother, A. Gil-Villegas, and G. Jackson. The liquid-crystalline phase behaviour of hard spherocylinders with terminal point dipoles. *Journal of Physics: Condensed Matter*, 8(47):9649–9655, 1999.

[179] W. McMillan. Simple Molecular Model for the Smectic A Phase of Liquid Crystals. *Physical Review A*, 4(3):1238–1246, 1971.

[180] D. J. Milliron, S. M. Hughes, Y. Cui, L. Manna, J. Li, L.-W. Wang, and A. P. Alivisatos. Colloidal nanocrystal heterostructures with linear and branched topology. *Nature*, 430(6996):190–5, 2004.

[181] L. C. H. Moh, M. D. Losego, and P. V. Braun. Solvent quality effects on scaling behavior of poly(methyl methacrylate) brushes in the moderate- and high-density regimes. *Langmuir : the ACS journal of surfaces and colloids*, 27(7):3698–702, 2011.

[182] P. A. Monson and M. Rigby. Virial equation of state for rigid spherocylinders. *Molecular Physics*, 35(5):1337–1342, 1978.

[183] M. Müller and F. Schmid. Incorporating fluctuations and dynamics in self-consistent field theories for polymer blends. *Advances in Polymer Science*, 185 (August):1–58, 2005.

[184] R. Netz and M. Schick. Liquid-Crystalline Phases of Semiflexible Diblock Copolymer Melts. *Physical Review Letters*, 77(2):302–305, 1996.

[185] Y. Ni, X. Ge, Z. Zhang, and Q. Ye. Fabrication and characterization of the plate-shaped ??-Fe2O3 nanocrystals. *Chemistry of Materials*, 14(3):1048–1052, 2002.

[186] T. Nishimura. Tables of 64-bit Mersenne twisters. *ACM Transactions on Modeling and Computer Simulation*, 10(4):348–357, 2000.

[187] N.-K. Oh, W.-C. Zin, J.-H. Im, J.-H. Ryu, and M. Lee. Organization of branched rod-coil molecules into a 3-D tetragonally perforated lamellar mesophase. *Chemical communications*, (9):1092–1093, 2004.

[188] B. D. Olsen and R. A. Segalman. Structure and Thermodynamics of Weakly Segregated Rod−Coil Block Copolymers. *Macromolecules*, 38(24):10127–10137, 2005.

[189] B. D. Olsen and R. A. Segalman. Nonlamellar Phases in Asymmetric Rod−Coil Block Copolymers at Increased Segregation Strengths. *Macromolecules*, 40(19): 6922–6929, 2007.

[190] B. D. Olsen and R. A. Segalman. Self-assembly of rod–coil block copolymers. *Materials Science and Engineering: R: Reports*, 62(2):37–66, 2008.

[191] B. D. Olsen, M. Shah, V. Ganesan, and R. A. Segalman. Universalization of the Phase Diagram for a Model Rod−Coil Diblock Copolymer. *Macromolecules*, 41 (18):6809–6817, 2008.

[192] L. Onsager. THE EFFECTS OF SHAPE ON THE INTERACTION OF COLLOIDAL PARTICLES. *Annals of the New York Academy of Sciences*, 51(4): 627–659, 1949.

[193] J. A. Osaheni and S. A. Jenekhe. Electroactive and Photoactive Rod-Coil Copolymers: Design, Synthesis, and Supramolecular Regulation of Photophysical Properties. *Journal of the American Chemical Society*, 117(28):7389–7398, 1995.

[194] R. Oslanec, J. Genzer, A. Faldi, R. J. Composto, and P. D. Garrett. Surface Enrichment in a Miscible Random Copolymer Blend: Influence of Polydispersity and Architecture. *Macromolecules*, 32(12):4098–4105, 1999.

[195] P. Padilla and E. Velasco. The isotropic-nematic transition for the hard Gaussian overlap fluid: Testing the decoupling approximation. *JOURNAL OF CHEMICAL PHYSICS*, 106(24):10299–10310, 1997.

[196] F. Palm, U. Henneboehle, and V. Erofeev. Improved verification of FSW-process modelling relating to the origin of material plasticity. *TWI (Hrsg.): Proceedings of . . .*, 290(5499):2123–2126, 2004.

[197] Q. Pang, Y. Cai, D. P. Nguyen, N. Regnault, N. Wang, R. Ferreira, and G. Bastard. CdSe Nano-tetrapods: Controllable Synthesis, Structure Analysis, and Electronic and Optical Properties. *Chemistry of Materials*, 17(21):5263–5267, 2005.

[198] D. A. Pardo, G. E. Jabbour, and N. Peyghambarian. Application of screen printing in the fabrication of organic light-emitting devices. *Advanced Materials*, 12(17): 1249–1252, 2000.

[199] R. G. Parr. Density Functional Theory. *Annual Review of Physical Chemistry*, 34 (1):631–656, 1983.

[200] J. Parsons. Nematic ordering in a system of rods. *Physical Review A*, 19(3): 1225–1230, 1979.

[201] A. Petrone, D. B. Lingerfelt, N. Rega, and X. Li. From charge-transfer to a charge-separated state: a perspective from the real-time TDDFT excitonic dynamics. *Physical chemistry chemical physics : PCCP*, 16(44):24457–65, 2014.

[202] N. H. Phuong, G. Germano, and F. Schmid. Elastic constants from direct correlation functions in nematic liquid crystals: A computer simulation study. *The Journal of Chemical Physics*, 115(15):7227, 2001.

[203] O. Pitois and B. François. Formation of ordered micro-porous membranes. *The European Physical Journal B*, 231(2):225–231, 1999.

[204] O. Pitois and B. François. Crystallization of condensation droplets on a liquid surface. *Colloid and Polymer Science*, 277(6):574–578, 1999.

[205] J. Polson and D. Frenkel. First-order nematic-smectic phase transition for hard spherocylinders in the limit of infinite aspect ratio. *Physical Review E*, 56(6): R6260–R6263, 1997.

[206] A. Poniewierski and R. Hołyst. Density-Functional Theory for Nematic and Smectic-A Ordering of Hard Spherocylinders. *Physical Review Letters*, 61(21): 2461–2464, 1988.

[207] A. Poniewierski and R. Hołyst. Density-functional theory for systems of hard rods. *Physical Review A*, 41(12):6871–6880, 1990.

[208] V. Pryamitsyn and V. Ganesan. Self-assembly of rod-coil block copolymers. *The Journal of chemical physics*, 120(12):5824–38, 2004.

[209] F. Pschenitzka and J. C. Sturm. Three-color organic light-emitting diodes patterned by masked dye diffusion. *Appl Phys Lett*, 74(13):1913–1915, 1999.

[210] S. Qi, H. Behringer, and F. Schmid. Using field theory to construct hybrid particle–continuum simulation schemes with adaptive resolution for soft matter systems. *New Journal of Physics*, 15(12):125009, 2013.

[211] G. Rabilloud. *High-Performance Polymer: Chemistry and Applications, Band 3*. Editions Technip, 2000.

[212] E. Raphael and P. G. de Gennes. Aggregation of flexible-rigid-flexible triblock copolymers. *Makromolekulare Chemie. Macromolecular Symposia*, 62(1):1–17, 1992.

[213] M. Reenders and G. ten Brinke. Compositional and Orientational Ordering in Rod−Coil Diblock Copolymer Melts. *Macromolecules*, 35(8):3266–3280, 2002.

[214] J. A. Rogers, Z. Bao, and L. Dhar. Fabrication of patterned electroluminescent polymers that emit in geometries with feature sizes into the submicron range. *Applied Physics Letters*, 73(3):294–296, 1998.

[215] L. S. Roman, O. Inganäs, T. Granlund, T. Nyberg, M. Svensson, M. R. Andersson, and J. C. Hummelen. Trapping light in polymer photodiodes with soft embossed gratings. *Advanced Materials*, 12(3):189–195, 2000.

[216] A. D. Rosato, Y. Lan, and D. T. Wang. Vibratory particle size sorting in multi-component systems. *Powder Technology*, 66(2):149–160, 1991.

[217] M. Rubinstein and R. Colby. *Polymer Physics*. Oxford University Press, 2003.

[218] J. H. Ryu, N. K. Oh, W. C. Zin, and M. Lee. Self-Assembly of Rod-Coil Molecules into Molecular Length-Dependent Organization. *Journal of the American Chemical Society*, 126(11):3551–3558, 2004.

[219] I. Santamaría-Holek and C. I. Mendoza. The rheology of concentrated suspensions of arbitrarily-shaped particles. *Journal of colloid and interface science*, 346(1): 118–26, 2010.

[220] N. Sary, L. Rubatat, C. Brochon, G. Hadziioannou, J. Ruokolainen, and R. Mezzenga. Self-Assembly of Poly(diethylhexyloxy-p-phenylenevinylene)-b-poly(4-vinylpyridine) Rod−Coil Block Copolymer Systems. *Macromolecules*, 40: 6990–6997, 2007.

[221] N. Sary, L. Rubatat, C. Brochon, G. Hadziioannou, and R. Mezzenga. Self-Assembly of Rod-Coil Block Copolymers for Photovoltaic Applications. *Macromolecular Symposia*, 268(1):28–32, 2008.

[222] N. Sary, F. Richard, C. Brochon, N. Leclerc, P. Lévêque, J.-N. Audinot, S. Berson, T. Heiser, G. Hadziioannou, and R. Mezzenga. A new supramolecular route for using rod-coil block copolymers in photovoltaic applications. *Advanced materials (Deerfield Beach, Fla.)*, 22(6):763–8, 2010.

[223] F. H. Schacher, P. A. Rupar, and I. Manners. Functional block copolymers: Nanostructured materials with emerging applications. *Angewandte Chemie - International Edition*, 51(32):7898–7921, 2012.

[224] J. Scheutjens and G. J. Fleer. Interaction between two adsorbed polymer layers. *Macromolecules*, 18(10):1882–1900, 1985.

[225] J. M. H. M. Scheutjens and G. J. Fleer. Statistical theory of the adsorption of interacting chain molecules. 1. Partition function, segment density distribution, and adsorption isotherms. *The Journal of Physical Chemistry*, 83(12):1619–1635, 1979.

[226] H. Schlaad, B. Smarsly, and M. Losik. The Role of Chain-Length Distribution in the Formation of Solid-State Structures of Polypeptide-Based Rod−Coil Block Copolymers. *Macromolecules*, 37(6):2210–2214, 2004.

[227] F. Schmid. Self-consistent field theories for complex fluids. *Journal of Physics: Condensed Matter*, 10:8105, 1998.

[228] F. Schmid. Theory and Simulation of Multiphase Polymer Systems. page 63, 2010.

[229] F. Schmid and N. H. Phuong. Spatial Order in Liquid Crystals: Computer Simulations of Systems of Ellipsoids. *Morphology of Condensed Matter*, pages 172–186, 2002.

[230] F. Schmid, S. Dolezel, O. Lenz, and S. Meinhardt. On ripples and rafts: Curvature induced nanoscale structures in lipid membranes. *Journal of Physics: Conference Series*, 487(1):012004, 2014.

[231] R. A. Segalman, B. McCulloch, S. Kirmayer, and J. J. Urban. Block Copolymers for Organic Optoelectronics. *Macromolecules*, 42(23):9205–9216, 2009.

[232] A. N. Semenov and A. R. Khokhlov. Statistical physics of liquid-crystalline polymers. *Soviet Physics Uspekhi*, 31(11):988–1014, 1988.

[233] A. N. Semenov and S. V. Vasilenko. Theory of the nematic-smectic-A transition in a melt of macromolecules consisting of a rigid and a flexible block. *Journal of Experimental and Theoretical Physics*, 63(1):70–79, 1986.

[234] E. M. Sevick and D. R. M. Williams. Anomalous height increases upon bending for an Alexander–de Gennes polymer brush. *The Journal of Chemical Physics*, 105(20):9334, 1996.

[235] I. F. Shadrin, M. R. Sharafutdinov, and A. M. Elyashevich. Computer Simulation of a Hard-Rod System: Structural Transitions and Clusters. *Journal of Chemical Information and Modeling*, 34(2):335–338, 1994.

[236] M. Shah and V. Ganesan. Correlations between Morphologies and Photovoltaic Properties of Rod−Coil Block Copolymers. *Macromolecules*, 43(1):543–552, 2010.

[237] R. Shashidhar, B. Ratna, and S. Prasad. Nematic-Smectic-A-Smectic-C Multicritical Point in a Single-Component System. *Physical Review Letters*, 53(22): 2141–2144, 1984.

[238] K. G. Soga, H. Guo, and M. J. Zuckermann. Polymer Brushes in a Poor Solvent. *Europhysics Letters (EPL)*, 29(7):531–536, 1995.

[239] A. M. Somoza and P. Tarazona. Nematic-Smectic-A-Smectic-C Transitions in Systems of Parallel Hard Molecules. *Physical Review Letters*, 61(22):2566–2569, 1988.

[240] A. M. Somoza and P. Tarazona. Density functional approximation for hard-body liquid crystals. *The Journal of Chemical Physics*, 91(1):517–527, 1989.

[241] A. M. Somoza and P. Tarazona. Nematic and smectic liquid crystals of hard spherocylinders. *Physical Review A*, 41(2):965–970, 1990.

[242] W. Song, P. Tang, Y. Yang, and A.-C. Shi. New numerical implementation of self-consistent field theory for semiflexible polymers. *Macromolecules*, 42(16): 6300–6309, 2009.

[243] W. Song, P. Tang, F. Qiu, Y. Yang, and A.-C. Shi. Phase behavior of rod-coil diblock copolymer and homopolymer blends from self-consistent field theory. *The journal of physical chemistry. B*, 115(26):8390–400, 2011.

[244] A. Stepanescu and E. Miraldi. Landau Theory of the nematic-isotropic phase transition. *International Journal of Modern Physics B*, 06(03n04):389–394, 1992.

[245] I. M. Storm, M. Kornreich, A. Hernandez-Garcia, I. K. Voets, R. Beck, M. A. Cohen Stuart, F. A. M. Leermakers, and R. de Vries. Liquid Crystals of Self-Assembled DNA Bottlebrushes. *The Journal of Physical Chemistry B*, 119(10): 4084–4092, 2015.

[246] S. I. Stupp. Supramolecular Materials: Self-Organized Nanostructures. *Science*, 276(5311):384–389, 1997.

[247] Y.-W. Su, S.-C. Lan, and K.-H. Wei. Organic photovoltaics. *Materials Today*, 15 (12):554–562, 2012.

[248] A. Subbotin, R. Stepanyan, M. Knaapila, O. Ikkala, and G. ten Brinke. Phase behavior and structure formation of hairy-rod supramolecules. *The European physical journal. E, Soft matter*, 12(2):333–45, 2003.

[249] B. Sun and N. C. Greenham. Improved efficiency of photovoltaics based on CdSe nanorods and poly(3-hexylthiophene) nanofibers. *Physical chemistry chemical physics : PCCP*, 8(30):3557–60, 2006.

[250] B. Sun, H. J. Snaith, A. S. Dhoot, S. Westenhoff, and N. C. Greenham. Vertically segregated hybrid blends for photovoltaic devices with improved efficiency. *Journal of Applied Physics*, 97(1):014914, 2005.

[251] Y. Tada, S. Akasaka, H. Yoshida, H. Hasegawa, E. Dobisz, D. Kercher, and M. Takenaka. Directed Self-Assembly of Diblock Copolymer Thin Films on Chemically-Patterned Substrates for Defect-Free Nano-Patterning. *Macromolecules*, 41(23): 9267–9276, 2008.

[252] J. Taffs, A. Malins, S. R. Williams, and C. P. Royall. A structural comparison of models of colloid-polymer mixtures. *Journal of physics. Condensed matter : an Institute of Physics journal*, 22(10):104119, 2010.

[253] Y. Tao, H. Zohar, B. D. Olsen, and R. A. Segalman. Hierarchical nanostructure control in rod-coil block copolymers with magnetic fields. *Nano letters*, 7(9): 2742–6, 2007.

[254] Y. Tao, B. McCulloch, S. Kim, and R. A. Segalman. The relationship between morphology and performance of donor–acceptor rod–coil block copolymer solar cells. *Soft Matter*, 5(21):4219, 2009.

[255] M. Taylor, R. Hentschke, and J. Herzfeld. Theory of Ordered Phases in a System of Parallel Hard Spherocylinders. *Physical Review Letters*, 62(7):800–803, 1989.

[256] K. K. Tenneti, X. Chen, C. Y. Li, Y. Tu, X. Wan, Q.-F. Zhou, I. Sics, and B. S. Hsiao. Perforated layer structures in liquid crystalline rod-coil block copolymers. *Journal of the American Chemical Society*, 127(44):15481–90, 2005.

[257] P. E. Theodorakis, W. Paul, and K. Binder. Analysis of the cluster formation in two-component cylindrical bottle-brush polymers under poor solvent conditions: a simulation study. *The European physical journal. E, Soft matter*, 34(5):1–12, 2011.

[258] P. D. Topham, A. J. Parnell, and R. C. Hiorns. Block copolymer strategies for solar cell technology. *Journal of Polymer Science Part B: Polymer Physics*, pages n/a–n/a, 2011.

[259] D. M. Trombly, V. Pryamitsyn, and V. Ganesan. Interfacial properties of statistical copolymer brushes in contact with homopolymer melts. *The Journal of chemical physics*, 134(15):154903, 2011.

[260] Y.-C. Tseng and S. B. Darling. Block Copolymer Nanostructures for Technology. *Polymers*, 2(4):470–489, 2010.

[261] Y. Tsukahara, Y. Ohta, and K. Senoo. Liquid crystal formation of multibranched polystyrene induced by molecular anisotropy associated with its high branch density. *Polymer*, 36(17):3413–3416, 1995.

[262] Y. Tu, X. Wan, H. Zhang, X. Fan, D. Lü, X. Chen, and Q.-F. Zhou. Self-assembly of rod-coil diblock copolymers—Influence of the rod length. *Chinese Journal of Polymer Science*, 21, 2003.

[263] Y. Tu, M. J. Graham, R. M. Van Horn, E. Chen, X. Fan, X. Chen, Q. Zhou, X. Wan, F. W. Harris, and S. Z. D. Cheng. Controlled organization of self-assembled rod-coil block copolymer micelles. *Polymer*, 50(22):5170–5174, 2009.

[264] R. Tuinier, T. Taniguchi, and H. H. Wensink. Phase behavior of a suspension of hard spherocylinders plus ideal polymer chains. *The European physical journal. E, Soft matter*, 23(4):355–65, 2007.

[265] R. Vácha and D. Frenkel. Relation between Molecular Shape and the Morphology of Self-Assembling Aggregates: A Simulation Study. *Biophysical Journal*, 101(6): 1432–1439, 2011.

[266] J. S. van Duijneveldt and M. P. Allen. Computer simulation study of a flexible-rigid-flexible model for liquid crystals. *Molecular Physics*, 92(5):855–870, 1997.

[267] J. S. van Duijneveldt and M. P. Allen. Free energy barriers for interlayer diffusion in the smectic-A phase of hard spherocylinders. *Molecular Physics*, 90(2):243–250, 1997.

[268] J. S. van Duijneveldt, A. Gil-Villegas, G. Jackson, and M. P. Allen. Simulation study of the phase behavior of a primitive model for thermotropic liquid crystals: Rodlike molecules with terminal dipoles and flexible tails. *The Journal of Chemical Physics*, 112(20):9092, 2000.

[269] R. Van Roij, P. Bolhuis, B. Mulder, and D. Frenkel. Transverse interlayer order in lyotropic smectic liquid crystals. *Physical Review E*, 52(2):R1277–R1280, 1995.

[270] S. Varga, A. Gábor, E. Velasco, L. Mederos, and F. J. Vesely. Demixed and ordered phases in hard-rod mixtures. *Molecular Physics*, 106(15):1939–1947, 2008.

[271] J. Veerman and D. Frenkel. Computer simulation of crystal nucleation of parallel hard spherocylinders. *Physica A: Statistical Mechanics and its Applications*, 156 (2):599–612, 1989.

[272] J. Veerman and D. Frenkel. Phase diagram of a system of hard spherocylinders by computer simulation. *Physical Review A*, 41(6):3237–3244, 1990.

[273] C. Vega and S. Lago. A fast algorithm to evaluate the shortest distance between rods. *Computers & Chemistry*, 18(1):55–59, 1994.

[274] C. Vega and P. A. Monson. Plastic crystal phases of hard dumbbells and hard spherocylinders. *The Journal of Chemical Physics*, 107(7):2696, 1997.

[275] F. J. Vesely. Lennard-Jones sticks: a new model for linear molecules. *The Journal of chemical physics*, 125(21):214106, 2006.

[276] J. Vieillard-Baron. The equation of state of a system of hard spherocylinders. *Molecular Physics*, 28(3):809–818, 1974.

[277] R. L. C. Vink and T. Schilling. Interfacial tension of the isotropic-nematic interface in suspensions of soft spherocylinders. *Physical Review E - Statistical, Nonlinear and Soft Matter Physics*, 71(5 Pt 1):051716, 2005.

[278] G. J. Vroege and H. N. W. Lekkerkerker. Phase transitions in lyotropic colloidal and polymer liquid crystals. *Reports on Progress in Physics*, 55(8):1241–1309, 1992.

[279] P. Wang, A. Abrusci, H. M. P. Wong, M. Svensson, M. R. Andersson, and N. C. Greenham. Photoinduced charge transfer and efficient solar energy conversion in a blend of a red polyfluorene copolymer with CdSe nanoparticles. *Nano letters*, 6 (8):1789–93, 2006.

[280] Q. Wang. Theory and simulation of the self-assembly of rod–coil block copolymer melts: recent progress. *Soft Matter*, 7(8):3711, 2011.

[281] U. Welling and G. Germano. Efficiency of linked cell algorithms. *Computer Physics Communications*, 182(3):611–615, 2011.

[282] H. H. Wensink and G. J. Vroege. Isotropic–nematic phase behavior of length-polydisperse hard rods. *The Journal of Chemical Physics*, 119(13):6868, 2003.

[283] A. Werner, F. Schmid, and M. Müller. Monte Carlo simulations of copolymers at homopolymer interfaces: Interfacial structure as a function of the copolymer density. *The Journal of chemical physics*, 110:5370, 1998.

[284] M. J. Westwater. On Edwards' model for long polymer chains. *Communications in Mathematical Physics*, 72(2):131–174, 1980.

[285] Wikipedia. http://upload.wikimedia.org/wikipedia/en/a/a0/Lyotropic1.jpg Date accessed: 2014/10/15.

[286] D. R. M. Williams and G. H. Fredrickson. Cylindrical micelles in rigid-flexible diblock copolymers. *Macromolecules*, 25(13):3561–3568, 1992.

[287] D. R. M. Williams and A. Halperin. Microphases of nematic diblock copolymers: Reentry and finite size effects. *Physical Review Letters*, 71(10):1557–1560, 1993.

[288] M. R. Wilson, A. B. Thomas, M. Dennison, and A. J. Masters. Computer simulations and theory of polymer tethered nanorods: the role of flexible chains in influencing mesophase stability. *Soft Matter*, 5(2):363, 2009.

[289] M. Wintermantel, K. Fischer, M. Gerle, R. Ries, M. Schmidt, K. Kajiwara, H. Urakawa, and I. Wataoka. Lyotropic Phases Formed by"Molecular Bottlebrushes". *Angewandte Chemie International Edition in English*, 34(1314):1472–1474, 1995.

[290] W.-Y. Wong and C.-L. Ho. Organometallic photovoltaics: a new and versatile approach for harvesting solar energy using conjugated polymetallaynes. *Accounts of chemical research*, 43(9):1246–56, 2010.

[291] J. Wu. Density functional theory for chemical engineering: From capillarity to soft materials. *AIChE Journal*, 52(3):1169–1193, 2006.

[292] L. Wu, E. A. Müller, and G. Jackson. Understanding and Describing the Liquid-Crystalline States of Polypeptide Solutions: A Coarse-Grained Model of PBLG in DMF. *Macromolecules*, 47(4):1482–1493, 2014.

[293] Y. Wu, C. Wadia, W. Ma, B. Sadtler, and A. P. Alivisatos. Synthesis and photovoltaic application of copper(I) sulfide nanocrystals. *Nano letters*, 8(8): 2551–5, 2008.

[294] G. Yang, P. Tang, Y. Yang, and Q. Wang. Self-assembled microstructures of confined rod-coil diblock copolymers by self-consistent field theory. *The journal of physical chemistry. B*, 114(46):14897–906, 2010.

[295] J. K. W. Yang, Y. S. Jung, J.-B. Chang, R. A. Mickiewicz, A. Alexander-Katz, C. A. Ross, and K. K. Berggren. Complex self-assembled patterns using sparse commensurate templates with locally varying motifs. *Nature nanotechnology*, 5(4): 256–260, 2010.

[296] A. Yassar, L. Miozzo, R. Gironda, and G. Horowitz. Rod–coil and all-conjugated block copolymers for photovoltaic applications. *Progress in Polymer Science*, 38 (5):791–844, 2013.

[297] M. Zanella, G. Bertoni, I. R. Franchini, R. Brescia, D. Baranov, and L. Manna. Assembly of shape-controlled nanocrystals by depletion attraction. *Chemical communications (Cambridge, England)*, 47(1):203–5, 2011.

[298] T. Zhao and X. Wang. Phase behavior of lyotropic rigid-chain polymer liquid crystal studied by dissipative particle dynamics. *The Journal of chemical physics*, 135(24):244901, 2011.

[299] X. Zhu, L. Wang, and J. Lin. Self-Assembly of Rod-Coil Multiblock Copolymers: A Strategy for Creating Hierarchical Smectic Structures. *The journal of physical chemistry. B*, 2013.

[300] Y.-C. Zhu, Y. Bando, D.-F. Xue, and D. Golberg. Nanocable-aligned ZnS tetrapod nanocrystals. *Journal of the American Chemical Society*, 125(52):16196–7, 2003.

[301] J. Zong, X. Zhang, and Q. Wang. Fast off-lattice Monte Carlo simulations of soft-core spherocylinders: isotropic-nematic transition and comparisons with virial expansion. *The Journal of chemical physics*, 137(13):134904, 2012.

[302] Z. Zuo, Y. Li, and H. Liu. The gas–liquid tunable self-assembly properties of rod–coil diblock copolymer: donor–acceptor alternating structure served as rod segment. *Colloid and Polymer Science*, 289(13):1469–1478, 2011.